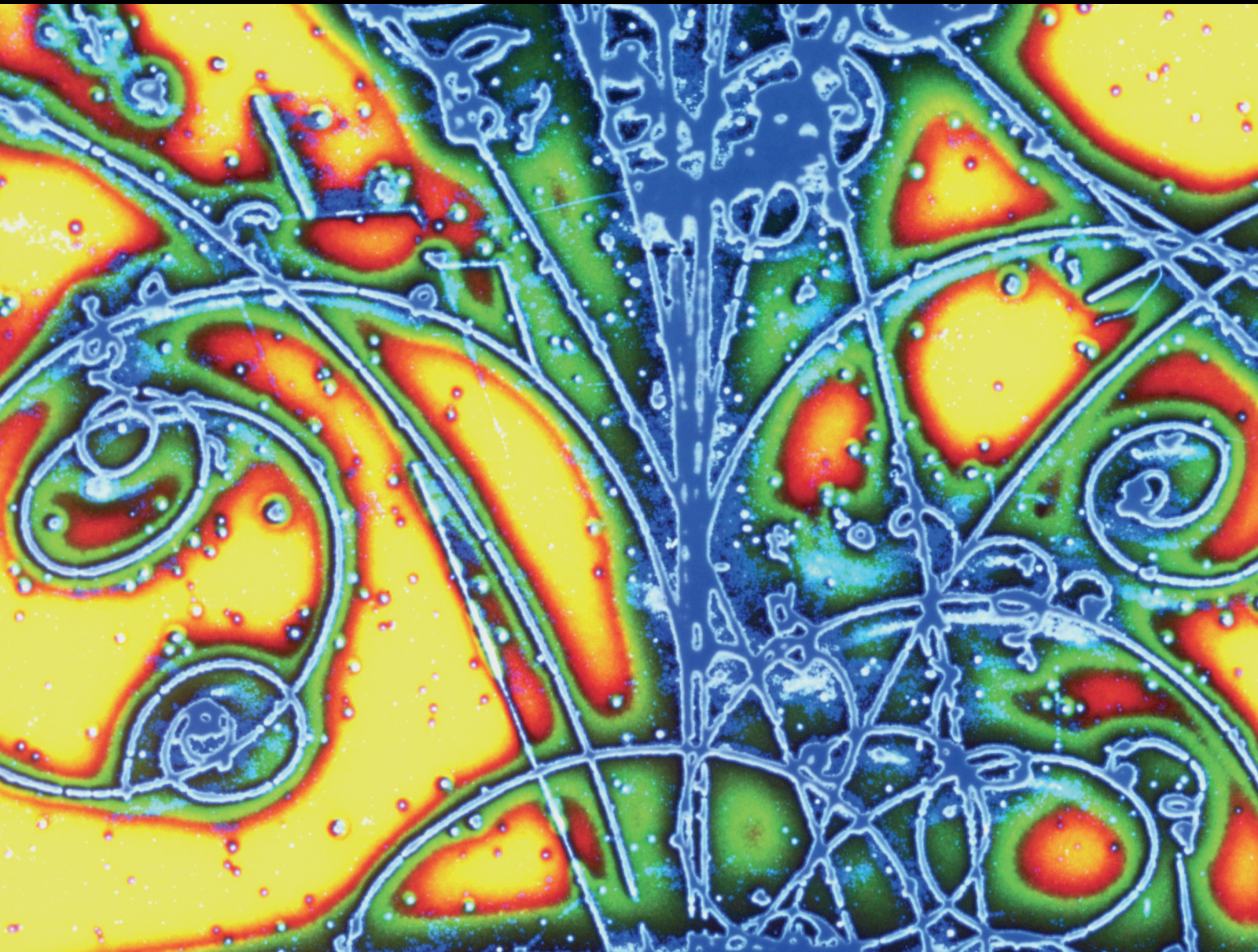# Properties of Particle Production and System Evolution in BES-Wide Energy Range

Lead Guest Editor: Fu-Hu Liu
Guest Editors: Sakina Fakhraddin, Raghunath Sahoo, Edward Sarkisyan-Grinbaum, and Bhartendu K. Singh

Properties of Particle Production and System Evolution in BES-Wide Energy Range

Properties of Particle Production and System Evolution in BES-Wide Energy Range

Lead Guest Editor: Fu-Hu Liu
Guest Editors: Sakina Fakhraddin, Raghunath Sahoo, Edward Sarkisyan-Grinbaum, and Bhartendu K. Singh

Contents

Editorial

Properties of Particle Production and System Evolution in BES-Wide Energy Range

Fu-Hu Liu [ID],[1] Sakina Fakhraddin,[2,3] Raghunath Sahoo [ID],[4] Edward K. Sarkisyan-Grinbaum,[5,6] and Bhartendu K. Singh[7]

[1]Institute of Theoretical Physics, Shanxi University, Taiyuan, Shanxi 030006, China
[2]Physics Department, College of Science & Arts in RK, Qassim University, Buraidah, 51452 Qassim, Saudi Arabia
[3]Physics Department, Faculty of Science, Sana'a University, P.O. Box 13499, Sana'a, Yemen
[4]Discipline of Physics, School of Basic Sciences, Indian Institute of Technology Indore, Indore 453552, India
[5]Experimental Physics Department, CERN, 1211 Geneva 23, Switzerland
[6]Department of Physics, The University of Texas at Arlington, Arlington, TX 76019, USA
[7]Physics Department, Banaras Hindu University, Varanasi 221005, India

Correspondence should be addressed to Fu-Hu Liu; fuhuliu@163.com

The beam energy scan (BES) program at the Relativistic Heavy Ion Collider (RHIC) in Brookhaven and Super Proton Synchrotron (SPS) at CERN performs nucleus-nucleus collisions in the energy range of 3-39 GeV/nucleon leading to high baryon density and temperature around the expected critical point of deconfinement phase transition. In addition, the Facility for Antiproton and Ion Research (FAIR) in GSI also performs nucleus-nucleus collisions in the BES energy region. The features of particle production and system evolution in these types of collisions attract high interest and are extensively studied both experimentally and theoretically. It is believed that above the critical energy of deconfinement phase transition, e.g., at RHIC and Large Hadron Collider (LHC), the properties of particle production and system evolution may differ from those at the BES (RHIC-BES, SPS-BES, and FAIR). These properties are related to those of early universe considered to go through the stages of high baryon density and temperature.

Large amount of data obtained by high-energy experiments worldwide is being published to be scrutinized. Different signatures such as the chemical and kinetic freeze-out temperature, effective temperature, speed of sound, tension of string between valence quarks in colliding nucleons, minimum distance between these quarks, chemical potential of

different types of particles and of different quark flavors, time evolution of collision system, and ratio of viscosity to entropy density are predicted by different models and can be obtained from the measured particle spectra allowing us to study the properties of the system formation and its evolution.

This special issue concerns many topics, for example, (i) description of particle distributions and correlations, studies of statistical laws and dynamical properties of particle production; (ii) studies of the properties of system evolution in beam energy scan program; (iii) extraction of different signatures based on the particle spectra, correlations, and yield ratios in BES-wide energy range; (iv) searches for the softest point of the equation of state and for the critical point of deconfinement phase transition; (v) comparison of the properties of particle production and system evolution at the BES energies with those at the RHIC and LHC energies; and (vi) comparison of the properties of particle production and system evolution in nucleus-nucleus collisions with those of small systems formed in particle collisions.

In the article "A Description of Transverse Momentum Distributions in $p + p$ Collisions at RHIC and LHC Energies" by J.-Q. Hui and Z.-J. Jiang, the authors assume the existence of longitudinal collective motion and long-range interactions in the hot and dense matter created in $p + p$ collisions. The

relativistic hydrodynamics incorporating with the nonextensive statistics is used to analyze the transverse momentum distributions of the particles. The investigation of the present paper shows that the hybrid model can give a good description of the currently available experimental data obtained in $p + p$ collisions at RHIC and LHC energies, except for p and $\bar{p}$ produced in the range of $p_T > 3.0$ GeV/c at $\sqrt{s} = 200$ GeV. This article confirms that the hydrodynamics is suitable for the smaller colliding systems such as $p + p$ collisions.

In the article "Out-of-Equilibrium Transverse Momentum Spectra of Pions at LHC Energies" by A. N. Tawfik, the author investigates the transverse momentum spectra of positive pions measured in the ALICE experiment by utilizing two thermal approaches; one is based on degeneracy of nonperfect Bose-Einstein gas and the other imposes an ad hoc finite pion-chemical potential. It is shown that the inclusion of missing hadron states and the out-of-equilibrium contribute greatly to the characterization of pion production. A reproduction of these transverse momentum spectra is achieved at pion-chemical potential of 120 MeV, and this covers the entire range of transverse momentum. This article confirms a manifestation of not-yet-regarded anomalous pion production, which is related to "anomalous" proton-to-pion ratios at top RHIC and LHC energies.

In the article "Contributions of Jets in Net Charge Fluctuations from the Beam Energy Scan at RHIC and LHC" by B. Ali et al., the authors study the dynamical net charge fluctuations in nucleus-nucleus collisions at RHIC-BES and LHC energies by a hadronic model. A Monte Carlo generator, HIJING, is used to generate events in two different modes, HIJING-default with jet quenching switched off and jet/minijet production switched off. A popular variable is used to study the net charge fluctuations in different centrality bins, and the findings are compared with the available experimental data. This article shows that nucleus-nucleus collisions can be treated as the superpositions of multiple nucleon-nucleon collisions. The findings also reveal that the production of jets and minijets plays a dominant role in reducing the strength of particle correlations and fluctuations.

In the article "Centrality Dependence of Multiplicity Fluctuations in Ion-Ion Collisions from the Beam Energy Scan at FAIR" by A. Chandra et al., the authors investigate the multiplicity distributions and event-by-event fluctuations in Au-Au collisions at FAIR energies. Events corresponding to FAIR energies are simulated in the framework of UrQMD model. It is observed that the mean and the width of multiplicity distributions monotonically increase with beam energy. The trend of variations of dispersion with mean number of participating nucleons for the centrality-bin width of 5% is in accord with the Central Limit Theorem. The multiplicity distributions in various centrality bins are observed to obey KNO scaling. The trends of variations of scaled variance with beam energy are also found to support the KNO scaling predictions for larger collision centrality.

The article "Kinetic Freeze-Out Temperature and Transverse Flow Velocity in Au-Au Collisions at RHIC-BES Energies" by M. Waqas and B.-C. Li studies the midrapidity transverse momentum spectra of charged hadrons produced in central and peripheral Au-Au collisions at RHIC-BES

energies. The blast-wave model with the Boltzmann-Gibbs statistics is adopted to fit available experimental data measured by the STAR Collaboration at the RHIC-BES energies. The authors observe that the kinetic freeze-out temperature, transverse flow velocity, mean transverse momentum, and initial temperature increase with collision energy in the considered RHIC-BES energy range and with event centrality from peripheral to central collisions. This article confirms the complex correlation between kinetic freeze-out temperature and transverse flow velocity.

The article "Elliptic Flow of Identified Particles in Pb–Pb Collisions at $\sqrt{s_{NN}} = 5.02$ TeV" by E.-Q. Wang et al. investigates the elliptic flow coefficients of particles $\pi^\pm$, $K^\pm$, $p + \bar{p}$, $\Lambda + \bar{\Lambda}$, and K_S^0 produced in Pb-Pb collisions at the center-of-mass energy of $\sqrt{s_{NN}} = 5.02$ TeV by using a Tsallis-Pareto-type function and the multisource thermal model. In the process of system evolution, deformation and translation occur for the isotropic emission source due to geometric structure, pressure gradient, and thermal diffusion effects, which leads to anisotropy in the azimuth distribution of identified particles. Based on these dynamic factors, the dependence of elliptic flow on transverse momentum is described. This article shows that source deformation plays a main role in the system evolution, and source translation can be neglected.

The article "Study of Spin–Spin Correlations between Quark and a Spin-1/2 Composite System" by S. Kaur and H. Dahiya studies the correlation between the fermion composite system and quark spins by using the light-cone quark-diquark model. The authors do the calculations for u-quark and d-quark in the fermion system by considering different polarization configurations of both. The contribution from scalar and axial-vector diquarks is taken into account. The overlap representation of light-front wave-functions is used for the calculations. The spin-spin correlations for u and d quarks are presented in transverse impact-parameter plane and transverse momentum plane as well. This article also confirms that the spin-spin correlations are related to the Wigner distributions by integrating which over transverse momentum the measurable quantities can be extracted.

In the article "Transverse Momentum and Pseudorapidity Dependence of Particle Production in Xe–Xe Collisions at $\sqrt{s_{NN}} = 5.44$ TeV" by Z.-L. Guo et al., the Tsallis statistics is combined with a multisource thermal model through the collision-system configuration. The improved model is used to investigate the transverse momentum and pseudorapidity of charged particles produced in Xe-Xe collisions at $\sqrt{s_{NN}} = 5.44$ TeV. The authors discuss detailedly the thermodynamic properties, which are taken from the transverse momentum distributions of charged particles for events with different centrality classes. The pseudorapidity spectra of charged particles for events with different centrality classes are also described consistently in the model. In addition, the model results estimate intuitively the longitudinal configuration of the collision system.

In the article "Investigation of Particle Distributions in Xe-Xe Collision at $\sqrt{s_{NN}} = 5.44$ TeV with the Tsallis Statistics" by H.-F. Zhao et al., the authors use the Tsallis statistics

to investigate the transverse momentum distribution of charged particles produced in Xe-Xe collisions at the LHC. Meanwhile, the nuclear modification factor of the charged particles is studied. To obtain the related results, the authors use a new attempt which is improved by the Tsallis statistics in relaxation time approximation. Considering relaxation time approximation of the collision term, the authors achieve the final-state distribution by solving the Boltzmann transport equation, where the initial distribution is inserted consistently. The calculated results are approximately in agreement with the experimental data measured by the ALICE Collaboration.

In the article "Centrality Dependence of Multiplicity Fluctuations from a Hydrodynamical Approach" by H.-H. Ma et al., the authors investigate the centrality dependence of the multiplicity fluctuations regarding the recent measurements from STAR Collaboration. By employing a hydrodynamical approach, this article is dedicated to the noncritical aspects of the phenomenon. To be specific, in addition to the thermal fluctuations, finite volume corrections, and resonance decay at the freeze-out surface, this model is focused on the properties of the hydrodynamic expansion of the system and the event-by-event initial fluctuations. The real signal of the critical point can only be obtained after subtracting the background which is investigated in this article. The results are also compared to those of the hadronic resonance gas and transport models.

In the article "Study of Di-Muon Production Process in pp Collision in CMS Data from Symmetry Scaling Perspective" by S. Bhaduri et al., two methodologies, namely, MF-DFA and MF-DXA analyses, are used for the study of scaling analysis of the dynamics of the di-muon production process using the primary data set of Run-A (2011) and Run-B (2012) of pp collisions at 7 and 8 TeV from CMS collaboration. The authors have analyzed how this scaling pattern has evolved from one rapidity range to the next one and how this change evolved from 7 TeV to 8 TeV. Many interesting findings are obtained by the novel method of data analysis. This new approach has the potential to provide clue to possible different dynamics behind di-muon production (including beyond the standard model) in different rapidity domains which may change with higher and higher energy.

The article "Intermittency Study of Charged Particles Generated in Pb-Pb Collisions at $\sqrt{s_{NN}} = 2.76$ TeV Using EPOS3" by R. Gupta and S. K. Malik studies the charged particle multiplicity fluctuations in Pb-Pb collisions for the events generated using EPOS3 (hydro and hydro+cascade). Normalized factorial moments (Fq) have been determined in the strict sense of intermittency being a power-law behavior of Fq with decreasing bin size. There is no significant scaling behavior in these moments with the decreasing bin size. The values of scaling exponent deduced for a few transverse momentum bins are greater than the value for the second-order phase transition predicted by the Ginzburg-Landau theory. Fractal dimensions decrease with the order of the moment, which indicates the existence of a multifractal nature of the studied events.

This issue brings together a collection of articles. We hope this will be a useful issue for researchers working in related areas. Meanwhile, we regret that more manuscripts submitted for publication in this issue have not been accepted following the reviewer's reports.

Conflicts of Interest

The editors declare that they have no conflicts of interest regarding the publication of this special issue.

Acknowledgments

Research Article

Intermittency Study of Charged Particles Generated in Pb-Pb Collisions at $\sqrt{s_{NN}} = 2.76\,\mathrm{TeV}$ Using EPOS3

Ramni Gupta [ID] and Salman Khurshid Malik [ID]

Department of Physics, University of Jammu, Jammu, Jammu and Kashmir, India

Correspondence should be addressed to Salman Khurshid Malik; maroozmalik@gmail.com

Charged particle multiplicity fluctuations in Pb-Pb collisions are studied for the central events generated using EPOS3 (hydro and hydro+cascade) at $\sqrt{s_{NN}} = 2.76\,\mathrm{TeV}$. Intermittency analysis is performed in the midrapidity region in two-dimensional (η, ϕ) phase space within the narrow transverse momentum (p_T) bins in the low $\mathrm{p_T}$ region ($p_T \leq 1.0\,\mathrm{GeV}/c$). Power-law scaling of the normalized factorial moments with the number of bins is not observed to be significant in any of the p_T bins. Scaling exponent ν, deduced for a few p_T bins, is greater than that of the value 1.304, predicted for the second-order phase transition by the Ginzburg-Landau theory. The link in the notions of fractality is also studied. Generalized fractal dimensions, D_q, are observed to decrease with the order of the moment q suggesting the multifractal nature of the particle generation in EPOS3.

1. Introduction

The strongly interacting dense state of matter, believed to represent QGP (quark-gluon plasma) after its creation in heavy-ion collision, rapidly cools into a spray of particles. This array of particles carry signals of QGP and its properties which can be directly and indirectly measured by detectors that are encircling the collision point. Of the myriad of analysis tools to understand the dynamics of this particle production [1] and phase changes in the matter while passing into the QGP phase from the hadronic phase and vice versa, an important one is the fluctuations study of the observables. Lattice QCD predicts large fluctuations being associated with the system undergoing phase transition. Multiplicity distributions characterize the system formed or any phase transition in the heavy-ion collisions. Studies of multiplicity fluctuations have prompted considerable advances in this area of research. Large particle density fluctuations in the JACEE event [2] and its explanation by normalized factorial moments triggered investigations of multiplicity fluctuation patterns in multihadronic events with decreasing domains of phase space [3]. The presence of power-law behaviour or

scale invariance of normalized factorial moments with decreasing phase space interval or increasing bins is termed as *intermittency* [4, 5]. Observation of intermittency signals the presence of self-similar and fractal nature of the particle production. If fluctuations have a dynamical origin, the underlying probability density will be reflected as intermittency behaviour. The existence of dynamical fluctuations can thus be studied using normalized factorial moments (NFMs) [4] in one-, two-, or three-dimensional phase space.

The idea of intermittency has been obtained from the theory of turbulent flow. There, it signifies as a property of turbulent fluid: vortices of fluid with different size alternate in such a way that they form self-similar structures. These vortices do not necessarily fill in the entire volume, but they instead create an intermittent pattern in the regions of laminar flow. This property is given by a power-law variation of the vortex-distribution moments on their size. So, the self-similar nature of vortices directly creates a relation between intermittency and fractality. Self-similar objects of nonintegral dimensions are called *fractals* [6]. A fractal dimension is a generalization of an ordinary topological dimensionality to nonintegers.

The proposal to look for intermittency also prompts a thorough study of phase-transition models. A very straightforward model that offers some hint on the nature of a second-order phase transition is the Ising model in two dimensions [7]. Intermittency in Ising model has been studied both analytically and numerically [8, 9], and the anomalous fractal dimension (d_q) is found to be 1/8, independent of the order of moment, q. It has been conjectured on this acount that intermittency may be monofractal in QCD second-order phase transition [10]. However, all types of interactions including heavy-ion collisions show multi-fractal behaviour [3, 11]. Also, Yang-Mills fields have been applied to QCD within asymptotic approximation where the fractal dimension is determined as a function of entropic index, and value obtained for entropic index is in good agreement with the experimental data [12]. For the first-order phase transition, all d_q are zero, and no intermittency was observed. Intermittency has also been studied in Ginzburg-Landau (GL) theory, which has been accustomed to explain the confinement of magnetic fields into fluxoids in a type-II superconductor. From the study of normalized factorial moments with decreasing phase space bins for the Ginzburg-Landau second-order formalism, the anomalous fractal dimension is observed not to be constant. It follows $d_q/d_2 = (q - 1)^{(\nu-1)}$, where ν is the scaling exponent [13]. ν is observed to be a universal quantity valid for all systems describable by the GL theory for the second-order phase transition, and it is independent of the underlying dimensions or the parameters of the model. This is of particular importance for a QCD phase transition, since neither the transition temperature nor the other important parameters are known there. If a signature of quark-hadron phase transition depends on the details of the heavy-ion collisions, e.g., nuclear sizes, collision energy, and transverse energy, then even after the system has passed the thresholds for the creation of QGP, such a signature is likely to be sensitive to this theory.

In this work, intermittency analysis is performed for the charged particles generated in the midrapidity region of the central events ($b \leq 3.5$ fm) from Pb-Pb collisions at $\sqrt{s_{NN}} = 2.76$ TeV using EPOS3 (hydro) and EPOS3 (hydro+cascade).

The plan of the paper is as follows: the EPOS3 model [14] is introduced in Section 2. The methodology of analysis is given in Section 3. In Section 4, observations and results are given followed by a summary in Section 5.

2. A Brief Introduction to EPOS3

EPOS3 [14–16] is a hybrid Monte-Carlo event generator with a 3+1D hydrodynamical expanding system. This model is based on flux tube initial conditions which are generated in the Gribov-Regge multiple scattering framework. The formalism is referred to as "Parton based Gribov Regge Theory", which is detailed in [17]. An individual scattering gives rise to a parton ladder and is called a *Pomeron*. Each parton ladder eventually shows up as flux tubes (or strings) and is identified by a pQCD hard process, plus initial, and final state linear parton emission. Satura-
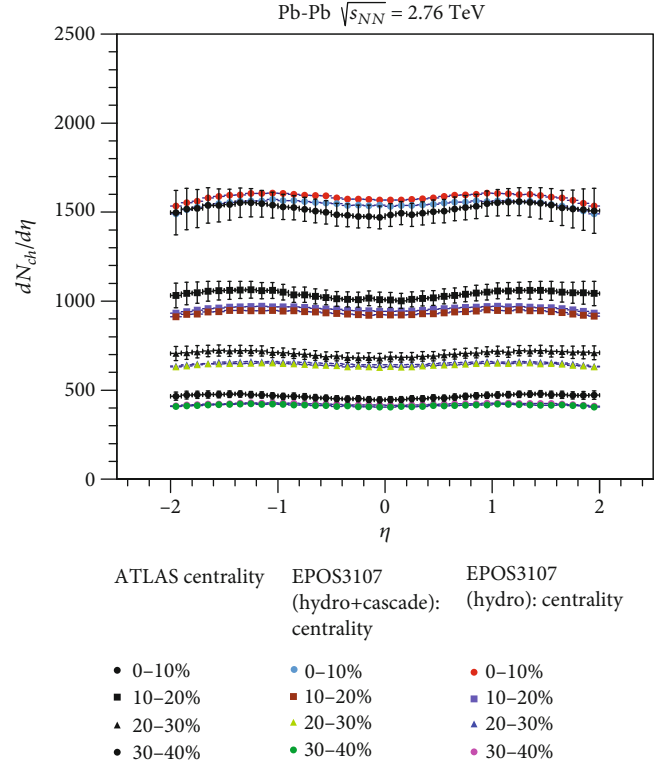
Figure 1: Charged particle pseudorapidity density distributions of EPOS3 (hydro) and EPOS3 (hydro+cascade) compared with that of the ATLAS data [20], for Pb-Pb collisions at $\sqrt{s_{NN}} = 2.76$ TeV.

tion scale, Q_s, is employed to consider nonlinear effects. This depends upon the energy and the number of participants attached to the pomeron under consideration.

For a pomeron, after multiple scatterings, the final state partonic system has two colour flux tubes, mainly longitudinal with transversely moving pieces carrying transverse momentum of the hard scattered partons. Each pomeron by virtue of its cylindrical topology has two flux tubes. The flux tubes also expand with time and gets fragmented into string segments of quark-antiquark pairs, resulting in more than two flux tubes. The high string density areas form the "*core*" (bulk matter) [16] and the low string density areas form the "*corona.*" The corona particles originate from the string decay by Schwinger mechanism. In EPOS3, only the core region thermalizes, flows, and hadronizes. The core undergoes viscous hydrodynamic evolution and as the hadronisation temperature ($T_H = 168$ MeV) is reached, Cooper-Frye mechanism [18] is applied to convert the fluid into particles. For hadronic cascade, all the hadrons participate from both core and corona. When the cascading mechanism is included in the modeling, EPOS3 might show self-similarity and thus intermittency effect [19]. EPOS3 is universal and unique in the sense that it treats pp, pA, and AA scatterings with the same core-corona procedure.

A sample of 66,350 and 23,502 minimum-biased events have been generated for Pb-Pb collisions $\sqrt{s_{NN}} = 2.76$ TeV using the hydro and the hydro+cascade mode of the EPOS3. The charged particle pseudorapidity density ($dN_{ch}/d\eta$) distributions of these events are shown in Figure 1, for various

centralities and are compared with that of ATLAS data [20] for the same system and energy. Where for the polar angle θ of the particle, measured with respect to the beam axis, the pseudorapidity (η) is defined as $\eta = -\ln \tan (\theta/2)$. In this work, analysis is performed for the charged particles generated in full azimuthal space with $|\eta| \leq 0.8$ in the most central events. It is observed (Figure 1) that in the midrapidity region of our interest ($|\eta| \leq 0.8$), charged particle pseudorapidity density of the EPOS3 generated central (0-10%) events, slightly overestimates the ATLAS data within errors.

Intermittency studies at low energies had limitation of statistics because a lesser number of particles were available per bin for the order of the moment $q \geq 2$. In the present collider experiments, with the availability of high multiplicity events per pseudorapidity unit both in pp and AA collisions the studies of local multiplicity fluctuations, dependent on the bin contents can be taken up, to get a clear and complete picture of the multiparticle production. Predictions for intermittency analysis of data at present collider energies are still not available. Present work is carried to study scaling behaviours of the charged particles multiplicity fluctuations and hence the intermittency in the EPOS3 model, which is based on the hydrodynamic particle production mechanism.

3. Methodology

Observation of spike events first noticed in the cosmic ray interaction [2] and later in the laboratory [3, 11] lead to great spurt of interest in the studies of intermittency in particle production in high-energy collisions. In [4, 5], groundbreaking work was done theoretically formulating the features of intermittency in the field of particle physics.

Intermittency is defined as the scale-invariance of NFM, F_q, with respect to changes in the size of phase space cells (bins) [4]. For one-dimensional phase space of rapidity Y, with cell δy (say), it is defined as

$$F_q(\delta y) \propto (\delta y)^{-\phi q} (\delta y \longrightarrow 0), \tag{1}$$

where F_qs are the NFM [4], of order q, where q is a positive integer and takes values ≥ 2 and $\phi_q > 0$ is called the "intermittency index" or "intermittency slope". In terms of the number of bins M in the phase space, where $M \propto 1/\delta$; Equation (1) can be written as

$$F_q(M) \propto M^{\phi_q}. \tag{2}$$

In [21, 22], it is proposed that NFM using *event* NFM be investigated at LHC energies where the charged particle density is very high. The event NFM, F_q^e, is defined as

$$F_q^e(M) = \frac{f_q^e(M)}{[f_1^e(M)]^q}, \tag{3}$$

with $f_q^e(M) = \langle n_m(n_m - 1) \cdots \cdots (n_m - q + 1) \rangle_e$, where $\langle \cdots \rangle_e$ is the averaging over all bins in an eth event, called horizontal

averaging, and n_m is bin multiplicity of the mth bin. NFM F_q for a sample of events, N_{evt}, is then

$$F_q(M) = \frac{1}{N_{evt}} \sum_{e=1}^{N_{evt}} F_q^e(M). \tag{4}$$

$F_q(M)$ enjoys the property of filtering out statistical fluctuations (or noise) [4, 23]. The scaling of the NFM, F_q, with number of bins M as in Equation (2) is referred here as *M-scaling*. Observation of this scaling would indicate the self-similarity in the spatial distribution of the particles. It has been observed that the Ginzburg-Landau formalism [13] for second-order phase transition, F_q, follows power-law as

$$F_q \propto F_2^{\beta_q}, \tag{5}$$

such that $\beta_q = (q - 1)^\nu$ with $\nu = 1.304$. Equation (5) is referred here as *F-scaling*. Its validity is independent of the scaling behaviour in Equation (2).

There exist more complicated self-similar objects which include fractal patterns with different noninteger dimensions, *multifractals* [3, 11, 24, 25]. Multifractals are characterized by generalized (or R'enyi) dimensions (D_q) which are decreasing functions of q. The thought of R'enyi dimensions D_q generalizes the idea of fractal dimension $D_0 = D_F$, information dimension D_1, and correlation dimension D_2. Consequently, the R'enyi dimension is often known as the generalized dimension. The anomalous fractal dimension (d_q) is related to the generalized dimension (D_q) by the relation

$$d_q = D - D_q, \tag{6}$$

where D is the topological dimension that represents the number of dimensions. A relation between the exponents of factorial moments, intermittency index (ϕ_q), and generalized moments can be devised at low values of q as

$$\phi_q + \tau(q) = (q - 1)D, \tag{7}$$

where the exponents are related to R'enyi dimensions and codimension as

$$\tau(q) = (q - 1)D_q,$$
$$\phi_q = (q - 1)d_q. \tag{8}$$

It is needed to stress that the slope τ_q has no dynamical feature of ϕ_q and needs to be corrected for the statistical contribution to be removed [26]. Increasing d_q with q is a signal of the multifractal system.

Here, intermittency and notion of fractality for charged particle multiplicity distribution is studied in the two-dimensional phase space (η, ϕ) of the events generated using EPOS3 for the Pb-Pb collision system at $\sqrt{s_{NN}} = 2.76$ TeV.

(a)

(b)
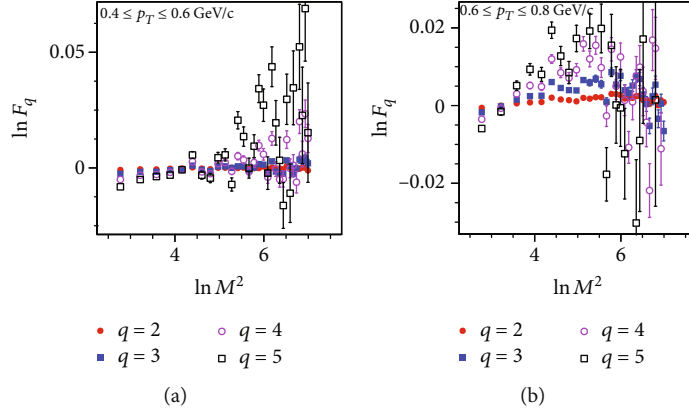
FIGURE 2: Log-Log F_q dependence on number of bins (M^2) for EPOS3-hydro events for the p_T bins $0.4 \leq p_T \leq 0.6$ GeV/c and $0.6 \leq p_T \leq 0.8$ GeV/c.

(a)

(b)
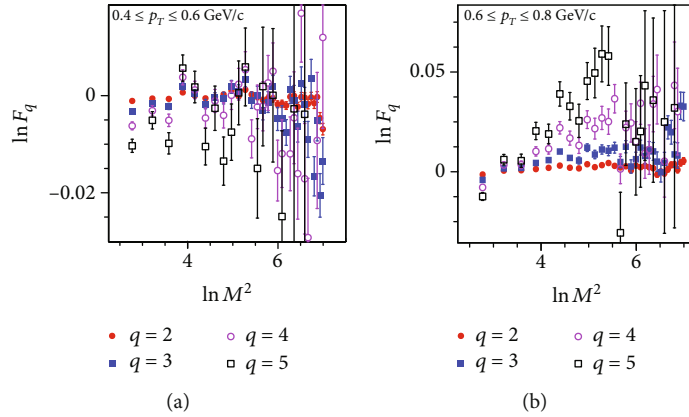
FIGURE 3: Log-Log F_q dependence on number of bins (M^2) for EPOS3-hydro+cascade events for the p_T bins $0.4 \leq p_T \leq 0.6$ GeV/c and $0.6 \leq p_T \leq 0.8$ GeV/c.

4. Analysis and Observations

A two-dimensional intermittency analysis in (η, φ) phase space in different p_T ($p_T = \sqrt{p_x^2 + p_y^2}$, where p_x and p_y are the momentum components in the transverse momentum plane) bins of varying widths ($0.2 \leq p_T \leq 0.4$ GeV/c, $0.4 \leq p_T \leq 0.6$ GeV/c, $0.6 \leq p_T \leq 0.8$ GeV/c, $0.8 \leq p_T \leq 1.0$ GeV/c, $0.2 \leq p_T \leq 0.6$ GeV/c, $0.2 \leq p_T \leq 0.8$ GeV/c, and $0.2 \leq p_T \leq 1.0$ GeV/c) are performed for two event samples for Pb-Pb collisions at $\sqrt{s_{NN}} = 2.76$ TeV generated using two modes of EPOS3. Central events with impact parameter $b \leq 3.5$ fm have been analyzed. In this work, charged particles (pions, kaons, and protons) generated in the kinematical region with $|\eta| \leq 0.8$, full φ coverage, and $p_T \leq 1.0$ GeV/c have been studied.

The methodology adopted for analysis is the same as in [27] for the SM AMPT model. The (η, ϕ) phase space in a p_T bin, for an event, is divided into a $M \times M$ matrix such that there are a total of M^2 bins. M is taken from 2 to 32 in an interval of 2. Number of charged particles in a bin, n_m, is the bin multiplicity in the mth bin. Event factorial moment, $F_q^e(M)$ (Equation (3)), is determined for $n_m \geq q$, where $q = 2$,

3, 4, and 5 is the order of the moment. $F_q^e(M)$ is obtained for all the events in the event sample. This gives the event factorial moment distribution and hence the $F_q(M)$ (Equation (4)). $F_q(M)$s are thus studied for their dependence on M and the second-order normalized factorial moments ($F_2(M)$).

From the study of dependence of F_q on M (M-scaling) for the various p_T bins, it is observed that for the small p_T bins with width $\Delta p_T = 0.2$ GeV/c ($0.2 \leq p_T \leq 0.4$ GeV/c, $0.4 \leq p_T \leq 0.6$ GeV/c, $0.6 \leq p_T \leq 0.8$ GeV/c, and $0.8 \leq p_T \leq 1.0$ GeV/c) M-scaling is absent in the case of both hydro and hydro+cascade events. For two bins, $\ln F_q$ vs $\ln M^2$ graphs for $q = 2, 3, 4, 5$ are given in Figure 2 (EPOS3 hydro) and Figure 3 (EPOS3 hydro+cascade). For the wider p_T bins with $\Delta p_T \geq 0.6$ GeV/c that is for $0.2 \leq p_T \leq 0.8$ GeV/c and $0.2 \leq p_T \leq 1.0$ GeV/c, scaling of F_q with M is observed in the lower M region followed by saturation effects at higher M region as observed in $\ln F_q$ vs $\ln M^2$ graph in Figure 4 for EPOS3 (hydro). For the same p_T bins that is $0.2 \leq p_T \leq 0.8$ GeV/c and $0.2 \leq p_T \leq 1.0$ GeV/c, Figure 5 shows the same graphs from EPOS3 (hydro+cascade) events. M-scaling is observed to be present in the low M region with saturation and

$0.2 \le p_T \le 0.8$ GeV/c

$0.2 \le p_T \le 1.0$ GeV/c

- $q = 2$ ○ $q = 4$
- $q = 3$ □ $q = 5$

- $q = 2$ ○ $q = 4$
- $q = 3$ □ $q = 5$

(a)   (b)
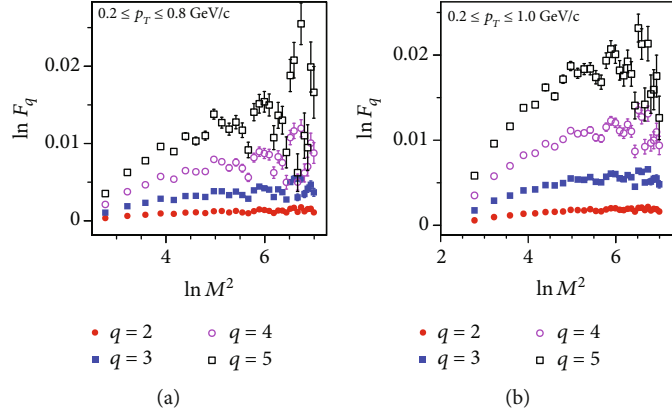
FIGURE 4: Log-Log F_q dependence on number of bins (M^2) for EPOS3-hydro events for the p_T bins $0.2 \le p_T \le 0.8$ GeV/c and $0.2 \le p_T \le 1.0$ GeV/c.

$0.2 \le p_T \le 0.8$ GeV/c

$0.2 \le p_T \le 1.0$ GeV/c

- $q = 2$ ○ $q = 4$
- $q = 3$ □ $q = 5$

- $q = 2$ ○ $q = 4$
- $q = 3$ □ $q = 5$

(a)   (b)
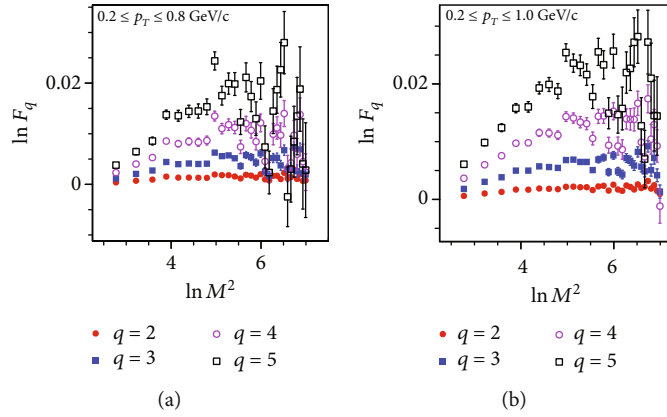
FIGURE 5: Log-Log F_q dependence on number of bins (M^2) for EPOS3-hydro+cascade events for the p_T bins $0.2 \le p_T \le 0.8$ GeV/c and $0.2 \le p_T \le 1.0$ GeV/c.

$0.2 \le p_T \le 0.8$ GeV/c

$0.2 \le p_T \le 1.0$ GeV/c

- $q = 3$
- $q = 4$
- ○ $q = 5$

- $q = 3$
- $q = 4$
- ○ $q = 5$

(a)   (b)
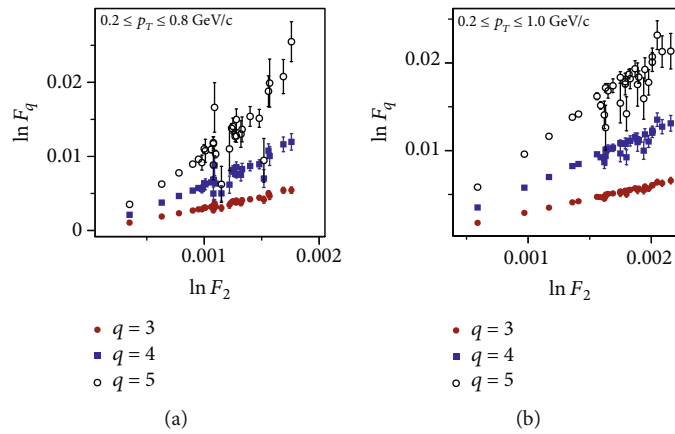
FIGURE 6: Log-Log F_q dependence on F_2 for EPOS3-hydro events for the p_T bins $0.2 \le p_T \le 0.8$ GeV/c and $0.2 \le p_T \le 1.0$ GeV/c.

overlapping effects at higher M. Absence of power-law or M-scaling in narrow p_T bins clearly indicates the absence of local density fluctuations and hence, the intermittency signal. The presence of weak intermittency in the wider p_T bins is probably due to number effect as average bin content

increases in the given phase space. The error bars are the statistical uncertainties, calculated using the error propagation formula as suggested in [28].

F_q is observed to show a linear dependence on F_2 even in the absence of M-scaling [13]. In Figures 6 and 7, $\ln F_q$ vs
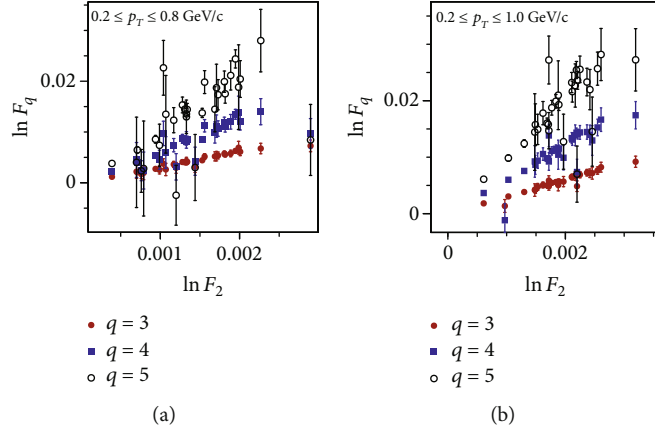
FIGURE 7: Log-Log F_q dependence on F_2 for EPOS3-hydro+cascade events for the p_T bins $0.2 \leq p_T \leq 0.8$ GeV/c and $0.2 \leq p_T \leq 1.0$ GeV/c.

TABLE 1: Scaling index values of the event samples.

Event sample	p_T bins (GeV/c)	Value of ν
Hydro	0.2-0.8	1.84 ± 0.19
	0.2-1.0	1.75 ± 0.12
Hydro+cascade	0.2-0.8	1.85 ± 0.33
	0.2-1.0	1.80 ± 0.26

$\ln F_2$ plots are given for the bins with $\Delta p_T \geq 0.6$ GeV/c, the same bins in which for M-scaling is observed for low M values. F_q is observed to follow power-law in F_2, whereas in the smaller p_T bins, F-scaling is also absent.

Scaling index, ν, is determined from the slope for $\ln \beta_q$ against $\ln (q-1)$. The scaling index, (ν) obtained for the two cases, is enlisted in Table 1. The NA22 data on particle production in hadronic collisions gives $\nu = 1.45 \pm 0.04$, heavy-ion experiments $\nu = 1.55 \pm 0.12$ [13], and $\nu = 1.459 \pm 0.021$ [29]. However, the average value of ν obtained here is 1.795 ± 0.156 EPOS3 (hydro) and 1.824 ± 0.295 EPOS3 (hydro+cascade), which is different from the value of 1.304 as is obtained from the GL formalism for the second-order phase transition. The values obtained here are significant, since the lattice QCD predicts continuous crossover type of phase transition [30].

For the two p_T bins in which M-scaling is observed for the low M-region, the d_qs have been calculated from the intermittency index (ϕ_q) and thus the fractal dimensions D_qs are determined and are plotted against q in Figure 8. The d_q grows in a way such that that the fractal (R'enyi) dimensions D_q are close to one. However in the data, the fractal dimensions are observed to be much smaller than one [3, 11, 31]. This observation indicates that EPOS3 in hydro and hydro+cascade mode do not have fractal behaviour. The D_q decreases faster with increasing order of the moment q and has similar behaviour for both the bins for the two modes of the EPOS3 modes. However, $D_2 < D_3$ contradicts the data [31, 32].
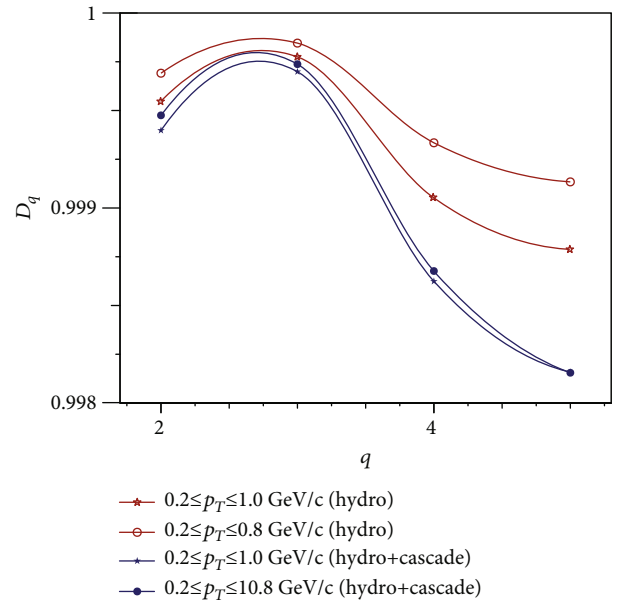
FIGURE 8: q dependence of fractal dimensions, D_q for the EPOS3 (hydro and hydro+cascade) events in the two p_T bins in which weak M-scaling and F-scaling, is observed.

5. Summary

An event-by-event intermittency analysis is performed for the charged particle multiplicity distributions of the events generated using two different modes of EPOS3 hydrodynamical model. Central events with $b \leq 3.5$ fm generated from Pb-Pb collisions at $\sqrt{s_{NN}} = 2.76$ TeV have been studied. The two-dimensional intermittency analysis is performed in (η, ϕ) phase space with $|\eta| \leq 0.8$ and full azimuth space in the narrow transverse momentum (p_T) bins in the region with $p_T \leq 1.0$ GeV/c with the objective to study the scaling behaviour of the charged particle multiplicity fluctuations as are introduced by the hydro and hydro+cascade modes of the EPOS3 model. In narrow p_T bins in the (η, ϕ) space, M-scaling is found to be absent

whereas weak M-scaling in two larger p_T bins with $\Delta p_T \geq$ 0.6 GeV/c viz, $0.2 \leq p_T \leq 0.8$ GeV/c, and $0.2 \leq p_T \leq 1.0$ GeV /c is observed. Absence of power-law of F_q with M indicates the absence of intermittency and hence self-similar behaviour in the local multiplicity fluctuations in charged particle generation in the events and hence the EPOS3 model. For the narrow p_T bins $\Delta p_T < 0.6\,GeV/c$, F-scaling which is independent of the observation of M-scaling is also absent. However, in the wider p_T bins $0.2 \leq p_T \leq 0.8$ GeV/c and $0.2 \leq p_T \leq 1.0$ GeV/c, F_q shows power-law with F_2. This is in contrast to what is observed in [27], where M-scaling as well as F-scaling is observed in the small p_T bins with $\Delta p_T \leq 0.2$ GeV/c. The average value of ν, the scaling exponent for these two bins from the two modes of EPOS3 is 1.809, a value different from 1.304, the value as obtained from Ginzburg-Landau theory for second-order phase transition. This suggests the absence of spatial fluctuations in the local charged particle generation that was not the case with the transport String Melting AMPT model [27]. In the larger phase space bins corresponding to $\Delta p_T \geq 0.6$ GeV/c in the low p_T region, M-scaling observed for the low M values is reflected in the value of generalized fractal dimension, D_q. D_q shows an inverse dependence on q for $q > 2$, thus the presence of multifractality in the larger phase space bins. This is in contrast to the observations at lower energies. Similar studies of experimental data from RHIC and LHC are yet not available. It would be interesting to see whether we get similar observations from the experiment or not.

Data Availability

The data used to support the findings of this study are available from the corresponding author upon request.

Conflicts of Interest

The authors declare that they have no conflicts of interest.

Acknowledgments

References

[1] S. Sarkar, H. Satz, and B. Sinha, "The physics of the quark-gluon plasma," in *Lecture Notes in Physics*, vol. 785, 2010.

[2] T. H. Burnett, S. Dake, M. Fuki et al., "Extremely high multiplicities in high-energy nucleus nucleus collisions," *Physical Review Letters*, vol. 50, no. 26, pp. 2062–2065, 1983.

[3] W. Kittel and E. A. De Wolf, *Soft Multihadron Dynamics*, World Scientific, Singapore, 2005.

[4] A. Bialas and R. Peschanski, "Moments of rapidity distributions as a measure of short-range fluctuations in high-energy collisions," *Nuclear Physics B*, vol. 273, no. 3-4, pp. 703–718, 1986.

[5] A. Bialas and R. Peschanski, "Intermittency in multiparticle production at high energy," *Nuclear Physics B*, vol. 308, no. 4, pp. 857–867, 1988.

[6] J. Brickmann, "B. Mandelbrot: the fractal geometry of nature, Freeman and Co., San Francisco 1982. 460 Seiten, Preis: £ 22,75," *Berichte der Bunsengesellschaft für physikalische Chemie*, vol. 89, no. 2, 1985.

[7] L. E. Reichl and J. H. Luscombe, "A modern course in statistical Physics, 2nd Edition," *American Journal of Physics*, vol. 67, no. 12, pp. 1285–1287, 1999.

[8] H. Satz, "Intermittency and critical behavior," *Nuclear Physics B*, vol. 326, pp. 613–618, 1989.

[9] B. Bambah, J. Fingberg, and H. Satz, "The onset of intermittent behaviour in the Ising model," *Nuclear Physics B*, vol. 332, no. 3, pp. 629–640, 1990.

[10] A. Bialas and R. C. Hwa, "Intermittency parameters as a possible signal for quark-gluon plasma formation," *Physics Letters B*, vol. 253, no. 3-4, pp. 436–438, 1991.

[11] E. A. De Wolf, I. M. Dremin, and W. Kittel, "Scaling laws for density correlations and fluctuations in multiparticle dynamics," *Physics Reports*, vol. 270, no. 1-2, pp. 1–141, 1996.

[12] A. Deppman, E. Megas, and D. P. Menezes, "Fractal structure in Yang-Mills fields and non extensivity," http://arxiv.org/abs/1905.06382.

[13] R. C. Hwa and M. T. Nazirov, "Intermittency in second-order phase transitions," *Physical Review Letters*, vol. 69, no. 5, pp. 741–744, 1992.

[14] K. Werner, B. Guiot, I. Karpenko, and T. Pierog, "Analyzing radial flow features in p-Pb and p-p collisions at several TeV by studying identified-particle production with the event generator EPOS3," *Physical Review C*, vol. 89, no. 6, 2014.

[15] K. Werner, I. Karpenko, T. Pierog, M. Bleicher, and K. Mikhailov, "Event-by-event simulation of the three-dimensional hydrodynamic evolution from flux tube initial conditions in ultrarelativistic heavy ion collisions," *Physical Review C*, vol. 82, no. 4, 2010.

[16] K. Werner, "Core-corona separation in ultra-relativistic heavy ion collisions," *Physical Review Letters*, vol. 98, no. 15, 2007.

[17] H. J. Drescher, M. Hladik, S. Ostapchenko, T. Pierog, and K. Werner, "Parton-based Gribov–Regge theory," *Physics Reports*, vol. 350, no. 2-4, pp. 93–289, 2001.

[18] F. Cooper and G. Frye, "Single-particle distribution in the hydrodynamic and statistical thermodynamic models of multiparticle production," *Physical Review D*, vol. 10, no. 1, pp. 186–189, 1974.

[19] G. Veneziano, *Proc. 3rd Workshop on Current Problems in High Energy Particle Theory, Florence*, R. Casalbuoni, S. Kövesi-Domokos, and G. Domokos, Eds., vol. 45, Johns Hopkins University Press, 1979.

[20] ATLAS Collaboration, "Measurement of the centrality dependence of the charged particle pseudorapidity distribution in lead–lead collisions at $\sqrt{S_{NN}} = 2.76$ TeV with the ATLAS detector," *Physics Letters B*, vol. 710, no. 3, pp. 363–382, 2012.

[21] R. C. Hwa, "Recognizing critical behavior amidst minijets at the large hadron collider," *Advances in High Energy Physics*, vol. 2015, Article ID 526908, 10 pages, 2015.

[22] R. C. Hwa and C. B. Yang, "Observable properties of quark–hadron phase transition at the large hadron collider," *Acta Physica Polonica B*, vol. 48, no. 1, p. 23, 2017.

[23] R. C. Hwa and C. B. Yang, "Local multiplicity fluctuations as a signature of critical hadronization in heavy-ion collisions at TeV energies," *Physical Review C*, vol. 85, no. 4, 2012.

[24] G. Paladin and A. Vulpiani, "Anomalous scaling laws in multifractal objects," *Physics Reports*, vol. 156, no. 4, pp. 147–225, 1987.

[25] J. Feder, *The Fractal Dimension*, Springer, US, Boston, MA, 1988.

[26] C. B. Chiu, K. Fialkowski, and R. C. Hwa, "Nonstatistical component of the multifractal spectral function," *Modern Physics Letters A*, vol. 5, no. 31, pp. 2651–2656, 1990.

[27] R. Sharma and R. Gupta, "Scaling properties of multiplicity fluctuations in the AMPT model," *Advances in High Energy Physics*, vol. 2018, Article ID 6283801, 7 pages, 2018.

[28] W. J. Metzger, "Estimating the uncertainties of factorial moments," in *preprint HEN-455*, Nijmegen University, 2004.

[29] P. L. Jain and G. Singh, "One- and two-dimensional analysis of intermittency in ultrarelativistic nucleus-nucleus interactions," *Physical Review C*, vol. 44, no. 2, pp. 854–858, 1991.

[30] T. Bhattacharya, M. I. Buchoff, N. H. Christ et al., "QCD phase transition with chiral quarks and physical quark masses," *Physical Review Letters*, vol. 113, no. 8, 2014.

[31] E. K. Sarkisyan, L. K. Gelovani, and G. G. Taran, "Fractality and fluctuations in charged particle pseudorapidity distributions in central C (Ne, Cu) collisions at 4.5A GeV/c," *Physics Letters B*, vol. 302, no. 2-3, pp. 331–335, 1993.

[32] E. K. Sarkisyan, L. K. Gelovani, G. G. Taran, and G. I. Sakharov, "Fractal analysis of pseudorapidity fluctuations in 4.5 A GeV/c C-(Ne, Cu) central collisions," *Physics Letters B*, vol. 318, no. 3, pp. 568–574, 1993.

Research Article

Study of Di-Muon Production Process in pp Collision in CMS Data from Symmetry Scaling Perspective

Susmita Bhaduri ⓘ**, Anirban Bhaduri** ⓘ**, and Dipak Ghosh** ⓘ

Deepa Ghosh Research Foundation, Kolkata 700031, India

Correspondence should be addressed to Susmita Bhaduri; susmita.sbhaduri@dgfoundation.in

An extensive knowledge of the dynamics of the process of pp collision serves as input to exhaustive theoretical models of strong interaction. This knowledge is also a baseline for a system to decipher the dynamics of AA collisions at relativistic and ultrarelativistic energies. Recent availability of di-muon data has triggered a spate of interests in revisiting strong interaction process, the study of which in detail is extremely important for enhancement of our understanding of not only the theory of strong interaction but also possible physics scenarios beyond the standard model. Apart from conventional approaches to the study of the dynamics of particle production in high-energy collision the present authors proposed a new approach with successful application in context of symmetry scaling in AA collision data from (ALICE-Collaboration, 2014) in the work (Bhaduri, S. et al., 2019) and pp collision data at 8 TeV from (CMS-collaboration, 2017) in the work (Bhaduri, S. et al., 2019) and also in other numerous works with different collision data. This different approach essentially analyses fluctuation pattern from the perspective of symmetry scaling or degree of self-similarity involved in the process. This was done with the help of multifractal scaling analysis and also multifractal cross-correlation analysis using the single variable of pseudorapidity values of di-muon data taken out from the primary dataset of RunA(2011) and RunB(2012) of the pp collision at 7 TeV and 8 TeV, respectively, from (CMS-collaboration, 2016, 2017). High degree of persistent long-range cross-correlations (MF-DXA) exist between pseudorapidity-value and its corresponding azimuthal-value for different rapidity ranges. The different values of scaling exponents (across rapidity ranges and energies) signify that there may be multiple processes other than those conjectured, involved in the underlying dynamics of the production process of oppositely charged di-muons resulting in different kinds of scaling. Otherwise, the scaling exponents at different degrees would have remained the same across the rapidity ranges and also for different energies.

1. Introduction

In the recent past, fluctuation and correlation have been analyzed widely using novel methods of studying nonstatistical fluctuation which resulted in the better understanding of the dynamics of the pionisation process. The methods including the process of intermittency were introduced by Bialas and Peschanski [1] who have observed association between intermittency indices and anomalous fractal dimension [2, 3]. After that, the parameters of Gq moment and Tq moment [4–8] were introduced which were deduced from various methods based on fractal concepts. Then distinctive approaches of *detrended fluctuation analysis (DFA) and*

multifractal-DFA (MF-DFA) [9, 10] were applied extensively for analyzing nonstationary, nonlinear properties of data series to investigate the long-range correlations inherent in the process of particle production [11–14]. Among various other contemporary works, self-similarity has been analyzed in the areas of particle physics which includes the production process of Jet and Top-quark in the experiments of Tevatron and LHC [15], the procedure of strangeness production in pp collisions at the RHIC [16] experiments, the phenomenon of proton spin and asymmetry inherent in jet production process [17] and the deciphering of the collective phenomena [18], and the process of establishment of the notion of self-similar symmetry of dark energy [19]. The

study of long-range cross-correlation between two nonstationary signals *detrended cross-correlation analysis (DXA)* had been presented by Podobnik and Stanley [20]. Wang et al. [21] introduced *multifractal-detrended cross-correlation analysis (MF-DXA)* by combining *MF-DFA* and *DXA* methods to examine higher degree of multifractal parameters of two cross-correlated series. MF-DXA method has been applied with substantially higher degree of accuracy in the analysis of the unrevealed cross-correlation in the various fields of physics, physiology finance, and power markets [20, 21] and also in the fields of particle physics [22].

The main aim of high-energy physics is to prove the existence of the creation of the QGP state, and also the study of the properties of this exotic state, by examining the final state of produced-hadrons, produced in huge numbers. Most of these final state particles may not be produced from the decay of the plasma directly, but rather they are produced or influenced by the hadronic cascade. Hence, studies of resonance states are of great importance because there is a variety of resonances, having very different lifespans, which signifies that these particles decay with differing probabilities in the hadronic stage, and therefore provide valuable information about that stage. We have performed the scaling analysis of the pseudorapidity space taken out from Pb-Pb VSD masterclass data at 2.76 TeV per nucleon pair from ALICE Collaboration [23] using both the method of complex network-based visibility graph and multifractal-DFA (MF-DFA) [9, 10], to study the prospective phase transition and the signature of QGP [24, 25]. We also studied multiplicity fluctuation process in nucleus-nucleus and hadron-nucleus interactions by applying complex network and chaos-based visibility graph methodology in quite a few recent works [22, 26–33]. These techniques have also been successfully applied to identify phase transitions in temperature-driven magnetization properties [34] and also in temperature-driven phase transition from liquid to vapour state [35]. In a recent study [36], different combinations of topological and kinematic input variables from the data of RunA(2011) of the *pp* collision at 7 TeV at CMS detector have been used, from which several ANNs (artificial neural networks) have been constructed, and then through comparison, the optimally configured ANN is selected .

The outcomes of the assessment of *pp* and *pA* systems should be used as a reference to validate the understanding of the processes which are expected to contribute to the dynamics of the process of di-muon production [37]. Moreover, apart from the analysis of *AA* collisions, an extensive knowledge of *pp* collisions is required both as an input to comprehensive theoretical models of strong interactions and also as a baseline to decipher the *AA* collisions at relativistic and ultrarelativistic energy levels. This has been of great interest in the area of theoretical and experimental physics. The process of soft particle generation from ultrarelativistic *pp* collisions is affected by the flavor distribution among the proton, quark hadronization, and baryon number transport. In the process of *AA* collisions, the magnitude of the spectrum of transverse momentum of charged particles in *pp* collisions serves as an important reference. A *pp* reference spectrum is required for *AA* collisions to probe for the effects

of probable initial states of the collision. The multiplicity distribution of particles generated in *pp* collisions and the multiplicity dependence of various global event features serve as rudimentary observables which reflect the features of the underlying dynamics of the process of particle production. Therein lies the importance of analyzing the dynamics of di-muon production process in *pp* collisions. In this work, we have attempted DFA, MF-DFA, and MF-DXA for the scaling analysis of the rapidity and energy dependence of the di-muon production process.

The rest of the paper is structured in the following manner. The objective of the study is elaborated in Section 2. Section 3 describes the methods of analysis. Section 3.1 presents the algorithm of DFA and MF-DFA, and Section 3.2 presents the method of MF-DXA in detail and the importance of the parameters—the width of multifractal spectrum and the cross-correlation exponent. Section 4.1 describes the data in detail. Section 4.2 describes the details of our study and the deductions from the test results. Section 5 details the physical importance of the proposed parameters and their relevance with regards to the dynamics of the di-muon production process and finally comes the conclusion.

2. Goal of the Study

Using *pp* collisions at a center-of-mass energy of $\sqrt{S} = 7$ TeV, the analysis of the production process of exclusive $\gamma\gamma \longrightarrow \mu^+\mu^-$ was carried out by the ATLAS and CMS collaborations [38]. A latest review work has been reported about the complexities involved in resonance production process for different high-energy collisions like *pp*, *pA*, and *AA* collisions at LHC(using data from ALICE collaboration), to analyze the complexity and eventually explain the inherent dynamics of the particle production process and the properties of the generated particles for the different collision system [39]. We have elaborated in Section 1 how after few successful ventures by the present authors in the field of analyzing the pionisation process in high-energy interaction using chaos-based procedures and being motivated by the different attempts reported to investigate the dynamics of the generation process of di-muon pairs in [39], we have attempted to revisit the di-muon production process in hadron-hadron interactions. We have proposed to implement the chaos-based methods of DFA, MF-DFA, and MF-DXA to analyze the energy and rapidity dependence of di-muon production process by utilizing a single variable of pseudorapidity values of di-muon data taken out of the primary dataset of RunA(2011) and RunB(2012) of the *pp* collision at 7 TeV and 8 TeV, respectively, from CMS collaboration [40, 41]. The rapidity and energy dependence of the process are examined by means of fundamental scaling parameter signifying the degree of symmetry scaling or scale-freeness in the di-muon production process, extracted by the proposed method.

(1) All these rigorous methods provide the information from the deepest level about the particle production process from the emergent di-muons produced from the *pp* collisions at 7 TeV and 8 TeV from CMS collaboration [40, 41].

(2) The study reveals that pseudorapidity spaces corresponding to different range of pseudorapidity values are highly scale free and possess multifractal characteristics. They also reveal how the scaling pattern changes from one rapidity range to another and also from one range of energy level to another

(3) For different rapidity range and at two different levels of energy, differences in the values of scaling exponent signify that there are multiple processes involved in the production process of oppositely charged di-muons which give rise to different kinds of scaling

Traditionally invariant-mass/transverse-momentum methods were used to probe various resonance states in high-energy collision. Apart from the J/Ψ peak observed in their invariant-mass spectrum, there can be existence of other upsilon states and other processes in principle contributing to the di-muon continuum due to open charm and open beauty decays. One may select different ranges of invariant mass by examining the pattern of invariant-mass spectrum of the events producing di-muons. For each such range, the pseudorapidity spaces corresponding to the produced di-muons would be extracted, and then for each of the spaces, the proposed scaling analysis may be done for different ranges of rapidity and energy. Any substantial change in scaling behavior indicated by the width of MF-DFA spectrum and the degree of multifractal cross-correlation may be attributed to the occurrence of different kinds of resonance states from which di-muons are produced in pp collisions. This may act as basic input for studying similar resonance production in pp collisions at higher energy and also for pA and AA collisions.

3. Method of Analysis

We have elaborated the multifractal-detrended fluctuation analysis (MF-DFA) method [9, 10, 42] used to calculate the Hurst exponent and the width of the multifractal spectrum. We have extracted these parameters for analyzing the fluctuation of data series extracted from the experimental data as elaborated in Section 4.1.

3.1. MF-DFA Method

(1) Here, we denote the experimental data series as $x(i)$ for $i = 1, 2, \cdots, N$, where N = number of points. The average of this series is computed as $\bar{x} = 1/N \sum_{i=1}^{N} x(i)$. Then, the collective deviation series for $x(i)$ is calculated as

$$X(i) \equiv \sum_{k=1}^{i} [x(k) - \bar{x}], i = 1, 2, \cdots, N. \quad (1)$$

This deduction of the average ($\bar{x}$) from the input data series is a conventional method of eliminating noise from the input data series. The result of this subtrac-

tion would be removed by the detrending process in the fourth step.

(2) $X(i)$ is then divided into N_s nonoverlapping segments, with $N_s \equiv \text{int}(N/s)$ and s as the length of the segment. In this experiment, s ranges from 16 (minimum) to 1024 (maximum) value in log scale

(3) For each s, a particular segment is denoted by $v(v = 1, 2, \cdots, N_s)$. Least-square fitting is performed for each segment to derive the local trend for that specific segment [9]. $x_v(i)$ denotes the least-square fitted polynomial for the segment v in series $X(i)$. $x_v(i)$ is computed according to the equation $x_v(i) = \sum_{k=0}^{m} C_k (i)^{m-k}$, with C_k as the kth coefficients of the fitted polynomial of degree m. Different kinds of fitting—-linear, quadratic, cubic, or higher m-order polynomial—may be used [10, 42]. In this experiment, linear least-square fitting is applied with $m = 1$

(4) Now, to detrend the data series, the least-square fitted polynomial is subtracted from the data series. There is existence of slow-varying trends in natural data series. In order to extract the scale invariant structure of the dissimilarity around the trend, detrending is necessary. For each value of s and segment $v \in 1, 2, \cdots, N_s$, detrending is executed by deducting the least-square fit $x_v(i)$ from the specific portion of the data series $X(i)$, for the segment v to calculate the variance which is denoted by $F^2(s, v)$ computed as

$$F^2(s, v) \equiv \frac{1}{s} \sum_{i=1}^{s} \{X[(v - 1)s + i] - x_v(i)\}^2, \quad (2)$$

with $s \in 16, 32, \cdots, 1024$ and $v \in 1, 2, \cdots, N_s$.

(5) Next, the qth order function of fluctuation, denoted by $F_q(s)$, is computed by averaging the values of $F^2(s, v)$ over all the segments (v) produced for each $s \in 16, 32, \cdots, 1024$ and for a specific q, as

$$F_q(s) \equiv \left\{ \frac{1}{N_s} \sum_{v=1}^{N_s} \left[F^2(s, v) \right]^{q/2} \right\}^{1/q}. \quad (3)$$

Here, $q \neq 0$ as in that case $1/q$ would blow up. In this experiment q varies from (-5) to $(+5)$. For $q = 2$, computation of $F_q(s)$ would sum up to conventional method of detrended fluctuation analysis (DFA) [9].

(6) The above steps are repeated for various values of $s \in 16, 32, \cdots, 1024$, and it is observed that for a particular q, $F_q(s)$ rises in value with increasing s. If the data series is long-range power correlated, then $F_q(s)$ vs s for a specific q will display power-law behavior

$$F_q(s) \propto s^{h(q)}. \quad (4)$$

If this type of scaling exists, then $\log_2[F_q(s)]$ depends on $\log_2 s$ in a linear fashion, where $h(q)$ is the slope which is dependent on q. $h(2)$ is alike to the so-called *Hurst exponent* [42]. So $h(q)$ is defined as the generalized Hurst exponent.

(7) The scaling pattern of the variance $F^2(s, v)$ is the same for all segments in case of a monofractal series. In other words, the averaging of $F^2(s, v)$ would show uniform scaling behavior for various values of q, and hence, $h(q)$ becomes independent of q for monofractals.

But if large and small fluctuations in the series have varying scaling pattern, then $h(q)$ becomes substantially dependent on q. In these cases, for positive values of q, $h(q)$ delineates the scaling pattern of the segments with large fluctuations, and for negative values of q, $h(q)$ describes scaling behavior of the segments with smaller fluctuations. The generalized Hurst exponent $h(q)$ for a multifractal data series is associated with the classical multifractal scaling exponent $\tau(q)$ according to

$$\tau(q) = qh(q) - 1. \tag{5}$$

(8) As multifractal series have numerous Hurst exponents, so $\tau(q)$ depends nonlinearly upon q [43]. The singularity spectrum, here denoted by $f(\alpha)$, is associated with $h(q)$ as

$$\alpha = h(q) + qh'(q), f(\alpha) = q[\alpha - h(q)] + 1. \tag{6}$$

Here, the singularity strength is denoted by α, and $f(\alpha)$ describes the dimension of the subset series denoted by α. Different values of $f(\alpha)$ for different α results into multifractal spectrum of $f(\alpha)$ which is an arc, and for this spectrum, the gap between the maximum and minimum values of α is the *width of the multifractal spectrum* or the measurement of the multifractality of the input data series.

(9) For $q = 2$, if $h(q)$ or $h(2) = 0.5$, no correlation exists in the data series. There is persistent long-range cross-correlations in the data series, which means a large value in the series is presumably to be followed by another large value in the series, if $h(2) > 0.5$, whereas for $h(2) < 0.5$, there would be antipersistent long-range correlations which implies that a large value would probably be followed by a small value in the series and vice versa.

3.2. MF-DXA Method. Wang et al. [21] have introduced *MF-DXA* method based on the *MF-DFA* method [10, 42] and analyzed the cross-correlation between two nonstationary series quantitatively. The broad steps for the *MF-DXA* method are as follows.

(1) Let $x(i)$ and $y(i)$ be two data series for $i = 1, 2, \cdots, N$, of length N. The mean of these series is calculated as $\bar{x} = 1/N \sum_{i=1}^{N} x(i)$ and $\bar{y} = 1/N \sum_{i=1}^{N} y(i)$, respectively. Then, accumulated deviation series for $x(i)$ and $y(i)$ are calculated as per equation (1) and denoted by $X(i)$ and $Y(i)$, respectively. Both $X(i)$ and $Y(i)$ are divided into N_s nonoverlapping segments, where $N_s = \text{int}(N/s)$, s is the length of the segment. In our experiment, s varies from a minimum of 16 to a maximum of 512 value in log scale

(2) For each s, we denote a particular segment by $v(v = 1, 2, \cdots, N_s)$. Here, $x_v(i)$ and $y_v(i)$ denote the least-square fitted polynomials for the segment v in $X(i)$ and $Y(i)$, respectively. $x_v(i)$ and $y_v(i)$ are calculated as per the equations $x_v(i) = \sum_{k=0}^{m} C_{xk}(i)^{m-k}$ and $y_v(i) = \sum_{k=0}^{m} C_{yk}(i)^{m-k}$, where C_{xk} and C_{yk} are the kth coefficients of the fit polynomials with degree m. For this experiment, m is taken as 1 [21].

For each s and segment v, $v = 1, 2, \cdots, N_s$, detrending is done by subtracting the least-square fits $x_v(i)$ and $y_v(i)$ from the part of the data series $X(i)$ and $Y(i)$, respectively, for the segment v. The covariance of the these residuals, denoted by $f_{xy}^2(s, v)$ for a particular s and v, is then calculated as follows.

$$f_{xy}^2(s, v) = \frac{1}{s} \sum_{i=1}^{s} \{X[(v-1)s + i] - x_v(i)\} \times \{Y[(v-1)s + i] - y_v(i)\}, \tag{7}$$

for each segment v, $v = 1, 2, \cdots, N_s$.

(3) Then, the qth order detrended covariance, denoted by $F_{xy}(q, s)$, is calculated by averaging $f_{xy}^2(s, v)$ over all the segments (v) generated for a particular s and q, as per the equation below [10, 21, 42].

$$F_{xy}(q, s) = \left\{ \frac{1}{N_s} \sum_{v=1}^{N_s} \left[f_{xy}^2(s, v) \right]^{q/2} \right\}^{1/q}. \tag{8}$$

Here, $q \neq 0$ because in that case, $1/q$ would blow up.

(4) The above process is repeated for different values of $s \in 16, 32, \cdots, 512$, and it can be seen that for a specific q, $F_{xy}(q, s)$ increases with increasing s. If the series are long-range power correlated, the relation between $F_{xy}(q, s)$ versus s for a particular q will show power-law behavior as below [21].

$$F_{xy}(q, s) \propto s^{h_{xy}(q)}. \tag{9}$$

If this kind of scaling exists, $\log_2[F_{xy}(q, s)]$ would depend linearly on $\log_2 s$, where $h_{xy}(q)$ is the slope

and represents the degree of the cross-correlation between the data series $x(i)$ and $y(i)$.

In general, $h_{xy}(q)$ depends on q. q ranges from negative to positive values. For $q = 2$, the method is referred as the so-called method of *DXA* [21].

(5) As confirmed from several experiments done by Wang et al. [21], if $h_{xy}(q) = 0.5$, there is no cross-correlation. Further, if $h_{xy}(q) > 0.5$, there are persistent long-range cross-correlations, where the large value of one variable, which is in this study the η values, is likely to be followed by a large value of another variable, which is the corresponding ϕ values, in the series, whereas in case of $h_{xy}(q) < 0.5$, there are antipersistent long-range cross-correlations, where a large value of one variable is most likely to be followed by a small value and vice versa in the series

(6) $h_{xy}(q)$ for $q = 2$, i.e., $h_{xy}(2)$, is the *DXA* exponent. As per Podobnik and Stanley, the cross-correlation exponent between two nonstationary series, denoted by γ_i, is calculated as per the equation $\gamma_i = 2 - 2\{h_{xy}(2)\}$ [20]. For uncorrelated data series, $\gamma_i = 1$, the lower the value of γ_i, the more correlated the data series are

4. Experimental Details

The datasets for the proposed analysis are taken out from two publicly available experimental primary datasets from CMS collaboration. The details of the data is given in Section 4.1, and the complete method of the experiment is explained in step by step in Section 4.2.

4.1. Data Description. The primary dataset of the *pp* collision at 8 TeV in AOD format from RunB of 2012 [40] and another dataset of *pp* collision at 7 TeV in the same AOD format from RunA of 2011 [41] of the CMS collaboration are taken as the source datasets for this experiment. The run numbers which are selected and qualified by CMS to be processed along with the appropriate parameters for generation of the collision datasets are provided in the links—*link1* and *link2* for 8 TeV and 7 TeV, respectively. These datasets are made available for experiment. We have extracted the pseudorapidity-η space and corresponding azimuthal-ϕ space for the generated di-muons from these runs qualified by CMS from the primary datasets in the following formats—text (.txt) and .root format. In this analysis, we have utilized these pseudorapidity space and the corresponding azimuthal space from the text (.txt) file.

4.2. Data Analysis and Results

(1) The pseudorapidity-η space for each of the datasets for 8 and 7 TeV extracted from the primary datasets of the CMS collaboration as described in Section 4.1 is divided into the following 5 ranges of η values

(a) −2.5 to −1.5

(b) −1.5 to −0.5

(c) −0.5 to 0.5

(d) 0.5 to 1.5

(e) 1.5 to 2.5

For all the 5 ranges, the η values are extracted from the full-phase space of the two source datasets and mapped to data series. The data series is plotted with the X-axis denoting the sequence number of η values and the Y corresponds to the η values corresponding to the sequence number as in the X-axis.

For each of these data series, the following values are calculated.

(i) The width of the multifractal spectrum

(ii) Degree of cross-correlation between the η space and their corresponding ϕ space

(2) For each of the 10 datasets (5 for 8 TeV and 5 for 7 TeV) created for the 5 ranges of pseudorapidity values, as specified in Step 1, the multifractal analysis is done and the width of multifractal spectrum is calculated as per the method elaborated in Section 3.1

The qth order detrended variance $F_q(s)$ is calculated as per equation (3) in the Step 5 of the MF-DFA methodology as described in Section 3.1. Figures 1(a) and 1(b) show the $\log_2[F_q(s)]$ vs $\log_2[s]s$ trend for $q = -5, 0, 5$, extracted for a particular range of η values for 8 and 7 TeV datasets, respectively.

Their linear trend confirms the power-law behavior of $F_q(s)$ versus s for all the values of q. Similar calculation is done for all the η ranges for both 8 and 7 TeV datasets, and similar trend is observed.

(3) For each of the η-data series corresponding to the ranges specified in Step 1, a randomized version of data is produced and widths of the multifractal spectrum are calculated as per the same methodology elaborated in Section 3.1. The calculated values of the parameters are compared to those for the experimental data. In Figures 2(a) and 2(b), the widths of the multifractal spectrum of the original datasets and their randomized versions calculated for one of the ranges η values are shown for 8 and 7 TeV datasets, respectively. The below points must be noted for the shape and widths of the multifractal spectrum of the original datasets and their randomized versions

(i) The shape of the multifractal spectrum does not necessarily have to be symmetric. The spectrum might have either a right or a left truncation that arises from the consistent/(almost
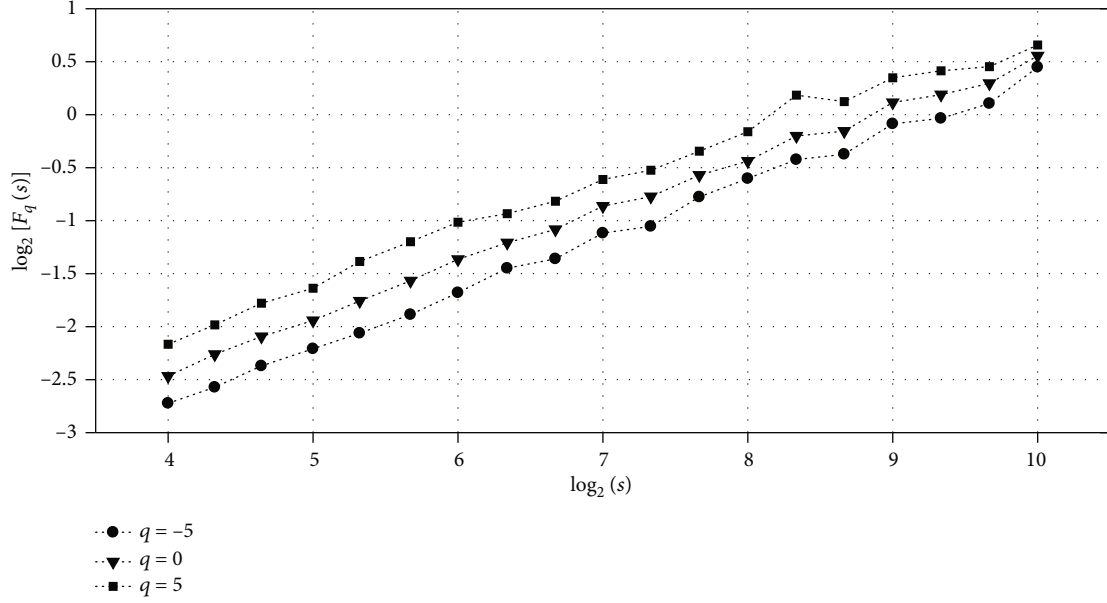
(a)
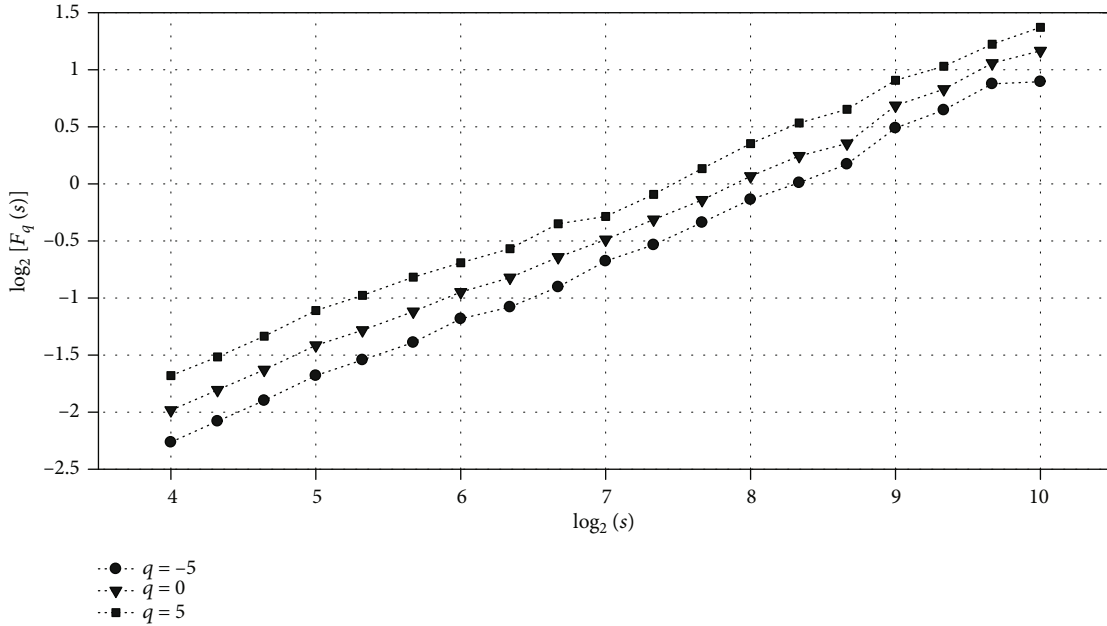
(b)

FIGURE 1: Trend of $\log_2[Fq(s)]$ vs $\log_2[s]s$ for $q = -5, 0, 5$, extracted for a particular range of η (a) for 8 TeV dataset and (b) for 7 TeV dataset.

constant) trend of Hurst exponents for positive or negative values of qs. The consistent trend of qth order Hurst exponent signifies that the qth order RMS (calculated as per the equations in Step 5 and Step 6 of Section 3.1) is not much sensitive to the extent of the local fluctuations

(ii) The width and trend of multifractal spectrum between the original and the randomized version of the particular η-space for 8 TeV dataset shown in Figure 2(a) shows that the spectrum for the randomized version has a long right tail

which signifies that the series have a multifractal structure not much affected by the local fluctuations with large magnitudes

(iii) Whereas the multifractal spectrum calculated for the original and the randomized version of the η-space for the same range of η values for 7 TeV dataset shown in Figure 2(b) shows that the spectrum for the randomized version has a long left tail, which means that the randomized series is not much sensitive to the local fluctuations with small magnitudes.
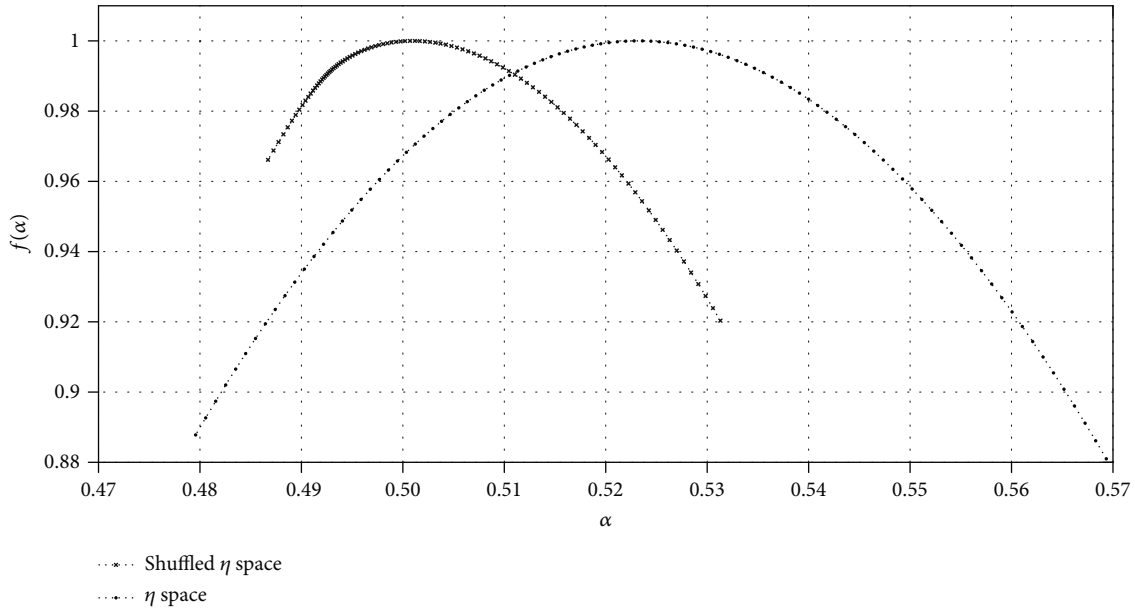
(a)
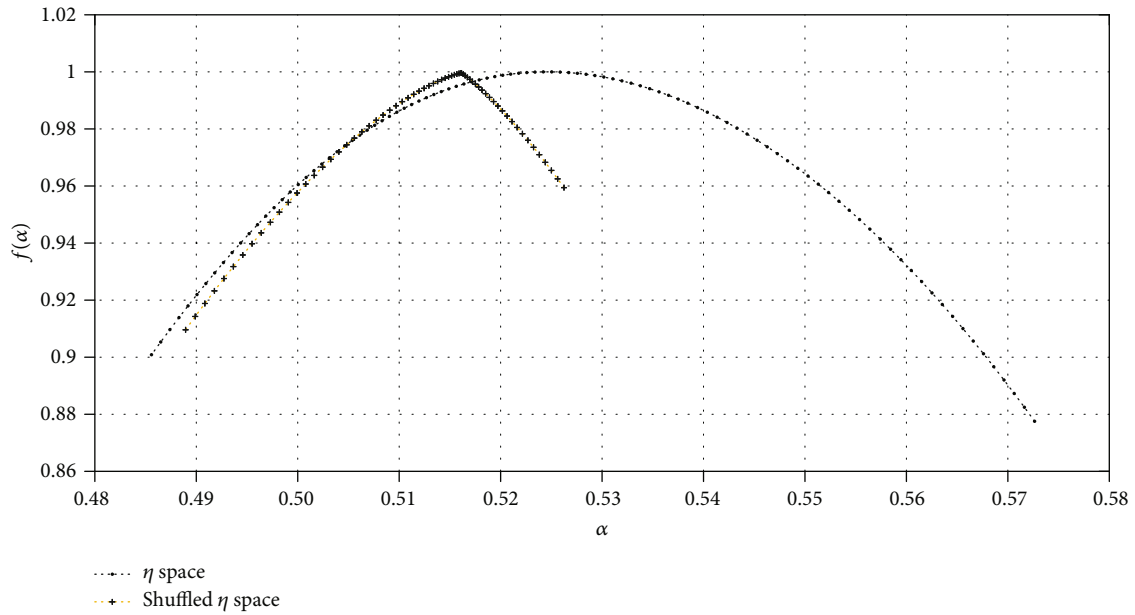
(b)

FIGURE 2: Comparison of the trend of different values of $f(\alpha)$ versus α between the original and the randomized version of the η space for a particular range of η values for (a) 8 TeV dataset and (b) 7 TeV dataset.

(iv) If the source data is long-range correlated, that is eradicated by the randomization process, and the data should start to become uncorrelated. This makes the multifractal spectrum or the scaling pattern of randomized series insensitive to the local fluctuations with large or small magnitudes, which is not the case with the actual experimental data. Hence, it results in the different widths of multifractal spectrum calculated the randomized version from those for the original version. Moreover, for two

completely different experimental datasets the randomized data may be different with regards to peak, shape, and trend. The width of the multifractal spectrum has normally been less for the randomized data than the one for the experimental data

(v) The main conclusion comes from the fact that the values of the width of the multifractal spectrum calculated experimental data being significantly different from shuffled ensembles
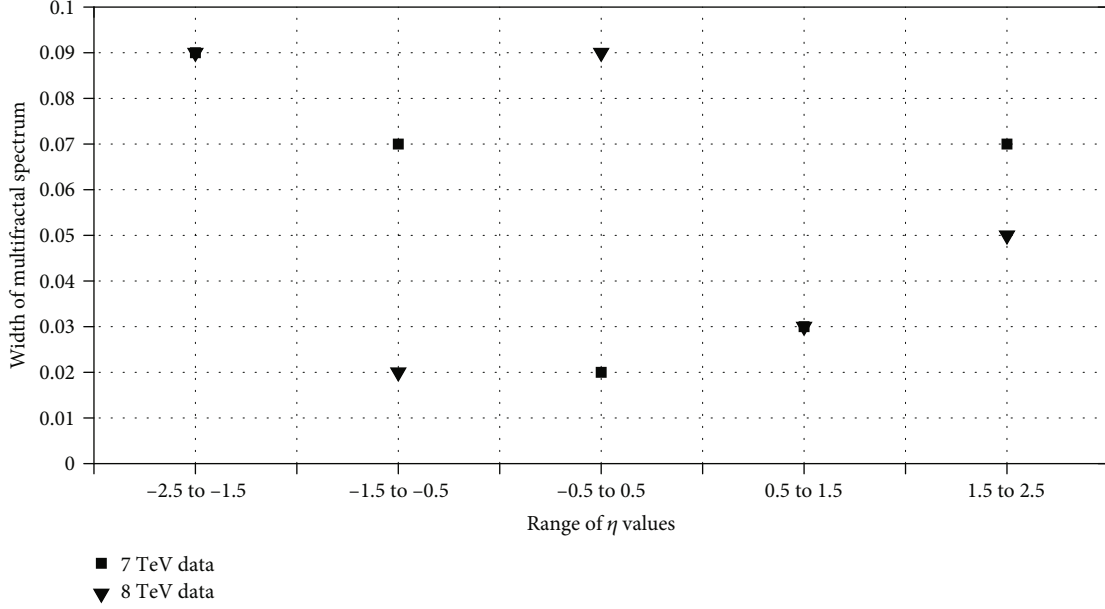
FIGURE 3: Comparison of the widths of the multifractal spectrum generated η spaces for all the 5 ranges of η values for 7 and 8 TeV datasets.

essentially confirms that the *degree* of scale-freeness is indicative of the dynamics inherent in the di-muon production process, and this *degree* of scale-freeness may be indicative of different processed responsible for di-muon production even beyond standard model (SM).

(vi) It is evident from the figures that the widths of the multifractal spectrum of the original datasets and their randomized versions differ substantially for both energies. Similar trend is observed from the comparison of the original and the randomized version of the 5 ranges of η values for both 8 and 7 TeV datasets

The comparison of the widths of the multifractal spectrum generated for the η spaces for all the 5 ranges of η values for 7 and 8 TeV datasets with respect to their rapidity and energy dependence is shown in Figure 3. It should be noted that:

(i) The comparison of the width of the multifractal spectrum of $f(\alpha)$, denoted by the difference between the maximum and minimum values of α, between the original and the randomized version of the η space for both energy ranges confirm the mutifractality of the original η spaces

(ii) For the 2nd, 3rd, and 5th range of η values, the widths of multifractal spectrum is substantially different between the energy ranges

(iii) For both 7 and 8 TeV the 1st and 4th range of η-space display minimum or no difference with respect to multifractality

TABLE 1: Comparison of the widths of the multifractal spectrum generated η spaces for all the 5 ranges of η values for 7 and 8 TeV datasets, between the original and the randomized version.

| η ranges | MF-DFA spectrum width | | | |
| | 8 TeV | | 7 TeV | |
	Original	Random	Original	Random
−2.5 to −1.5	0.09	0.06	0.09	0.04
−1.5 to −0.5	0.02	0.01	0.07	0.02
−0.5 to 0.5	0.09	0.04	0.02	0.04
0.5 to 1.5	0.03	0.02	0.03	0.04
1.5 to 2.5	0.05	0.04	0.07	0.06

(iv) The degree of multifractality is found to be the least for 2nd and 3rd range for 8 and 7 TeV data, respectively

Table 1 details the widths of the multifractal spectrum of the original datasets and their randomized versions for all the 10 datasets (5 for 8 and 5 for 7 TeV) corresponding to the η values. The values of the width of MF-DFA spectrum, essentially is an indicator of inherent symmetry and scale-freeness (different at different energy and rapidity ranges) with which the produced di-muons create the signatures in terms of η values. The values of these parameters in experimental data being significantly different from shuffled ensembles confirm that this inherent symmetry and degree of scale-freeness is never the outcome of randomization process but is indicative of the dynamics involved in the di-muon production process.

(4) For each of the 10 datasets (5 for 8 and 5 for 7 TeV) of η values extracted for the ranges specified in
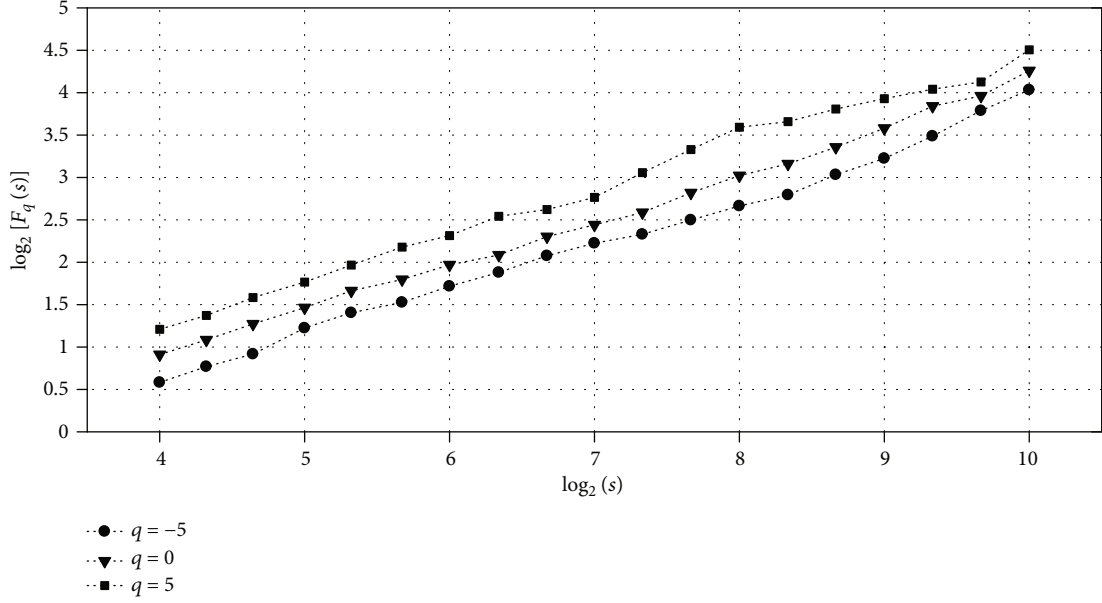
(a)
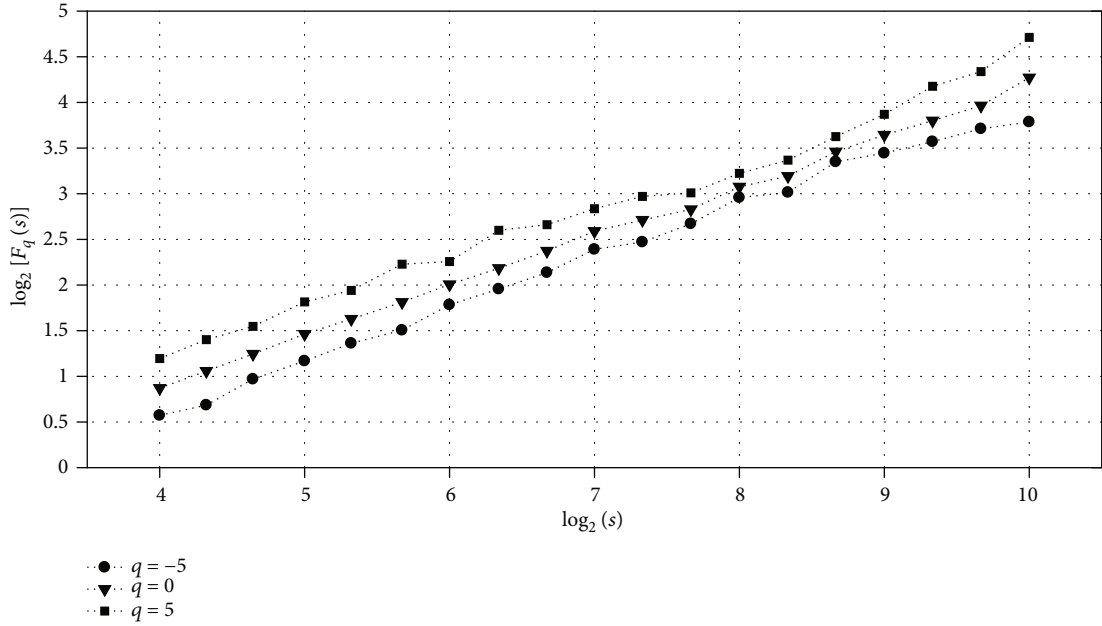
(b)

FIGURE 4: Trend of $\log_2[F_q(s)]$ vs $\log_2[s]s$ for $q = -5, 0, 5$, analyzed for the ϕ space corresponding to the η space for (a) 8 TeV dataset, as shown in Figure 1(a), and (b) 7 TeV dataset, as shown in Figure 1(b).

Step 1, the corresponding azimuthal-ϕ space is also extracted. The 10 corresponding ϕ space is sorted in the ascending order and then mapped into data series. They in turn are mapped into a two-dimensional space with their sequence along the X-axis and the corresponding values of ϕ along the Y-axis

(5) For the 10 ϕ spaces (5 for 8 and 5 for 7 TeV), the qth order detrended variance $F_q(s)$ is analyzed as per equation (3) in Step 5 of the MF-DFA methodology as described in Section 3.1. Figures 4(a) and 4(b)

show the $\log_2[F_q(s)]$ vs $\log_2[s]s$ trend for $q = -5, 0,$ 5, extracted for corresponding ϕ values for the same range of η values for which the same trend is shown in Figures 1(a) and 1(b) for 8 and 7 TeV datasets, respectively

It is to be noted that the linear trend confirms the power-law behavior of $F_q(s)$ versus s for all the values of q for the ϕ spaces. The same analysis is done for all the ϕ spaces corresponding to the η ranges for both 8 and 7 TeV datasets, and a similar trend is observed.
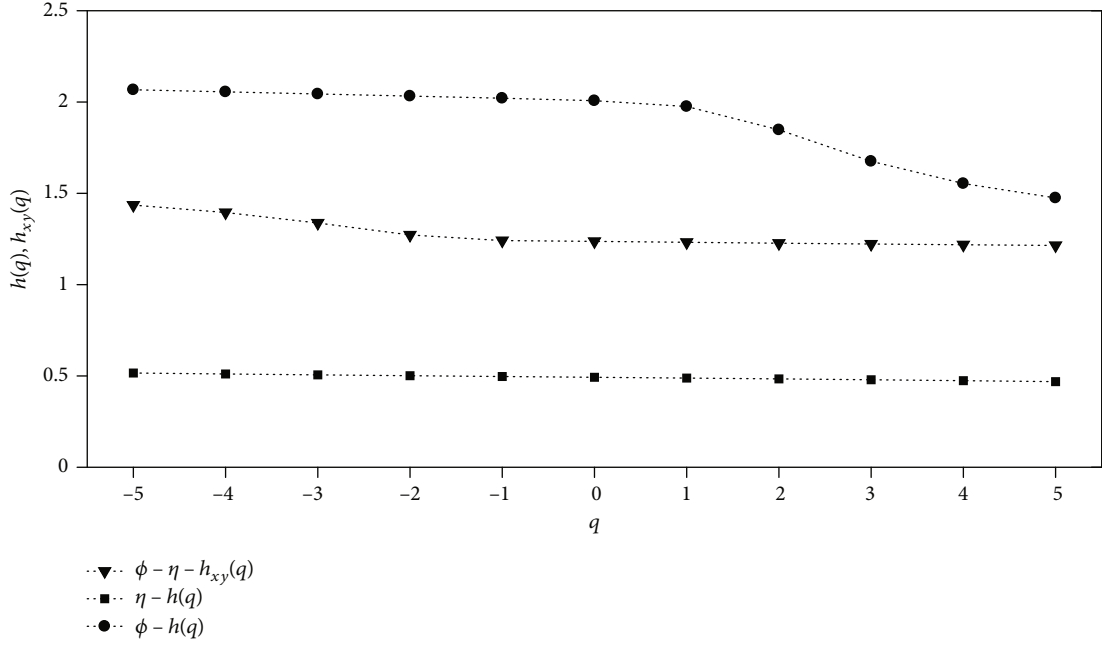
(a)
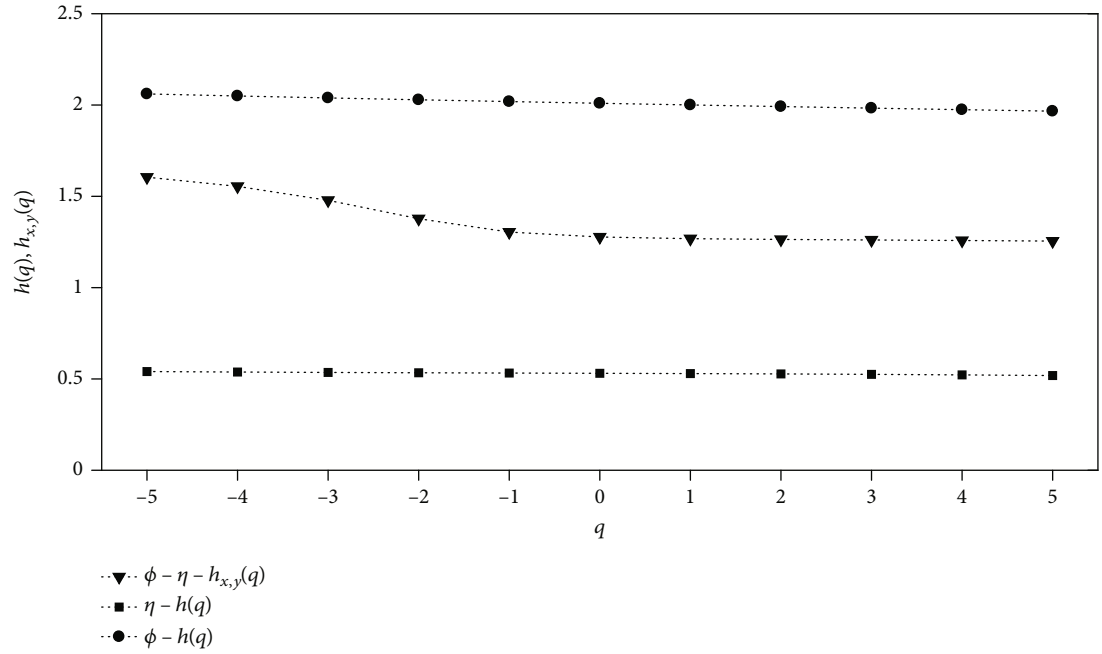
(b)

Figure 5: Trend of $h(q)$ and $h_{x,y}(q)$ versus q for $q = -5, -4, \cdots, 5$, calculated for a particular range of η values and their corresponding ϕ values for (a) 8 TeV dataset and (b) 7 TeV dataset.

(6) Multifractal cross-correlation analysis is done as per the method described in Section 3.2 between the 10 pairs of datasets (5 for 8 TeV and 5 for 7 TeV), one being the sorted ϕ values and the other being the corresponding η values. The trend of generalized Hurst exponent $(h(q))$ for different order (q) is analyzed for all the 10 pairs of η and ϕ datasets as per the process described in Section 3.1. Along with that, for the same pairs of data-

sets the degree of cross-correlation$(h_{x,y}(q))$ for different order (q) is analyzed as per the methodology described in Section 3.2. The trend of $h(q)$ and $h_{x,y}(q)$ versus q for the particular sample pair of η and ϕ space for which trends of $\log_2[F_q(s)]$ vs $\log_2[s]s$ are shown in Figure 1(a) (η space) and Figure 4(a) (ϕ space) for 8 TeV dataset and Figure 1(b) (η space) and Figure 4(b) (ϕ space) for 7 TeV dataset is shown in Figures 5(a) and

5(b) for 8 and 7 TeV datasets, respectively. The values are shown in the figures for $q = -5, -4, \cdots, 5$. It should be noted that:

(i) As shown in Figures 5(a) and 5(b), the trend of dependence of $h(q)$ on q for individual η and ϕ spaces confirm their multifractality and the same for $h_{x,y}(q)$ on q for the same pair of η and ϕ spaces confirm their cross-correlation for both 8 and 7 TeV datasets

(ii) Figures 5(a) and 5(b) show that $h(q)$ decreases at a lower rate for the increasing values of negative qs for both φ and η data ranges in both energies of 8 and 7 TeV. This signifies that for negative values of q, the qth order RMS (calculated as per the equations in Step 4 and Step 5 of Section 3.1) is not much sensitive to the local fluctuations with small magnitudes for the datasets (ϕ and η) for both energies

However, for the ϕ data series corresponding to the particular range of η at 8 TeV, $h(q)$ decreases at a higher rate for positive values of q than the corresponding ones calculated for the same range of η at 7 TeV. This means, in this case, $h(q)$ is a bit more affected by the local fluctuations with large magnitudes, resulting in higher rate of decrease for $h(q)$ with increasing order of positive q for the ϕ data series of 8 TeV than the corresponding one for 7 TeV data. This has happened because there may exist fluctuations with comparatively large magnitude for the φ data series for higher energy—8 TeV than the one for 7 TeV.

(i) It is further observed in Figures 5(a) and 5(b) that $h_{x,y}(q)$ (calculated as per the equation in Step 4 of Section 3.2) for multifractal cross-correlation changes almost at the same rate for both 8 and 7 TeV energies. It should be noted that the maximum and minimum values of $h_{x,y}(q)$ for 8 and 7 TeV are different; however, the change of $h_{x,y}(q)$ with the increasing values of q is almost the same. Although for 8 TeV, there is higher rate of decrease for $h(q)$ with increasing order of positive qs for the ϕ data series than the corresponding one for 7 TeV data, resulting from possible higher magnitude of fluctuation for ϕ data series, that decreasing trend gets nullified while calculating the covariance of ϕ data series and corresponding η data series at 8 TeV energy. Hence, the trend of $h_{x,y}(q)$ with the increasing values of q is almost the same for both energies. However, this has resulted in the lower ranges of the values of degree of cross-correlation $h_{x,y}(q)$ for 8 TeV, making them less cross-correlated

(ii) For $q = 2$, both $h(q)$ and $h_{x,y}(q)$ are >0.5 and for ϕ space $h(q)$ is much higher than that for the corresponding η space

(iii) Also, $h_{x,y}(q)$ is much higher than 0.5 for the pair of datasets for $q = 2$. This suggests the presence of long-range correlation and persistence in both spaces

(iv) Moreover, there is a drop in the value of $h_{x,y}(q)$ around $q = -1$. In most of the previous works, it has been shown that there exists similar trend of $h_{x,y}(q)$ or the degree of cross-correlation with increasing values of order or q, as seen in the present analysis

(v) Similar analysis has been done for all the 10 pairs of datasets, and similar trend is observed for all of them

(7) Figures 6(a) and 6(b) show the comparison of the trend of different values of $f(\alpha)$ versus α for the same η, ϕ spaces and the same trend calculated for their cross-correlation, for 8 and 7 TeV datasets, respectively

(i) For both energy ranges, width of the cross-correlation curve is the maximum, followed by the width of the multifractal spectrum of the ϕ space and then that of the η space

(ii) Again, similar trend is observed for all the pairs of datasets in this experiment. The more wide the spectrum is, the more degree of multifractality is inherent in the data series

(8) The qth order detrended covariance $F_{xy}(q, s)$ is calculated for a particular range of η values and their corresponding ϕ values as per the Step 4 of the MF-DXA methodology described in Section 3.2, and the trend of $\log_2[F_{xy}(q, s)]$ vs $\log_2[s]$ for $q = -5, 0, 5$ is shown in Figures 7(a) and 7(b) for 8 and 7 TeV datasets, respectively

(i) Their linear trend (more prominent for the values of $q > 0$) confirms the power-law behavior of $F_{xy}(q, s)$ versus s for all the values of q

(ii) Similar calculation is done for all the η ranges and their corresponding ϕ spaces, for both 8 and 7 TeV datasets, and similar trend is observed

As explained in Step 5 of the MF-DXA methodology described in section 3.2, here, $h_{xy}(q) > 0.5$ implies that there are persistent long-range cross-correlations, where a large value in ϕ space is likely to have an equally large corresponding η value. The higher the value of $h_{xy}(q)$, the higher the cross-correlation. Figures 7(a) and 7(b) show how the qth

(a)

(b)
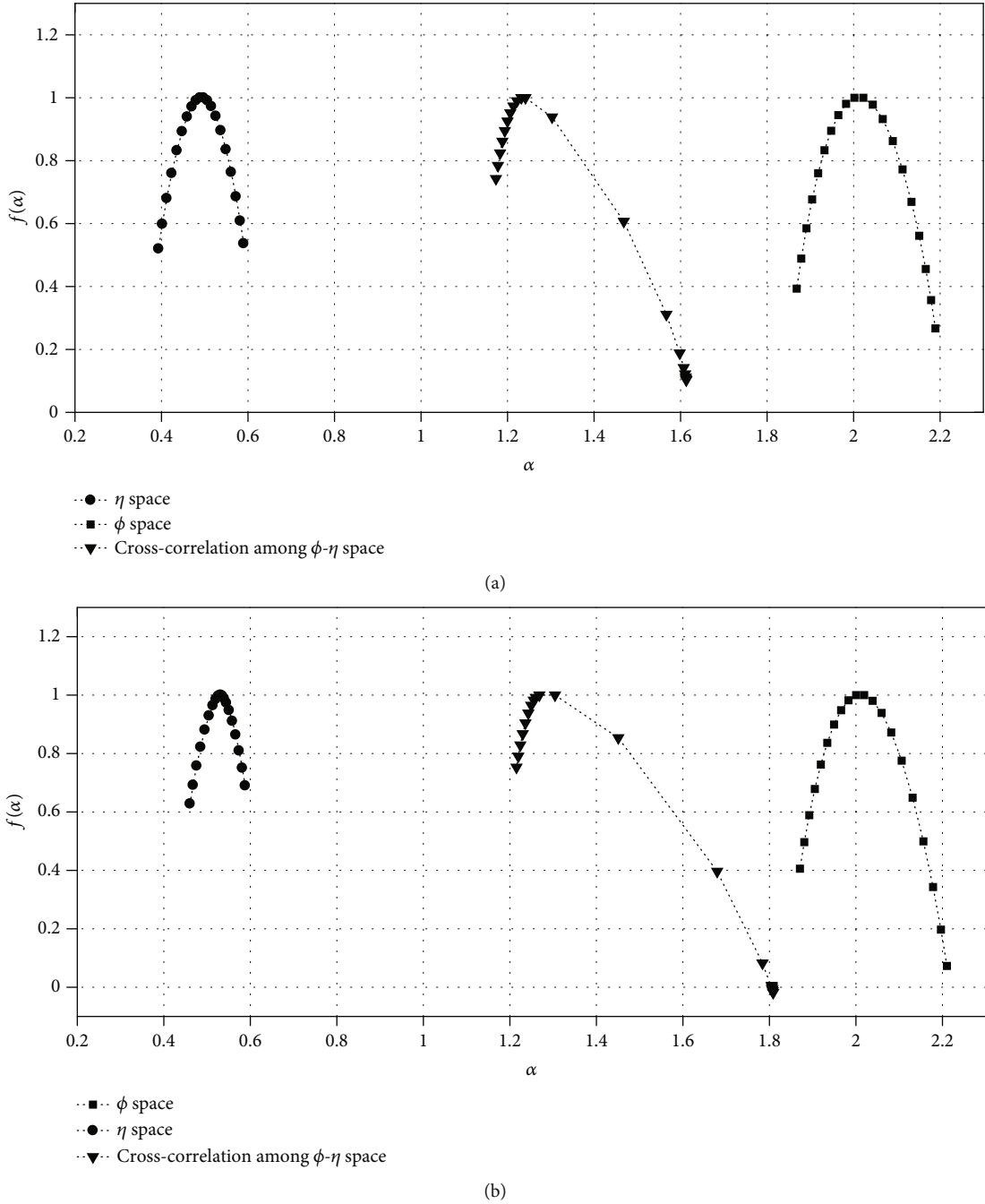
FIGURE 6: Comparison of the trend of different values of $f(\alpha)$ versus α among the same η, ϕ spaces and the same trend calculated for their cross-correlation, for the (a) 8 TeV dataset and (b) 7 TeV dataset.

order detrended covariance or $F_{xy}(q,s)$ varies with increasing values of scale (s) in log scale. The straight line fitting of $F_{xy}(q,s)$ versus s in log scale is shown in the figures and the relevant power-law coefficients or degree of cross-correlations ($h_{xy}(q)$) are also shown in the fitting equations in the diagram. It is evident from the figures that for negative values of q, degree of cross-correlation is higher than that for positive values of q. Covariance of small magnitudes are reflected more prominently for nega-

tive values of q, which signifies that the average cross-correlation between φ spaces and their corresponding η spaces fluctuates more for the values of $q < 0$ and gives rise higher value of $h_{xy}(q)$. This fluctuation becomes lesser as q increases from $q = -5, -4, \cdots, -1$. For positive values of q ($q \geq 0$), the qth order detrended covariance starts to fluctuate very less and gives rise to lesser values of $h_{xy}(q)$. Hence, the value of $h_{xy}(q)$ also changes more for $q < 0$ than for $q > 0$. This different degree of

(a)
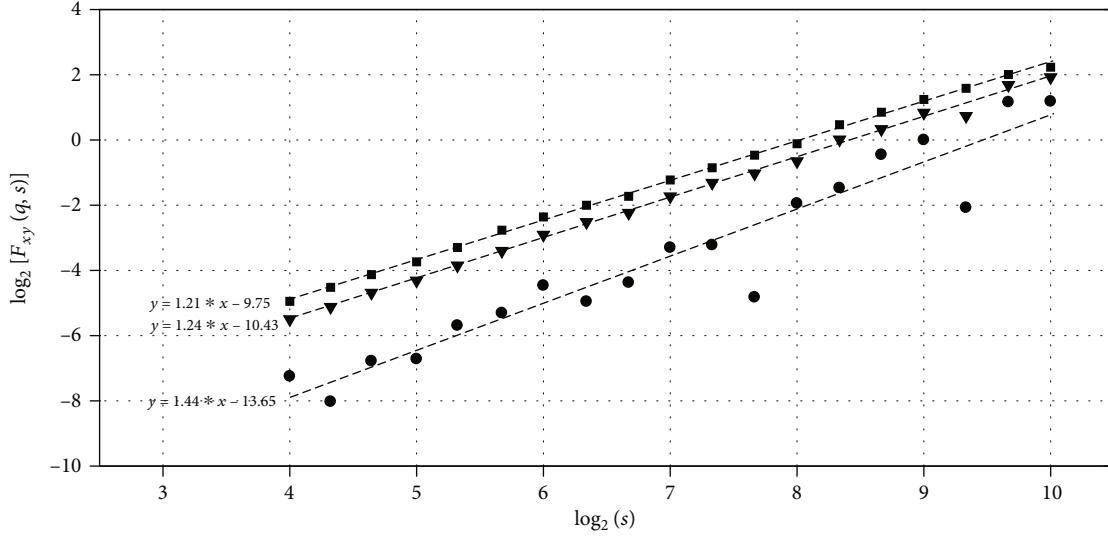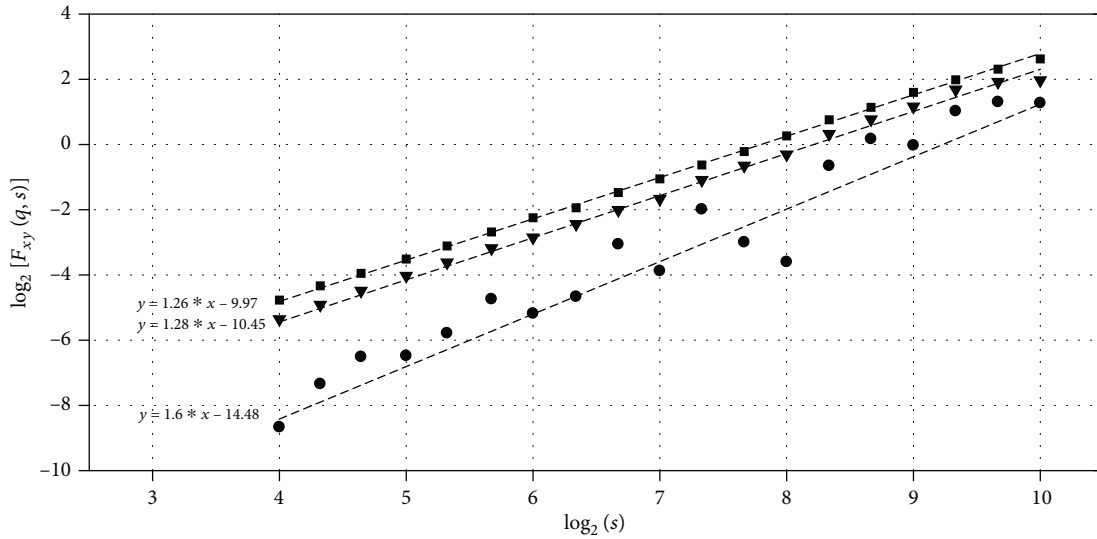
(b)

FIGURE 7: Trend of $\log_2[F_{xy}(q, s)]$ vs $\log_2[s]$ for $q = -5, 0, 5$, calculated for a particular range of η values and their corresponding φ values for (a) 8 TeV dataset and (b) 7 TeV dataset.

detrended covariance between φ values and their corresponding η values for different values of q gives a range of $h_{x,y}(q)$ forming the multifractal cross-correlation spectrum.

Figures 7(a) and 7(b) show that the qth order detrended covariance or $F_{xy}(q, s)$ calculated for large values of a particular η space and its corresponding ϕ space having large values is fluctuating more with increasing scale (s) for negative

values of q yielding to comparatively higher values of $h_{xy}(q)$—power-law coefficient. Also, for $q > 0$, $F_{xy}(q, s)$ would flatten or change in almost constant rate with s as evident in the figures and yielding to comparatively lesser values of $h_{xy}(q)$ for both 8 and 7 TeV energies. For calculating the degree of multifractal cross-correlation denoted by γ_is, the trend of $F_{xy}(q, s) \propto s^{h_{xy}(q)}$ for $q = 2$ is analyzed [20], as elaborated in Section 3.2. Further, in most of the
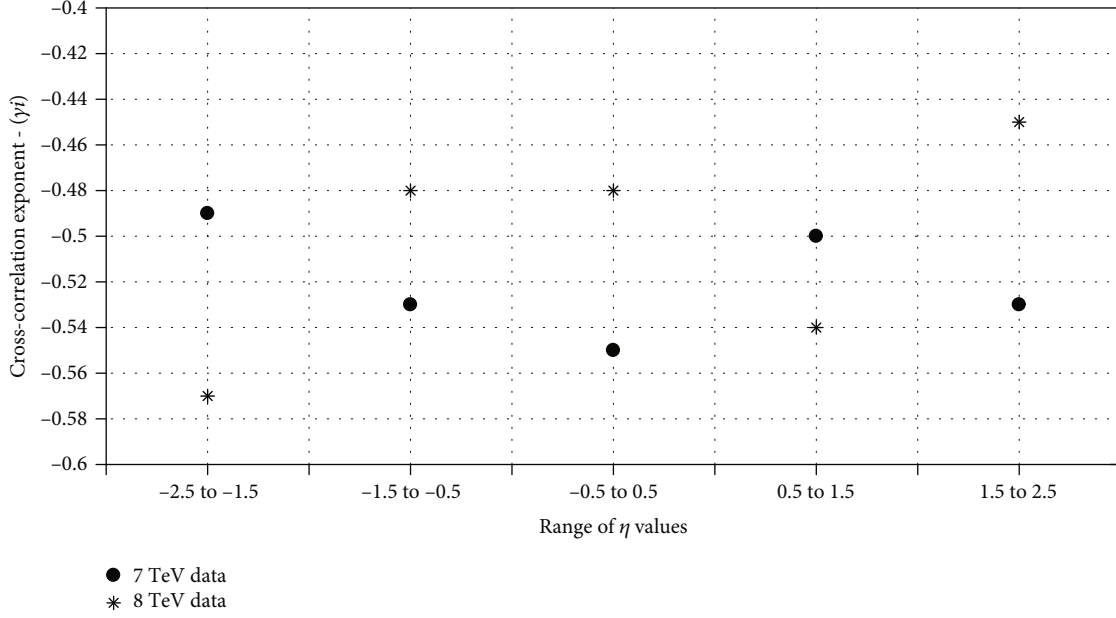
FIGURE 8: Comparison of multifractal cross-correlation coefficient (γ_i) between φ and η spaces for all the 5 ranges of η values for 7 and 8 TeV datasets.

TABLE 2: Comparison of the experimental values of multifractal cross-correlation coefficients (γ_i) between ϕ and η spaces for all the 5 ranges of η values for 7 and 8 TeV datasets, between the original and the randomized version.

η ranges	MFD-XA coefficients (γ_i)			
	8 TeV		7 TeV	
	Orig	Rand	Orig	Rand
−2.5 to −1.5	−0.57	1.01	−0.49	0.94
−1.5 to −0.5	−0.48	1.00	−0.53	0.99
−0.5 to 0.5	−0.48	1.02	−0.55	1.00
0.5 to 1.5	−0.54	0.98	−0.50	1.01
1.5 to 2.5	−0.45	0.96	−0.53	0.94

previous works, it had been shown that $F_{xy}(q, s)$ varies with increasing values of scale or s in log scale for different order or values of q, in similar manner as it is varying in this experiment.

(9) Two sets of multifractal cross-correlation coefficient, denoted by γ_i for $i = 1, 2, \cdots, 5$ for each of the 8 and 7 TeV datasets, are computed as per the method described in Section 3.2. This way, the degree of cross-correlation between ϕ and η spaces for all the 5 ranges of η values as specified in Step 1 for both 8 and 7 TeV datasets are calculated

(10) Then, each of the azimuthal ϕ spaces extracted in Step 4 is randomized, and the multifractal cross-correlation coefficients between the randomized ϕ spaces and the corresponding η spaces are extracted for both 8 and 7 TeV datasets are calculated as per the method described in Section 3.2

(11) Figure 8 shows the comparison of multifractal cross-correlation coefficients (γ_i) between ϕ and η spaces for all the 5 ranges of η values for 7 and 8 TeV datasets with respect to their rapidity as well as energy dependence. Here, we notice that:

 (i) For both 7 and 8 TeV data, all the 5 η spaces are highly cross-correlated with their corresponding ϕ spaces

(ii) It should be noted that $\gamma_i = 1$ for uncorrelated data series. The more correlated the data series are, the lower the value of γ_i. For 8 TeV data, the first range of η values is most cross-correlated with the corresponding ϕ space, and the most cross-correlated range for 7 TeV data is the third one

The comparison of γ_is for all the 5 η ranges for 7 and 8 TeV datasets between the original and the randomized version is shown in Table 2. The values of the parameter, γ_i, calculated for experimental data being significantly different from the shuffled ensembles, confirm that this inherent degree of multifractal cross-correlation between each η space and its corresponding ϕ space is never the outcome of randomization process but is indicative of the inherent multifractal cross-correlation among η and corresponding ϕ values in the di-muon production process.

(12) Hence, the values of γ_is calculated for the original and the randomized version differ substantially, clearly establishing the statistical significance of the results obtained from the actual data.

5. Conclusion

Oppositely charged di-muon production is the outcome of several hypothetical processes and investigation for such processes have been the goal of experiment of pp collision at 7 and 8 TeV and also at other energies at the CMS collaboration. However, the present investigation, as we have pointed out earlier, is based on a deep-rooted dynamics of di-lepton production process in hadron-hadron interaction from the basic perspective of symmetry-based scaling in different pseudorapidity ranges in two different energies. We have used two rigorous and robust methodologies, namely, MF-DFA and MF-DXA, for the scaling analysis of the dynamics of the di-muon production process using di-muon data taken from the primary dataset of RunA(2011) and RunB(2012) of the pp collision at 7 TeV and 8 TeV, respectively, from CMS collaboration. We have analyzed how this scaling pattern has evolved from one rapidity range to the next one and how this change evolved from lower energy range of 7 TeV to the higher one 8 TeV, and the findings are listed below.

(1) The linear trend of $F_q(s)$ vs s for all the values of q for all the 5 ranges of η values for 8 and 7 TeV datasets confirms the fractality as well as the multifractality of all the pseudorapidity spaces. Figures 1(a) and 1(b) show similar trend for a particular range of η values for both energy ranges. Similar linear trend is observed for the ϕ spaces corresponding to the η spaces, which again confirm the fractality and the multifractality of the ϕ spaces as well. Figures 4(a) and 4(b) show the linear trend calculated for the ϕ spaces corresponding to the particular η range for both energy ranges

(2) Table 1 and Figure 3 show how the widths of the multifractal spectrum differ from one η space to the other and how they in turn differ from one energy range to another. It is interesting to note that for both 7 and 8 TeV energies, the η space corresponding to the first range of η has the maximum width of multifractal spectrum/degree of complexity, or in other words, they are most multifractal in nature among the other five ranges. Moreover, they have exactly the same value for the parameter. As for the minimum width of multifractal spectrum, the second η range for 8 TeV data and third η range for 7 TeV data is 0.02 which is again the same for both energy ranges

(3) The linear trend of $\log_2[F_{xy}(q,s)]$ vs $\log_2 s$ for $q = -5, 0, 5$ which is shown in Figures 7(a) and 7(b) for 8 and 7 TeV datasets, respectively, for the same specific η range and its corresponding ϕ space confirms the self-similar cross-correlation between the spaces which is evident from the goodness-of-fit for all the values of q. Similar trend is observed for the rest of the η ranges

(4) Table 2 and the Figure 8 show that for both 7 and 8 TeV data, all the 5 η spaces are highly cross-correlated with their corresponding ϕ spaces and how the degree of cross-correlation changes from one η space to the other and from one energy range to another. It should be noted that the degree of multifractal cross-correlation, γ_i, is maximum for the first η range for 8 TeV data, and the same is maximum for the third range of 7 TeV data. γ_i is minimum for the fifth η range for 8 TeV data and for the first range of 7 TeV data

This analysis manifests different degree of symmetry scaling or scale-freeness in different pseudorapidity domains and at the same time different degree of cross-correlation between pseudorapidity and azimuthal space at both energy. The differences in the values of scaling and cross-correlation exponents representing the *degree of symmetry scaling* and *degree of cross-correlation*, respectively, calculated for different ranges of rapidity and at two different energy values, indicate the existence of several processes involved in the production process of oppositely charged di-muons giving rise to varying *degree* of scaling. The observed difference of *degree of symmetry scaling* in different rapidity domains at two different energy values may provide a clue for exploring other processes in regards to di-muon production even from the perspective beyond the standard model. This novel method has the prospect for applications in different high-energy interactions to detect not only different possible resonance states but also for identification of exotic resonance states proposed by theories.

Data Availability

The data used to support the findings of this study are included within the submitted article in Section 3.1, which says the data used in the experiment is extracted from pp collision at 8 and 7 TeV of the CMS collaboration. The DOI and other details are given in the manuscript. The data is publicly available for experiment by CMS (CERN Opendata).

Conflicts of Interest

The authors declare that they have no conflicts of interest.

Acknowledgments

References

[1] A. Bialas and R. Peschanski, "Moments of rapidity distributions as a measure of short-range fluctuations in high-energy collisions," *Nuclear Physics B*, vol. 273, no. 3-4, pp. 703–718, 1986.

[2] A. Bialas and R. Peschanski, "Intermittency in multiparticle production at high energy," *Nuclear Physics B*, vol. 308, no. 4, pp. 857–867, 1988.

[3] E. A. De Wolf, I. M. Dremin, and W. Kittel, "Scaling laws for density correlations and fluctuations in multiparticle dynamics," *Physics Reports*, vol. 270, no. 1-2, pp. 1–141, 1996.

[4] R. C. Hwa, "Fractal measures in multiparticle production," *Physical Review D*, vol. 41, no. 5, pp. 1456–1462, 1990.

[5] G. Paladin and A. Vulpiani, "Anomalous scaling laws in multifractal objects," *Physics Reports*, vol. 156, no. 4, pp. 147–225, 1987.

[6] P. Grassberger and I. Procaccia, "Dimensions and entropies of strange attractors from a fluctuating dynamics approach," *Physica D: Nonlinear Phenomena*, vol. 13, no. 1-2, pp. 34–54, 1984.

[7] T. C. Halsey, M. H. Jensen, L. P. Kadanoff, I. Procaccia, and B. I. Shraiman, "Fractal measures and their singularities the characterization of strange sets," *Physical Review A*, vol. 33, no. 2, pp. 1141–1151, 1986.

[8] F. Takagi, "Multifractal structure of multiplicity distribution in particle collisions at high energies," *Physical Review Letters*, vol. 72, no. 1, pp. 32–35, 1994.

[9] C. K. Peng, S. V. Buldyrev, S. Havlin, M. Simons, H. E. Stanley, and A. L. Goldberger, "Mosaic organization of DNA nucleotides," *Physical Review E*, vol. 49, no. 2, pp. 1685–1689, 1994.

[10] J. W. Kantelhardt, S. A. Zschiegner, E. Koscielny-Bunde, S. Havlin, A. Bunde, and H. E. Stanley, "Multifractal detrended fluctuation analysis of nonstationary time series," *Physica A: Statistical Mechanics and its Applications*, vol. 316, no. 1-4, pp. 87–114, 2002.

[11] UA1 Collaboration, "Multifractal analysis of minimum bias events in $\sqrt{s} = 630\, GeV \bar{p} p$ collisions," *Zeitschrift für Physik C Particles and Fields*, vol. 56, pp. 37–46, 1992.

[12] M. K. Suleymanov, M. Sumbera, and I. Zborovsky, *Entropy and Multifractal Analysis of Multiplicity Distributions from Pp Simulated Events up to LHC Energies*, 2003.

[13] Y. X. ZHANG, W. Y. QIAN, and C. B. YANG, "Multifractal structure of pseudorapidity and azimuthal distributions of the shower particles in Au + Au collisions," *International Journal of Modern Physics A*, vol. 18, pp. 2809–2816, 2007.

[14] E. G. Ferreiro and C. Pajares, "High multiplicity *pp* events and *J/ψ* production at energies available at the CERN Large Hadron Collider," *Physical Review C*, vol. 86, no. 3, 2012.

[15] M. V. Tokarev, T. G. Dedovich, and I. Zborovský, "Self-similarity of Jet and Top-quark production at Tevatron and LHC," in *Particle Physics at the Year of Centenary of Bruno Pontecorvo*, pp. 186–190, 2015.

[16] M. Tokarev and I. Zborovský, "Self-similarity of strangeness production in pp collisions at RHIC," *Journal of Physics: Conference Series*, vol. 668, 2016.

[17] M. V. Tokarev and I. Zborovský, "Self-similarity of proton spin and asymmetry of jet production," *Physics of Particles and Nuclei Letters*, vol. 12, no. 2, pp. 214–220, 2015.

[18] E. G. Baldina and A. A. Baldin, "Relativistically invariant self-similarity approach for description of collective phenomena," *EPJ Web of Conferences*, vol. 138, 2017.

[19] T. Sonoda, *Application of self-similar symmetry model to dark energy*, Preprint, 2018.

[20] B. Podobnik and H. E. Stanley, "Detrended crosscorrelation analysis: a new method for analyzing two nonstationary time series," *Physical Review Letters*, vol. 100, no. 8, 2008.

[21] F. Wang, G. P. Liao, X. Y. Zhou, and W. Shi, "Multifractal detrended cross-correlation analysis for power markets," *Nonlinear Dynamics*, vol. 72, no. 1-2, pp. 353–363, 2013.

[22] S. Bhaduri and D. Ghosh, "Pion fluctuation in high-energy collisions — a chaos-based quantitative estimation with visibility graph technique," *Acta Physica Polonica B*, vol. 48, no. 4, p. 741, 2017.

[23] ALICE-Collaboration, *Pb-Pb VSD masterclass data sample at 2.76 TeV per nucleon pair*, CERN, 2014.

[24] S. Bhaduri, A. Bhaduri, and D. Ghosh, "Pion fluctuation study in Pb–Pb collision at 2.76 TeV per nucleon pair from ALICE experiment with chaos and complex network-based methods," *Physics of Particles and Nuclei Letters*, vol. 16, no. 3, pp. 229–239, 2019.

[25] S. Bhaduri, A. Bhaduri, and D. Ghosh, *Pion Fluctuation Study in Pb-Pb Collision at 3.5TeV from ALICE Experiment with Chaos and Complex Network-based Methods*, Technical Report, 2018.

[26] S. Bhaduri, A. Bhaduri, and D. Ghosh, "Symmetry-scaling based complex network approach to explore exotic hadronic states in high-energy collision," *Physics of Particles and Nuclei Letters*, vol. 16, no. 6, pp. 779–788, 2019.

[27] S. Bhaduri and D. Ghosh, "Multiplicity fluctuation and phase transition in high-energy collision — a chaos-based study with complex network perspective," *International Journal of Modern Physics A*, vol. 31, no. 35, p. 1650185, 2016.

[28] S. Bhaduri, A. Bhaduri, and D. Ghosh, "Study of multiplicity dependence of pion fluctuations in $\pi^- $–AgBr collisions at 350 GeV using complex network approach," *Pramana-Journal of Physics*, vol. 92, no. 1, 2019.

[29] A. Bhaduri and D. Ghosh, "Quantitative assessment of heart rate dynamics during meditation: an ECG based study with Multi-Fractality and visibility graph," *Frontiers in Physiology*, vol. 7, 2016.

[30] S. Bhaduri and D. Ghosh, "Fractal study of pion void probability distribution in ultrarelativistic nuclear collision and its target dependence," *Modern Physics Letters A*, vol. 31, no. 27, p. 1650158, 2016.

[31] A. Bhaduri, S. Bhaduri, and D. Ghosh, "Azimuthal pion fluctuation in ultra relativistic nuclear collisions and centrality dependence—a study with chaos based complex network analysis," *Physics of Particles and Nuclei Letters*, vol. 14, no. 4, pp. 576–583, 2017.

[32] S. Bhaduri, A. Bhaduri, and D. Ghosh, "A new approach of chaos and complex network method to study fluctuation and phase transition in nuclear collision at high energy," *The European Physical Journal A*, vol. 53, no. 6, 2017.

[33] S. Bhaduri, A. Bhaduri, and D. Ghosh, "Clan-Model of particle production process-revisited in chaos-based complex network scenario," *Physics of Particles and Nuclei Letters*, vol. 15, no. 4, pp. 446–455, 2018.

[34] L. Zhao, W. Li, C. Yang et al., "Multifractal and network analysis of phase transition," *PLoS One*, vol. 12, p. 23, 2016.

[35] G. F. Zebende, M. V. S. da Silva, A. C. P. Rosa, A. S. Alves, J. C. O. de Jesus, and M. A. Moret, "Studying long-range correlations in a liquid-vapor-phase transition," *Physica A: Statistical Mechanics and its Applications*, vol. 342, no. 1-2, pp. 322–328, 2004.

[36] CMS Collaboration, "Search for supersymmetry in events with opposite-sign dileptons and missing transverse energy using an artificial neural network," *Physical Review D*, vol. 87, no. 7, 2013.

[37] A. Uras, "Low-mass dimuon measurements in pp, p-Pb and Pb-Pb collisions with ALICE at the LHC," *Journal of Physics: Conference Series*, vol. 668, 2016.

[38] The ATLAS Collaboration, "Measurement of the exclusive $\gamma\gamma \longrightarrow \mu^+\mu^-$ process in proton–proton collisions at $\sqrt{s} = 13$ TeV with the ATLAS detector," *Physics Letters B*, vol. 777, pp. 303–323, 2018.

[39] K. Werner, A. G. Knospe, C. Markert et al., "Resonance production in high energy collisions from small to big systems," *EPJ Web of Conferences*, vol. 171, 2018.

[40] CMS-collaboration, *MuOniaParked primary dataset in AOD format from Run of 2012 (/MuOniaParked/Run2012B-22Jan2013-v1/AOD)*, CERN, 2017.

[41] CMS-collaboration, *MuOnia primary dataset in AOD format from RunA of 2011 (/MuOnia/Run2011A-12Oct2013-v1/AOD)*, CERN, 2016.

[42] J. W. Kantelhardt, E. Koscielny-Bunde, H. H. A. Rego, S. Havlin, and A. Bunde, "Detecting long-range correlations with detrended fluctuation analysis," *Physica A*, vol. 295, no. 3-4, pp. 441–454, 2001.

[43] Y. Ashkenazy, S. Havlin, P. C. Ivanov, C. K. Peng, V. Schulte-Frohlinde, and H. E. Stanley, "Magnitude and sign scaling in power-law correlated time series," *Physica A: Statistical Mechanics and its Applications*, vol. 323, pp. 19–41, 2003.

Research Article

Centrality Dependence of Multiplicity Fluctuations from a Hydrodynamical Approach

Hong-Hao Ma,[1] Kai Lin [iD],[2,3] Wei-Liang Qian [iD],[1,3,4] and Bin Wang[1,5,6]

[1]*School of Physical Science and Technology, Yangzhou University, 225002 Yangzhou, Jiangsu, China*
[2]*Hubei Subsurface Multi-Scale Imaging Key Laboratory, Institute of Geophysics and Geomatics, China University of Geosciences, 430074 Wuhan, Hubei, China*
[3]*Escola de Engenharia de Lorena, Universidade de São Paulo, 12602-810 Lorena, SP, Brazil*
[4]*Faculdade de Engenharia de Guaratinguetá, Universidade Estadual Paulista, 12516-410 Guaratinguetá, SP, Brazil*
[5]*Collaborative Innovation Center of IFSA (CICIFSA), Shanghai Jiao Tong University, 200240 Shanghai, China And*
[6]*School of Aeronautics and Astronautics, Shanghai Jiao Tong University, 200240 Shanghai, China*

Correspondence should be addressed to Wei-Liang Qian; wlqian@usp.br

As one of the possible signals for the whereabouts of the critical point on the QCD phase diagram, recently, the multiplicity fluctuations in heavy-ion collisions have aroused much attention. It is a crucial observation of the Beam Energy Scan program of the Relativistic Heavy Ion Collider. In this work, we investigate the centrality dependence of the multiplicity fluctuations regarding the recent measurements from STAR Collaboration. By employing a hydrodynamical approach, the present study is dedicated to the noncritical aspects of the phenomenon. To be specific, in addition to the thermal fluctuations, finite volume corrections, and resonance decay at the freeze-out surface, the model is focused on the properties of the hydrodynamic expansion of the system and the event-by-event initial fluctuations. It is understood that the real signal of the critical point can only be obtained after appropriately subtracting the background; the latter is investigated in the present work. Besides the experimental data, our results are also compared to those of the hadronic resonance gas, as well as the transport models.

1. Introduction

Described by the quantum field theory, the properties of a static system located in the vicinity of a fixed point are governed by its universality class, in terms of the respective critical exponents. The latter dictates the scaling relations among different observables, as well as power-law divergences of relevant physical quantities, such as correlation length and particle fluctuations. In fact, it has been speculated that the chiral phase transition of the QCD matter is of second order, related to the spontaneous symmetry breaking of the QCD vacuum. However, the nonperturbative nature of QCD poses tremendous difficulties for the analytic approach in terms of the theory of the renormalization group. Therefore, one has to resort to either numerical or phenomenological methods. Lattice QCD simulations [1,

2] have found a smooth crossover at vanishing baryon density and for the limit of large strange quark mass. On the other hand, at finite chemical potential, one usually turns to model calculations. A considerable amount of efforts [3–7] indicates the occurrence of a first-order phase transition between the hadronic and quark-gluon plasma (QGP). Therefore, a critical point is expected where the first-order phase transition line terminates.

The hot and dense matter created in the heavy-ion nuclear collision, however, is not a static system. It evolves in time and may pass through the vicinity of the critical point. Moreover, the freeze-out hypersurface, where the hadrons become mostly free particles and stream to the detector, is not necessarily close to the critical point. Nonetheless, it is expected that resultant final state hadrons carry valuable information about the critical phenomon.

On the theoretical side, many efforts have been devoted to the topic [8, 9]. As an exceedingly complicated problem, it might be governed simultaneously by distinct mechanisms. Effective field theory at finite temperature has been employed to evaluate the moments of particle multiplicities. It is speculated by the so-called σ model [10–12] that higher moments are sensitive to the phase structure of the QCD matter. To be specific, the normalized fourth-order cumulant of multiplicity distribution might be a nonmonotonic function of collision energy. Regarding the fact that the system created in heavy-ion collision evolves rapidly in time, it is essential to take the dynamical effect of system evolution into account. Tentatives along this train of thought [13] also lead to a variety of models. For instance, the chiral fluid dynamics [14–17] divides the physics into two parts. On the one hand, the quark degree of freedom is treated to be in an equilibrated heat bath, which evolves mostly in accordance with a hydrodynamical picture. On the other hand, the chiral field is responsible for carrying the physics of symmetry spontaneous breaking, and the transition is triggered by the scalar density of the quark field. In a more recent version of the chiral model, a resultant Langevin equation is used to describe the chiral field. Besides, another vital factor, namely, the critical slowing down, is implemented by another approach, the Hydro+ model [18]. Here, the physics in question is that in the vicinity of the critical point, the time scale to achieve local equilibrium becomes comparable to that for global equilibrium. There are other relevant features, which are essential even in the framework of conventional hydrodynamics, due to the existence of a critical point. These include the modification to the equation of state (EoS), thermal [19], nonequilibrium [20], fluctuations on the freeze-out surface, and experimental uncertainties and cuts, in addition to other spurious contributions [21, 22].

On the experimental side, the ongoing Beam Energy Scan (BES) program [23–27] at the Relativistic Heavy Ion Collider (RHIC) is dedicated to exploring the phase diagram of QCD.

The program is to carry out Au+Au collisions ranging from 3.0 to 62.4 GeV. Therefore, the properties of the critical point in question, if any, are likely to be captured by the data. The measurements, in turn, are aiming at the high baryon density region of the QCD matter. To be specific, the measured quantities are those sensitive to the underlying physics while accessible experimentally. The higher cumulants of conserved charges, as well as their combinations, are promising candidates recalling the above discussions. As a matter of fact, measurements of multiplicity fluctuations were carried out in BES-I and have been further scheduled for BES-II programs, and have drawn much attention recently in the literature.

For the latter, the conditions for the conservation of net charges are explicitly considered, and the effect was shown to be substantial. In addition, resonance decay was shown to cause nonnegligible deviation from pure statistical distributions [28–30]. For the most part, the obtained results [30–35] are manifestly consistent with the experimental data [36, 37].

The present work involves an effort to address the multiplicity fluctuations from a hydrodynamic viewpoint.

It is a further progress concerning a recent attempt [38] to evaluate multiplicity fluctuations using a hydrodynamical model. Our approach does not explicitly involve the physics of critical phenomenon as mentioned above, but it is aimed at providing an estimation of the background signal from a mostly thermalized expanding system. In fact, it is understood, a significant portion of the measured multiplicity fluctuation comes from the thermal fluctuations. This has been confirmed from the calculations by using the Hadron Resonance Gas (HRG) models in the context of either grand canonical ensemble (GCE) [30–32] or canonical ensemble regarding conserved charges [28, 29, 33]. The present model takes into account thermal fluctuations by using the formalism of GCE. Also, volume correction and resonance decay are implemented in the code regarding hadron emission. The hydrodynamic evolution is solved by using the Smoothed Particle Hydrodynamics (SPH) algorithm. In our approach, every fluid element, denoted by an SPH particle, corresponds to a quantum GCE. The information concerning the system expansion is recorded on the freeze-out surface.

The rest of the paper is organized as follows. In the following section, we briefly review our hydrodynamical model, as well as thermodynamical fluctuations and resonance decay. The results of numerical simulations are presented and discussed in Section 3. The last section is dedicated to concluding remarks.

2. A Hydrodynamic Approach for Multiplicity Fluctuations

In this section, we briefly describe the model employed in the present study. The temporal expansion of the system is described by SPheRIO [39], a hydrodynamic code for an ideal relativistic fluid based on the SPH algorithm. In terms of discrete Lagrangian coordinates, individual fluid motion is mimicked, known as SPH particle. For the time being, we neglect any dissipative effects, and the Cooper-Frye sudden freeze-out is assumed for a constant temperature. The latter, as discussed below, provides the baseline to evaluate the thermal fluctuations in the corresponding local rest frame. For the present study, the model parameters have been determined as to reproduce the experimental data regarding the particle spectra [40–47].

On the freeze-out surface, every SPH particle is treated as a quantum GCE at a given temperature. Therefore, a hydrodynamic event can be viewed as a collection of GCE ensembles represented by SPH particles. As discussed in Ref. [38], we do not explicitly incorporate global charge conservation at the freeze-out surface. It is noted that progress has been made very recently about implementing canonical or microcanonical systems in a hydrodynamical approach [48].

In a hydrodynamic approach, each fluid element is considered to be in local equilibrium. Usually, the volume in a static homogeneous system should be replaced by a time-like 3-surface σ_μ. In the case of the SPH method, the latter is further expressed in terms of SPH degrees

of freedom. To be specific,

$$E\frac{d^3N_i}{dp^3} = \sum_j \frac{\nu_j n_{j\mu} p^\mu}{s_j |n_{j\rho} u_j^\rho|} \theta\left(u_{j\delta} p^\delta\right) \langle n_i(u_{j\nu} p^\nu, x)\rangle, \quad (1)$$

where p and E are the momentum and energy of the emitted hadron, respectively, the subscript i indicates particle species, the sum in j is carried out for SPH particles, ν_j and s_j represent the total entropy and entropy density of the j-th SPH particle, respectively. $n_i(u_{j\nu} p^\nu, x)$ is defined in the context of a static statistical ensemble in the comoving frame, as will be discussed below. Subsequently, the ensemble average of particle number reads

$$\langle N_i \rangle = \int p\perp dp\perp dy d\phi \sum_j \frac{\nu_j n_{j\mu} p^\mu}{s_j |n_{j\rho} u_j^\rho|} \theta\left(u_{j\delta} p^\delta\right) \langle n_i(u_{j\nu} p^\nu, x)\rangle. \quad (2)$$

It is straightforward to show that the covariance is

$$\langle \Delta N_i \Delta N_j \rangle = \int p\perp dp\perp dy d\phi \sum_j \frac{\nu_j n_{j\mu} p^\mu}{s_j |n_{j\rho} u_j^\rho|} \theta\left(u_{j\delta} p^\delta\right) v_i^2(u_{j\nu} p^\nu, x), \quad (3)$$

where again $v_i^2(u_{j\nu} p^\nu, x)$ is defined in the context of the static statistical ensemble. The formalism for high-order moments can be derived in a similar fashion [38].

On an event-by-event basis, the hadrons emitted from an individual SPH particle, in its comoving frame of reference, can be treated as a statistical ensemble. For the latter, the particle number fluctuations have been extensively discussed, and relevant results can be found in Ref. [49]. To be specific, the GCE average value and variance of the occupation density in the momentum space read [28, 29]

$$\langle n_{p,i} \rangle = \frac{1}{\exp\left[\left(\sqrt{p^2 + m_i^2} - \mu_i\right)/T\right] - \gamma_i}, \quad (4)$$

$$\langle \Delta n_{p,i}^2 \rangle \equiv \langle \left(n_{p,i} - \langle n_{p,i}\rangle\right)^2 \rangle = \langle n_{p,i}\rangle\left(1 + \gamma_i\langle n_{p,i}\rangle\right), \quad (5)$$

where T is the temperature, m_i, μ_i are the particle mass and chemical potential of species i, respectively, and γ_i corresponds to Bose (+1), Fermi (−1), or Boltzmann (0) statistics.

In our approach, the fluctuations are independent for different particle species as well as different momentum spaces; the covariance reads

$$\langle \Delta n_{p,i} \Delta n_{k,j} \rangle = \delta_{ij} \delta_{pk} v_{p,i}^2, \quad (6)$$

where $\Delta n_{p,i} = n_{p,i} - \overline{n_{p,i}}$ and $v_{p,i}^2 = \Delta n_{p,i}^2$, defined in Equation (5).

By summing up different momentum states, the average number of particles of species i is found to be

$$\langle N_i \rangle = \sum_p \langle n_{p,i} \rangle = \frac{g_i V}{2\pi^2} \int_0^\infty p^2 dp \langle n_{p,i} \rangle. \quad (7)$$

The variance and covariance can be evaluated as follows:

$$\langle \Delta N_i \Delta N_j \rangle = \sum_{p,k} \langle \Delta n_{p,i} \Delta n_{k,j} \rangle = \delta_{i,j} \sum_p v_{p,i}^2. \quad (8)$$

Besides, higher statistical moments of multiplicity distributions like skewness $S \propto \langle \Delta N^3 \rangle$ and kurtosis $\kappa \propto \langle \Delta N^4 \rangle$ are also of particular importance. These quantities can be evaluated, and the resultant expressions can be found in the Appendix of Ref. [38].

The resonance decay can be considered by employing the generating function method introduced in Ref. [28]. In general, resonance decay brings about additional fluctuations on top of the thermodynamical ones.

3. Numerical Results and Discussions

We carried out hydrodynamic simulations of Au+Au collisions at 200 GeV by using SPheRIO code for different centrality windows. The number of participants of each event is thus subtracted, and the events are thus reorganized in accordance with the existing data of the BES program [26, 27].

The IC are generated by using NeXuS [50, 51]. The results presented below are from simulations carried out for 980 events for the 0-5%, 1039 events for the 6%-15%, 1138 events for the 15%-25%, 1112 events for the 25%-35%, 994 events for the 35%-45%, 966 events for the 45%-55%, and 985 events for the 60%-80% centrality windows, respectively. The number of participants is extracted from individual events and then assigned to respective centrality bins. For a given bin, the average number of participants, as well as the IC, is calculated. Subsequently, the hydrodynamical calculations are carried out by employing the averaged IC.

In Figure 1, we show the calculated dynamical fluctuations of particle ratios K/π, K/p, and p/π as functions of the numbers of participants. By definition, the quantity $\nu_{\text{dyn},p/\pi}$ measures the deviation in the ratios of p/π from those of a Poissonian distribution. To be specific, it reads

$$\nu_{\text{dyn},p/\pi} = \frac{\langle N_p(N_p - 1)\rangle}{\langle N_p\rangle^2} + \frac{\langle N_\pi(N_\pi - 1)\rangle}{\langle N_\pi\rangle^2} - 2\frac{\langle N_p N_\pi\rangle}{\langle N_p\rangle\langle N_\pi\rangle}. \quad (9)$$

The results of hydrodynamic simulations by SPheRIO and those of UrQMD as well as HRG models are presented together with the data from the STAR Collaborations [26].

The SPheRIO results show a reasonably consistent trend observed in the data. A similar agreement was also obtained by the transport model, UrQMD. These two approaches are intrinsically different from that for a static system, in terms of the HRG model with resonance decays. The latter does
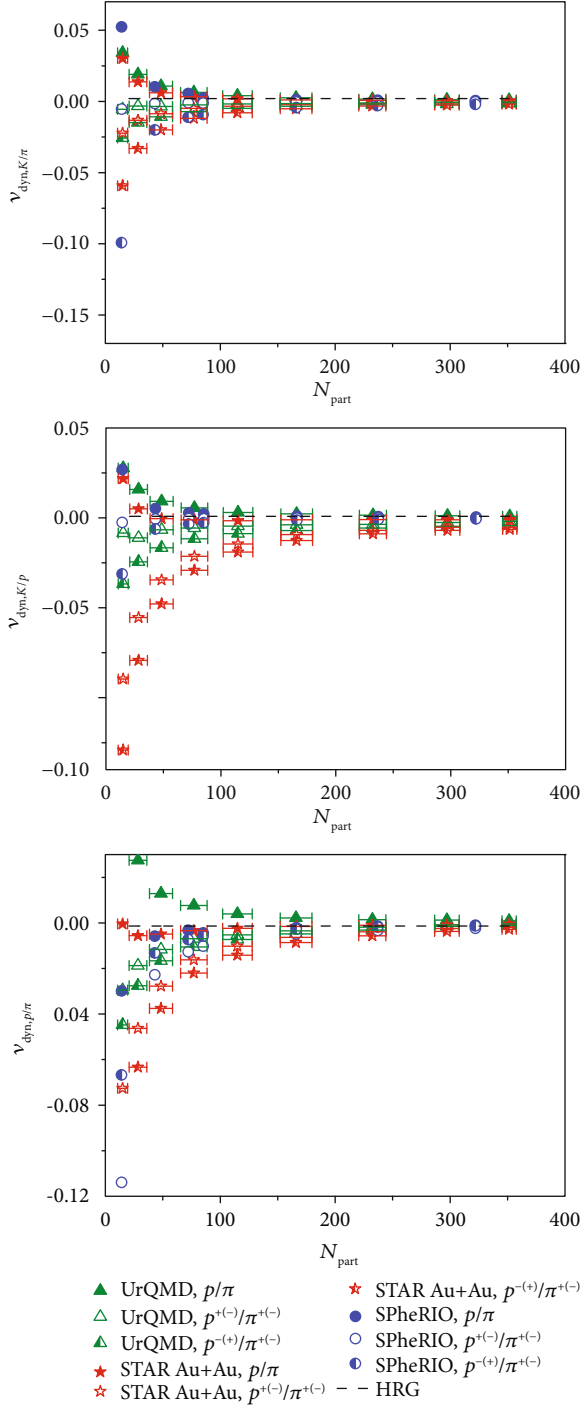
FIGURE 1: The centrality dependence of the calculated dynamical fluctuations of particle ratio K/π, p/π, and K/p for Au+Au collisions at 200 GeV. The STAR data are from Ref. [26], presented by filled, open, half-filled red stars. The SPheRIO results are given by the filled, open, half-filled blue circle. The UrQMD model calculations are shown in the filled, open, half-filled green triangle. The dashed black line presents the HRG calculations.

not depend on the volume or overall multiplicity. On the other hand, it is observed that the results from SPheRIO or UrQMD do scale with multiplicity. This indicates that the difference can be attributed to the finite volume of the sys-

tem, associated with the system expansion, as presented in both models. For more central collisions, the obtained N_{part} dependence of dynamical fluctuations from SPheRIO and UrQMD calculations is less prominent, and the magnitudes are close to that of the HRG model. As one goes to more peripheral collisions, the centrality dependence becomes more pronounced, especially when $N_{\text{part}} < 100$. For the hydrodynamical viewpoint, the observed difference from a pure thermal ensemble is due to the inhomogenous and anisotropic freeze-out surface elements, which is originated from the IC. For more peripheral collisions, the IC becomes more irregular as the hydrodynamical picture starts to fail. For event-by-event initial conditions, it has been observed [38] that the multiplicity fluctuations become the dominant factor. Therefore, from a theoretical viewpoint, the present framework provides a possibility to separate several different sources of multiplicity fluctuations, namely, the thermal fluctuations, resonance decay, hydrodynamical expansion, and initial state event-by-event fluctuations. As anyone of the above factors can be switched on and off independent of others, their respective effect can be investigated individually.

In Figure 2, we present various cumulant ratios at different centralities obtained by SPheRIO. The corresponding results obtained by the HRG models are also shown. The STAR measurements [37] are for Au+Au collisions at 200 GeV. The products $\kappa\sigma^2$ and $S\sigma$ are determined in terms of the ratios of particle number cumulants, which can be evaluated by using their respective definitions and the information of the freeze-out surface. In particular, $\kappa\sigma^2$ is expected to be equal to 1 for ideal Poissonian distribution. Therefore, the calculated quantity measures the deviation from a static homogeneous classical ensemble. For a hydrodynamic approach, such deviations come from the inhomogeneity, collective motion, resonance decay, and event-by-event IC fluctuations. Numerically, the results by the HRG model indicate that resonance decay does not imply a significant effect, when comparing against other factors. SPheRIO results present a similar tendency for the cases of σ^2/M and $S\sigma$, when compared to those of STAR data. This indicates a significant part of the net charge fluctuations can be understood within the framework of an approach that appropriately considers the system expansion. On the other hand, the resultant $\kappa\sigma^2$, although nonvanishing, are found to be relatively insignificant with respect to those of σ^2/M and $S\sigma$. It is particularly evident when one compares those against the difference between the experimental data and HRG results. By definition, kurtosis involves contributions up to the fourth moment of the particle distribution. Compared to the other two quantities, it measures higher moments of multiplicity fluctuations and is potentially more sensitive to the critical phenomenon [10, 11]. While the hydrodynamical model has mostly captured the characteristics of σ^2/M and $S\sigma$, the same approach is shown to be incapable of reproducing the main feature of the measured $\kappa\sigma^2$. The hydrodynamic results on kurtosis do not show a significant difference from those of HRG. In fact, the effect of system expansion seems to push the results towards a "wrong" direction further. Therefore, it is speculated that the experimentally observed nonmonotonical dependence of kurtosis on the centrality might imply
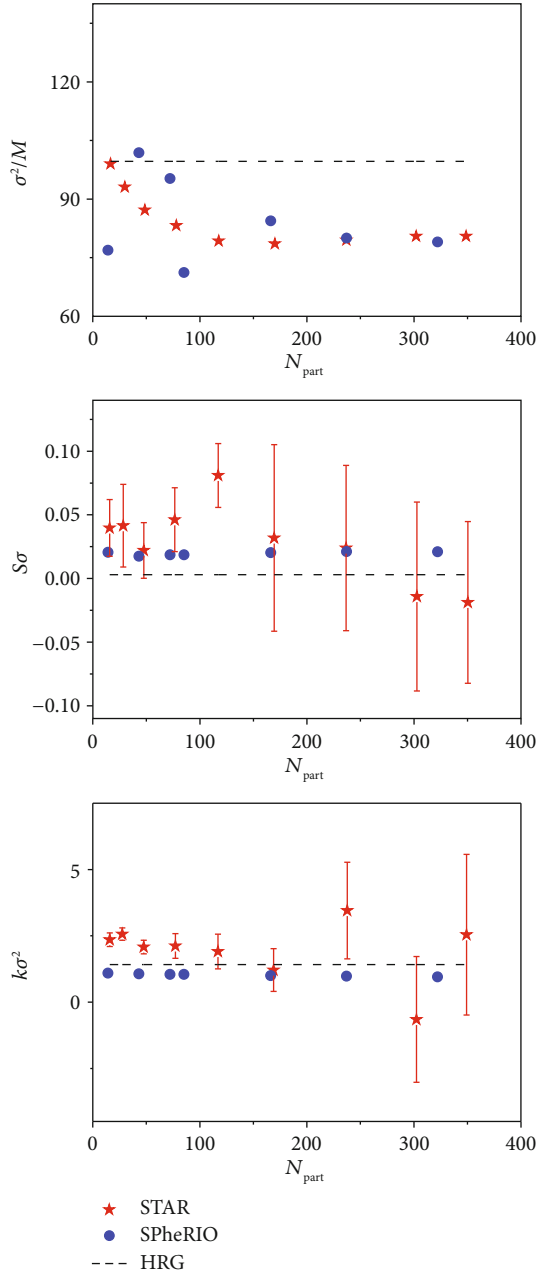
Figure 2: (Color online.) The centrality dependence of the calculated higher moments of multiplicity of net charge. The results are for Au+Au collisions at 200 GeV. The STAR data are from Ref. [27], presented by filled red stars. The SPheRIO results are shown in the filled blue circle, and the dashed black line gives that from the HRG calculations process. To be specific, we further investigate the effect of the IC, as well as the temporal expansion of the system. The hydrodynamical model employed in the study does not contain any additional free parameters, as the existing ones have been determined in reproducing the particle spectra in previous studies.

crucial information, as it might be an interesting observable regarding the goal to capture crucial information about the critical point. Unfortunately, it lies out of the scope of the present approach.

4. Concluding Remarks

To summarize, this work is devoted to studying the centrality dependence of the multiplicity fluctuations in heavy-ion nuclear collisions by using the hydrodynamical model SPheRIO. Our approach is focused on some of the noncritical aspects of the multiplicity fluctuations. This is because apart from the critical phenomenon in the vicinity of the critical point, many other possible sources also affect the multiplicity fluctuations. To extract relevant pieces of information from the experimental data, these noncritical fluctuations need to be carefully subtracted. Previous studies by the HRG model, the effects of thermal fluctuations, finite volume correction, and resonance decay have been studied. The present model continues the ongoing effort to include further additional features encoded in terms of the freeze-out.

The obtained results are compared to those of the HRG, UrQMD models, and the experimental data. Overall, regarding the existing data, the results obtained by SPheRIO show that the hydrodynamical expansion plays an essential role regarding the centrality dependence of multiplicity fluctuations. From the theoretical viewpoint, the calculations of centrality dependence might provide a scheme to separate the effects of various noncritical aspects concerning multiplicity fluctuations. It might be meaningful to carry out a further regarding other aspects, such as the effect of EoS, particularly regarding the region with finite baryon density. Further study in this direction is in progress.

Data Availability

The experimental data used to support the findings of this study can be found in the related references.

Conflicts of Interest

The authors declare that they have no conflicts of interest.

Acknowledgments

References

[1] Z. Fodor and S. D. Kat, "Lattice determination of the critical point of QCD at finite T and μ," *Journal of High Energy Physics*, vol. 2002, no. 3, 2002.

[2] F. Karsch, "Lattice results on QCD thermodynamics," 2002, http://arxiv.org/abs/0103314.

[3] M. A. Halasz, A. D. Jackson, R. E. Shrock, M. A. Stephanov, and J. J. M. Verbaarschot, "Phase diagram of QCD," *Physical Review D*, vol. 58, no. 9, 1998.

[4] J. Berges and K. Rajagopal, "Color superconductivity and chiral symmetry restoration at nonzero baryon density and temperature," 1999, http://arxiv.org/abs/9804233.

[5] M. Stephanov, K. Rajagopal, and E. Shuryak, "Signatures of the tricritical point in QCD," *Physical Review Letters*, vol. 81, no. 22, pp. 4816–4819, 1998.

[6] T. M. Schwarz, S. P. Klevansky, and G. Papp, "Phase diagram and bulk thermodynamical quantities in the Nambu–Jona-Lasinio model at finite temperature and density," *Physical Review C*, vol. 60, no. 5, 1999.

[7] Z. Fodor and S. D. Katz, "Critical point of QCD at finite T and μ, lattice results for physical quark masses," *Journal of High Energy Physics*, vol. 2004, no. 4, 2004.

[8] M. Asakawa and M. Kitazawa, "Fluctuations of conserved charges in relativistic heavy ion collisions: An introduction," *Progress in Particle and Nuclear Physics*, vol. 90, pp. 299–342, 2016.

[9] X. Luo and N. Xu, "Search for the QCD critical point with fluctuations of conserved quantities in relativistic heavy-ion collisions at RHIC: an overview," *Nuclear Science and Techniques*, vol. 28, no. 8, 2017.

[10] M. A. Stephanov, "Non-Gaussian fluctuations near the QCD critical point," *Physical Review Letters*, vol. 102, no. 3, 2009.

[11] M. A. Stephanov, "Sign of kurtosis near the QCD critical point," *Physical Review Letters*, vol. 107, no. 5, 2011.

[12] B. J. Schaefer and M. Wagner, "QCD critical region and higher moments for three-flavor models," *Physical Review D*, vol. 85, no. 3, 2012.

[13] K. Paech, H. Stöcker, and A. Dumitru, "Hydrodynamics near a chiral critical point," *Physical Review C*, vol. 68, no. 4, 2003.

[14] D. T. Son and P. Surowka, "Hydrodynamics with triangle anomalies," *Physical Review Letters*, vol. 103, no. 19, 2009.

[15] M. Nahrgang, S. Leupold, C. Herold, and M. Bleicher, "Non-equilibrium chiral fluid dynamics including dissipation and noise," *Physical Review C*, vol. 84, no. 2, 2011.

[16] M. Nahrgang, C. Herold, S. Leupold, I. Mishustin, and M. Bleicher, "The impact of dissipation and noise on fluctuations in chiral fluid dynamics," *Journal of Physics G: Nuclear and Particle Physics*, vol. 40, no. 5, 2013.

[17] C. Herold, M. Nahrgang, I. Mishustin, and M. Bleicher, "Chiral fluid dynamics with explicit propagation of the Polyakov loop," *Physical Review C*, vol. 87, no. 1, 2013.

[18] M. Stephanov and Y. Yin, "Hydrodynamics with parametric slowing down and fluctuations near the critical point," *Physical Review D*, vol. 98, no. 3, 2018.

[19] J. Li, H.-j. Xu, and H. Song, "Noncritical fluctuations of (net) charges and (net) protons from the iebe-vishnu hybrid model," *Physical Review C*, vol. 97, no. 1, 2018.

[20] L. Jiang, P. Li, and H. Song, "Correlated fluctuations near the QCD critical point," *Physical Review C*, vol. 94, no. 2, 2016.

[21] M. Hippert, E. S. Fraga, and E. M. Santos, "Critical versus spurious fluctuations in the search for the QCD critical point," *Physical Review D*, vol. 93, no. 1, 2016.

[22] M. Hippert and E. S. Fraga, "Multiplicity fluctuations near the QCD critical point," *Physical Review D*, vol. 96, no. 3, 2017.

[23] B. Mohanty and the STAR Collaboration, "STAR experiment results from the beam energy scan program at the RHIC," *Journal of Physics G: Nuclear and Particle Physics*, vol. 38, no. 12, p. 124023, 2011.

[24] L. Kumar, "STAR Results from the RHIC Beam Energy Scan-I," *Nuclear Physics A*, vol. 904-905, pp. 256c–263c, 2013.

[25] C. Yang, "The STAR beam energy scan phase II physics and upgrades," *Nuclear Physics A*, vol. 967, pp. 800–803, 2017.

[26] H. Wang, *Study of Particle Ratio Fluctuations and Charge Balance Functions at RHIC, [P.h.D. thesis]*, Michigan State University, 2012.

[27] L. Adamczyk, J. K. Adkins, G. Agakishiev et al., "Beam energy dependence of moments of the net-charge multiplicity distributions in Au+ Au collisions at RHIC," *Physical Review Letters*, vol. 113, no. 9, 2014.

[28] V. V. Begun, M. I. Gorenstein, M. Hauer, V. P. Konchakovski, and O. S. Zozulya, "Multiplicity fluctuations in hadron-resonance gas," *Physical Review C*, vol. 74, no. 4, 2006.

[29] F. Becattini, A. Keranen, L. Ferroni, and T. Gabbriellini, "Multiplicity fluctuations in a hadron gas with exact conservation laws," *Physical Review C*, vol. 72, no. 6, 2005.

[30] J. Fu, "Higher moments of net-proton multiplicity distributions in heavy ion collisions at chemical freeze-out," *Physics Letters B*, vol. 722, no. 1-3, pp. 144–150, 2013.

[31] J. Fu, "Statistical model analysis of K/π and p/π fluctuations in heavy-ion collisions," *Physics Letters B*, vol. 679, no. 3, pp. 209–213, 2009.

[32] J. Fu, "Statistical model analysis of particle ratio fluctuations in heavy-ion collisions," *Physical Review C*, vol. 85, no. 6, 2012.

[33] J.-H. Fu, "Higher moments of multiplicity fluctuations in a hadron-resonance gas with exact conservation laws," *Physical Review C*, vol. 96, no. 3, 2017.

[34] F. Karsch and K. Redlich, "Probing freeze-out conditions in heavy ion collisions with moments of charge fluctuations," *Physics Letters B*, vol. 695, no. 1-4, pp. 136–142, 2011.

[35] P. Garg, D. K. Mishra, P. K. Netrakanti et al., "Conserved number fluctuations in a hadron resonance gas model," *Physics Letters B*, vol. 726, no. 4-5, pp. 691–696, 2013.

[36] T. J. Tarnowsky, "Charge dependence and scaling properties of dynamical K/π, p/π, and K/p fluctuations from the STAR experiment," *Acta Physica Polonica B*, vol. 5, no. 2, p. 515, 2012.

[37] J. Thäder, "Higher Moments of Net-Particle Multiplicity Distributions," *Nuclear Physics A*, vol. 956, pp. 320–323, 2016.

[38] H.-H. Ma, D. Wen, K. Lin et al., "Hydrodynamic results on multiplicity fluctuations in heavy-ion collisions," *Physical Review C*, vol. 101, no. 2, 2020.

[39] Y. Hama, T. Kodama, and O. Socolowski Jr., "Topics on hydrodynamic model of nucleus-nucleus collisions," *Brazilian Journal of Physics*, vol. 35, no. 1, pp. 24–51, 2005.

[40] W.-L. Qian, R. Andrade, O. Socolowski Jr, F. Grassi, T. Kodama, and Y. Hama, "Distribution of hyperons in 200A GeV Au-Au in smoothed particle hydrodynamics," *Brazilian Journal of Physics*, vol. 37, no. 2C, pp. 767–769, 2007.

[41] W. L. Qian, P. Mota, R. Andrade et al., "Decomposition of fluctuating initial conditions and flow harmonics," *Journal of Physics G: Nuclear and Particle Physics*, vol. 41, no. 1, 2013.

[42] R. P. G. Andrade, F. Grassi, Y. Hama, T. Kodama, and W. L. Qian, "Importance of granular structure in the initial

conditions for the elliptic flow," *Physical Review Letters*, vol. 101, no. 11, 2008.

[43] W.-L. Qian, R. Andrade, F. Gardim, F. Grassi, and Y. Hama, "Origin of trigger-angle dependence of di-hadron correlations," *Physical Review C*, vol. 87, no. 1, 2013.

[44] D. M. Dudek, W. L. Qian, C. Wu et al., "Effects of equation of state on hydrodynamic expansion, spectra, flow harmonics and two-pion interferometry," *International Journal of Modern Physics E*, vol. 27, no. 7, 2018.

[45] W. M. Castilho, W.-L. Qian, F. G. Gardim, Y. Hama, and T. Kodama, "Hydrodynamic approach to the centrality dependence of di-hadron correlations," *Physical Review C*, vol. 95, no. 6, 2017.

[46] W. M. Castilho, W.-L. Qian, Y. Hama, and T. Kodama, "Event-plane dependent di-hadron correlations with harmonic v_n subtraction in a hydrodynamic model," *Physics Letters B*, vol. 777, pp. 369–373, 2018.

[47] W. M. Castilho and W.-L. Qian, "Centrality and transverse momentum dependence of dihadron correlations in a hydrodynamic model," *Nuclear Physics A*, vol. 974, pp. 35–44, 2018.

[48] D. Oliinychenko and V. Koch, "Microcanonical Particlization with Local Conservation Laws," *Physical Review Letters*, vol. 123, no. 18, 2019.

[49] L. D. Landau, "EM Lifshitz Statistical Physics," *Course of Theoretical Physics*, vol. 5, pp. 396–400, 1980.

[50] H. J. Drescher, F. M. Liu, S. Ostapchenko, T. Pierog, and K. Werner, "Initial condition for quark-gluon plasma evolution," *Physical Review C*, vol. 65, no. 5, 2002.

[51] H. J. Drescher, M. Hladik, S. Ostapchenko, T. Pierog, and K. Werner, "Parton-based Gribov-Regge theory," *Physics Reports*, vol. 350, no. 2-4, pp. 93–289, 2001.

Research Article

Investigation of Particle Distributions in Xe-Xe Collision at $\sqrt{s_{\mathrm{NN}}} = 5.44\,\mathrm{TeV}$ with the Tsallis Statistics

Hai-Fu Zhao [iD]**, Bao-Chun Li** [iD]**, and Hong-Wei Dong** [iD]

College of Physics and Electronics Engineering, Collaborative Innovation Center of Extreme Optics, State Key Laboratory of Quantum Optics and Quantum Optics Devices, Shanxi University, Taiyuan 030006, China

Correspondence should be addressed to Bao-Chun Li; libc2010@163.com

The distribution characteristic of final-state particles is one of the significant parts in high-energy nuclear collisions. The transverse momentum distribution of charged particles carries essential evolution information about the collision system. The Tsallis statistics is used to investigate the transverse momentum distribution of charged particles produced in Xe-Xe collisions at $\sqrt{s_{\mathrm{NN}}} = 5.44$ TeV. On this basis, we reproduce the nuclear modification factor of the charged particles. The calculated results agree approximately with the experimental data measured by the ALICE Collaboration.

1. Introduction

One of the major goals of high-energy nucleus-nucleus (AA) collisions is to study quark-gluon plasma (QGP) at high energy density and high temperature. The Large Hadron Collider (LHC) has performed different species of collisions at one or more energies, such as lead-lead, proton-lead, and proton-proton collisions. The Xe-Xe ion collision [1, 2] at $\sqrt{s_{\mathrm{NN}}} = 5.44$ TeV is a new collision experiment and is an intermediate-size collision system at the LHC. Since the mass number value of xenon is between proton and lead, it helps us to understand the system-scale effect of the final-state particle properties in ion collisions at high energy [3–6]. Compared with the sphere of the Pb nucleus, the deformation of the Xe nucleus is long and flattened in collisions. The deformed shape of Xe will provide us with different kinds of collision configurations. The deformed Xe nucleus will affect the initial condition of the reaction. How much impact does the deformation have on particle production and distribution? Many charged particles are produced and measured in the AA collisions. The investigation of the particle spectra is of great interest and is very helpful for comprehending the collision reaction mechanism and the particle production

process in the different species of collision systems at different center-of-mass energies [7–13].

With respect to the final-state observations, the experimental transverse momentum p_T spectrum is of great significance in understanding the production process of the moving particles. In past years, theoretical efforts have been carried out in statistical models to analyze the particle spectra over a broad range of collision energies [14–18]. At RHIC and LHC energies, the p_T spectra have been investigated intensively in various collision systems like Au+Au, Pb+Pb, and pp at different energies. A statistical model can achieve some features in treating the multiparticle system in RHIC and LHC. Recently, the ALICE Collaboration reported the p_T spectra and nuclear modification factors of charged particles produced in Xe-Xe collisions at $\sqrt{s_{\mathrm{NN}}} = 5.44$ TeV [1]. The nuclear modification factor R_{AA} is also an important observation and can provide information about the dynamics of QGP matter at extreme densities and temperatures [19–26].

In this paper, we discuss the p_T spectra and the nuclear modification factor R_{AA} in the Tsallis statistics. By the investigation of the p_T spectra, we extract the parameters, which provide the calculation foundation for the nuclear modification factor R_{AA}.

2. Description of the Particle Distribution in the Tsallis Statistics

The Tsallis statistics has been widely used to study the properties of final-state particles produced in nucleus-nucleus and proton-proton collisions at high energy [27–30]. In The Tsallis statistics, more than one version of the Tsallis distribution is used to investigate particle distributions. According to the Tsallis statistics, the number of the particles is

$$N = gV \int \frac{d^3p}{(2\pi)^3} \left[1 + (q-1)\frac{E-\mu}{T} \right]^{-(1/q-1)}, \tag{1a}$$

$$N = gV \int \frac{d^3p}{(2\pi)^3} \left[1 + (q-1)\frac{E-\mu}{T} \right]^{-(q/q-1)}, \tag{1b}$$

where g and μ are the degeneracy factor and the chemical potential of the multiparticle system, respectively. T and q are the Tsallis temperature and the degree parameter of deviation from equilibrium, respectively. The first equation and second equation are two versions. The second equation (equation (1b)) can naturally meet the thermodynamic consistency [31–33]. At $\mu = 0$, the transverse momentum distribution is

$$\frac{d^2N}{dydp_T} = \frac{gVp_T\sqrt{p_{p_T}^2 + m^2}\cosh y}{(2\pi)^2}$$

$$\cdot \left[1 + (q-1)\frac{\sqrt{p_{p_T}^2 + m^2}\cosh y}{T} \right]^{-(q/q-1)} . \tag{2}$$

The nuclear modification factor R_{AA} acts as a probe to understand the nuclear medium effect in the AA collision and is a measure of the particle production modification. It is typically expressed as a ratio of the particle p_T spectra in AA collisions to that in pp collisions:

$$R_{AA}(p_T) = \frac{d^2N^{AA}/dydp_T}{\langle T_{AA}\rangle d^2\sigma^{pp}/dydp_T}, \tag{3}$$

where N^{AA} is the production yield in AA collisions and σ^{pp} is the production cross-section in pp collisions. The average nuclear overlap function $\langle T_{AA}\rangle$ is estimated via a Glauber model of nuclear collisions. The R_{AA} is also expressed as

$$R_{AA} = \frac{f_{fin}}{f_{in}}, \tag{4}$$

where f_{in} is the distribution of the initial particles produced at an early time of the hadronization. Then, these particles interact with the medium system. The function f_{fin} is the distribution of the final-state particles, which no longer interact with each other.

According to the Boltzmann transport equation, the distribution of the particles $f(x, p, t)$ is

$$\frac{df(x,p,t)}{dt} = \frac{\partial f}{\partial t} + v \cdot \nabla_x f + F \cdot \nabla_p f = C[f]. \tag{5}$$

The evolution of the particle distribution is attributed to its interaction with the medium particles. The terms v and F are the velocity and the external force, respectively. In relaxation time approximation, the collision term $C[f]$ is given by

$$C[f] = -\frac{f - f_{eq}}{\tau}, \tag{6}$$

where τ is the relaxation time. The Boltzmann local equilibrium distribution f_{eq} is

$$f_{eq} = \frac{gV}{(2\pi)^2}p_T m_T e^{-(m_T/T_{eq})}, \tag{7}$$

where T_{eq} is the equilibrium temperature of the QCD phase transition. Considering $\nabla_x f = 0$ and $F = 0$, the distribution of the particles $f(x, p, t)$ is

$$\frac{df(x,p,t)}{dt} = \frac{\partial f}{\partial t} = \frac{f - f_{eq}}{\tau}. \tag{8}$$

A solution of the equation is

$$f_{fin} = f_{eq} + \left(f_{in} - f_{eq} \right)e^{-(t_f/\tau)}, \tag{9}$$

where t_f is the freeze-out time. The initial distribution is taken as the Tsallis distribution, i.e., equation (2). Therefore, the final-state distribution is

$$f_{fin} = \frac{gV}{(2\pi)^2}p_T m_T e^{-(m_T/T_{eq})}$$

$$+ \frac{gV}{(2\pi)^2}p_T m_T \left\{ \left[1 + (q-1)\frac{m_T}{T} \right]^{-(q/q-1)} \right. $$

$$\left. - e^{-(m_T/T_{eq})} \right\} \cdot e^{-(t_f/\tau)}. \tag{10}$$

Then, the nuclear modification factor R_{AA} is obtained as

$$R_{AA} = \frac{f_{eq}}{f_{in}} + \left(1 - \frac{f_{eq}}{f_{in}} \right)e^{-(t_f/\tau)}$$

$$= \frac{e^{-(m_T/T_{eq})}}{(1 + (q-1)(m_T/T))^{-(q/q-1)}}$$

$$+ \left[1 - \frac{e^{-(m_T/T_{eq})}}{(1 + (q-1)(m_T/T))^{-(q/q-1)}} \right]e^{-(t_f/\tau)}. \tag{11}$$
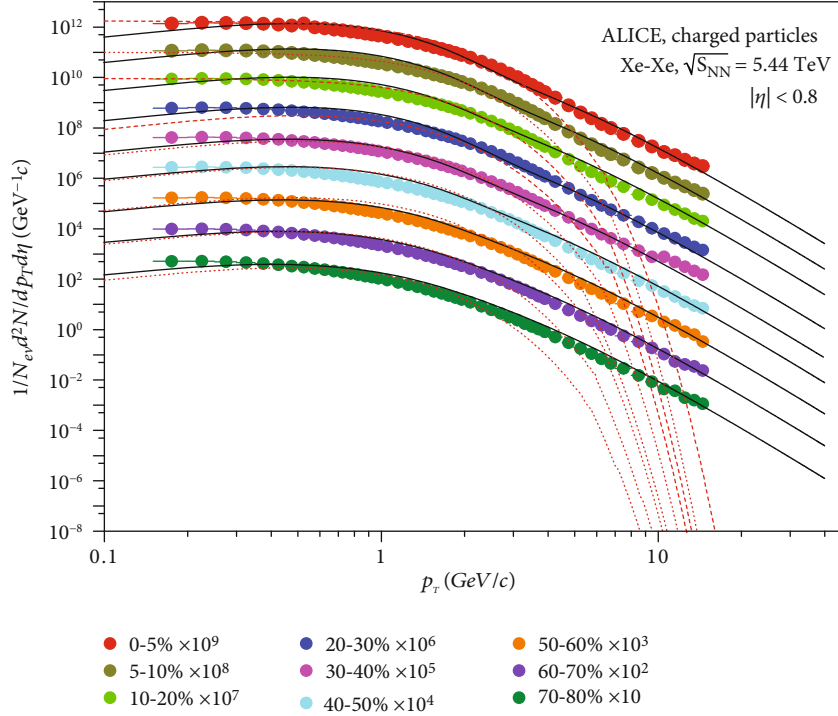
FIGURE 1: Transverse momentum distributions of charged particles produced in the Xe-Xe collision at $\sqrt{s_{NN}} = 5.44$ TeV. The filled circles indicate the experimental data in 0-5%, 5-10%, 10-20%, 20-30%, 30-40%, 40-50%, 50-60%, 60-70%, and 70-80% centrality classes [1]. The solid lines are the results of equation (2), and the dotted lines are the results of the Boltzmann statistics.

The equation is the calculation basis of the nuclear modification factor. In the relaxation time approximation, the R_{AA} is derived in the Tsallis statistics.

3. Discussions and Conclusions

In this section, we discuss the transverse momentum spectra and the nuclear modification factor of the charged particles produced in Xe-Xe collisions at $\sqrt{s_{NN}} = 5.44$ TeV. The transverse momentum contributes significantly to the characterization of the matter formed in high energy collisions because p_T is sensitive to the matter properties at an early time. The transverse momentum spectra in the kinematic range $0.15 < p_T < 50$ GeV/c and $|\eta| < 0.8$ are presented for nine centrality classes in Figure 1. The filled circles indicate the experimental data measured by the ALICE Collaboration [1]. The lines are the results of equation (2). The value of T_{eq} is 0.24 GeV. The model results are in agreement with the experimental data. The maximum value of χ^2 is 0.942 and the minimum is 0.205. The other parameters used in the calculation are listed in Table 1. The nonequilibrium degree q is a constant value. The freeze-out time t increases with increasing collision centrality. The final-state transverse momentum spectra for different centralities are determined by the temperature T, at which there are no interactions between the final-state particles. By the analysis of the p_T spectra, the thermodynamics parameters are extracted.

TABLE 1: Values of q, T, and t taken in Figure 1.

Centrality	q	T	t_f/τ
0-5%	1.125	0.196	1.581
5-10%	1.125	0.191	1.381
10-20%	1.125	0.187	1.005
20-30%	1.125	0.185	1.252
30-40%	1.125	0.180	0.788
40-50%	1.125	0.178	0.586
50-60%	1.125	0.175	0.360
60-70%	1.125	0.169	0.226
70-80%	1.125	0.165	0.115

The dotted lines are the results of the Boltzmann statistics, which can agree with the experimental data in the low p_T range.

The nuclear modification factor is also an important observation and is a measure of the particle-production modification. In Figure 1, we compare the p_T spectra of the model results and the experiment data, and can extract the parameters, which are required in the calculation of the nuclear modification factor R_{AA}. Figure 2 presents the nuclear modification factor R_{AA} of charged particles as a function of p_T in Xe-Xe at $\sqrt{s_{NN}} = 5.44$ TeV collisions. The filled circles indicate the experimental data measured by the ALICE Collaboration [1]. The lines are the results
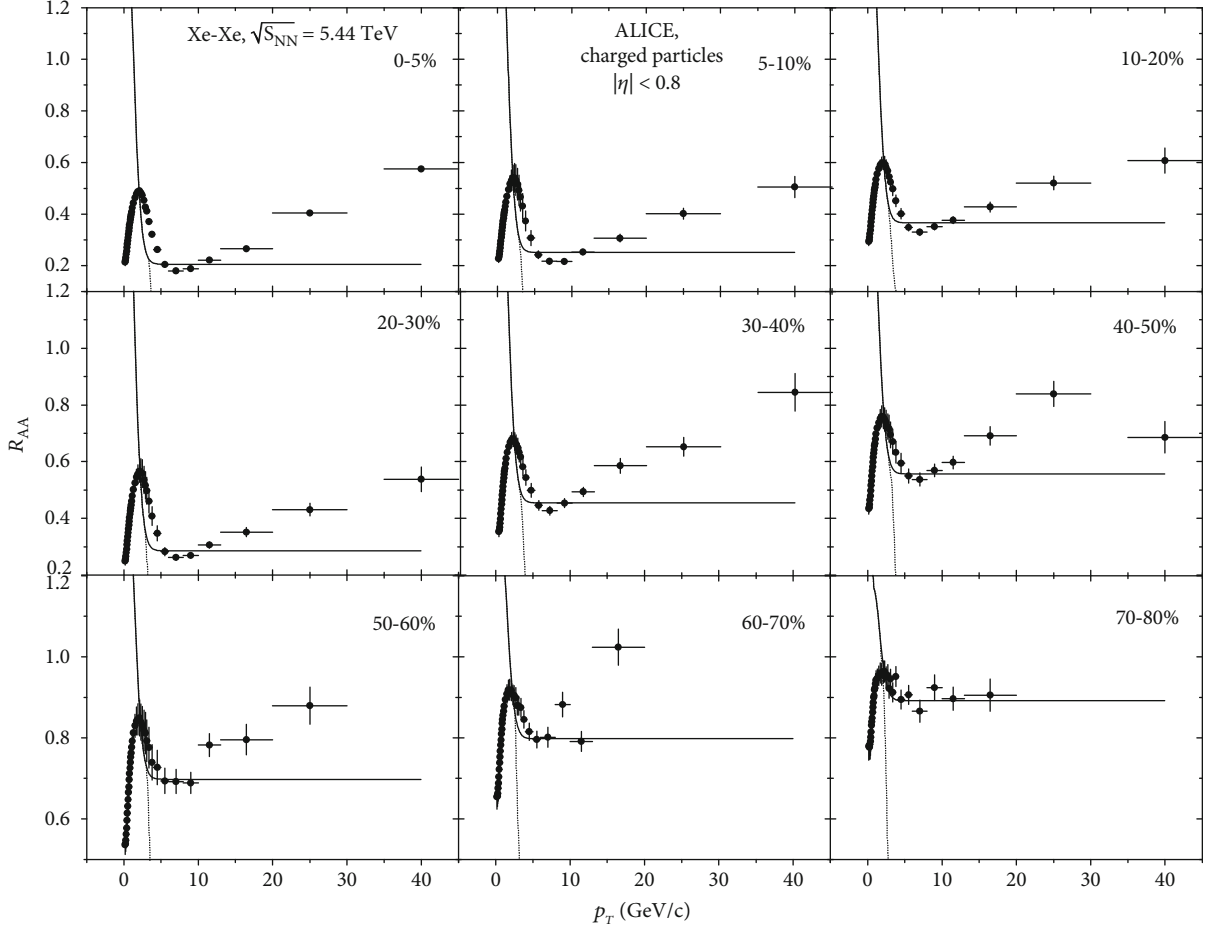
FIGURE 2: Nuclear modification factor R_{AA} as a function of p_T in the Xe-Xe collision at $\sqrt{s_{NN}} = 5.44$ TeV. The filled circles indicate the experimental data in 0-5%, 5-10%, 10-20%, 20-30%, 30-40%, 40-50%, 50-60%, 60-70%, and 70-80% centrality classes [1]. The lines are the results of equation (11) and the dotted lines are the results of the Boltzmann statistics.

of equation (11). The parameters used in the calculation are determined by the model results in Figure 1. The nuclear modification factor R_{AA} depends strongly on the collision centrality. The R_{AA} rises linearly at low p_T (about below 2.2 GeV). At high p_T, the R_{AA} first declines linearly and then rises slowly. The model can approximately describe the nuclear modification factor at the high p_T region, as shown in Figure 3. The dotted lines are the results of the Boltzmann statistics. Same as the above description of the transverse momentum spectra, they agree with the experimental data at low p_T.

Both experimentally and theoretically, the study of the particle spectra can contribute to our understanding of the particle production and the evolution dynamics in the collision system. The Tsallis statistics has attracted extensive attention due to the investigation of final-state particles produced in nuclear collisions at high energies. Compared with Levy-Tsallis, Boltzmann, and Blast wave, the Tsallis distribution can describe the transverse momentum spectra at a large range. It can extract the temperature and the nonequilibrium degree, which provide the requirements of the R_{AA} calculation. It is suc-

cessful in explaining the experimental data of the transverse momentum spectra and can obtain some thermodynamics information, such as the temperature and the chemical potential. In our previous work [34–37], the statistics model is only used to study the transverse momentum spectra of particles produced in one or more collision systems at different energies. The present work is a new attempt. The model is improved by the Tsallis statistics in relaxation time approximation. Considering relaxation time approximation of the collision term, we achieve the final-state distribution by solving the Boltzmann transport equation, where the initial distribution is inserted consistently. And, the expression of the R_{AA} calculation in the Tsallis statistics is derived. In our previous work [31–34], the Tsallis distribution can describe the p_T distributions of particles produced in one or more collision systems, such as p, Cu, Au, and Pb collisions at various energies. Compared with these collision systems, the Xe nucleus has a moderate prolate deformation. But, p_T distributions in Xe-Xe collisions can also be described well by the Tsallis distribution. The improved model can not only describe transverse momentum spectra but also
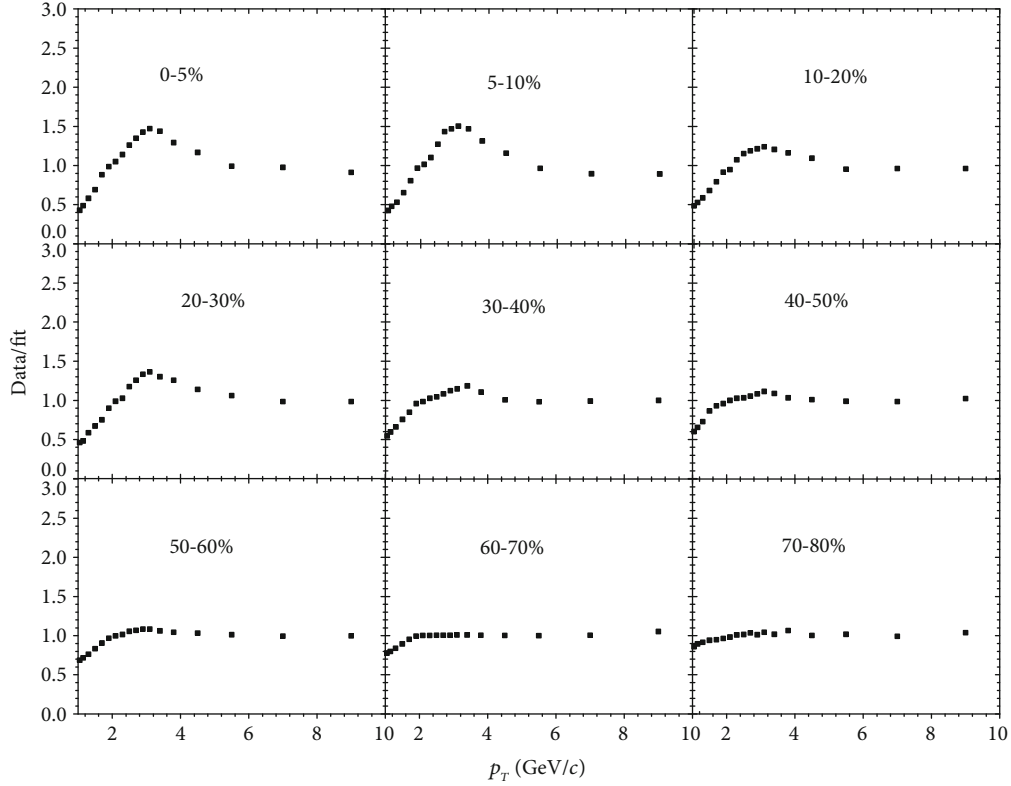
FIGURE 3: The data/fit of R_{AA} as a function of p_T for the different centrality classes.

reproduce the nuclear modification factor of particles in Xe-Xe collisions at $\sqrt{s_{NN}} = 5.44$ TeV in different centrality classes.

Data Availability

The used data in the model calculation are available and have been listed in Table 1.

Conflicts of Interest

The authors declare that they have no conflicts of interest.

Acknowledgments

References

[1] ALICE Collaboration, "Transverse momentum spectra and nuclear modification factors of charged particles in Xe-Xe collisions at $\sqrt{s_{NN}} = 5.44$ TeV," *Physics Letters B*, vol. 788, pp. 166–179, 2019.

[2] The CMS collaboration, "Charged-particle nuclear modification factors in XeXe collisions at $\sqrt{s_{NN}} = 5.44$ TeV," *Journal of High Energy Physics*, vol. 2018, no. 10, 2018.

[3] S. Kundu, D. Mallick, and B. Mohanty, "Study of charged particle multiplicity, average transverse momentum and azimuthal anisotropy in Xe+Xe collisions at $\sqrt{s_{NN}} = 5.44$ TeV using AMPT model," *European Physical Journal A: Hadrons and Nuclei*, vol. 55, no. 9, 2019.

[4] B. G. Zakharov, "Monte Carlo Glauber model with meson cloud: predictions for $_{5.44}$ TeV Xe + Xe collisions," *The European Physical Journal C*, vol. 78, no. 5, p. 427, 2018.

[5] K. J. Eskola, H. Niemi, R. Paatelainen, and K. Tuominen, "Predictions for multiplicities and flow harmonics in 5.44 TeV Xe +Xe collisions at the CERN Large Hadron Collider," *Physical Review C*, vol. 97, no. 3, 2018.

[6] B. Kim and Alice Collaboration, "ALICE results on system-size dependence of charged-particle multiplicity density in p-Pb, Pb-Pb and Xe-Xe collisions," *Nuclear Physics A*, vol. 982, pp. 279–282, 2019.

[7] F. Bellini and Alice Collaboration, "Testing the system size dependence of hydrodynamical expansion and thermal particle production with π, K, p, and ϕ in Xe -Xe and Pb-Pb collisions with ALICE," *Nuclear Physics A*, vol. 982, pp. 427–430, 2019.

[8] K. Deja and K. Kutak, "Rapidity dependence of the average transverse momentum in p+p and p+Pb collisions revisited," *Physical Review D*, vol. 95, no. 11, 2017.

[9] S. Ragoni, "Production of pions, kaons and protons in Xe–Xe collisions at $\sqrt{s_{NN}} = 5.44$ TeV," *PoS LHCP*, vol. 2018, 2018.

[10] D. S. D. Albuquerque and Alice Collaboration, "Hadronic resonances, strange and multi-strange particle production in Xe-Xe and Pb-Pb collisions with ALICE at the LHC," *Nuclear Physics A*, vol. 982, pp. 823–826, 2019.

[11] D. Sekihata and Alice Collaboration, "Energy and system dependence of nuclear modification factors of inclusive

charged particles and identified light hadrons measured in p-Pb, Xe-Xe and Pb- Pb collisions with ALICE," *Nuclear Physics A*, vol. 982, pp. 567–570, 2019.

[12] The ALICE collaboration, "Transverse momentum spectra and nuclear modification factors of charged particles in pp, p-Pb and Pb-Pb collisions at the LHC," *Journal of High Energy Physics*, vol. 2018, no. 11, 2018.

[13] T. Bhattacharyya, J. Cleymans, A. Khuntia, P. Pareek, and R. Sahoo, "Radial flow in non-extensive thermodynamics and study of particle spectra at LHC in the limit of small $(q - 1)$," *The European Physical Journal A*, vol. 52, no. 2, 2016.

[14] V. Begun, W. Florkowski, and M. Rybczynski, "Explanation of hadron transverse-momentum spectra in heavy-ion collisions at $\sqrt{S_{NN}} = 2.76$ TeV within a chemical nonequilibrium statistical hadronization model," *Physical Review C*, vol. 90, no. 1, 2014.

[15] B. C. Li, Y. Y. Fu, L. L. Wang, E. Q. Wang, and F. H. Liu, "Transverse momentum distributions of strange hadrons produced in nucleus–nucleus collisions at $\sqrt{S_{NN}} = 62.4$ and 200 GeV," *Journal of Physics G: Nuclear and Particle Physics*, vol. 39, 2012.

[16] A. A. Bylinkin, N. S. Chernyavskaya, and A. A. Rostovtsev, "Predictions on the transverse momentum spectra for charged particle production at LHC-energies from a two component model," *European Physical Journal C: Particles and Fields*, vol. 75, no. 4, article 3392, 2015.

[17] H. Zhao and F.-H. Liu, "Chemical potentials of quarks extracted from particle transverse momentum distributions in heavy ion collisions at RHIC energies," *Advances in High Energy Physics*, vol. 2014, Article ID 742193, 14 pages, 2014.

[18] R. F. Si, H. L. Li, and F. H. Liu, "Comparing standard distribution and its Tsallis form of transverse momenta in high energy collisions," *Advances in High Energy Physics*, vol. 2018, Article ID 7895967, 12 pages, 2018.

[19] T. T. Wang and Y. G. Ma, "Nucleon-number scalings of anisotropic flows and nuclear modification factor for light nuclei in the squeeze-out region," *European Physical Journal A: Hadrons and Nuclei*, vol. 55, no. 6, 2019.

[20] A. M. Sirunyan, A. Tumasyan, W. Adam et al., "Measurement of nuclear modification factors of $\Upsilon(1S)$, $\Upsilon(2S)$, and $\Upsilon(3S)$ mesons in PbPb collisions at $\sqrt{s_{NN}} = 5.02$ TeV," *Physics Letters B*, vol. 790, no. 270, pp. 270–293, 2019.

[21] M. Goharipour and S. Rostami, "Probing nuclear modifications of parton distribution functions through the isolated prompt photon production at energies available at the CERN Large Hadron Collider," *Physical Review C*, vol. 99, no. 5, 2019.

[22] A. M. Sirunyan, A. Tumasyan, W. Adam et al., "Nuclear modification factor of D^0 mesons in PbPb collisions at $\sqrt{s_{NN}} = 5.02$ TeV," *Physics Letters B*, vol. 782, pp. 474–496, 2018.

[23] S. Acharya, F. Torales-Acosta, D. Adamová et al., "Centrality and pseudorapidity dependence of the charged-particle multiplicity density in Xe-Xe collisions at $\sqrt{s_{NN}} = 5.02$ TeV," *Physics Letters B*, vol. 790, pp. 35–48, 2019.

[24] S. Acharya, F. T. Acosta, D. Adamová et al., "Inclusive J/ψ production in Xe -Xe collisions at $\sqrt{s_{NN}} = 5.02$ TeV," *Physics Letters B*, vol. 785, pp. 419–428, 2018.

[25] V. Khachatryan, A. M. Sirunyan, A. Tumasyan et al., "Charged-particle nuclear modification factors in PbPb and pPb collisions at $\sqrt{S_{NN}} = 5.02$ TeV," *Journal of High Energy Physics*, vol. 2017, no. 4, p. 1, 2017.

[26] Z. L. She, G. Chen, and F. X. Liu http://arxiv.org/abs/1909.07070.

[27] M. Rybczynski and Z. Wlodarczyk, "Tsallis statistics approach to the transverse momentum distributions in p–p collisions," *European Physical Journal C: Particles and Fields*, vol. 74, no. 2, p. 2785, 2014.

[28] A. S. Parvan, "Comparison of Tsallis statistics with the Tsallis-factorized statistics in the ultrarelativistic pp collisions," *European Physical Journal A: Hadrons and Nuclei*, vol. 52, no. 12, 2016.

[29] A. Deppman, "Thermodynamics with fractal structure, Tsallis statistics, and hadrons," *Physical Review D*, vol. 93, no. 5, 2016.

[30] Z. Tang, Y. Xu, L. Ruan, G. van Buren, F. Wang, and Z. Xu, "Spectra and radial flow in relativistic heavy ion collisions with Tsallis statistics in a blast-wave description," *Physical Review C*, vol. 79, no. 5, article 051901, 2009.

[31] J. Cleymans and D. Worku, "The Tsallis distribution in proton–proton collisions at $\sqrt{s} = 0.9$ TeV at the LHC," *Journal of Physics G: Nuclear and Particle Physics*, vol. 39, no. 2, 2012.

[32] J. Cleymans and D. Worku, "Relativistic thermodynamics: Transverse momentum distributions in high-energy physics," *European Physical Journal A: Hadrons and Nuclei*, vol. 48, no. 11, 2012.

[33] M. D. Azmi and J. Cleymans, "Transverse momentum distributions in proton–proton collisions at LHC energies and Tsallis thermodynamics," *Journal of Physics G: Nuclear and Particle Physics*, vol. 41, no. 6, 2014.

[34] H. R. Wei, F. H. Liu, and R. A. Lacey, "Disentangling random thermal motion of particles and collective expansion of source from transverse momentum spectra in high energy collisions," *Journal of Physics G: Nuclear and Particle Physics*, vol. 43, no. 12, p. 125102, 2016.

[35] B. C. Li, Y. Z. Wang, and F. H. Liu, "Formulation of transverse mass distributions in Au–Au collisions at $\sqrt{s_{NN}} = 200$ GeV/nucleon," *Physics Letters B*, vol. 725, no. 4-5, pp. 352–356, 2013.

[36] F. H. Liu, T. Tian, H. Zhao, and B. C. Li, "Extracting chemical potentials of quarks from ratios of negatively/positively charged particles in high-energy collisions," *European Physical Journal A: Hadrons and Nuclei*, vol. 50, no. 3, 2014.

[37] B. C. Li, Z. Zhang, J. H. Kang, G. X. Zhang, and F. H. Liu, "Tsallis Statistical Interpretation of Transverse Momentum Spectra in High- Energy pA Collisions," *Advances in High Energy Physics*, vol. 2015, Article ID 741816, 10 pages, 2015.

Research Article

Transverse Momentum and Pseudorapidity Dependence of Particle Production in Xe–Xe Collision at $\sqrt{s_{NN}} = 5.44$ TeV

Zhang-Li Guo [iD],[1,2] **Bao-Chun Li** [iD],[1,2] **and Hong-Wei Dong** [iD][1,2]

[1]*College of Physics and Electronics Engineering, State Key Laboratory of Quantum Optics and Quantum Optics Devices, Shanxi University, Taiyuan 030006, China*
[2]*Collaborative Innovation Center of Extreme Optics, Shanxi University, Taiyuan 030006, China*

Correspondence should be addressed to Bao-Chun Li; libc2010@163.com

Through the collision-system configuration, the Tsallis statistics is combined with a multisource thermal model. The improved model is used to investigate the transverse momentum and pseudorapidity of particles produced in Xe–Xe collisions at $\sqrt{s_{NN}} = 5.44$ TeV. We discuss detailedly the thermodynamic properties, which are taken from the transverse momentum p_T distributions of π, K, and p for different centralities. The pseudorapidity η spectra of charged particles for different centralities are described consistently in the model. And, the model result can estimate intuitively the longitudinal configuration of the collision system.

1. Introduction

The important goal of the ultrarelativistic heavy-ion collisions is to find and study the Quark–Gluon Plasma (QGP), which is a new matter state of strongly interacting quarks and gluons at high temperature and density [1–3]. From 2010 to 2019, the Large Hadron Collider (LHC) has mainly carried out *p-p*, *p*-Pb, and Pb–Pb collision experiments at various collision energies, which can provide different types of collision-system configurations. In 2017, the LHC performed a different kind of hadron collision at high energy, i.e. the first Xe^{129} ion collisions at $\sqrt{s_{NN}} = 5.44$ TeV [4–7]. Since the nucleons of the Xe^{129} nucleus is fewer than that of Pb^{208} nucleus, the investigation of Xe-ion collisions can roughly bridge or connect the gap between *p* and Pb ion collisions. As a good intermediate-size system, the Xe–Xe colliding system brings a wonderful opportunity to discuss the colliding-system size dependence of multiparticle production in high-energy nuclear collisions [8, 9]. The nucleus collisions at high energies offer numerous experimental data about charged particle production, such as pions, kaons, and protons. The particle production in the collision contains the interaction effects between hard and soft QCD processes. The feature discussion of the particle distribution can be used to infer the evolution and dynamics of different collision systems at different center of mass energies.

With respect to the final-state observables in these collisions, the particle transverse momentum and pseudorapidity multiplicity are two key measurements to understand the particle-production process and the matter evolution under the extreme conditions. The transverse momentum spectra are very important because they can provide essential information about QGP created in the collisions. The charged-particle pseudorapidity multiplicity is related to the early geometry of the collision system and is of great interest to investigate the properties of the collision-system evolution. Recently, the ALICE Collaboration measured charged-particle transverse momentum spectra and multiplicity density in Xe–Xe collisions at $\sqrt{s_{NN}} = 5.44$ TeV at the LHC [5, 6]. In this work, the transverse momentum spectra are analyzed in an improved multisource thermal model, where the Tsallis statistics [10–13] is imported. Combined with the collision picture, we also discuss the charged-particle pseudorapidity density for different collision centralities. The investigation of the particle production in different collision systems can help us understand the matter evolution in the different collisions.

2. The Particle Spectra in the Improved Multisource Thermal Model

In high-energy nucleon or nuclei collisions, the thermodynamic information of the system evolution is very rich. These identified particles produced in the collisions may be regarded as a multiparticle system. The identified particles emit from

different sources. We can assume that many emission sources are formed in the interacting system [14–17]. In the stationary reference frame of a considered source, the distribution function of the particle momentum p' is given by

$$f_{p'}(p') = \frac{1}{N}\frac{dN}{dp'} = Cp'^2\left[1 + (q-1)\frac{\sqrt{p'^2 + m_0^2} - \mu}{T}\right]^{-q/(q-1)},$$
(1)

where C, T, and q is the normalization constant, the temperature and the nonequilibrium degree parameter, respectively. The q value is close to 1. For the chemical potential $\mu = 0$, the distribution function is

$$f_{p'}(p') = \frac{1}{N}\frac{dN}{dp'} = Cp'^2\left[1 + (q-1)\frac{m_T}{T}\right]^{-q/(q-1)}.$$
(2)

When q tends to 1, the density function is the standard Boltzmann distribution. The particle momentum function $p' = g(R_1)$ can be obtained by the Monte Carlo calculation, $\int_0^{p'} f(p')\,dp' < R_1 < \int_0^{p'+dp'} f(p')\,dp'$. The particle rapidity y' is

$$y' = \frac{1}{2}\ln\frac{E' + p'_z}{E' - p'_z},$$
(3)

where E' and $p'_z = p'\cos\theta'$ is the energy and longitudinal momentum, respectively. The pseudorapidity and the transverse momentum are

$$\eta' = -\ln\left[\tan\frac{\theta'}{2}\right] = \frac{1}{2}\ln\left(\frac{p' + p'_z}{p' - p'_z}\right),$$
(4)

$$p'_T = \sqrt{p'^2_x + p'^2_y} = p'\sin\theta',$$
(5)

where $\theta' = \arctan\left[2\sqrt{r_2(1 - r_2)}/(1 - 2r_2)\right]$ is the particle emission angle and is calculated by the Monte Carlo method. The parameter r_2 is a random number distributed evenly in [0, 1]. Due to $p_T = p'_T$, the distribution function of the particle transverse-momentum in the laboratory reference system frame is

$$f_{p_T}(p_T) = \frac{1}{N}\frac{d^2N}{dp_T d\eta} = C_T p_T m_T \cosh\eta'\left[1 + (q-1)\frac{m_T\cosh\eta'}{T}\right]^{-q/(q-1)}.$$
(6)

In contrast to the transverse momentum, the particle pseudorapidity η in the laboratory reference system frame is not easy to calculate. Since η' is a result of the source reference frame, one source is only considered in Equation (1). For the calculation of the pseudorapidity, the space scale of the collision system cannot be ignored at the pseudorapidity η space. Along the beam, these sources can be grouped into four categories as follows: a projectile leading-particle source with a pseudorapidity shift η_{plp}, a projectile cylinder composed of a series of sources with pseudorapidity shifts η_{pc} ($\eta_{pc}^{\min} \leq \eta_{pc} \leq \eta_{pc}^{\max}$), a target cylinder composed of a series of sources with pseudorapidity shifts $\eta_{tc}^{\min} \leq \eta_{tc} \leq \eta_{tc}^{\max}$ and a target leading-particle

source with a pseudorapidity shift η_{tlp}. In the laboratory reference system frame, the Monte Carlo pseudorapidity function of particles from the four parts can be written as

$$\eta_1 = \eta_{plp} + \eta',$$
(7)

$$\eta_2 = \eta_{pc} + \eta', \quad \eta_{pc}^{\min} \leq \eta_{pc} \leq \eta_{pc}^{\max},$$
(8)

$$\eta_3 = \eta_{tc} + \eta', \quad \eta_{tc}^{\min} \leq \eta_{tc} \leq \eta_{tc}^{\max},$$
(9)

$$\eta_4 = \eta_{tlp} + \eta'.$$
(10)

By the p' distribution function Equation (1), we can obtain the source pseudorapidity η' in the stationary reference frame. Then, the pseudorapidity distribution in the laboratory reference frame can be derived from the η space scale of the collision system, which is described by the collision Equations (9) and (10).

3. Discussions and Conclusions

Figure 1 shows transverse momentum p_T distributions of pions π, kaons K and protons p produced in Xe–Xe collisions at $\sqrt{s_{NN}} = 5.44$ TeV. The filled circles indicate the experimental data [5] for nine centrality bins (from 0% to 5% central collisions to 70–80% peripheral collisions). The lines are the results of the Equation (6). For pions, kaons and protons, the nonequilibrium degrees are $q = 1.141$, $q = 1.080$ and $q = 1.022$, respectively. For the same particles, the q is a constant value in each interval of the centrality. This reflects nonequivalent excitation of the thermal sources of the three particles in the centrality classes. The temperatures for the three kinds of particles are shown in Tables 1–3 with χ^2/ndf and increase with the increase of the collision centrality. The p_T differential cross sections for different collision centralities are governed by the temperature T, where the reaction system freezes out and the considered particles will no longer interact. The particles at low p_T region are more close to a thermal equilibrium and the particles at high p_T region are more close to be produced in a hard scatterings, which is determined by pQCD [18, 19]. The temperature is used to reflect quantitatively the excitation of emission sources of final-state particles.

From pions to protons, these particle masses affect the slope of the transverse momentum p_T spectra. So, the temperature T and nonequilibrium degree q depend on the final-state particle mass. With increasing particle mass, the temperature T increases generally and the nonequilibrium degree q decreases. The mass dependence may originate from the deformed nuclei, Xe. With the matter produced in the collision moving at a finite velocity, the Lorentz-boost magnitude of the momentum distribution occurs obviously and is proportional to the particle mass. Therefore, the q values of π, K and p systems are different. This shows how close the three systems are to the kinetic equilibrium.

Figure 2 shows pseudorapidity η spectra of charged particles produced in Xe–Xe collisions at $\sqrt{s_{NN}} = 5.44$ TeV. The filled circles indicate the experimental data [6] for twelve centrality bins (from 0% to 2.5% central collisions to 80–90% peripheral collisions). The lines are the results of the Equations

(a) Pion

(b) Kaons

(c) Proton
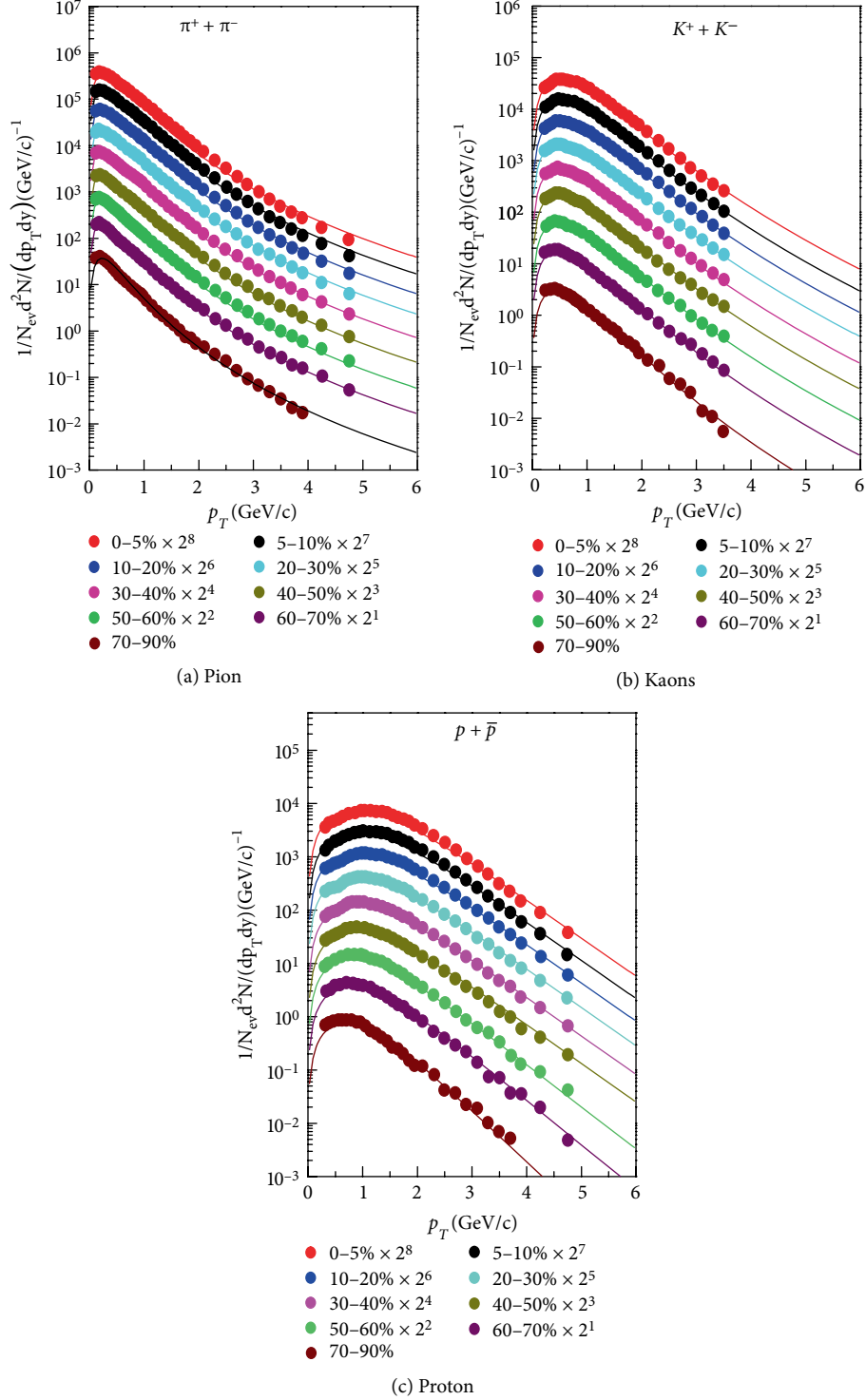
FIGURE 1: Transverse momentum distributions of π, K and p in Xe–Xe collisions at $\sqrt{s_{NN}} = 5.44$ Tev. The filled circles indicate the experimental data in nine centrality bins [5]. The lines are the results of Equation (6).

(7)–(10). The heights of the pseudorapidity spectra exhibit strong centrality dependences. It is because the number of observed particles is approximately proportional to the number of collision participant nucleons, which is a function of the impact parameter [20–23]. The configuration parameters of the thermalized cylinder are shown in Table 4. The η_{pc}^{max} and

η_{pc}^{min} slightly increase with collision centralities. The pseudorapidity distributions of the peripheral collision are wider than that of the most central collision. So, the length of the thermalized cylinder at η space decreases with the impact parameter. It means the number of thermal sources produced in Xe–Xe collision increases with centralities. The source

TABLE 1: Values of parameters used in Figure 1(a). The unit of T is GeV.

Centrality	T	χ^2/ndf
0–5%	0.101	0.447
5–10%	0.100	0.283
10–20%	0.099	0.124
20–30%	0.098	0.150
30–40%	0.097	0.202
40–50%	0.096	0.261
50–60%	0.095	0.312
60–70%	0.094	0.286
70–90%	0.091	0.472

TABLE 2: Values of parameters used in Figure 1(b). The unit of T is GeV.

Centrality	T	χ^2/ndf
0–5%	0.202	0.165
5–10%	0.200	0.160
10–20%	0.199	0.144
20–30%	0.198	0.105
30–40%	0.196	0.275
40–50%	0.195	0.369
50–60%	0.191	0.424
60–70%	0.183	0.571
70–90%	0.166	0.601

TABLE 3: Values of parameters used in Figure 1(c). The unit of T is GeV.

Centrality	T	χ^2/ndf
0–5%	0.382	0.317
5–10%	0.381	0.295
10–20%	0.379	0.210
20–30%	0.378	0.226
30–40%	0.377	0.305
40–50%	0.374	0.514
50–60%	0.342	0.590
60–70%	0.324	0.646
70–90%	0.278	0.675

FIGURE 2: Pseudorapidity density of charged particles produced in Xe–Xe collisions at $\sqrt{s_{NN}}$ = 5.44 Tev. The filled circles indicate the experimental data in 12 centrality bins [6]. The lines are the results of the Equations (7)–(10).

TABLE 4: Values of parameters corresponding to the curves in Figure 2.

Centrality	η_{pc}^{max}	η_{pc}^{min}	η_{plp}	k
0–2.5%	3.70	0.05	4.60	0.101
2.5–5%	3.70	0.05	4.60	0.101
5–7.5%	3.70	0.07	4.60	0.101
10–20%	3.70	0.06	4.60	0.101
20–30%	3.75	0.06	4.60	0.101
30–40%	3.80	0.06	4.60	0.101
40–50%	3.80	0.06	4.60	0.101
50–60%	3.85	0.06	4.60	0.101
60–70%	3.90	0.06	4.60	0.101
70–80%	3.95	0.06	4.60	0.101
80–90%	4.00	0.06	4.60	0.101

contributions from different categories are seen intuitively and the configuration of the collision system is quantized visually. It helps us understand the influence of the collision-system size and the evolution information of the produced matter in the collision [24, 25].

In reference [6], the experimental data of the pseudorapidity spectra in Xe–Xe collision at $\sqrt{s_{NN}}$ = 5.44TeV are first presented. In this paper, the Tsallis statistics is combined with the collision-system configuration, i e., the multisource thermal model. The improved model is used to investigate the particle production in the intermediate-size collision system, Xe–Xe collision [20, 26]. By the study of the transverse momentum p_T distributions of π, K and p, the temperature and nonequilibrium degree are obtained. The centrality dependence and the particle mass

dependence are discussed. Based on the result, the pseudorapidity η spectra of charged particles are reproduced. The model can describe both transverse momentum spectra and pseudorapidity spectra. The configuration of the intermediate-size collision system is quantized visually by the collision picture, which can characterize the primary properties of the collision system.

Data Availability

Our paper is a theoretical investigation. This paper has explained how to calculate the theoretical results in detail.

Conflicts of Interest

The authors declare that they have no conflicts of interest.

Acknowledgments

References

[1] B. I. Abelev, M. M. Aggarwal, Z. Ahammed et al., "Azimuthal charged-particle correlations and possible local strong parity violation," *Physical Review Letters*, vol. 103, p. 251601, 2009.

[2] J. Adam, D. Adamova, M. M. Aggarwal et al., "Correlated event-by-event fluctuations of flow harmonics in Pb-Pb collisions at $\sqrt{s_{NN}}$ = 2.76 Tev," *Physical Review Letters*, vol. 117, no. 22, p. 182301, 2016.

[3] K. Tuchin, "Particle production in strong electromagnetic fields in relativistic heavy-ion collisions," *Advances in High Energy Physics*, vol. 2013, Article ID 490495, 34 pages, 2013.

[4] S. Acharya, F. T. Acosta, D. Adamová et al., "Inclusive J/ψ production in Xe–Xe collisions at $\sqrt{s_{NN}}$=5.44 TeV," *Physics Letters B*, vol. 785, pp. 419–428, 2018.

[5] S. Ragoni, "Production of pions, kaons and protons in Xe–Xe collisions at $\sqrt{s_{NN}}$=2.76 TeV," *Proceedings of Science Large Hadron Collider Physics*, vol. 2018, p. 085, 2018.

[6] S. Acharya, F. Torales-Acosta, D. Adamová et al., "Centrality and pseudorapidity dependence of the charged-particle multiplicity density in Xe–Xe collisions at √sNN = 5.44 TeV," *Physics Letters B*, vol. 790, pp. 35–48, 2019.

[7] D. S. D. Albuquerque [ALICE Collaboration], "Hadronic resonances, strange and multi-strange particle production in Xe–Xe and Pb–Pb collisions with ALICE at the LHC," *Nuclear Physics A*, vol. 982, pp. 823–826, 2019.

[8] B. Kim [ALICE Collaboration], "ALICE results on system-size dependence of charged-particle multiplicity density in p–Pb, Pb–Pb and Xe–Xe collisions," *Nuclear Physics A*, vol. 982, p. 279, 2019.

[9] F. Bellini [ALICE Collaboration], "Testing the system size dependence of hydrodynamical expansion and thermal particle production with π, K, p, and φ in Xe–Xe and Pb–Pb collisions with ALICE," *Nuclear Physics A*, vol. 982, pp. 427–430, 2019.

[10] C. Tsallis, "Possible generalization of Boltzmann-Gibbs statistics," *Journal of Statistical Physics*, vol. 52, no. 1–2, pp. 479–487, 1988.

[11] B. I. Abelev, J. Adams, M. M. Aggarwal et al., "Strange particle production in $p+p$ collisions at √s=200 GeV," *Physical Review C*, vol. 75, no. 6, p. 064901, 2007.

[12] J. Cleymans and D. Worku, "The Tsallis distribution in proton–proton collisions at $\sqrt{s_{NN}}$ = 0.9 TeV at the LHC," *Journal of Physics G: Nuclear and Particle Physics*, vol. 39, no. 2, p. 025006, 2012.

[13] Z. Tang, Y. Xu, L. Ruan, G. van Buren, F. Wang, and Z. Xu, "Spectra and radial flow in relativistic heavy ion collisions with Tsallis statistics in a blast-wave description," *Physical Review C*, vol. 79, no. 5, p. 051901, 2009.

[14] B. C. Li, Y. Y. Fu, L. L. Wang, E. Q. Wang, and F. H. Liu, "Transverse momentum distributions of strange hadrons produced in nucleus–nucleus collisions at $\sqrt{s_{NN}}$ = 5.44 and 200 GeV," *Journal of Physics G: Nuclear and Particle Physics*, vol. 39, no. 2, p. 025009, 2012.

[15] B. C. Li, Y. Y. Fu, L. L. Wang, and F. H. Liu, "Dependence of elliptic flows on transverse momentum and number of participants in Au+Au collisions at $\sqrt{s_{NN}}$ = 200 GeV," *Journal of Physics G: Nuclear and Particle Physics*, vol. 40, no. 2, p. 025104, 2013.

[16] S. K. Tiwari and C. P. Singh, "Particle production in ultrarelativistic heavy-ion collisions: a statistical-thermal model review," *Advances in High Energy Physics*, vol. 2013, Article ID 805413, 27 pages, 2013.

[17] J. Yang, Y. Y. Ren, and W. N. Zhang, "Pion transverse momentum spectrum, elliptic flow, and interferometry in the granular source model for RHIC and LHC heavy ion collisions," *Advances in High Energy Physics*, vol. 2015, Article ID 846154, 18 pages, 2015.

[18] J. Adam, D. Adamová, M. M. Aggarwal et al., "Multiplicity dependence of charged pion, kaon, and (anti)proton production at large transverse momentum in p–Pb collisions at $\sqrt{s_{NN}}$ = 5.02 TeV," *Physics Letters B*, vol. 760, p. 720, 2016.

[19] G. Giacalone, J. Noronha-Hostler, M. Luzum, and J. Y. Ollitrault, "Confronting hydrodynamic predictions with Xe-Xe data," *Nuclear Physics A*, vol. 982, pp. 371–374, 2019.

[20] B. G. Zakharov, "Monte Carlo Glauber model with meson cloud: predictions for 5.44 TeV Xe + Xe collisions," *The European Physical Journal C*, vol. 78, no. 5, p. 427, 2018.

[21] M. L. Miller, K. Reygers, S. J. Sanders, and P. Steinberg, "Glauber modeling in high-energy nuclear collisions," *Annual Review of Nuclear and Particle Science*, vol. 57, no. 1, pp. 205–243, 2007.

[22] M. Alvioli, H. Holopainen, K. J. Eskola, and M. Strikman, "Initial-state anisotropies and their uncertainties in ultrarelativistic heavy-ion collisions from the Monte Carlo Glauber model," *Physical Review C*, vol. 85, no. 3, p. 034902, 2012.

[23] M. Biyajima and T. Mizoguchi, "Analyses of multiplicity distributions and Bose-Einstein correlations at the LHC using negative binomial distribution and generalized Glauber-Lachs formula," *The European Physical Journal A*, vol. 54, no. 6, p. 105, 2018.

[24] S. Acharya, F. Torales-Acosta, D. Adamová et al., "Inclusive J/ψ production in Xe–Xe collisions at $\sqrt{s_{NN}}$ = 5.44 TeV," *Physics Letters B*, vol. 785, pp. 419–428, 2018.

[25] S. Tripathy, S. De, M. Younus, and R. Sahoo, "Predictions for azimuthal anisotropy in Xe+Xe collisions at $\sqrt{s_{NN}}$ = 5.44 TeV using a multiphase transport model," *Physical Review C*, vol. 98, p. 064904, 2018.

[26] K. J. Eskola, H. Niemi, R. Paatelainen, and K. Tuominen, "Predictions for multiplicities and flow harmonics in 5.44 TeV Xe+Xe collisions at the CERN Large Hadron Collider," *Physical Review C*, vol. 97, no. 3, p. 034911, 2018.

Research Article

Elliptic Flow of Identified Particles in Pb–Pb Collisions at $\sqrt{s_{NN}} = 5.02$ TeV

Er-Qin Wang [iD],[1] **Yin-Qun Ma,**[1] **Li-Na Gao** [iD],[1] **and San-Hong Fan**[2]

[1]*Department of Physics, Taiyuan Normal University, Jinzhong, Shanxi 030619, China*
[2]*School of Life Science, Shanxi University, Taiyuan, Shanxi 030006, China*

Correspondence should be addressed to Er-Qin Wang; wangeq@tynu.edu.cn

In this paper, by using a Tsallis-Pareto-type function and the multisource thermal model, the elliptic flow coefficients of particles $\pi^{\pm}$, $K^{\pm}$, $p + \bar{p}$, $\Lambda + \bar{\Lambda}$, and K_S^0 produced in Pb–Pb collisions at the center-of-mass energy of $\sqrt{s_{NN}} = 5.02$ TeV are investigated. In the process of collisional evolution, because of geometric structure, pressure gradient, and thermal diffusion effects, deformation and translation occurred in the isotropic emission source, leading to anisotropy in the azimuth distribution of the final-state particles. Based on these dynamic factors, the dependence of elliptic flow on transverse momentum is described as well.

1. Introduction

As collision energy has gradually increased in recent years, high-energy physics has developed rapidly. On the one hand, the energy range of nucleus-nucleus collisions has been broadened [1–4]. On the other hand, the kinds of final-state particles measured by detectors have become more explicit [5–7]. This creates better conditions for obtaining a deep understanding of the collision mechanism. The distribution of high-energy final-state particles is important to understand the evolutionary mechanism of fluid dynamics, whereas the flow effect of final-state particles is meaningful for the new material form, quark-gluon plasma (QGP) [8–10]. The formation of QGP requires an extremely high-temperature, high-density environment. It is a state of released quarks and gluons that is similar to an ideal fluid. From an anisotropic azimuth analysis of final-state particles measured at the Relativistic Heavy Ion Collider (RHIC) [11] and the Large Hadron Collider (LHC) [12], it can be seen that the generated material unaffected by gravity is QGP under the condition of strong coupling. The quarks and gluons in the high-temperature, high-density state are affected by multiple factors. By means of the pressure gradient, the heterogeneity of energy density and the asymmetry of the geometric structure at the early stage of collisions are converted to the anisotropy of final-state particle momentum and finally manifest as the flow effect [13, 14].

In the evolutionary process of high-energy collisions, there are two main stages, chemical freeze-out and dynamic freeze-out. The former occurs in the formation stage of different kinds of particles, and the decay and generation of particles remain in dynamic balance. This is an inelastic collision process. The second process occurs later, in the diffusion stage. Momentum and energy are maintained in a thermal equilibrium state in an elastic collision process. After the two stages, as the temperature drops, the final-state particles are ejected from the action system. Various physical properties of the final-state particles are then measured by detectors, such as the longitudinal momentum spectrum [15, 16], the rapidity (pseudorapidity) distribution [17, 18], the multiplicity distribution [19, 20], and the flow effect [21–30]. By analysis of the final-state distribution using various theoretical models, the dynamic evolutionary mechanism, phase graph information, and particle attribution of quantum chromodynamics were deduced.

In noncentral nucleus-nucleus collisions, the main coefficient of the flow effect is the second-order harmonic, which is called elliptic flow (v_2). The value is used to represent collective motion in the system. Collective motion is one of the characteristics formed in collisions of QGP. The flow effect that is caused by the asymmetry of the initial geometric structure and the heterogeneous energy of the action system includes direct flow, elliptic flow, and triangular flow. All the

harmonics are quantified by the coefficient (v_n) of Fourier decomposition [31, 32]:

$$\frac{dN}{d\varphi} \propto 1 + 2 \sum v_n \cos[n(\varphi - \Psi_n)]. \tag{1}$$

Similar long-range ridge structures and positive coefficients v_2 have been observed in experiments [21]. In theory, it is assumed that these are based on the collective effect caused by hydrodynamic evolution of colliding particles.

Previous studies [33–35] have presented a description of elliptic flow over a smaller range. Moreover, the isotropic hypothesis on the transverse plane and the translation and expansion effects of the emission source are used. In this paper, based on the multisource thermal model, using the distribution of the Tsallis-Pareto-type function, and at the center-of-mass energy of $\sqrt{s_{NN}} = 5.02\,\text{TeV}$, the dependence of the elliptic flow of the identified particles ($\pi^{\pm}$, $K^{\pm}$, $p + \overline{p}$, $\Lambda + \overline{\Lambda}$, and K_S^0) in different centrality intervals in Pb–Pb collisions on transverse momentum is described [36]. The multisource thermal model is a statistical model that is based on the one-dimensional string model [37] and the fireball model [38] and was developed from the thermalized cylinder model [39, 40]. According to the multisource thermal model, many local emission sources are formed along the incident direction in high-energy collisions, and the final-state particles and jets are generated by these emission sources. In the rest frame of an emission source, the source is isotropic, that is, the final particles produced by the emission source are assumed to emit isotropically. Due to differences in impact parameters, centralities, position in space, or energy density, the emission source's temperature, excitation degree, and particle yield ratio may vary. In comparison with previous work [33–35] by the multisource thermal model, not only is the range of transverse momentum larger, but also the identification of the final-state particles is more accurate.

2. Model and Formulation

In this paper, using the multisource thermal model [41–45] and a Tsallis-Pareto-type function [46–49], the elliptic flow of identified particles in Pb–Pb collisions is analyzed. For each source in the multisource model, the Tsallis-Pareto-type function shows excellent reproducibility of the spectral measurement of many particles; the form is:

$$\frac{d^2N}{dy\,dp_T} = \frac{dN}{dy} K p_T \left[1 + \frac{m_T - m_0}{nC} \right]^{-n}, \tag{2}$$

where

$$K = \frac{(n-1)(n-2)}{nC[nC + (n-2)m_0]}, \tag{3}$$

$$m_T = \sqrt{m_0^2 + p_T^2}, \tag{4}$$

where m_0 is the rest mass, y is the rapidity, and N is the number of particles. According to some nonextensive thermodynamic particle models, the free parameter C, which is related to the average particle energy, represents the mean effective temperature in the interacting system, dN/dy is the particle output at different rapidity intervals, and n indicate the nonextensivity of the process, which is the departure of the spectra from the Boltzmann distribution. After integrating for rapidity, the distribution density function of the transverse momentum is:

$$f(p_T) = \frac{dN}{dp_T} = N_0 K p_T \left[1 + \frac{m_T - m_0}{nC} \right]^{-n}, \tag{5}$$

where N_0 denotes the normalization constant, which depends on the free parameters n and C. Hence, it is natural that $\int_0^{\infty} f(p_T) dp_T = 1$.

Related work [50] has shown that the transverse momentum distribution of the final-state particles formed in nucleus-nucleus collisions satisfies the Tsallis-Pareto-type function. In accordance with the Monte Carlo method, by Equation (5), the transverse momentum p_T can be extracted. In this expression, R_0 represents random numbers uniformly distributed on [0, 1], and p_T can be given as:

$$\int_0^{p_T} f(p_T) dp_T < R_0 < \int_0^{p_T + dp_T} f(p_T) dp_T. \tag{6}$$

Under the assumption of an isotropic emission source, the azimuth distribution of final-state particles is even, and the distribution function is:

$$f_\varphi(\varphi) = \frac{1}{2\pi}. \tag{7}$$

By the Monte Carlo method, the random number of the azimuth can be obtained as:

$$\varphi = 2\pi R, \tag{8}$$

where R represents a random number distributed on [0, 1]. Let the beam direction be the Oz axis, and let the reaction plane be the xOz plane. Therefore, the momentum components are

$$p_x = p_T \cos\varphi, \tag{9}$$

$$p_y = p_T \sin\varphi. \tag{10}$$

Due to the geometric structure of the participant, the pressure gradient, and interaction with the medium, the emission source deforms and translates in its rest frame. Hence, an anisotropic emission source is introduced in the multisource thermal model. To quantify the deformation and translation of the emission source, $a_x (a_y)$ and $b_x (b_y)$ express the deformation and translation of the emission source along the $Ox (Oy)$ axis, $a_x > 1 (< 1)$ represents expansion (compression), and $b_x > 0 (< 0)$ represents translation along the positive (negative) axis. Generally, for particles with different centrality intervals and transverse momentum, different $a_x (a_y)$ or $b_x (b_y)$ are obtained. As a first approximation, the empirical relationship can be expressed as:

$$a_x = 1 + k_1 \exp\left(-\frac{p_T}{\lambda_1}\right) + k_2 p_T, \tag{11}$$

where k_1, λ_1, k_2 are free parameters. For simplicity, the default is $a_y = 1$ and $b_{x,y} = 0$. Because of deformation, the above p_x is revised to become:

$$p'_x = a_x p_x + b_x. \tag{12}$$

Then the converted transverse momentum is:

$$p'_T = \sqrt{p'^2_x + p^2_y}. \tag{13}$$

Finally, the elliptic flow of final-state particles can be represented as:

$$v_2 = \left\langle \frac{p'^2_x - p^2_y}{p'^2_x + p^2_y} \right\rangle. \tag{14}$$

3. Comparisons with Experimental Data

Using the multisource thermal model, the anisotropic spectrum data of various particles generated in Pb–Pb collisions at $\sqrt{s_{NN}} = 5.02$ TeV [36] are studied and analyzed. The particles $\pi^\pm, K^\pm, p + \overline{p}, \Lambda + \overline{\Lambda}$, and K^0_S are located in different centrality intervals within 0–70% and depend on v_2 of the transverse momentum p_T. The rapidity is in the range $|y| < 0.5$. For particles $\pi^\pm, K^\pm$, and $p + \overline{p}$, the measurements in hypercenter collisions (0–1%) are also shown.

Figure 1 shows the elliptic flow $v_2(p_T)$ of meson $\pi^\pm$ generated in a Pb–Pb collision at energy $\sqrt{s_{NN}} = 5.02$ TeV in different centrality intervals. The data measured by the ALICE Collaboration in different centrality intervals are represented by different solid symbols, and the statistical and systematic errors are both considered in the error bar [36]. The curves are fitted to results generated by the Tsallis-Pareto-type function in the framework of the multisource thermal model. Table 1 shows the fitted free parameters (C, n, k_1, λ_1, and k_2), χ^2 and the degrees of freedom (dof). Clearly the model results are consistent with the experimental data. In the calculation, the data fitting indicates that the effective temperature C increases as the centrality percentage decreases, but that the value of n remains unchanged and is assumed to be 9. It is obvious that v_2 increases with p_T in the low p_T region, and then decreases slowly in the high p_T region. The transverse momentum corresponding to the maximum value increases with increasing particle mass. This trend is reflected in the values of k_1, λ_1, and k_2. Moreover, it is not hard to find that the parameter k_1 first increases rapidly with the centrality percentage and then slowly decreases. Finally, the values of χ^2/dof are in a reasonable range, which is not only affected by experimental errors, but is also related to the inaccuracy of the theoretical calculation results.

Figure 2 shows the $v_2(p_T)$ of $K^\pm$ in the given centrality interval. Similarly to Figure 1, the solid symbols also represent the experimental data recorded by the ALICE Collaboration, and the error bar includes the statistical and systematic errors. The curves are the results of fitting using the Tsallis-Pareto-type function. The fitting parameters χ^2 and dof are also listed in Table 1. It is apparent that the experimental data are well fitted by the model results. In the calculation, the values of effective temperature C decrease from the central to peripheral collisions and are systematically larger than those for particles
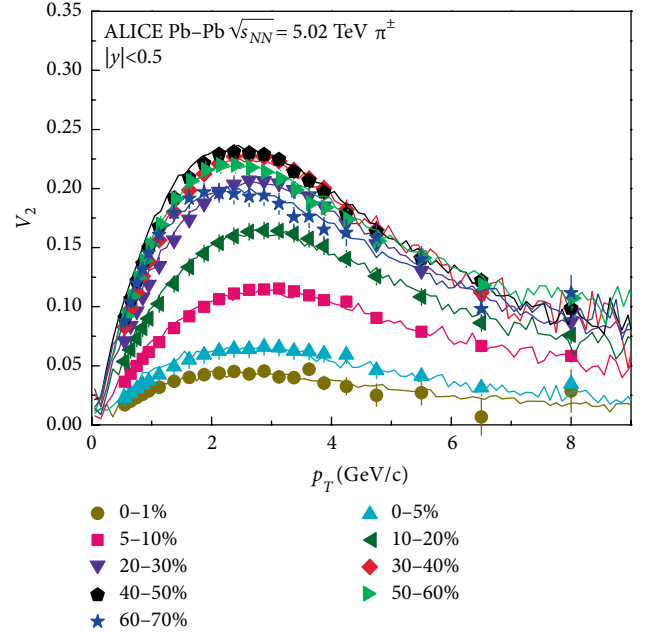
FIGURE 1: $v_2(p_T)$ of $\pi^\pm$ in a given centrality interval arranged into panels of various centrality classes [36]. The data, which were measured by the ALICE collaboration in various centrality classes, are represented in the figure by different symbols. Statistical and systematic uncertainties are shown as bars. The curves are the results of this study fitted using the Tsallis-Pareto-Type function and the multisource ideal gas model.

$\pi^\pm$. As the centrality percentage increases, the values of k_1 first increase rapidly, then slowly decrease, as shown in Figure 1.

Figure 3 shows the v_2 of $p + \overline{p}$, which depends on the transverse momentum. Figures 4 and 5 show the relationship between the elliptic flow and the transverse momentum spectrum of $\Lambda + \overline{\Lambda}$ and K^0_S, respectively. The solid symbols are the data points, and the curves show the model results. The fitted parameter values, dof and χ^2, are included in Table 1. It is evident that the fits are in good agreement with the experimental data. However, as shown in Figure 4, in the given centrality interval of 60–70%, there is a datum point located at $p_T = 9$ Gev/c that deviates seriously from the fitted value. The physical mechanism underlying this deviation is not yet understood. Similarly, when moving from central to peripheral collisions, C increases, and k_1 increases rapidly, then decreases slowly. Overall, the model fits the spectrum $v_2(p_T)$ of identified particles measured in different centrality intervals by ALICE in Pb + Pb collisions at approximately $\sqrt{s_{NN}} = 5.02$ TeV.

Based on the fitted results shown in Figures 1–5, Figure 6 shows the dependency relationship between the expansion factor a_x and the transverse momentum p_T in the given centrality interval for different particles $\pi^\pm, K^\pm, p + \overline{p}, \Lambda + \overline{\Lambda}$, and K^0_S. For a certain particle, $a_x(p_T)$ are different in different centrality intervals. The curves with maximum and minimum dependency relationship were chosen based on Equation (11) and are represented by solid and dashed lines, respectively. The variation trends are similar, but the ranges are slightly different. Furthermore, as the particle mass increases, the range also increases. Figure 7 shows the fitting parameter C,

TABLE 1: Values of C, n, k_1, λ_1, k_2, χ^2 number of degrees of freedom (dof) corresponding to the fits in Figures 1–5.

Figure	Particles	Centrality	C(GeV)	n	k_1	λ_1	k_2	χ^2/dof
	$\pi^{\pm}$	0–1%	1.00	9	0.17	2.35	0.001	4/17
	$\pi^{\pm}$	0–5%	1.10	9	0.27	2.35	0.001	6/17
	$\pi^{\pm}$	5–10%	1.10	9	0.49	2.35	0.004	2/17
	$\pi^{\pm}$	10–20%	0.80	9	0.60	2.35	0.004	3/17
Figure 1	$\pi^{\pm}$	20–30%	0.60	9	0.65	2.35	0.004	2/17
	$\pi^{\pm}$	30–40%	0.50	9	0.64	2.35	0.004	2/17
	$\pi^{\pm}$	40–50%	0.40	9	0.59	2.35	0.004	7/17
	$\pi^{\pm}$	50–60%	0.40	9	0.54	2.35	0.006	1/17
	$\pi^{\pm}$	60–70%	0.40	9	0.48	2.40	0.005	11/17
	$K^{\pm}$	0–1%	2.60	9	0.28	2.35	0.000	5/12
	$K^{\pm}$	0–5%	2.20	9	0.40	2.35	0.000	12/12
	$K^{\pm}$	5–10%	1.70	9	0.66	2.35	0.002	8/12
	$K^{\pm}$	10–20%	1.25	9	0.86	2.25	0.002	4/12
Figure 2	$K^{\pm}$	20–30%	1.00	9	0.98	2.15	0.003	2/12
	$K^{\pm}$	30–40%	0.72	9	0.83	2.35	0.002	6/12
	$K^{\pm}$	40–50%	0.68	9	0.84	2.20	0.002	2/12
	$K^{\pm}$	50–60%	0.55	9	0.64	2.35	0.003	1/12
	$K^{\pm}$	60–70%	0.40	9	0.44	2.40	0.005	1/12
	$p + \overline{p}$	0–1%	3.50	9	0.40	2.40	0.002	10/15
	$p + \overline{p}$	0–5%	4.40	9	0.70	2.40	0.002	33/15
	$p + \overline{p}$	5–10%	2.80	9	1.05	2.35	0.002	25/15
	$p + \overline{p}$	10–20%	1.70	9	1.25	2.35	0.006	18/15
Figure 3	$p + \overline{p}$	20–30%	1.30	9	1.25	2.35	0.007	23/15
	$p + \overline{p}$	30–40%	1.10	9	1.25	2.35	0.007	12/15
	$p + \overline{p}$	40–50%	0.95	9	1.10	2.35	0.006	8/15
	$p + \overline{p}$	50–60%	0.75	9	0.97	2.35	0.006	2/15
	$p + \overline{p}$	60–70%	0.75	9	0.77	2.35	0.006	1/15
	$\Lambda + \overline{\Lambda}$	0–5%	4.20	9	0.58	3.00	0.005	12/7
	$\Lambda + \overline{\Lambda}$	5–10%	3.00	9	1.20	2.55	0.007	3/7
	$\Lambda + \overline{\Lambda}$	10–20%	2.10	9	1.57	2.30	0.009	2/7
	$\Lambda + \overline{\Lambda}$	20–30%	1.40	9	1.60	2.30	0.009	1/7
Figure 4	$\Lambda + \overline{\Lambda}$	30–40%	1.10	9	1.42	2.40	0.009	1/7
	$\Lambda + \overline{\Lambda}$	40–50%	0.90	9	1.26	2.55	0.005	1/7
	$\Lambda + \overline{\Lambda}$	50–60%	0.80	9	1.07	2.50	0.009	1/7
	$\Lambda + \overline{\Lambda}$	60–70%	0.60	9	0.70	2.50	0.005	4/7
	K_s^0	0–5%	2.10	9	0.38	2.20	0.002	3/8
	K_s^0	5–10%	1.70	9	0.65	2.20	0.002	2/8
	K_s^0	10–20%	1.20	9	0.78	2.20	0.006	1/8
	K_s^0	20–30%	0.90	9	0.83	2.20	0.005	1/8
Figure 5	K_s^0	30–40%	0.70	9	0.79	2.20	0.008	1/8
	K_s^0	40–50%	0.60	9	0.73	2.20	0.006	1/8
	K_s^0	50–60%	0.55	9	0.63	2.40	0.003	1/8
	K_s^0	60–70%	0.40	9	0.44	2.45	0.005	1/8
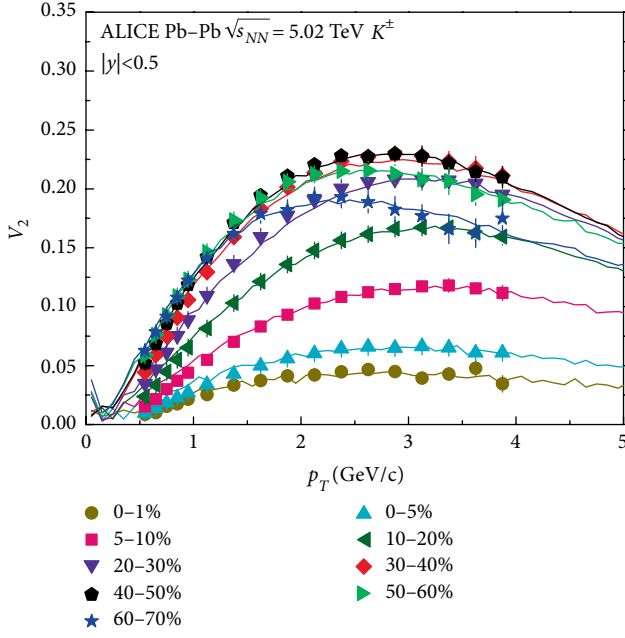
FIGURE 2: As for Figure 1, but showing $v_2(p_T)$ of $K^{\pm}$ for a given centrality [36].

FIGURE 4: As for Figure 1, but showing $v_2(p_T)$ of $\Lambda + \overline{\Lambda}$ for a given centrality [36].

FIGURE 3: As for Figure 1, but showing $v_2(p_T)$ of $p + \bar{p}$ for a given centrality [36].
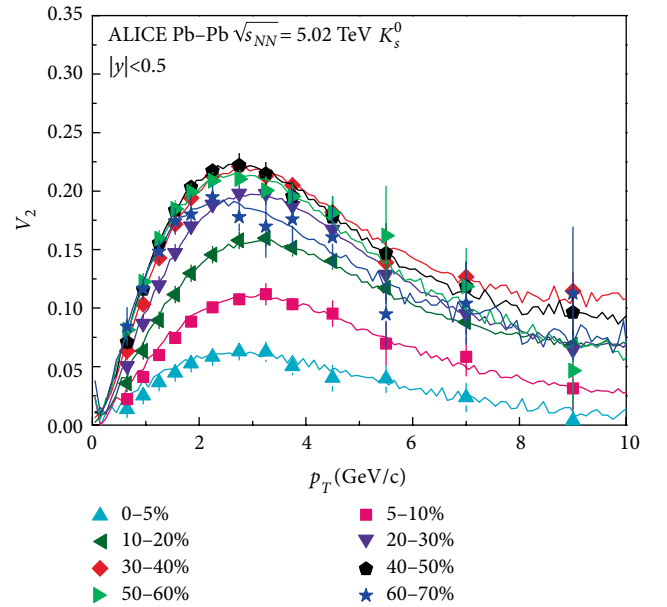
FIGURE 5: As for Figure 1, but showing $v_2(p_T)$ of K_s^0 for a given centrality [36].

which depends on the variation of centrality. When moving from central to peripheral collisions, the effective temperature C gradually declines.

4. Discussion and Conclusions

According to the fitted results from the above comparisons, the fitted free parameter C is actually not the real temperature (the kinetic freeze-out temperature) of the emission source, but the effective temperature. As is well known, the interacting system at kinetic freeze-out (the last stage of collision) is influenced not only by thermal motion, but also by the flow effect. The real temperature of the emission source should reflect the thermal motion of the particles, and therefore the real temperature of the source is the kinetic freeze-out temperature. The effective temperature extracted from the elliptic flow spectrum includes thermal motion and the flow effect of the particles. By dissecting the effective temperature, it is possible to
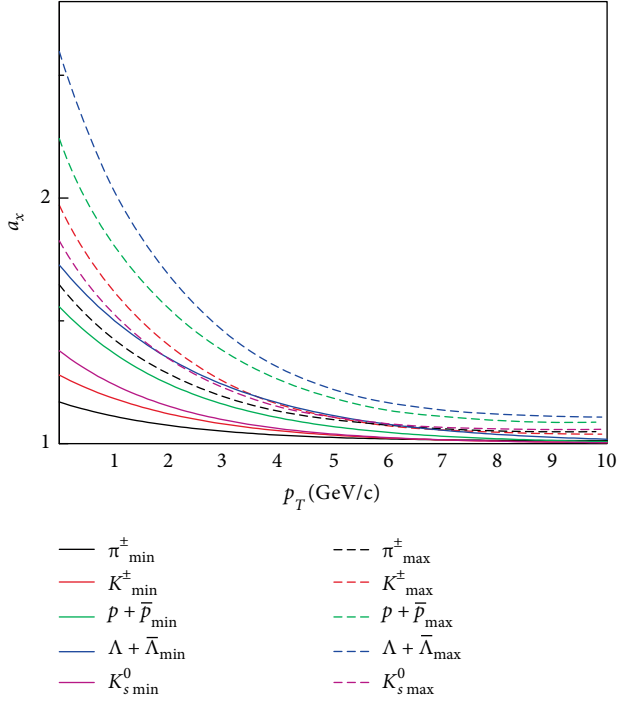
FIGURE 6: Transverse momentum dependency on the deformation parameter a_x of $\pi^{\pm}$, $K^{\pm}$, $p + \overline{p}$, $\Lambda + \overline{\Lambda}$, and K_s^0. The curves are the results of this fitted based on Equation (11).
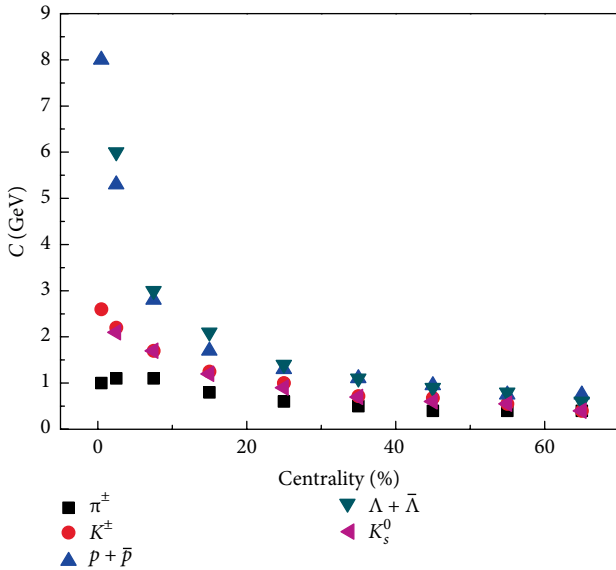
FIGURE 7: Free parameter C dependency on the centrality classes.

obtain the real temperature of the interacting system. The relationships between effective temperature, real temperature, and flow velocity are not totally clear. Therefore, the value of effective temperature obtained in this work is higher than the kinetic freeze-out temperature.

Table 1 shows that the parameter k_1 first increases rapidly with centrality percentage and then decreases slowly. It reaches a maximum as the centrality percentage reaches about 30%. In addition, Figure 6 shows that a_x decreases with increasing

transverse momentum p_T. However, Figure 7 shows that the parameter C declines gradually from central to peripheral collisions. As for the dependency relationship, it can be readily understood.

From the participant-spectator geometric structure, it can be seen that as centrality percentage increases, the extent of the overlapping parts decreases, whereas the asymmetry rises. There is an approximate linear relationship between the elliptic flow and the eccentricity ratio of the participant. Hence, with increasing centrality percentage, the elliptic flow also grows. However, v_2 of particles in peripheral collisions is slightly smaller than in central collisions. This may be due to shorter system life under peripheral collisions, resulting in small v_2. Hence, k_1 first increases rapidly with the centrality percentage and then decreases slowly.

However, as the centrality percentage rises, the effective temperature C declines gradually. In accordance with the geometric structure of collisions, as the centrality percentage decreases, the number of involved nucleons increases, and the overlapping parts also increase, leading to higher energy density and strength of interaction, which manifests as higher temperature. The effective temperature C obtained in this study was higher than the true temperature. The reason for this was that the effective temperature incorporates the true temperature and the flow effect. The value excluding the flow effect should be equal to the true temperature. Figure 7 shows that for particles with considerable mass, the low variation ranges of effective temperature are similar.

In short, based on the multisource model, by introducing a Tsallis-Pareto-type function, the elliptic flow of identified particles generated in Pb–Pb collisions at $\sqrt{s_{NN}} = 5.02$ TeV was correctly analyzed. Therefore, in the collision process, the asymmetry, expansion, and translation effects of geometric structure affect the dynamics of the final-state particles.

Data Availability

The data used to support the findings of this study are included within the article.

Ethical Approval

The authors declare that they are in compliance with ethical standards regarding the content of this paper.

Conflicts of Interest

The authors declare that they have no conflicts of interest regarding the publication of this paper.

Aknowledgments

References

[1] M. Aaboud et al. (ATLAS Collaboration), "Measurement of the t̄tZ and t̄t W cross sections in proton-proton collisions at $\sqrt{s} = 13$ TeV with the ATLAS detector," *Physical Review D*, vol. 99, p. 072009, 2019.

[2] M. Aaboud et al. (ATLAS Collaboration), "Measurement of the four-lepton invariant mass spectrum in 13 TeV proton-proton collisions with the ATLAS detector," *Journal of High Energy Physics*, vol. 04, p. 048, 2019.

[3] M. Aaboud et al. (The ATLAS and CMS Collaborations), "Combinations of single-top-quark production cross-section measurements and $|f_{LV}V_{tb}|$ determinations at $\sqrt{s} = 7$ and 8 TeV with the ATLAS and CMS experiments," *Journal of High Energy Physics*, vol. 05, p. 088, 2019.

[4] R. Aaij et al. (LHCb Collaboration), "Measurement of B^+, B^0 and Λ_b^0 production in pPb collisions at $\sqrt{s_{NN}} = 8.16$ TeV," *Physical Review D*, vol. 99, p. 052011, 2019.

[5] A. M. Sirunyan et al. (CMS Collaboration), "Measurement of the t̄t production cross section, the top quark mass, and the strong coupling constant using dilepton events in pp collisions at $\sqrt{s} = 13$ TeV," *European Physical Journal C*, vol. 79, p. 368, 2019.

[6] A. M. Sirunyan et al. (CMS Collaboration), "Observation of two excited B^+_c states and measurement of the B^+_c (2S) mass in *pp* collisions at $\sqrt{s} = 13$ TeV," *Physical Review Letters*, vol. 122, p. 132001, 2019.

[7] J. Adam et al. (STAR Collaboration), "Measurement of the longitudinal spin asymmetries for weak boson production in proton-proton collisions at $\sqrt{s} = 510$ GeV," *Physical Review D*, vol. 99, p. 051102, 2019.

[8] B. B. Back et al. (PHOBOS Collaboration), "The PHOBOS perspective on discoveries at RHIC," *Nuclear Physics A*, vol. 757, no. 1–2, pp. 28–101, 2005.

[9] C. Aidala et al. (PHENIX Collaboration), "Creation of quark–gluon plasma droplets with three distinct geometries ," *Nature Physics*, vol. 15, no. 3, p. 214, 2019.

[10] I. Arsene et al. (BRAHMS Collaboration), "Quark gluon plasma and color glass condensate at RHIC? the perspective from the BRAHMS experiment ," *Nuclear Physics A*, vol. 757, p. 1, 2005.

[11] K. Adcox et al. (PHENIX Collaboration), "Formation of dense partonic matter in relativistic nucleus-nucleus collisions at RHIC," *Nuclear Physics A*, vol. 757, p. 184, 2005.

[12] S. Chatrchyan et al. (CMS Collaborataion), "Measurement of the elliptic anisotropy of charged particles produced in PbPb collisions at $\sqrt{s_{NN}} = 2.76$ TeV," *Physical Review C*, vol. 87, p. 014902, 2013.

[13] D. Derendarz et al. (ATLAS Collaboraion), "Flow harmonics in Pb + Pb collisions at $\sqrt{S_{NN}} = 2.76$ TeV with the ATLAS detector," *Nuclear Physics A*, vol. 931, p. 1002, 2014.

[14] B. Schenke, P. Tribedy, and R. Venugopalan, "Fluctuating glasma initial conditions and flow in heavy ion collisions," *Physical Review Letters*, vol. 108, p. 252301, 2012.

[15] V. Khachatryan et al. (CMS Collaboration), "Measurement of the transverse momentum spectrum of the Higgs boson produced in pp collisions at $\sqrt{s} = 8$ TeV using H→WW decays," *Journal of High Energy Physics*, vol. 03, p. 032, 2017.

[16] A. Adare et al. (PHENIX Collaboration), "Identified charged hadron production in p + pcollisions at $\sqrt{s} = 200$ and 62.4 GeV," *Physical Review C*, vol. 83, p. 064903, 2011.

[17] B. Abelev et al. (ALICE Collaboration), "Pseudorapidity Density of Charged Particles in p + PbCollisions at $\sqrt{s_{NN}} = 5.02$ TeV," *Physical Review Letters*, vol. 110, p. 032301, 2013.

[18] G. J. Alner et al. (UA5 Collaboration), "A general study of proton-antiproton physics at $\sqrt{s} = 546$-GeV," *Physics Reports-Review Section of Physics Letters*, vol. 154, p. 247, 1987.

[19] Z. Valentina et al. (ALICE Collaboration), "Charged-particle multiplicity distributions over a wide pseudorapidity range in proton–proton collisions with ALICE," *Nuclear Physics A*, vol. 956, pp. 529–532, 2016.

[20] A. Adare et al. (PHENIX Collaboration), "Measurement of higher cumulants of net-charge multiplicity distributions in Au + Au collisions at $\sqrt{s_{NN}} = 7.7 – 200$ GeV," *Physical Review C*, vol. 93, p. 011901, 2016.

[21] S. Acharya et al. (ALICE Collaboration), "Anisotropic flow in Xe–Xe collisions at $\sqrt{s_{NN}} = 5.44$ TeV," *Physics Letters B*, vol. 784, p. 82, 2018.

[22] M. Aaboud et al. (ATLAS Collaboration), "Measurement of the azimuthal anisotropy of charged particles produced in $\sqrt{s_{NN}} = 5.02$ TeV Pb + Pb collisions with the ATLAS detector," *European Physical Journal C*, vol. 78, p. 997, 2018.

[23] D. Solanki, P. Sorensen, S. Basu, R. Raniwala, and T. K. Nayak, "Beam energy dependence of elliptic and triangular flow with the AMPT model," *Physics Letters B*, vol. 720, no. 4–5, pp. 352–357, 2013.

[24] G. Aad et al. (ATLAS Collaboration), "Measurement of the pseudorapidity and transverse momentum dependence of the elliptic flow of charged particles in lead–lead collisions at $\sqrt{s_{NN}} = 2.76$ TeV with the ATLAS detector," *Physics Letters B*, vol. 707, pp. 330–348, 2012.

[25] K. Aamodt et al. (ALICE Collaboration), "Elliptic Flow of Charged Particles in Pb–Pb Collisions at $\sqrt{s_{NN}} = 2.76$ TeV," *Physical Review Letters*, vol. 105, p. 252302, 2010.

[26] B. I. Abelev et al. (STAR Collaboration), "Charged and strange hadron elliptic flow in Cu + Cucollisions at $\sqrt{s_{NN}} = 62.4$ and 200 GeV," *Physical Review C*, vol. 81, p. 044902, 2010.

[27] S. Afanasiev et al. (PHENIX Collaboration), "Elliptic flow for phi mesons and (anti)deuterons in Au+Au collisions at sqrt(s_NN) = 200 GeV," *Physical Review Letter*, vol. 99, p. 052301, 2007.

[28] C. Alt et al. (NA49 Collaboration), "Directed and elliptic flow of charged pions and protons in Pb + Pbcollisions at 40 A and 158 AGeV," *Physical Review C*, vol. 68, p. 034903, 2003.

[29] A. M. Poskanzer et al. (NA49 Collaboration), "Centrality dependence of directed and elliptic flow at the SPS," *Nuclear Physics A*, vol. 661, pp. 341–344, 1999.

[30] L. Adamczyk et al. (STAR Collaboration), "Centrality and transverse momentum dependence of elliptic flow of multistrange hadrons and ϕ meson in Au+Au collisions at $\sqrt{s_{NN}} = 200$ GeV," *Physical Review Letters*, vol. 116, p. 062301, 2016.

[31] S. Voloshin and Y. Zhang, "Flow study in relativistic nuclear collisions by fourier expansion of azimuthal particle distributions," *Journal of Physics C*, vol. 70, no. 4, pp. 665–671, 1996.

[32] A. M. Poskanzer and S. A. Voloshin, "Methods for analyzing anisotropic flow in relativistic nuclear collisions," *Physical Review C*, vol. 58, p. 1671, 1998.

[33] Y.-H. Chen and F.-H. Liu, "Event patterns extracted from anisotropic spectra of charged particles produced in Pb–Pb

collisions at 2.76 TeV," *European Physical Journal A*, vol. 53, p. 230, 2017.

[34] E. Q. Wang, H. R. Wei, B. C. Li, and F. H. Liu, "Dependence of elliptic flow on participant nucleon number in Au + Au collisions at $\sqrt{s_{NN}} = 200$ GeV," *Physical Review C*, vol. 83, p. 034906, 2011.

[35] B.-C. Li, Y.-Y. Fu, E.-Q. Wang, X.-J. Wen, and F.-H. Liu, "Dependence of elliptic flow on transverse momentum in $\sqrt{s_{NN}} = 200$ GeV Au-Au and $\sqrt{s_{NN}} = 2.76$ TeV Pb–Pb collisions," *Chinese Physics Letters*, vol. 29, no. 7, p. 072501, 2012.

[36] S. Acharya et al. (ALICE Collaboration), "Anisotropic flow of identified particles in Pb–Pb collisions at $\sqrt{s_{NN}} = 5.02$ TeV," *Journal of High Energy Physics*, vol. 09, p. 006, 2018.

[37] K. Werner, "Strings, pomerons and the VENUS model of hadronic interactions at ultrarelativistic energies," *Physics Reports-Review Section of Physics Letters*, vol. 232, p. 87, 1993.

[38] G. D. Westfall, J. Gosset, P. J. Johansen et al., "Nuclear fireball model for proton inclusive spectra from relativistic heavy-ion collisions," *Physical Review Letters*, vol. 37, p. 1202, 1976.

[39] F. H. Liu and Y. A. Panebratsev, "Pseudorapidity distribution of shower particles in heavy ion induced interactions in nuclear emulsion at high energy," *Physical Review C*, vol. 59, p. 1798, 1999.

[40] F. H. Liu and Y. A. Panebratsev, "Baryon rapidity distribution in nucleus-nucleus collisions at ultrarelativistic energies," *Physical Review C*, vol. 59, p. 1193, 1999.

[41] F. H. Liu and J. S. Li, "Isotopic production cross section of fragments in ^{56}Fe+p and ^{136}Xe(^{124}Xe) + Pb reactions over an energy range from 300 A to 1500 AMeV," *Physical Review C*, vol. 78, p. 044602, 2008.

[42] F. H. Liu, "Unified description of multiplicity distributions of final-state particles produced in collisions at high energies," *Nuclear Physics A*, vol. 810, no. 1–4, pp. 159–172, 2008.

[43] F. H. Liu, N. N. Abd Allah, and B. K. Singh, "Dependence of black fragment azimuthal and projected angular distributions on polar angle in silicon-emulsion collisions at 4.5 AGeV/c," *Physical Review C*, vol. 69, p. 057601, 2004.

[44] F. H. Liu, "Longitudinal and transverse flows of protons in 2–8 AGeV Au − Au collisions," *Europhysics Letters*, vol. 63, no. 2, p. 193, 2003.

[45] F. H. Liu, Y. Q. Gao, T. Tian, and B. C. Li, "Unified description of transverse momentum spectrums contributed by soft and hard processes in high-energy nuclear collisions," *European Physical Journal A*, vol. 50, p. 94, 2014.

[46] A. M. Sirunyan et al. (CMS Collaboration), "Measurement of charged pion, kaon, and proton production in proton-proton collisions at $\sqrt{s} = 13$ TeV," *Physical Review D*, vol. 96, p. 112003, 2017.

[47] C. Tsallis, "Possible generalization of Boltzmann-Gibbs statistics," *Journal of Statistical Physics*, vol. 52, no. 1–2, pp. 479–487, 1988.

[48] T. S. Biro, G. Purcsel, and K. Urmossy, "Non-extensive approach to quark matter," *The European Physical Journal A*, vol. 40, pp. 325–340, 2009.

[49] V. Khachatryan et al. (CMS Collaboration), "Transverse-momentum and pseudorapidity distributions of charged hadrons in pp collisions at $\sqrt{s} = 0.9$ and 2.36 TeV," *Journal of High Energy Physics*, vol. 02, p. 041, 2010.

[50] X. W. He, H. R. Wei, and F. H. Liu, "Chemical potentials of light hadrons and quarks from yield ratios of negative to positive particles in high energy pp collisions," *Journal of Physics G: Nuclear and Particle Physics*, vol. 46, p. 025102, 2019.

Research Article

Study of Spin–Spin Correlations between Quark and a Spin-1/2 Composite System

Satvir Kaur and Harleen Dahiya [iD]

Department of Physics, Dr. B.R. Ambedkar National Institute of Technology, Jalandhar 144011, India

Correspondence should be addressed to Harleen Dahiya; dahiyah@nitj.ac.in

We study the correlation between the fermion composite system and quark spins by using the light-cone quark–diquark model. We do the calculations for u-quark and d-quark in the fermion system by considering different polarization configurations of both. The contribution from scalar and axial-vector diquarks is taken into account. The overlap representation of light-front wavefunctions is used for the calculations. The spin–spin correlations for u and d quarks are presented in transverse impact-parameter plane and transverse momentum plane as well.

1. Introduction

To get precise information of hadrons in terms of its constituents, Wigner distributions of quark and gluon were introduced by Ji [1, 2]. Wigner distribution is a quantum phase-space distribution concealing the joint position and momentum space distribution on the internal structure of the hadron. As these distributions are quasi-probabilistic distributions, one cannot measure them directly. Applying certain limits on Wigner distributions provide the probabilistic three-dimensional distributions namely generalized parton distributions (GPDs) [3–6] and transverse momentum-dependent distributions (TMDs) [7–10]. The reduction to GPDs is based on the integration of five-dimensional Wigner distributions over transverse momentum at zero skewness. While at the forward limit, i.e., when there is no momentum transfer from initial to final state of hadron $(\Delta_\perp = 0)$, the TMDs can be obtained by integrating Wigner distributions over transverse impact-parameter co-ordinates. Further integrating GPDs upon certain limits leads to obtaining parton distribution functions (PDFs), charge distributions, form factors, etc. [11–18]. Wigner distributions are also supportive for evaluating the spin–spin correlations between a spin-1/2 composite system and a quark inside the fermion system. Theoretical studies on quark and gluon Wigner distributions in spin-1/2 and spin-0 composite systems have been successfully carried out in Refs. [19–27].

The spectator model formulated in light-cone framework [28–31] is used to evaluate the Wigner distributions as it is successful in evaluating T-even and T-odd TMDs of the proton [7]. The model is successful in explaining the standard parton distribution functions, quasi-parton distribution functions [32]. Further, in Ref. [33], the authors analyse the agreement of quasi-GPDs with the standard GPDs. The concept of quasi-PDF is carried out in Refs. [34–39]. Since, the fermion composite system is considered to be a bound state of three quarks, i.e., *uud*, the spectators are assumed to be scalar or axial-vector depending upon the spin, i.e., either spin-0 or spin-1. In this work, we investigate the correlation between the quark spin and spin of fermion system by using the Wigner distributions evaluated in Ref. [27]. The quark Wigner distributions were calculated by considering different configuration combinations of quark spin direction and proton spin direction. The overlap representation of light-front wavefunctions is taken into account to evaluate the Wigner operators having different cases, depending upon the polarization of quark, i.e., either unpolarized, longitudinally-polarized or transversely-polarized. The Wigner operator is associated with the Wigner distributions by a Fourier transformation of total momentum transferred to the final state of the system. Furthermore, we include the longitudinal polarization vector into the LFWFs along with the transverse polarization vector, and evaluate the Wigner distribution using the overlap form of these LFWFs.

Afterwards, we take the difference between both respective Wigner distributions, i.e., including the longitudinal polarization vector $\left(\rho^{(a)l}\right)$ and by not including the longitudinal polarization vector $\left(\rho^{(a)}\right)$. The aim behind the determination of difference between the Wigner distributions is just to get the effect of longitudinal polarization vector in LFWFs.

The plan of the paper is as follows. In Section 2, we briefly discuss about the light-front quark–diquark model used. In Section 3, the definitions of Wigner distribution in terms of polarization configurations of quark and spin-1/2 composite system are given. We also introduce various spin–spin correlations between the quark and composite system in this section. Further, in Section 4, we evaluate the difference between the correlators related to the Wigner distributions in terms of overlap form of LFWFs for the cases where longitudinal polarization vector is taken into account as well as the case without longitudinal polarization vector. Also, the results of different spin–spin correlations are discussed. At last, the summary and conclusions are presented in Section 5.

2. Light-Front Quark–Diquark Model

In the light-front quark–diquark model, the spin-1/2 composite system is considered to be a bound state of a quark and a diquark. In this model, a valence quark interacts with the external photon, and the other two valence quarks bound together are treated as a single diquark state. Here, the diquark can be scalar (spin-0) or axial-vector (spin-1). The composite spin-1/2 particle state $|\Psi; S\rangle$ is defined as

$$|\Psi; \pm\rangle = c_s |u\ s^0\rangle^{\pm} + c_a |u\ a^0\rangle^{\pm} + c'_a |d\ a^1\rangle^{\pm}. \quad (1)$$

Here, the scalar–isoscalar diquark state, vector–isoscalar diquark state, and vector–isovector diquark state are denoted by $|u\ s^0\rangle$, $|u\ a^0\rangle$, and $|d\ a^1\rangle$, respectively.

The hadronic light-cone Fock state $|\Psi(P^+, \mathbf{P}_\perp, S_z)\rangle$ expansion in terms of constituent eigenstates is defined as [40]

$$|\Psi(P^+, \mathbf{P}_\perp, S_z)\rangle = \sum_{n,\lambda_i} \int \prod_{i=1}^{n} \frac{dx_i d^2\mathbf{p}_{\perp i}}{\sqrt{x_i}16\pi^3} 16\pi^3 \delta\left(1 - \sum_{i=1}^{n} x_i\right)$$
$$\cdot \delta^{(2)}\left(\sum_{i=1}^{n} \mathbf{p}_{\perp i}\right) \times |n; x_i P^+, x_i \mathbf{P}_\perp$$
$$+ \mathbf{p}_{\perp i}, \lambda_i\rangle \psi_n(x_i, \mathbf{p}_{\perp i}, \lambda_i), \quad (2)$$

where $x_i = p_i^+/P^+$ is light-cone momentum fraction and $\mathbf{p}_{\perp i}$ is the relative momentum of the ith constituent of the hadron. The helicity of ith constituent is denoted by λ_i. The Fock states of n-particle are normalized as follows

$$\langle n; p_i'^+, \mathbf{p}'_{\perp i}, \lambda_i' | n; p_i^+, \mathbf{p}_{\perp i}, \lambda_i\rangle$$
$$= \prod_{i=1}^{n} 16\pi^3 p_i^+ \delta(p_i'^+ - p_i^+)\delta^{(2)}(\mathbf{p}'_{\perp i} - \mathbf{p}_{\perp i})\delta_{\lambda_i'\lambda_i}. \quad (3)$$

As the system is considered as a two-particle system (a quark and a diquark), therefore, by substituting $n = 2$, the Fock state expansion for scalar diquark $\left(|u\ s^0\rangle\right)$ leads to

$$|u\ s^0(P^+, \mathbf{p}_\perp)\rangle^{\pm} = \sum_{\lambda_q} \int \frac{dx d^2\mathbf{p}_\perp}{\sqrt{x(1-x)}16\pi^3} \psi_{\lambda_q}^{\pm}(x, \mathbf{p}_\perp)|xP^+, \mathbf{p}_\perp, \lambda_q\rangle. \quad (4)$$

Similarly, the expansion of axial-vector diquark component is expressed as

$$|\mu\ V(P^+, \mathbf{p}_\perp)\rangle^{\pm}$$
$$= \sum_{\lambda_q, \lambda_D} \int \frac{dx d^2\mathbf{p}_\perp}{\sqrt{x(1-x)}16\pi^3} \psi_{\lambda_q \lambda_D}^{\pm}(x, \mathbf{p}_\perp)|xP^+, \mathbf{p}_\perp, \lambda_q, \lambda_D\rangle, \quad (5)$$

where the respective helicities of quark and diquark are denoted by λ_q and λ_D. Here, μ can be u-quark or d-quark and V denotes the axial vector diquark, either isoscalar or isovector.

The wavefunctions related to the scalar diquark are defined as [7]

$$\psi_+^+(x, \mathbf{p}_\perp) = \frac{m + xM}{x}\varphi(x, \mathbf{p}_\perp),$$
$$\psi_-^+(x, \mathbf{p}_\perp) = -\frac{p_x + ip_y}{x}\varphi(x, \mathbf{p}_\perp),$$
$$\psi_+^-(x, \mathbf{p}_\perp) = \frac{p_x - ip_y}{x}\varphi(x, \mathbf{p}_\perp),$$
$$\psi_-^-(x, \mathbf{p}_\perp) = \frac{m + xM}{x}\varphi(x, \mathbf{p}_\perp),$$
$$\quad (6)$$

with

$$\varphi(x, \mathbf{p}_\perp) = -\frac{g_s}{\sqrt{1-x}}\frac{x(1-x)}{\mathbf{p}_\perp^2 + \left[xM_s^2 + (1-x)m^2 - x(1-x)M^2\right]}. \quad (7)$$

Similarly, the wavefunctions related to axial-vector diquark are defined as

$$\psi_{+(1/2)+1}^+(x, \mathbf{p}_\perp) = \frac{(p_x - ip_y)}{x(1-x)}\phi(x, \mathbf{p}_\perp),$$
$$\psi_{+(1/2)-1}^+(x, \mathbf{p}_\perp) = -\frac{(p_x + ip_y)}{(1-x)}\phi(x, \mathbf{p}_\perp),$$
$$\psi_{-(1/2)+1}^+(x, \mathbf{p}_\perp) = \frac{(m + xM)}{x}\phi(x, \mathbf{p}_\perp),$$
$$\psi_{-(1/2)-1}^+(x, \mathbf{p}_\perp) = 0,$$
$$\psi_{+(1/2)+1}^-(x, \mathbf{p}_\perp) = 0,$$
$$\psi_{+(1/2)-1}^-(x, \mathbf{p}_\perp) = -\frac{(m + xM)}{x}\phi(x, \mathbf{p}_\perp),$$
$$\psi_{-(1/2)+1}^-(x, \mathbf{p}_\perp) = -\frac{(p_x - ip_y)}{(1-x)}\phi(x, \mathbf{p}_\perp),$$
$$\psi_{-(1/2)-1}^-(x, \mathbf{p}_\perp) = \frac{(p_x + ip_y)}{x(1-x)}\phi(x, \mathbf{p}_\perp).$$
$$\quad (8)$$
$$\quad (9)$$

$$\phi(x, \mathbf{p}_\perp) = -\frac{g_a}{\sqrt{1-x}}\frac{x(1-x)}{\mathbf{p}_\perp^2 + \left[xM_a^2 + (1-x)m^2 - x(1-x)M^2\right]}. \quad (10)$$

The above wavefunctions for axial-vector diquark are defined corresponding to the light-cone transverse polarization vectors satisfying $\epsilon(\pm) \cdot \epsilon^*(\pm) = -1$, $\epsilon(\pm) \cdot \epsilon^*(\mp) = 0$ and $(P - p) \cdot \epsilon(\pm) = 0$ given below:

$$\epsilon(P - p, +) = \left[\frac{p_x + ip_y}{\sqrt{2}(1-x)P^+}, 0, -\frac{1}{\sqrt{2}}, -\frac{i}{\sqrt{2}} \right], \quad (11)$$

$$\epsilon(P - p, -) = \left[-\frac{p_x - ip_y}{\sqrt{2}(1-x)P^+}, 0, \frac{1}{\sqrt{2}}, -\frac{i}{\sqrt{2}} \right]. \quad (12)$$

In addition to this, the third longitudinal polarization vector is also included with the transverse polarization vectors. It satisfies $\epsilon(0) \cdot \epsilon^*(0) = -1$, $\epsilon(0) \cdot \epsilon^*(\pm) = 0$, and $(P - p) \cdot \epsilon(0) = 0$.

$$\epsilon(P - p, 0) = \frac{1}{M_a} \left[\frac{\mathbf{p}_\perp^2 - M_a^2}{2(1-x)P^+}, (1-x)P^+, -p_x, -p_y \right]. \quad (13)$$

The light-cone wavefunctions corresponding to above longitudinal polarization vector are defined as

$$\psi_{+0}^+(x, \mathbf{p}_\perp) = \frac{\mathbf{p}_\perp^2 - xM_a^2 - mM(1-x)^2}{\sqrt{2}x(1-x)M_a} \phi(x, \mathbf{p}_\perp),$$

$$\psi_{-0}^+(x, \mathbf{p}_\perp) = \frac{(m+M)}{\sqrt{2}M_a}(p_x + ip_y)\phi(x, \mathbf{p}_\perp),$$

$$\psi_{+0}^-(x, \mathbf{p}_\perp) = \frac{(m+M)}{\sqrt{2}M_a}(p_x - ip_y)\phi(x, \mathbf{p}_\perp),$$

$$\psi_{-0}^-(x, \mathbf{p}_\perp) = -\frac{\mathbf{p}_\perp^2 - xM_a^2 - mM(1-x)^2}{\sqrt{2}x(1-x)M_a} \phi(x, \mathbf{p}_\perp), \quad (14)$$

where M_a, M and m are axial-vector diquark mass, spin-1/2 particle mass, and constituent quark mass, respectively.

3. Wigner Distributions and Spin–Spin Correlations

The five-dimensional Wigner distribution of quark, also known as quantum phase-space distribution, is defined as [41]

$$\rho^{[\Gamma]}(\mathbf{b}_\perp, \mathbf{k}_\perp, x, S) \equiv \int \frac{d^2\Delta_\perp}{(2\pi)^2} e^{-i\Delta_\perp \cdot \mathbf{b}_\perp} W^{[\Gamma]}(\Delta_\perp, \mathbf{k}_\perp, x, S), \quad (15)$$

where the correlator $W^{[\Gamma]}(\Delta_\perp, \mathbf{k}_\perp, x; S)$ is

$$W^{[\Gamma]}(\Delta_\perp, \mathbf{k}_\perp, x; S)$$
$$= \frac{1}{2} \int \frac{dz^- d^2 z_\perp}{(2\pi)^3} e^{ik\cdot z} \left\langle P''; S \left| \bar{\psi}\left(-\frac{z}{2}\right) \Gamma \mathcal{W}_{[-(z/2),(z/2)]} \right. \right.$$
$$\left. \left. \cdot \psi\left(\frac{z}{2}\right) \right| P'; S \right\rangle \Big|_{z^+=0}. \quad (16)$$

Here, Γ defines the Dirac gamma matrices and $\Gamma = \gamma^+, \gamma^+\gamma^5, i\sigma^{j+}\gamma^5$. The states of the composite system are defined in Eqs. (4) and (5) based on whether the diquark is scalar or

axial-vector. By substituting Eqs. (4) and (5) in Eq. (16), one can get the overlap form of the Wigner distribution.

The phase-space distributions based on the configurations of various polarizations, i.e., ρ_{XY}, where X defines the polarization of composite system and Y stands for the polarization of quark, are defined as [24, 25, 27]

$$\rho_{UU}(\mathbf{b}_\perp, \mathbf{p}_\perp, x)$$
$$= \frac{1}{2}\left[\rho^{[\gamma^+]}(\mathbf{b}_\perp, \mathbf{p}_\perp, x; +\hat{S}_z) + \rho^{[\gamma^+]}(\mathbf{b}_\perp, \mathbf{p}_\perp, x; -\hat{S}_z)\right], \quad (17)$$

$$\rho_{UL}(\mathbf{b}_\perp, \mathbf{p}_\perp, x)$$
$$= \frac{1}{2}\left[\rho^{[\gamma^+\gamma_5]}(\mathbf{b}_\perp, \mathbf{p}_\perp, x; +\hat{S}_z) + \rho^{[\gamma^+\gamma_5]}(\mathbf{b}_\perp, \mathbf{p}_\perp, x; -\hat{S}_z)\right], \quad (18)$$

$$\rho_{UT}^j(\mathbf{b}_\perp, \mathbf{p}_\perp, x)$$
$$= \frac{1}{2}\left[\rho^{[i\sigma^{+j}\gamma_5]}(\mathbf{b}_\perp, \mathbf{p}_\perp, x; +\hat{S}_z) + \rho^{[i\sigma^{+j}\gamma_5]}(\mathbf{b}_\perp, \mathbf{p}_\perp, x; -\hat{S}_z)\right], \quad (19)$$

$$\rho_{LU}(\mathbf{b}_\perp, \mathbf{p}_\perp, x)$$
$$= \frac{1}{2}\left[\rho^{[\gamma^+]}(\mathbf{b}_\perp, \mathbf{p}_\perp, x; +\hat{S}_z) - \rho^{[\gamma^+]}(\mathbf{b}_\perp, \mathbf{p}_\perp, x; -\hat{S}_z)\right], \quad (20)$$

$$\rho_{LL}(\mathbf{b}_\perp, \mathbf{p}_\perp, x)$$
$$= \frac{1}{2}\left[\rho^{[\gamma^+\gamma_5]}(\mathbf{b}_\perp, \mathbf{p}_\perp, x; +\hat{S}_z) - \rho^{[\gamma^+\gamma_5]}(\mathbf{b}_\perp, \mathbf{p}_\perp, x; -\hat{S}_z)\right], \quad (21)$$

$$\rho_{LT}^j(\mathbf{b}_\perp, \mathbf{p}_\perp, x)$$
$$= \frac{1}{2}\left[\rho^{[i\sigma^{+j}\gamma_5]}(\mathbf{b}_\perp, \mathbf{p}_\perp, x; +\hat{S}_z) - \rho^{[i\sigma^{+j}\gamma_5]}(\mathbf{b}_\perp, \mathbf{p}_\perp, x; -\hat{S}_z)\right], \quad (22)$$

$$\rho_{TU}^i(\mathbf{b}_\perp, \mathbf{p}_\perp, x)$$
$$= \frac{1}{2}\left[\rho^{[\gamma^+]}(\mathbf{b}_\perp, \mathbf{p}_\perp, x; +\hat{S}_i) - \rho^{[\gamma^+]}(\mathbf{b}_\perp, \mathbf{p}_\perp, x; -\hat{S}_i)\right], \quad (23)$$

$$\rho_{TL}^i(\mathbf{b}_\perp, \mathbf{p}_\perp, x)$$
$$= \frac{1}{2}\left[\rho^{[\gamma^+\gamma_5]}(\mathbf{b}_\perp, \mathbf{p}_\perp, x; +\hat{S}_i) - \rho^{[\gamma^+\gamma_5]}(\mathbf{b}_\perp, \mathbf{p}_\perp, x; -\hat{S}_i)\right], \quad (24)$$

$$\rho_{TT}(\mathbf{b}_\perp, \mathbf{p}_\perp, x)$$
$$= \frac{1}{2}\delta_{ij}\left[\rho^{[i\sigma^{+j}\gamma_5]}(\mathbf{b}_\perp, \mathbf{p}_\perp, x; +\hat{S}_i) - \rho^{[i\sigma^{+j}\gamma_5]}(\mathbf{b}_\perp, \mathbf{p}_\perp, x; -\hat{S}_i)\right], \quad (25)$$

and finally the pretzelous Wigner distribution as

$$\rho_{TT}^\perp(\mathbf{b}_\perp, \mathbf{p}_\perp, x)$$
$$= \frac{1}{2}\epsilon_{ij}\left[\rho^{[i\sigma^{+j}\gamma_5]}(\mathbf{b}_\perp, \mathbf{p}_\perp, x; +\hat{S}_i) - \rho^{[i\sigma^{+j}\gamma_5]}(\mathbf{b}_\perp, \mathbf{p}_\perp, x; -\hat{S}_i)\right]. \quad (26)$$

Here, in the subscript of Wigner distributions, U, L and T explains whether the quark or a fermion composite system is unpolarized, longitudinally-polarized or transversely-polarized.

To extract information about the correlation between quark spin and fermion system spin, the Wigner distributions of quarks in the proton having different helicities are evaluated. For $\Gamma = \gamma^+ (1 + \lambda \gamma^5)/2$ and $\vec{S} = \Lambda \hat{S}_z$, the longitudinal Wigner distribution of the quark in the fermion system having helicities λ and Λ, respectively, is defined as

$$
\rho_{\Lambda\lambda}(\mathbf{b}_\perp, \mathbf{p}_\perp, x) \\
= \frac{1}{2}\Big[\rho^{[\gamma^+]}\big(\mathbf{b}_\perp, \mathbf{p}_\perp, x, \Lambda\hat{S}_z\big) + \lambda\rho^{[\gamma^+\gamma^5]}\big(\mathbf{b}_\perp, \mathbf{p}_\perp, x, \Lambda\hat{S}_z\big)\Big]. \tag{27}
$$

The above equation can be expressed in terms of polarization configurations of quark and proton as

$$
\rho_{\Lambda\lambda}(\mathbf{b}_\perp, \mathbf{p}_\perp, x) = \frac{1}{2}[\rho_{UU}(\mathbf{b}_\perp, \mathbf{p}_\perp, x) + \Lambda\rho_{LU}(\mathbf{b}_\perp, \mathbf{p}_\perp, x) \\
+ \lambda\rho_{UL}(\mathbf{b}_\perp, \mathbf{p}_\perp, x) + \Lambda\lambda\rho_{LL}(\mathbf{b}_\perp, \mathbf{p}_\perp, x)]. \tag{28}
$$

For the quark Wigner distributions, considering the spin directions of quark and composite system to be in the longitudinal direction, the helicities Λ and λ take different forms, i.e., $\Lambda = \uparrow, \downarrow$ and $\lambda = \uparrow, \downarrow$.

Similar to the longitudinal Wigner distributions, the Wigner distributions for quark having the transverse polarization $\lambda_\perp = \Uparrow, \Downarrow$ in the composite system having transverse polarization $\Lambda_\perp = \Uparrow, \Downarrow$, for $\Gamma = (\gamma^+ + \Lambda_\perp i\sigma^{j+}\gamma^5)/2$ and $\vec{S} = \Lambda_\perp \hat{S}_i$ is given as

$$
\rho_{\Lambda_\perp\lambda_\perp}(\mathbf{b}_\perp, \mathbf{p}_\perp, x) = \frac{1}{2}\Big[\rho^{[\gamma^+]}\big(\mathbf{b}_\perp, \mathbf{p}_\perp, x, \Lambda_\perp\hat{S}_i\big) \\
+ \Lambda_\perp\rho^{[i\sigma^{j+}\gamma^+]}\big(\mathbf{b}_\perp, \mathbf{p}_\perp, x, \Lambda_\perp\hat{S}_i\big)\Big]. \tag{29}
$$

In terms of polarization configurations, the above equation can be expressed as

$$
\rho^i_{\Lambda_\perp\lambda_\perp}(\mathbf{b}_\perp, \mathbf{p}_\perp, x) = \frac{1}{2}[\rho_{UU}(\mathbf{b}_\perp, \mathbf{p}_\perp, x) + \Lambda_\perp\rho^i_{TU}(\mathbf{b}_\perp, \mathbf{p}_\perp, x) \\
+ \lambda_\perp\rho^i_{UT}(\mathbf{b}_\perp, \mathbf{p}_\perp, x) + \Lambda_\perp\lambda_\perp\rho_{TT}(\mathbf{b}_\perp, \mathbf{p}_\perp, x)]. \tag{30}
$$

Further, for the quark having spin in longitudinal direction and fermion system spin in transverse direction and vice-versa, the respective Wigner distributions $\rho^i_{\Lambda_\perp\lambda}$ and $\rho^j_{\Lambda\lambda_\perp}$ are defined as

$$
\rho^i_{\Lambda_\perp\lambda}(\mathbf{b}_\perp, \mathbf{p}_\perp, x) = \frac{1}{2}\Big[\rho_{UU}(\mathbf{b}_\perp, \mathbf{p}_\perp, x) + \Lambda_\perp\rho^i_{TU}(\mathbf{b}_\perp, \mathbf{p}_\perp, x) \\
+ \lambda\rho_{UL}(\mathbf{b}_\perp, \mathbf{p}_\perp, x) + \Lambda_\perp\lambda\rho^i_{TL}(\mathbf{b}_\perp, \mathbf{p}_\perp, x)\Big] \tag{31}
$$

and

$$
\rho^j_{\Lambda\lambda_\perp}(\mathbf{b}_\perp, \mathbf{p}_\perp, x) = \frac{1}{2}\Big[\rho_{UU}(\mathbf{b}_\perp, \mathbf{p}_\perp, x) + \Lambda\rho_{LU}(\mathbf{b}_\perp, \mathbf{p}_\perp, x) \\
+ \lambda_\perp\rho^j_{UT}(\mathbf{b}_\perp, \mathbf{p}_\perp, x) + \Lambda\lambda_\perp\rho^j_{LT}(\mathbf{b}_\perp, \mathbf{p}_\perp, x)\Big]. \tag{32}
$$

4. Results

Using the overlap form of LFWFs for axial-vector diquark, the difference between the Wigner operators for the case where longitudinal polarization vector is included and for the case where the longitudinal polarization vector is not included (from Eqs. (9) and (14)), we have

$$
W^{(a)l}_{UL} - W^{(a)}_{UU} \\
= \frac{1}{16\pi^3}\Bigg[\frac{\big(\mathbf{p}''^2_\perp - xM_a^2 - xM(1-x)^2\big)\big(\mathbf{p}'^2_\perp - xM_a^2 - xM(1-x)^2\big)}{x^2(1-x)^2} \\
+ \frac{(m+M)}{2M_a^2x^2}\Big(\mathbf{p}_\perp^2 - \frac{(1-x)^2}{4}\Delta_\perp^2\Big)\Bigg]\phi^\dagger(x, \mathbf{p}''_\perp)\phi(x, \mathbf{p}'_\perp), \tag{33}
$$

$$
W^{(a)l}_{UL} - W^{(a)}_{UL} = \frac{i}{16\pi^3}\frac{(m+M)^2}{2M_a^2x^2}(1-x)\big(p_x\Delta_y - p_y\Delta_x\big) \\
\cdot \phi^\dagger(x, \mathbf{p}''_\perp)\phi(x, \mathbf{p}'_\perp), \tag{34}
$$

$$
W^{(a)l}_{UT} - W^{(a)}_{UT} = \frac{i}{16\pi^3}\frac{(m+M)}{2M_a^2x^2}\Bigg[\big(\mathbf{p}''^2_\perp - xM_a^2 - xM(1-x)^2\big) \\
\cdot \Big(p_y - \frac{(1-x)}{2}\Delta_y\Big) + \big(\mathbf{p}'^2_\perp - xM_a^2 - xM(1-x)^2\big) \\
\cdot \Big(p_y + \frac{(1-x)}{2}\Delta_y\Big)\Bigg]\phi^\dagger(x, \mathbf{p}''_\perp)\phi(x, \mathbf{p}'_\perp), \tag{35}
$$

$$
W^{(a)l}_{LU} - W^{(a)}_{LU} = -\frac{i}{16\pi^3}\frac{(m+M)^2}{2M_a^2x^2}(1-x)\big(p_x\Delta_y - p_y\Delta_x\big) \\
\cdot \phi^\dagger(x, \mathbf{p}''_\perp)\phi(x, \mathbf{p}'_\perp), \tag{36}
$$

$$
W^{(a)l}_{LL} - W^{(a)}_{LL} \\
= \frac{1}{16\pi^3}\Bigg[\frac{\big(\mathbf{p}''^2_\perp - xM_a^2 - xM(1-x)^2\big)\big(\mathbf{p}'^2_\perp - xM_a^2 - xM(1-x)^2\big)}{x^2(1-x)^2} \\
- \frac{(m+M)}{2M_a^2x^2}\Big(\mathbf{p}_\perp^2 - \frac{(1-x)^2}{4}\Delta_\perp^2\Big)\Bigg]\phi^\dagger(x, \mathbf{p}''_\perp)\phi(x, \mathbf{p}'_\perp), \tag{37}
$$

$$
W^{(a)l}_{LT} - W^{(a)}_{LT} = \frac{1}{16\pi^3}\frac{(m+M)}{2M_a^2x^2}\Bigg[\big(\mathbf{p}''^2_\perp - xM_a^2 - xM(1-x)^2\big) \\
\cdot \Big(p_x - \frac{(1-x)}{2}\Delta_x\Big) + \big(\mathbf{p}'^2_\perp - xM_a^2 - xM(1-x)^2\big) \\
\cdot \Big(p_x + \frac{(1-x)}{2}\Delta_x\Big)\Bigg]\phi^\dagger(x, \mathbf{p}''_\perp)\phi(x, \mathbf{p}'_\perp), \tag{38}
$$

$$
W^{(a)l}_{TU} - W^{(a)}_{TU} = \frac{1}{16\pi^3}\frac{(m+M)}{2M_a^2x^2}\Bigg[\big(\mathbf{p}''^2_\perp - xM_a^2 - xM(1-x)^2\big) \\
\cdot \Big(p_x - \frac{(1-x)}{2}\Delta_x\Big) - \big(\mathbf{p}'^2_\perp - xM_a^2 - xM(1-x)^2\big) \\
\cdot \Big(p_x + \frac{(1-x)}{2}\Delta_x\Big)\Bigg]\phi^\dagger(x, \mathbf{p}''_\perp)\phi(x, \mathbf{p}'_\perp), \tag{39}
$$

FIGURE 1: The plot of Wigner distribution $\rho_{\uparrow\uparrow}(\mathbf{b}_\perp, \mathbf{p}_\perp)$ in transverse impact-parameter plane and transverse momentum plane for u-quark (left panel) and d-quark (right panel).

$$W_{TL}^{(a)l} - W_{TL}^{(a)} = -\frac{i}{16\pi^3}\frac{(m+M)}{2M_a^2 x^2}\left[\left(\mathbf{p}_\perp''^2 - xM_a^2 - xM(1-x)^2\right)\right.$$
$$\cdot \left(p_y - \frac{(1-x)}{2}\Delta_y\right) + \left(\mathbf{p}_\perp'^2 - xM_a^2 - xM(1-x)^2\right)$$
$$\left.\cdot \left(p_y + \frac{(1-x)}{2}\Delta_y\right)\right]\phi^\dagger(x,\mathbf{p}_\perp'')\phi(x,\mathbf{p}_\perp'),$$
$$(40)$$

$$W_{TT}^{(a)l} - W_{TT}^{(a)}$$
$$= -\frac{1}{16\pi^3}\left[\frac{\left(\mathbf{p}_\perp''^2 - xM_a^2 - xM(1-x)^2\right)\left(\mathbf{p}_\perp'^2 - xM_a^2 - xM(1-x)^2\right)}{x^2(1-x)^2}\right.$$
$$\left.+ \frac{(m+xM)^2}{2M_a^2 x^2}\left(\left(p_x^2 - p_y^2\right) - \frac{(1-x)^2}{4}\left(\Delta_x^2 - \Delta_y^2\right)\right)\right]\phi^\dagger(x,\mathbf{p}_\perp'')\phi(x,\mathbf{p}_\perp').$$
$$(41)$$

Further, the correlator W_{XY} is related to the Wigner distribution as

$$\rho_{XY}(\mathbf{b}_\perp, \mathbf{p}_\perp, x, S) = \int \frac{d^2\mathbf{\Delta}_\perp}{(2\pi)^2}e^{-i\mathbf{\Delta}_\perp \cdot \mathbf{b}_\perp}W_{XY}(\mathbf{\Delta}_\perp, \mathbf{p}_\perp, x, S), \quad (42)$$

where X and Y are the composite particle and quark polarizations, respectively.

In this work, the DGLAP region for quarks is used to evaluate the Wigner distributions, i.e., $0 < x < 1$. The respective momenta of initial and final state of struck quark in symmetric frame are defined as

$$\mathbf{p}_\perp' = \mathbf{p}_\perp - (1-x)\frac{\mathbf{\Delta}_\perp}{2},$$
$$\mathbf{p}_\perp'' = \mathbf{p}_\perp + (1-x)\frac{\mathbf{\Delta}_\perp}{2}. \quad (43)$$

The superposition of scalar and axial-vector diquark results into the quark flavors as [7]

FIGURE 2: The plot of Wigner distribution $\rho_{\uparrow\downarrow}(\mathbf{b}_\perp, \mathbf{p}_\perp)$ in transverse impact-parameter plane and transverse momentum plane for u-quark (left panel) and d-quark (right panel).

$$\rho^u = c_s^2 \rho^{u(s)} + c_a^2 \rho^{u(a)},$$
$$\rho^d = c_a'^2 \rho^{d(a')}, \qquad (44)$$

where the superscripts (s), (a), and (a') denote the scalar–isoscalar, vector–isoscalar and vector–isovector diquarks, respectively. The mass values and couplings for diquarks have been summarized in Table 1.

We plot the Wigner distributions of the quark in the fermion system having spins in longitudinal direction, i.e., $\rho_{\Lambda\lambda}$. Here, we take two cases for the discussion on the longitudinal Wigner distributions: (i) spin direction of composite system and quark to be $\Lambda = \uparrow$ and $\lambda = \uparrow$, i.e., $\rho_{\uparrow\uparrow}$, (ii) proton polarization $\Lambda = \uparrow$ and quark polarization $\lambda = \downarrow$, i.e., $\rho_{\uparrow\downarrow}$. In Figures 1(a) and 1(b), we plot the longitudinal distribution $\rho_{\uparrow\uparrow}$ for u-quark and d-quark, respectively. We see the distribution effects in transverse impact-parameter plane and transverse momentum

TABLE 1: The diquark masses M_X and couplings c_X for the scalar–isoscalar, vector–isoscalar diquark, and vector–isovector diquark.

Diquark	ud (Scalar s)	ud (Axial-vector a)	uu (Axial-vector a')
M_X in GeV	0.822 ± 0.053	1.492 ± 0.173	0.890 ± 0.008
c_X	0.847 ± 0.111	1.061 ± 0.085	0.880 ± 0.008

plane. The distribution shows circular behaviour with the peaks shifting towards $b_x < 0$ and $p_x < 0$ in impact-parameter plane and momentum plane, respectively. In momentum plane, as shown in Figures 1(c) and 1(d), we observe the distortion along b_x at the higher values of impact-parameter co-ordinate. In this model, the distributions ρ_{UL} and ρ_{LU} are same for axial-vector diquark. Based on the different combinations of helicities, we get the different cases from Eq. (16) as follows,
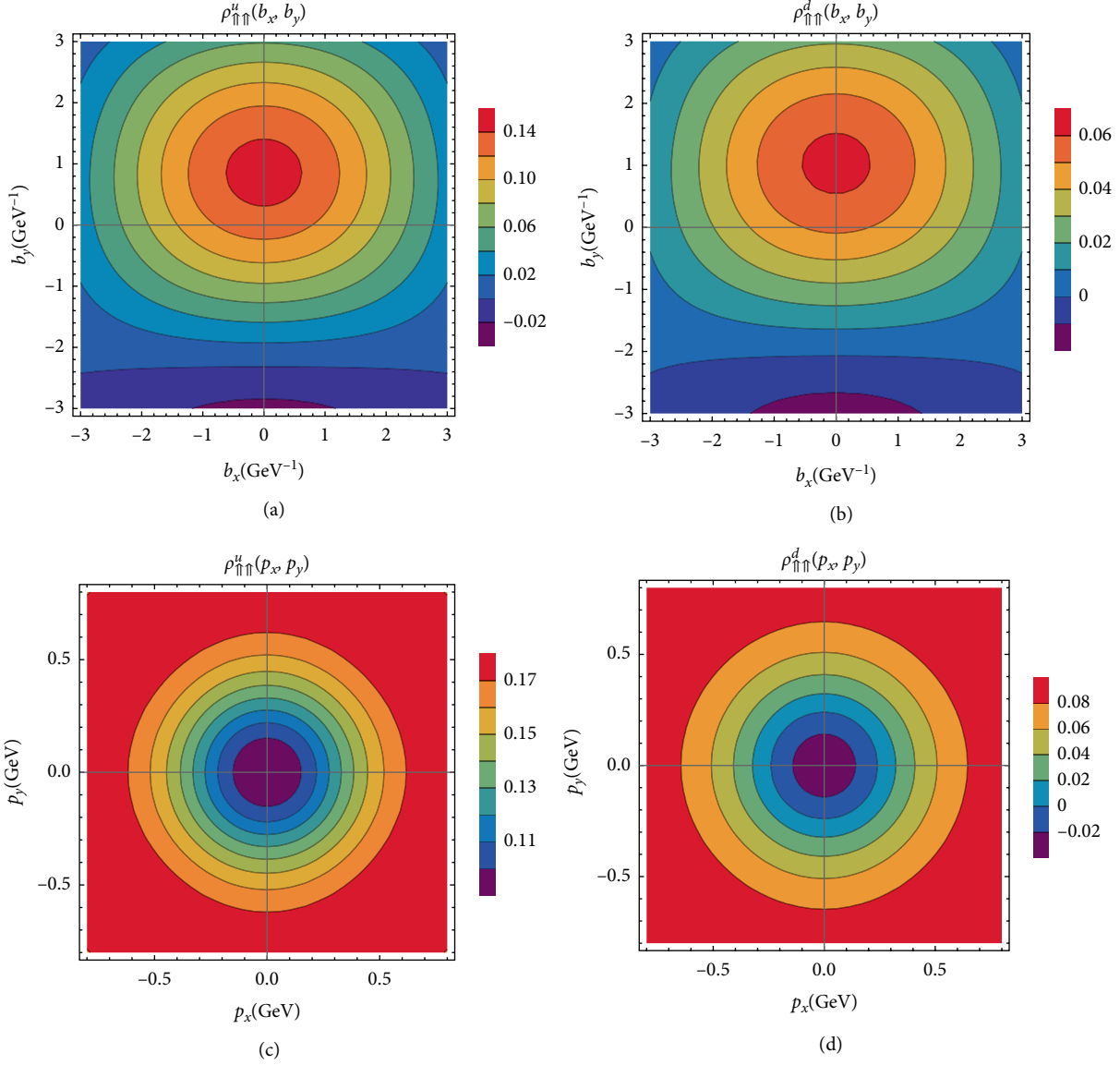
FIGURE 3: The plot of Wigner distribution $\rho_{\Uparrow\Uparrow}(\mathbf{b}_\perp, \mathbf{p}_\perp)$ in transverse impact-parameter plane and transverse momentum plane for u-quark (left panel) and d-quark (right panel).

For scalar diquark

$$\rho_{\uparrow\uparrow} = \frac{1}{2}[\rho_{UU} + \rho_{LL}],$$

$$\rho_{\uparrow\downarrow} = \frac{1}{2}[\rho_{UU} - 2\rho_{UL} - \rho_{LL}], \tag{45}$$

For axial-vector diquark

$$\rho_{\uparrow\uparrow} = \frac{1}{2}[\rho_{UU} + 2\rho_{UL} + \rho_{LL}],$$

$$\rho_{\uparrow\downarrow} = \frac{1}{2}[\rho_{UU} - \rho_{LL}]. \tag{46}$$

We plot the quark Wigner distribution having respective longitudinal polarization of quark $\lambda = \downarrow$ and fermion system $\Lambda = \uparrow$ in Figure 2. The distortion is observed in impact-parameter plane which gets more noticeable at the increasing values of $\mathbf{b}_\perp$ for u-quark and d-quark. The effect of distortion is more

in case of u-quark as compared to d-quark. In momentum plane, the distortion is seen at the center of the u-quark distribution. The distribution plots look nearly similar for $\Lambda = \lambda$ and $\Lambda \neq \lambda$, as Eqs. (45) and (46) contribute the same terms. The polarities are opposite for distribution of $\Lambda = \lambda$ in $\mathbf{p}_\perp$-plane and $\mathbf{b}_\perp$-plane. Since the distribution contributions from ρ_{UU} and ρ_{LL} are circularly symmetric (shown in Ref. [27]), the distortion appears in the plots of $\rho_{\uparrow\uparrow}$ and $\rho_{\uparrow\downarrow}$ due to the addition of terms ρ_{UL} and ρ_{LU}. In other words, the contribution from $\rho_{\uparrow\uparrow}$ is cirularly symmteric, because the interference of ρ_{UL} and ρ_{LU} is destructive, but when we add the axial vector part along with the scalar part to get the distribution of u-quark and d-quark in proton, the distortion takes place. Similar is the case of $\rho_{\uparrow\downarrow}$, however here the unpolarized-longitudinal Wigner distribution and longitudinal-unplarized Wigner distribution interfere destructively in axial-vector diquark case instead in scalar-diquark case, constructive interference is there. These

$\rho^u_{\Uparrow\Downarrow}(b_x, b_y)$

(a)

$\rho^d_{\Uparrow\Downarrow}(b_x, b_y)$

(b)

$\rho^u_{\Uparrow\Downarrow}(p_x, p_y)$

(c)

$\rho^d_{\Uparrow\Downarrow}(p_x, p_y)$

(d)
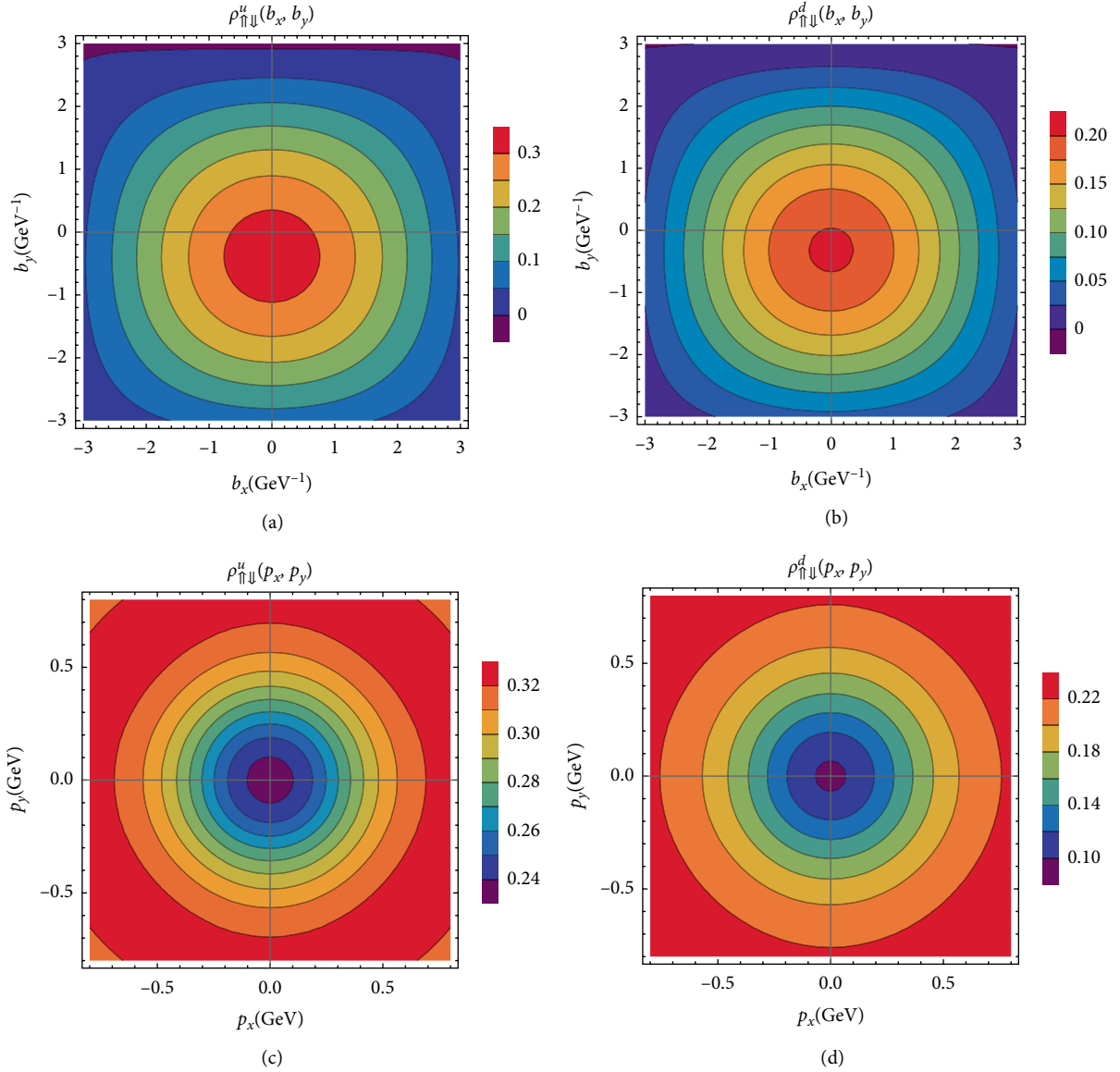
FIGURE 4: The plot of Wigner distribution $\rho_{\Uparrow\Downarrow}(\mathbf{b}_\perp, \mathbf{p}_\perp)$ in transverse impact-parameter plane and transverse momentum plane for u-quark (left panel) and d-quark (right panel).

interferences when added up accordingly, as Eqs. (45) and (46), cause the sideway shifts of distributions as shown in Figures 1 and 2.

The transverse Wigner distribution has been plotted in Figure 3 for the case with the quark having helicity as $\lambda = \Uparrow$ in the fermion composite system with helicity $\Lambda = \Uparrow$. The distortion in the distribution $\rho_{\Uparrow\Uparrow}$ shifts along the positive b_y direction in impact-parameter plane for both u-quark and d-quark. In $\mathbf{p}_\perp$-plane, circularly symmteric distribution is observed, which is more focused at the center in case of u-quark, while it extends more to the higher values of transverse momentum of d-quark. For $\rho_{\Uparrow\Downarrow}$, the distortion is in opposite direction of b_y for u-quark and d-quark when compared with $\rho_{\Uparrow\Uparrow}$ in impact-parameter plane (as shown in upper panels of Figures 3 and 4). In this work, we take the polarization direction of quark and proton along x-axis. From Eq. (29) and

Ref. [27], we find that in impact-parameter plane, the distortion comes due to ρ^1_{UT} and ρ^1_{TU}, as they show dipolar distributions except the case of ρ_{UU} and ρ_{TT}. However, in momentum plane, the strong correlation between the distributions ρ_{UU}, ρ^1_{UT}, ρ^1_{TU} and ρ_{TT}, leads to the circular symmetric behaviour of distributions $\rho_{\Uparrow\Uparrow}$ and $\rho_{\Uparrow\Downarrow}$ for both quarks (as shown in lower panels of Figures 3 and 4).

Further, we plot the distribution $\rho_{\uparrow\Uparrow}$ in Figure 5, which describes the correlation between spin of quark $\lambda_\perp = \Uparrow$ and spin of composite system $\lambda = \uparrow$. In impact-parameter plane, the distortion is clearly visible. This distortion is due to the Wigner distributions ρ_{UT} and ρ_{LU} as the dipolar distribution from these terms along b_y and b_x (shown in Ref. [27]) adds up resulting in $\rho_{\uparrow\Uparrow}$ in this model. Similarly, due to these terms, distortion is observed in $\mathbf{b}_\perp$-plane in case of $\rho_{\uparrow\Downarrow}$ as shown in Figure 6. Because of the opposite transverse spin direction of
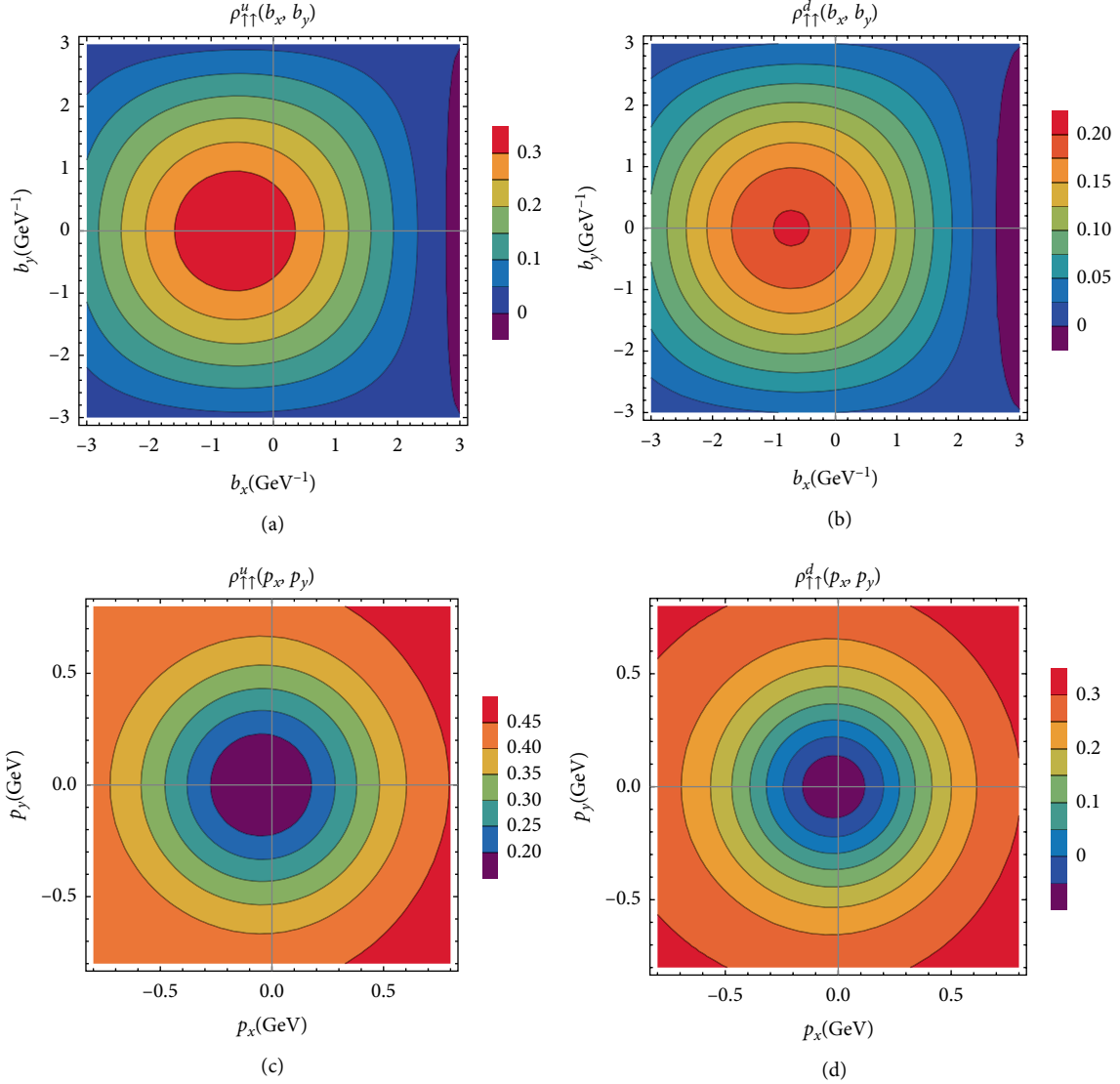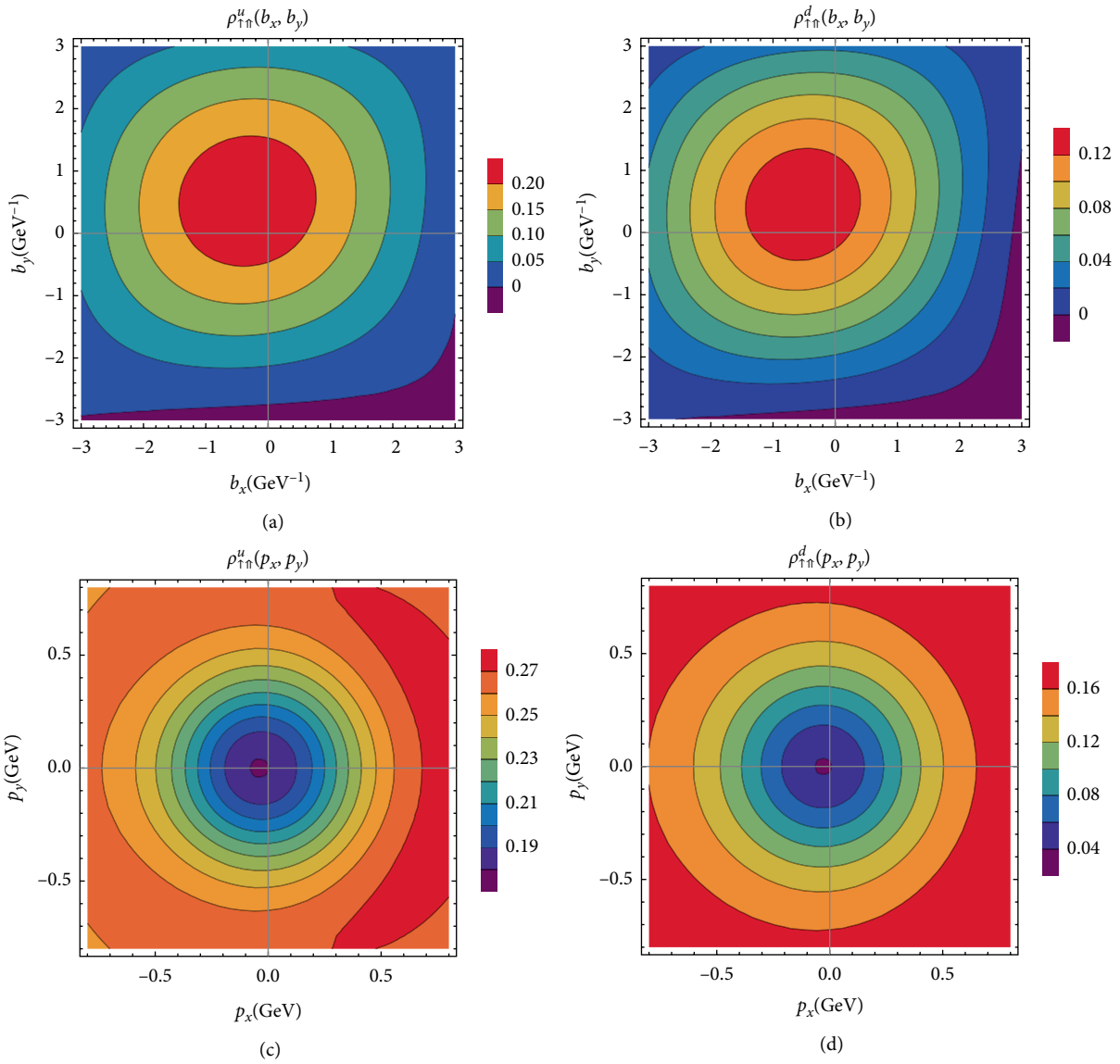
FIGURE 5: The plot of Wigner distribution $\rho_{\uparrow\Uparrow}(\mathbf{b}_\perp, \mathbf{p}_\perp)$ in transverse impact-parameter plane and transverse momentum plane for u-quark (left panel) and d-quark (right panel).
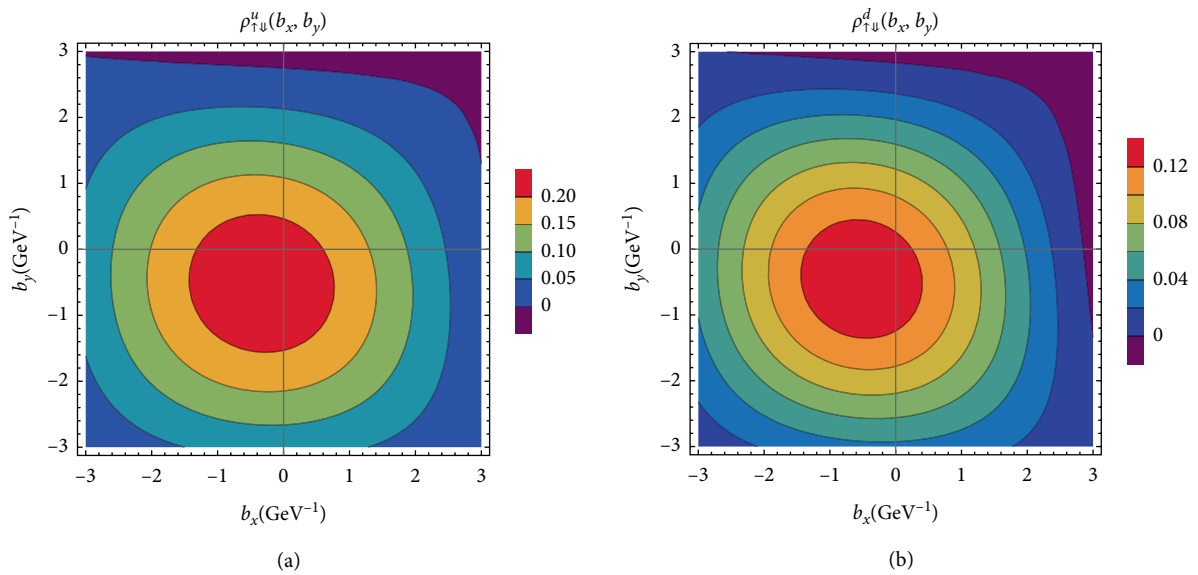
FIGURE 6: Continued.

$\rho^u_{\uparrow\Downarrow}(p_x, p_y)$

(c)

$\rho^d_{\uparrow\Downarrow}(p_x, p_y)$

(d)
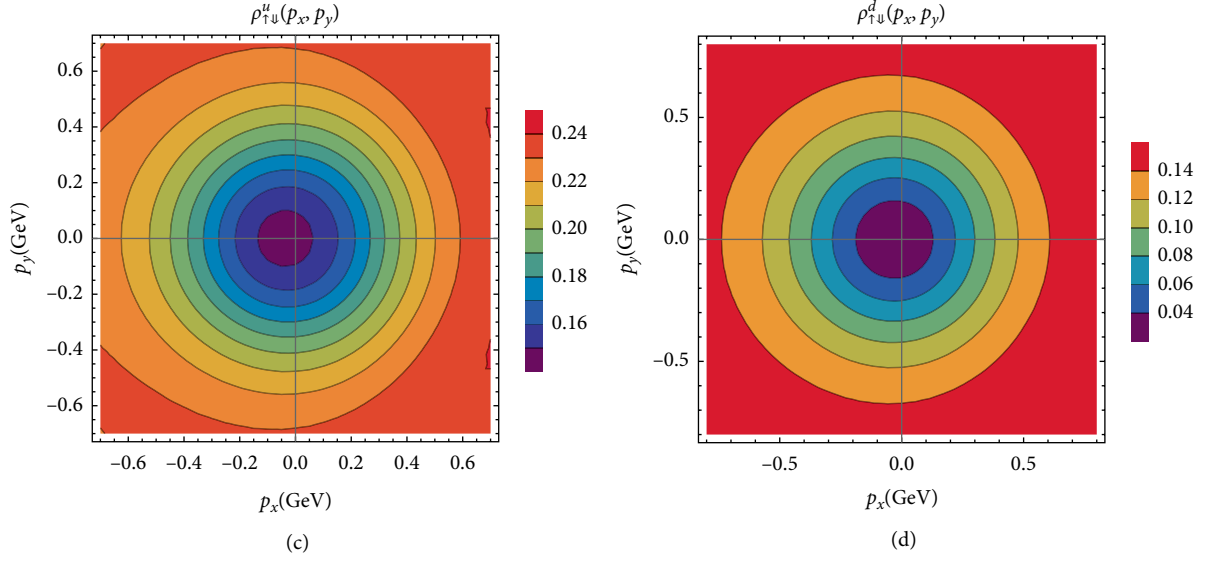
FIGURE 6: The plot of Wigner distribution $\rho_{\uparrow\Downarrow}(\mathbf{b}_\perp, \mathbf{p}_\perp)$ in transverse impact-parameter plane and transverse momentum plane for u-quark (left panel) and d-quark (right panel).

$\rho^u_{\Uparrow\uparrow}(b_x, b_y)$

(a)

$\rho^d_{\Uparrow\uparrow}(b_x, b_y)$

(b)

$\rho^u_{\Uparrow\uparrow}(p_x, p_y)$

(c)

$\rho^d_{\Uparrow\uparrow}(p_x, p_y)$

(d)
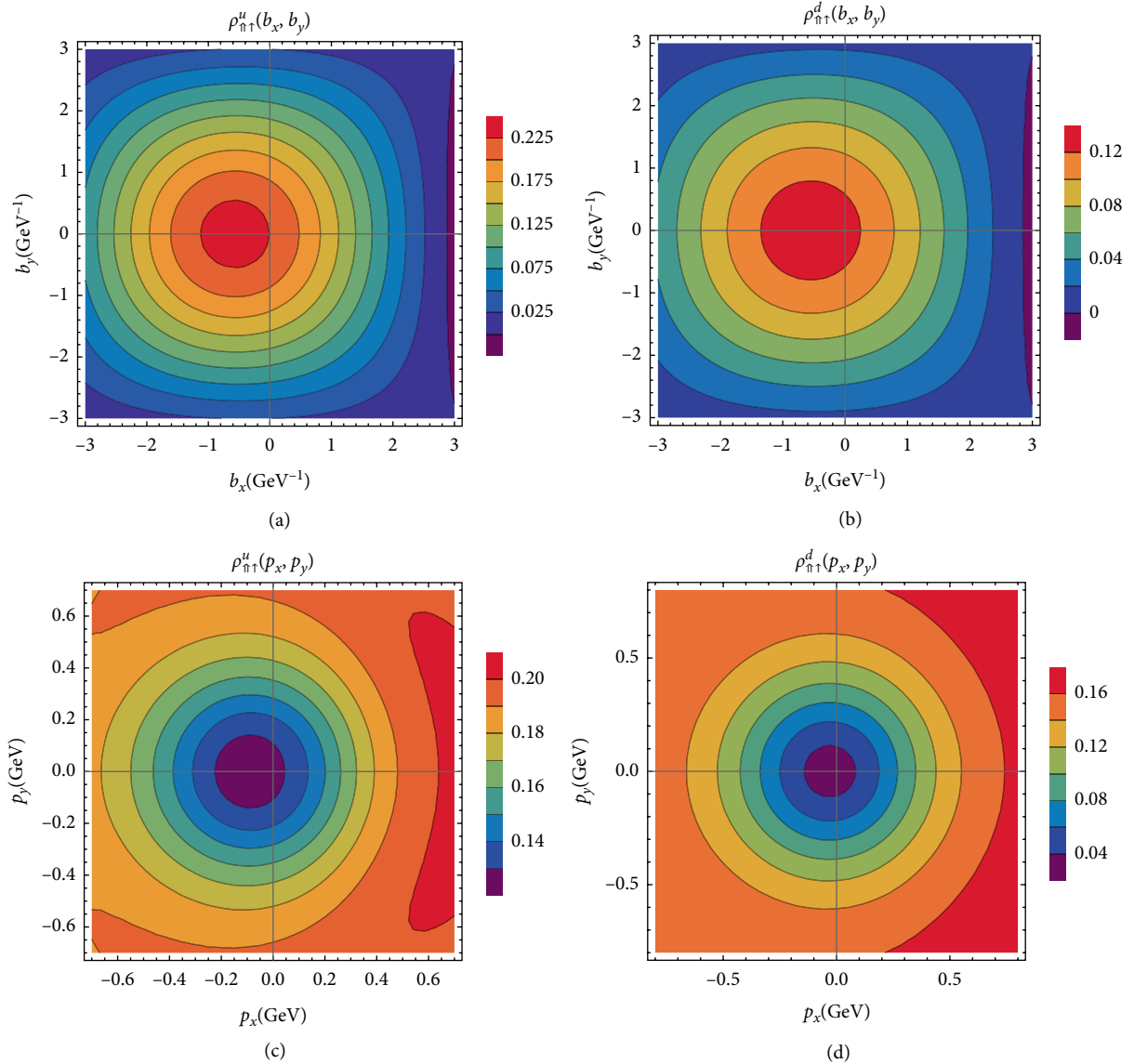
FIGURE 7: The plot of Wigner distribution $\rho_{\Uparrow\uparrow}(\mathbf{b}_\perp, \mathbf{p}_\perp)$ in transverse impact-parameter plane and transverse momentum plane for u-quark (left panel) and d-quark (right panel).

$\rho^u_{\Uparrow\downarrow}(b_x, b_y)$

(a)

$\rho^d_{\Uparrow\downarrow}(b_x, b_y)$

(b)

$\rho^u_{\Uparrow\downarrow}(p_x, p_y)$
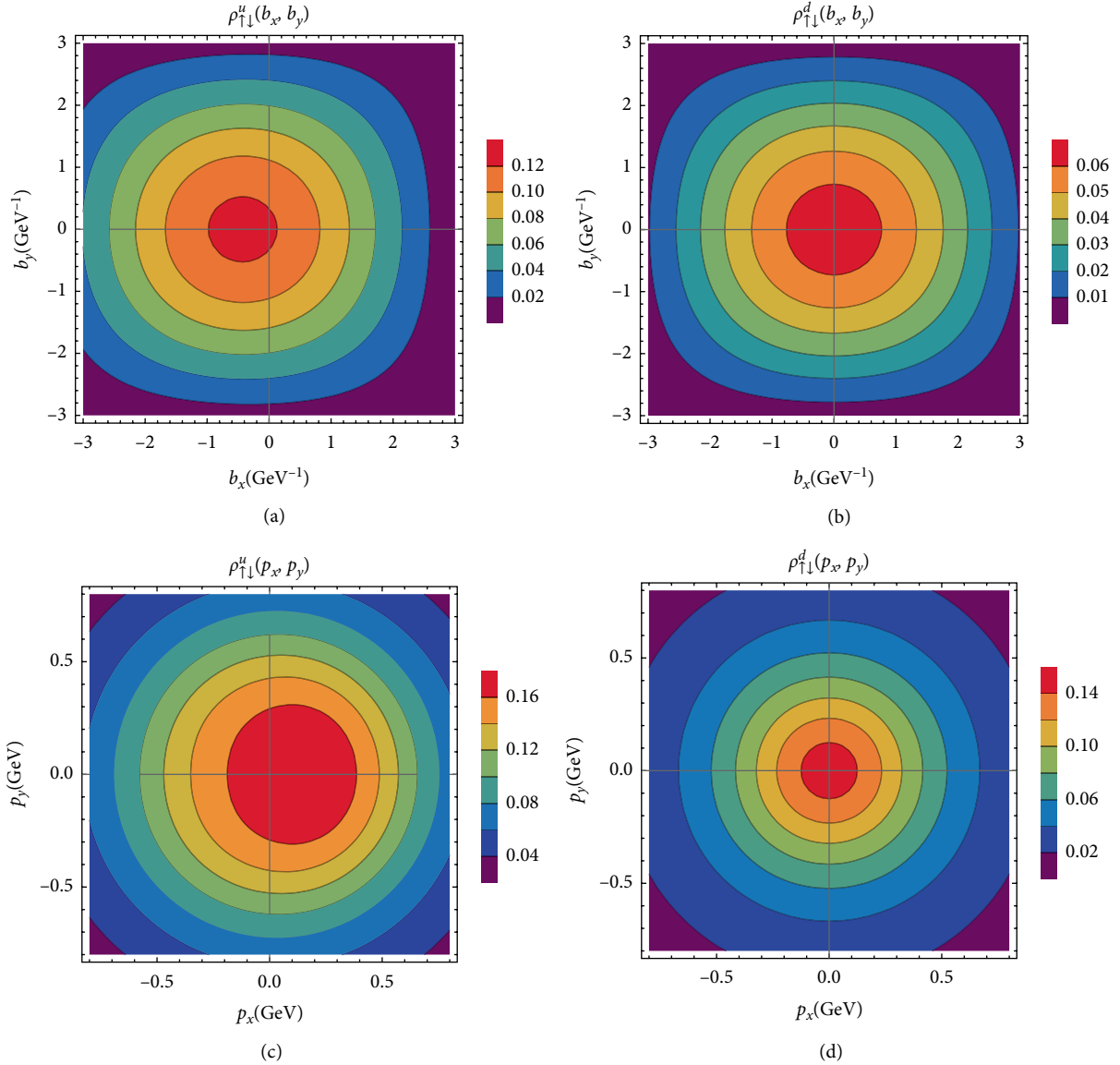
(c)

$\rho^d_{\Uparrow\downarrow}(p_x, p_y)$

(d)
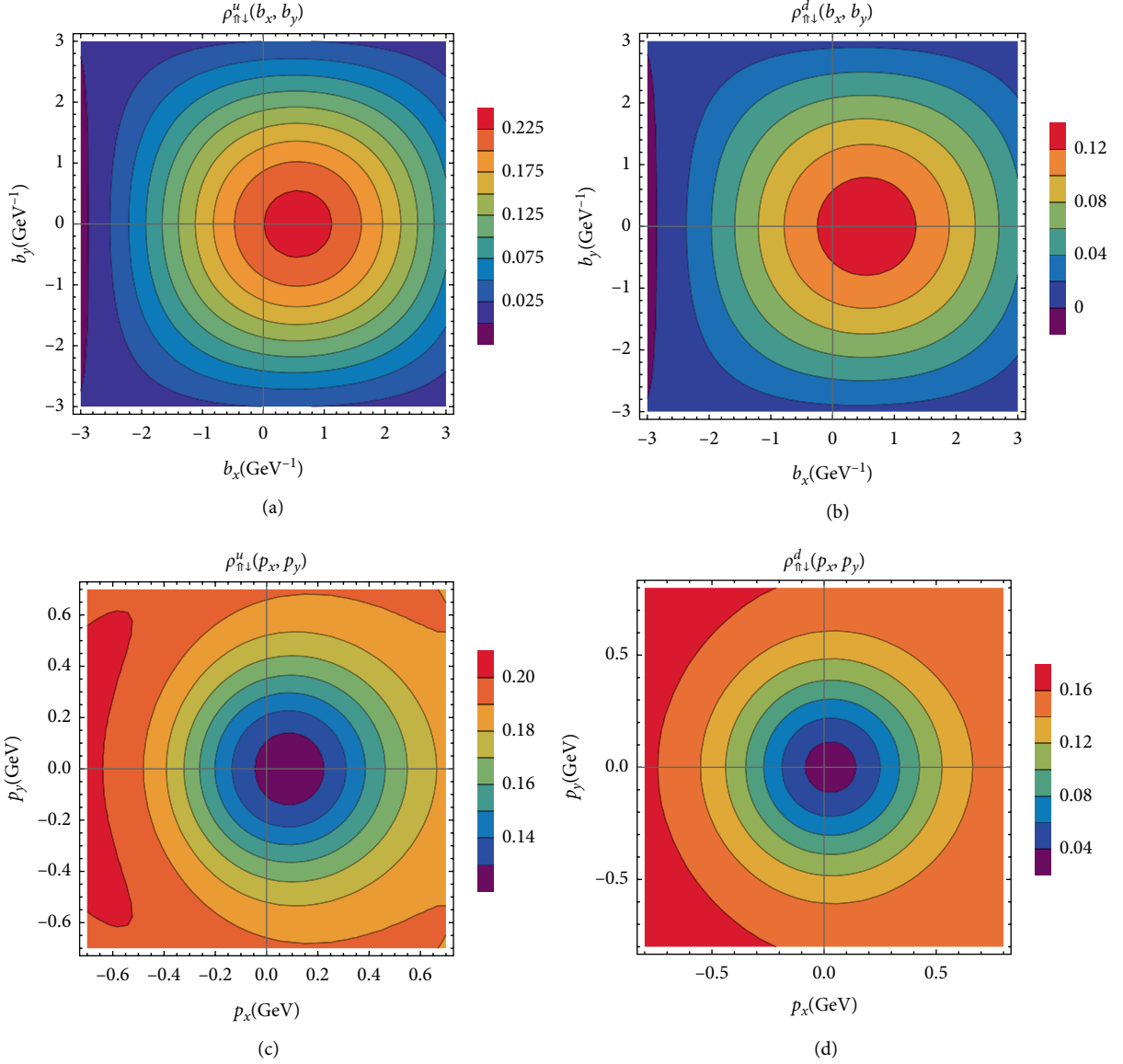
FIGURE 8: The plot of Wigner distribution $\rho_{\Uparrow\downarrow}(\mathbf{b}_\perp, \mathbf{p}_\perp)$ in transverse impact-parameter plane and transverse momentum plane for u-quark (left panel) and d-quark (right panel).

quark in two cases, $\rho_{\uparrow\Downarrow}$ causes the distortion along negative b_y while for $\rho_{\uparrow\Uparrow}$, it is in the direction of positive b_y. In momentum plane, we observe the distortion along negative p_x for u-quark and d-quark when quark longitudinal spin direction is positive and proton transverse spin direction is positive (or negative). The observed distortion is more along negative p_x in case of d-quark as compared to u-quark for $\rho_{\uparrow\Uparrow}$, while for $\rho_{\uparrow\Downarrow}$, it is more distorted in case of u-quark.

In Figure 7, we plot the distribution $\rho_{\Lambda\perp,\lambda}$, which explains the correlation between the transverse spin of composite system and longitudinal spin of quark, both along positive directions. Also the distortion comes from the correlation between the transverse spin of composite system along positive direction and longitudinal spin of quark along negative direction, shown in Figure 8. From Eq. (31), the distributions ρ_{UU}, ρ^i_{TU}, ρ_{UL}, and ρ^i_{TL} are summed up according to the spin direction of composite system to get $\rho_{\Uparrow\uparrow}$

and $\rho_{\Uparrow,\downarrow}$. The resulting plotted distortion is along $b_x < 0 (p_x < 0)$ and $b_x > 0 (p_x > 0)$ for $\rho_{\Uparrow\uparrow}$ and $\rho_{\Uparrow\downarrow}$, respectively, for u and d quarks in $\mathbf{b}_\perp$-plane ($\mathbf{p}_\perp$-plane).

5. Conclusions

We have presented the results of spin–spin correlations between the u-quark (or d-quark) and fermion composite system spins in light-front quark–diquark model evaluated from the Wigner distributions. The contribution from both the scalar and axial-vector diquarks is considered to get the distributions of u and d quarks. We consider the axial vector diquark to be further distinguished between the isoscalar or isovector depending upon the realistic analysis. First, we consider the spins of quark and fermion system in longitudinal

direction, i.e., λ and Λ, respectively. Similarly, the correlation between transverse spin directions of quark $\left(\lambda_\perp\right)$ and composite particle $\left(\Lambda_\perp\right)$ is evaluated. Further, the different combinations are taken into account, i.e., when quark spin is in longitudinal direction and spin of composite particle is in transverse direction and vice-versa, i.e., $\rho_{\Lambda_\perp\lambda}$ and $\rho_{\Lambda\lambda_\perp}$. All these results are presented in transverse impact-parameter plane ($\mathbf{b}_\perp$-plane) and transverse momentum plane ($\mathbf{p}_\perp$-plane). We observe that the distortions in the correlations seen in both planes are due to the effect of different Wigner distributions.

The spin–spin correlations are related to the Wigner distributions and the quantum mechanical version of quark Wigner distributions have not yet been measured experimentally. The measurable quantities can be extracted from Wigner distributions by integrating them over transverse position or transverse momentum of quark. These quantities can be experimentally measured via DVCS or Drell–Yan processes. Further, since the Wigner distributions are related to GTMDs through Fourier transformations, they can be accessible through exclusive double Drell–Yan process.

Data Availability

There was no other data used to support this study and the data generated from the theoretical calculations of the present studies has been included in the manuscript.

Conflicts of Interest

The authors declare that they have no conflicts of interest.

Acknowledgments

References

[1] X. Ji, "Viewing the proton through "color" filters," *Physical Review Letters*, vol. 91, no. 6, Article ID 062001, 2003.

[2] A. V. Belitsky, X. Ji, and F. Yuan, "Quark imaging in the proton via quantum phase-space distributions," *Physical Review Letters*, vol. 69, no. 7, Article ID 074014, 2004.

[3] M. Diehl, "Generalized parton distributions," *Physical Reports*, vol. 388, no. 2-4, pp. 41–277, 2003.

[4] X. Ji, "Generalized parton distributions," *Annual Review of Nuclear and Particle Science*, vol. 54, no. 1, pp. 413–450, 2004.

[5] A. V. Belitsky and A. V. Radyushkin, "Unraveling hadron structure with generalized parton distributions," *Physical Reports*, vol. 418, no. 1-6, pp. 1–387, 2005.

[6] M. Garcon, "An introduction to the generalized parton distributions," *The European Physical Journal A*, vol. 18, no. 2-3, pp. 389–394, 2003.

[7] A. Bacchetta, F. Conti, and M. Radici, "Transverse-momentum distributions in a diquark spectator model," *Physical Review D*, vol. 78, no. 7, Article ID 074010, 2008.

[8] S. Meissner, A. Metz, and K. Goeke, "Relations between generalized and transverse momentum dependent parton distributions," *Physical Review D*, vol. 76, no. 3, Article ID 034002, 2007.

[9] B.-W. Xiao, F. Yuan, and J. Zhou, "Transverse momentum dependent parton distributions at small-x," *Nuclear Physics B*, vol. 921, pp. 104–126, 2017.

[10] J. C. Collins and D. E. Soper, "Parton distribution and decay functions," *Nuclear Physics B*, vol. 194, no. 3, pp. 445–492, 2008.

[11] G. A. Miller, "Charge densities of the neutron and proton," *Physical Review Letters*, vol. 99, no. 11, Article ID 112001, 2007.

[12] M. Diehl and P. Kroll, "Nucleon form factors, generalized parton distributions and quark angular momentum," *The European Physical Journal C*, vol. 73, no. 4, Article ID 2397, 2013.

[13] M. Guidal, M. V. Polyakov, A. V. Radyushkin, and M. Vanderhaeghen, "Nucleon form factors from generalized parton distributions," *Physical Review D*, vol. 72, no. 5, Article ID 054013, 2005.

[14] D. S. Hwang, D. S. Kim, and J. Kim, "Charge distributions in transverse coordinate space and in impact parameter space," *Physics Letters B*, vol. 669, no. 5, pp. 345–351, 2008.

[15] M. Guidal, M. V. Polyakov, A. V. Radyushkin, and M. Vanderhaeghen, "Nucleon form factors from generalized parton distributions," *Physical Review D*, vol. 72, no. 5, Article ID 054013, 2005.

[16] D. S. Hwang, D. S. Kim, and J. Kim, "Charge distributions in transverse coordinate space and in impact parameter space," *Physical Review B*, vol. 669, no. 5, pp. 345–351, 2008.

[17] V. E. Lyubovitskij, T. Gutsche, and A. Faessler, "Electromagnetic structure of the nucleon in the perturbative chiral quark model," *Physical Review C*, vol. 64, no. 6, Article ID 065203, 2001.

[18] B. Pasquini and S. Boffi, "Electroweak structure of the nucleon, meson cloud, and light-cone wave functions," *Physical Review D*, vol. 76, no. 7, Article ID 074011, 2007.

[19] C. Lorcé, B. Pasquini, X. Xiong, and F. Yuan, "Quark orbital angular momentum from Wigner distributions and light-cone wave functions," *Physical Review D*, vol. 85, Article ID 114006, 2012.

[20] A. Mukherjee, S. Nair, and V. K. Ojha, "Quark Wigner distributions and orbital angular momentum in light-front dressed quark model," *Physical Review D*, vol. 90, no. 1, Article ID 014024, 2014.

[21] T. Liu and B.-Q. Ma, "Strong decays of the XYZ states," *Physical Review D*, vol. 91, no. 3, Article ID 034019, 2015.

[22] C. Lorcé and B. Pasquini, "Multipole decomposition of the nucleon transverse phase space," *Physical Review D*, vol. 93, no. 3, Article ID 034040, 2016.

[23] J. More, A. Mukherjee, and S. Nair, "Quark Wigner distributions using light-front wave functions," *Physical Review D*, vol. 95, no. 7, Article ID 074039, 2017.

[24] D. Chakrabarti, T. Maji, C. Mondal, and A. Mukherjee, "Quark Wigner distributions and spin–spin correlations," *Physical Review D*, vol. 95, no. 7, Article ID 074028, 2017.

[25] N. Kumar and C. Mondal, "Wigner distributions for an electron," *Nuclear Physics B*, vol. 931, pp. 226–249, 2018.

[26] Z.-L. Ma and Z. Lu, "Quark Wigner distribution of the pion meson in light-cone quark model," *Physical Review D*, vol. 98, no. 5, Article ID 054024, 2018.

[27] S. Kaur and H. Dahiya, "Wigner distributions and GTMDs in a proton using light-front quark–diquark model," *Nuclear Physics B*, vol. 937, pp. 272–302, 2018.

[28] P. A. M. Dirac, "Forms of relativistic dynamics," *Reviews of Modern Physics*, vol. 21, no. 3, pp. 392–399, 1949.

[29] A. Harindranath, "An introduction to light-front dynamics for pedestrians," 1998, https://arxiv.org/abs/hep-ph/9612244.

[30] S. J. Brodsky and G. F. de Teramond, "Light-front dynamics and AdS/QCD correspondence: the pion form factor in the space- and time-like regions," *Physical Review D*, vol. 77, no. 5, Article ID 056007, 2008.

[31] W.-M. Zhang, "Light-front dynamics and light-front QCD," *Chinese Journal of Physics*, vol. 32, Article ID 717808, 1994.

[32] L. Gamberg, Z.-B. Kang, I. Vitev, and H. Xing, "Quasi-parton distribution functions: a study in the diquark spectator model," *Physics Letters B*, vol. 743, pp. 112–120, 2015.

[33] S. Bhattacharya, C. Cocuzza, and A. Metz, "Generalized quasi parton distributions in a diquark spectator model," *Physics Letters B*, vol. 788, pp. 453–463, 2019.

[34] V. Braun, P. Gornicki, and L. Mankiewicz, "Ioffe-time distributions instead of parton momentum distributions in the description of deep inelastic scattering," *Physical Review D*, vol. 51, no. 11, pp. 6036–6051, 1995.

[35] A. J. Chambers, R. Horsley, Y. Nakamura et al., "Nucleon structure functions from operator product expansion on the lattice," *Physical Review Letter*, vol. 118, Article ID 242001, 2017.

[36] Z.-Y. Fan, Y.-B. Yang, A. Anthony, H.-W. Lin, and K.-F. Liu, "Gluon quasi-parton-distribution functions from lattice QCD," *Physical Review Letter*, vol. 121, no. 24, Article ID 242001, 2018.

[37] A. V. Radyushkin, "Quasi-parton distribution functions, momentum distributions, and pseudo-parton distribution functions," *Physical Review D*, vol. 96, no. 3, Article ID 034025, 2017.

[38] H. W. Lin, J. W. Chen, S. D. Cohen, and X. Ji, "Flavor structure of the nucleon sea from lattice QCD," *Physical Review D*, vol. 91, no. 5, Article ID 054510, 2015.

[39] C. Alexandrou, K. Cichy, V. Drach et al., "Lattice calculation of parton distributions," *Physical Review D*, vol. 92, no. 1, Article ID 014502, 2015.

[40] S. J. Brodsky, M. Diehl, and D. S. Hwang, "Light-cone wavefunction representation of deeply virtual compton scattering," *Nuclear Physics B*, vol. 596, no. 1-2, pp. 99–124, 2001.

[41] C. Lorcé and B. Pasquini, "Quark Wigner distributions and orbital angular momentum," *Physical Review D*, vol. 84, no. 1, Article ID 014015, 2011.

Research Article

Kinetic Freeze-Out Temperature and Transverse Flow Velocity in Au-Au Collisions at RHIC-BES Energies

Muhammad Waqas and Bao-Chun Li

Institute of Theoretical Physics & Department of Physics & State Key Laboratory of Quantum Optics and Quantum Optics Devices, Shanxi University, Taiyuan, Shanxi 030006, China

Correspondence should be addressed to Bao-Chun Li; libc2010@163.com

By using the method of data-driven reanalysis, the midrapidity transverse momentum (p_T) spectra of charged hadrons (π^+, K^+, and p) produced in central and peripheral gold-gold (Au-Au) collisions from the Beam Energy Scan (BES) program at the Relativistic Heavy Ion Collider (RHIC) are fitted by using the blast-wave model with the Boltzmann-Gibbs statistics. The model results are in agreement with the experimental data measured by the STAR Collaboration at the RHIC-BES energies. We observe that the kinetic freeze-out temperature (T_0), transverse flow velocity (β_T), mean transverse momentum ($\langle p_T \rangle$), and initial temperature (T_i) increase with collision energy as well as with event centrality.

1. Introduction

One of the most fundamental questions in high energy and nuclear physics is to determine the phase structure of the strongly interacting quantum chromodynamics (QCD) matter [1–3]. The yield ratios, transverse momentum (p_T) spectra, and other data for various identified particles produced in proton-proton (pp), proton-nucleus (pA), and nucleus-nucleus (AA) collisions at high energies are important observable quantities for determining the phase structure. The experimental facilities such as the Relativistic Heavy Ion Collider (RHIC) and the Large Hadron Collider (LHC) provide excellent tools to study the properties of Quark-Gluon Plasma (QGP) [4–6], which are expected to create collision events with high multiplicities.

The phase diagram of the QCD matter is usually expressed in terms of the chemical freeze-out temperature (T_{ch}) and the baryon chemical potential (μ_B) [7, 8]. Besides, other quantities such as the kinetic freeze-out temperature (T_{kin} or T_0) and transverse flow velocity (β_T) are useful to understand the phase diagram [9]. To search for the possible critical energy in the phase transition from hadronic matter to QGP in high-energy collisions, the STAR Collaboration

has been performing the Beam Energy Scan (BES) program [10–13] at the RHIC. Besides, other experiments at similar or lower energies at other accelerators are scheduled [14, 15].

Generally, the processes of high-energy collisions result possibly in three main stages [16–18]:

(i) The initial stage: at this stage, the collisions are in the beginning. The temperature at this stage is called the initial temperature which is one of the main factors to affect the particle spectra, which is less studied in the community comparatively. After the initial state, the "fireball" leads to a decrease in the temperature and finally to the hadronization

(ii) The chemical freeze-out stage: at this stage, the inner collisions among various particles are elastic and the yield ratios of differential types of particles remain invariant. The chemical freeze-out temperature T_{ch} can be obtained from the particle ratios, which is much studied in the community comparatively

(iii) The kinetic freeze-out stage: at this stage, the scattering processes stop, the hadrons decouple from the rest of the system, and the hadron's energy/momentum

spectra freeze in time. The temperature at this stage is known as the kinetic freeze-out temperature T_0 which can be obtained from the p_T spectra

When one studies T_0 from the p_T spectra, the effect of β_T should be eliminated. If the effect of β_T is not eliminated in the temperature, this temperature is called the effective temperature (T_{eff} or T). At the stage of kinetic freeze-out, T_0 and β_T are two important parameters which describe the thermal motion of the produced particles and the collective expansion of the emission source, respectively. The spectra in a low-p_T region ($p_T = 2 - 3$ GeV/c) which is mainly contributed by the soft excitation process essentially separate the contribution of the thermal motion and the collective expansion, if one only extracts T_0 and β_T. The spectra in a high-p_T region are contributed by the hard scattering process which is not needed in extracting T_0 and β_T.

We are very interested in the extraction of T_0 and β_T in collisions at the RHIC-BES energies which are very suitable to study the spectra in a low-p_T region, where the spectra in a high-p_T region are not produced due to not too high energies. In this work, the double-differential p_T spectra of charged particle dependences on collision energy and event centrality in gold-gold (Au-Au) collisions are analyzed with the blast-wave model with the Boltzmann-Gibbs statistics by means of data-driven analysis. The model results are compared with the data measured by the STAR Collaboration at the RHIC-BES energies [19, 20].

The remainder of this work consists of The Method and Formalism, Results and Discussion, and Conclusions. We shall describe the remanent parts orderly.

2. The Method and Formalism

Various methods can be used for the extraction of T_0 and β_T, e.g., the blast-wave model with the Boltzmann-Gibbs statistics [21–23], the blast-wave model with the Tsallis statistics [24–26], an alternative method by using the Boltzmann-Gibbs statistics [22, 27–33], and the alternative method by using the Tsallis distribution [33–39]. In this work, we choose the blast-wave model with the Boltzmann-Gibbs statistics due to its similarity with the ideal gas model in thermodynamics and few parameters. However, these methods only describe the spectra in the low-p_T region. For the spectra in the high-p_T region if available, the Hagedorn function which is known as the inverse power law [40, 41] can be used. We shall discuss these issues in detail as follows.

In general, there are two main processes responsible for the contribution of p_T spectra. They are (i) the soft excitation process which contributes the soft component in the low-p_T region and (ii) the hard scattering process which contributes the hard component in the whole p_T region if one uses the general superposition function or in the high-p_T region if one uses the usual step function.

For the soft component, according to Refs. [21–23], the probability density function of the p_T spectra in the blast-wave model with the Boltzmann-Gibbs statistics results in

$$
\begin{aligned}
f_1(p_T) &= \frac{1}{N}\frac{dN}{dp_T} \\
&= C_{p_T m_T}\int_0^R r\,dr \times I_0\left[\frac{p_T\sinh(\rho)}{T_0}\right] K_1\left[\frac{m_T\cosh(\rho)}{T_0}\right],
\end{aligned}
\tag{1}
$$

where N is the number of particles, C is the normalization constant, $m_T = \sqrt{p_T^2 + m_0^2}$ is the transverse mass, m_0 is the rest mass of the considered particle, r and R are the radial position and the maximum radial position, respectively, I_0 and K_1 are the modified Bessel functions of the first and second kinds, respectively, $\rho = \tanh^{-1}[\beta(r)]$ is the boost angle, $\beta(r) = \beta_S(r/R)^{n_0}$ is a self-similar flow profile, β_S is the flow velocity on the surface, and $n_0 = 2$ is used in the original form [21]. Particularly, $\beta_T = (2/R^2)\int_0^R r\beta(r)dr = 2\beta_S/(n_0 + 2) = 0.5\beta_S$. The parameter n_0 is used in different works, e.g., $n_0 = 1$ or noninteger in Refs. [22, 24, 42], which corresponds to the centrality from the center to the periphery.

Equation (1) and similar or related functions are not enough to describe the whole p_T spectra. In particular, the maximum p_T reaches up to 100 GeV/c in collisions at the LHC [43]. Then, one needs other functions such as the Tsallis–Lévy- [44, 45] or Tsallis–Pareto-type function [44, 46] and the Hagedorn function [40, 41] or inverse power law [47–49] to the spectra in high- and very high-p_T regions. In this work, the hard component is simply represented by the inverse power law. That is,

$$
f_2(p_T) = \frac{1}{N}\frac{dN}{dp_T} = Ap_T\left(1 + \frac{p_T}{p_0}\right)^{-n},
\tag{2}
$$

where p_0 and n are free parameters and A is the normalization constant which is related to the free parameters.

However, the structure of p_T spectra is very complex. In fact, several regions have been observed and analyzed in Ref. [50]. These regions include the first one with $p_T < 4 - 6$ GeV/c, the second one with $4 - 6$ GeV/$c < p_T < 17 - 20$ GeV/c, and the third one with $p_T > 17 - 20$ GeV/c. Different regions may correspond to different mechanisms. The first p_T region in our discussion is regarded as the region of the soft excitation process, while the second and third p_T regions are regarded as the regions of the hard and the very hard excitation process, respectively. In particular, a special region with $p_T < 0.2 - 0.3$ GeV/c is considered due to the resonant production in some cases, and it is regarded as the region of the very soft excitation process.

Generally, the whole p_T region discussed above can be uniformly superposed by two methods: (i) the general superposition in which the contribution regions of different components overlap each other and (ii) the Hagedorn model (the usual step function) [40] in which there is no overlapping of different regions of different components.

Considering $f_1(p_T)$, $f_2(p_T)$, $f_{VS}(p_T)$, and $f_{VH}(p_T)$ which denote the probability density functions by the soft, hard, very soft, and very hard components, respectively, where

$f_{\mathrm{VS}}(p_{\mathrm{T}})$ and $f_{\mathrm{VH}}(p_{\mathrm{T}})$ are assumed to be in the form of $f_1(p_{\mathrm{T}})$ and $f_2(p_{\mathrm{T}})$, respectively, the unified superposition according to the first method is

$$f_0(p_{\mathrm{T}}) = \frac{1}{N}\frac{dN}{dp_{\mathrm{T}}} = k_{\mathrm{VS}}f_{\mathrm{VS}}(p_{\mathrm{T}}) + kf_1(p_{\mathrm{T}})$$
$$+ (1 - k - k_{\mathrm{VS}} - k_{\mathrm{VH}})f_2(p_{\mathrm{T}}) + k_{\mathrm{VH}}f_{\mathrm{VH}}(p_{\mathrm{T}}), \tag{3}$$

where k_{VS} is the contribution fraction of the very soft component, while k and k_{VH} denote the contributions of the soft and very hard components, respectively.

The step function can be used to structure the superposition according to the Hagedorn model [40]; i.e.,

$$f_0(p_{\mathrm{T}}) = \frac{1}{N}\frac{dN}{dp_{\mathrm{T}}} = A_{\mathrm{VS}}\theta(p_{\mathrm{VS}} - p_{\mathrm{T}})f_{\mathrm{VS}}(p_{\mathrm{T}})$$
$$+ A_1\theta(p_{\mathrm{T}} - p_{\mathrm{VS}})\theta(p_1 - p_{\mathrm{T}})f_1(p_{\mathrm{T}}) \tag{4}$$
$$+ A_2\theta(p_{\mathrm{T}} - p_1)\theta(p_{\mathrm{VH}} - p_{\mathrm{T}})f_2(p_{\mathrm{T}})$$
$$+ A_{\mathrm{VH}}\theta(p_{\mathrm{T}} - p_{\mathrm{VH}})f_{\mathrm{VH}}(p_{\mathrm{T}}),$$

where A_{VS}, A_1, A_2, and A_{VH} are the constants which make the interfacing components link to each other perfectly.

Particularly, if the contributions of the very soft and very hard components can be neglected, Equations (3) and (4) are, respectively, simplified to be

$$f_0(p_{\mathrm{T}}) = \frac{1}{N}\frac{dN}{dp_{\mathrm{T}}} = kf_1(p_{\mathrm{T}}) + (1 - k)f_2(p_{\mathrm{T}}), \tag{5}$$

$$f_0(p_{\mathrm{T}}) = \frac{1}{N}\frac{dN}{dp_{\mathrm{T}}} = A_1\theta(p_1 - p_{\mathrm{T}})f_1(p_{\mathrm{T}}) + A_2\theta(p_{\mathrm{T}} - p_1)f_2(p_{\mathrm{T}}). \tag{6}$$

Further, if the contribution of the hard component at the RHIC-BES energies can be neglected, Equations (5) and (6) are simplified to be the same form:

$$f_0(p_{\mathrm{T}}) = \frac{1}{N}\frac{dN}{dp_{\mathrm{T}}} = f_1(p_{\mathrm{T}}). \tag{7}$$

This work deals with Au-Au collisions at the RHIC-BES energies, for which Equation (7), i.e., Equation (1), is suitable. In the following section, we shall use Equation (1) to fit the experimental data measured by the STAR Collaboration at the RHIC-BES energies [19, 20].

In particular, the mean $p_{\mathrm{T}}(\langle p_{\mathrm{T}}\rangle)$ and the root-mean-square $p_{\mathrm{T}}(\sqrt{\langle p_{\mathrm{T}}^2\rangle})$ can be expressed, respectively, as

$$\langle p_{\mathrm{T}}\rangle = \int_0^{p_{\mathrm{T\,max}}} p_{\mathrm{T}}f_0(p_{\mathrm{T}})dp_{\mathrm{T}}, \tag{8}$$

$$\sqrt{\langle p_{\mathrm{T}}^2\rangle} = \sqrt{\int_0^{p_{\mathrm{T\,max}}} p_{\mathrm{T}}^2 f_0(p_{\mathrm{T}})dp_{\mathrm{T}}}, \tag{9}$$

due to

$$\int_0^{p_{\mathrm{Tmax}}} f_0(p_{\mathrm{T}})dp_{\mathrm{T}} = 1, \tag{10}$$

where p_{Tmax} denotes the maximum p_{T} considered by us. In this work, we take $p_{\mathrm{Tmax}} = 2.5\,\mathrm{GeV}/c$.

It should be noted that although only Equation (1) is used in the analysis, we would like to continue to have the statement and formalism for other functions or distributions such as the inverse power law and its superposition with thermal distribution and the discussions on the very soft, hard, and very hard components. In fact, due to the existence of other functions or distributions, the mentioned method of data-driven reanalysis can be used in the spectra in wide p_{T} coverage, which is not the case in this work. In addition, it is possible to use simultaneously the (very) soft and (very) hard components in other cases which are more universal.

3. Results and Discussion

Figure 1 presents the event centrality-dependent double-differential p_{T} spectra, $(1/2\pi p_{\mathrm{T}})d^2N/dp_{\mathrm{T}}dy$, of π^+, K^+, and p produced in the midrapidity interval $|y| < 0.1$ in Au-Au collisions at the center-of-mass energy per nucleon pair $\sqrt{sNN} = 7.7\,\mathrm{GeV}$ at the RHIC-BES, where y denotes the rapidity. The symbols represent the experimental data measured by the STAR Collaboration [19], and the curves are our fitting results by using the blast-wave model with the Boltzmann-Gibbs statistics, Equation (1) [21–23]. The spectra in centrality classes 0–5%, 5–10%, 10–20%, 20–30%, 30–40%, 40–50%, 50–60%, 60–70%, and 70–80% are scaled by 1, 1/2, 1/4, 1/6, 1/8, 1/10, 1/12, 1/14, and 1/16, respectively. In the fit, the least-square method is used to determine the best values of parameters. The related parameters along with χ^2 and degree of freedom (dof) are listed in Table 1, where the centrality classes are listed together. One can see that Equation (1) fits well the data in Au-Au collisions at 7.7 GeV at the RHIC.

Figure 2 is the same as Figure 1, but it shows the p_{T} spectra at $\sqrt{sNN} = 11.5\,\mathrm{GeV}$. One can see that Equation (1) fits well the data in Au-Au collisions at 11.5 GeV at the RHIC-BES.

Figure 3 is also the same as Figure 1, but it shows the p_{T} spectra at $\sqrt{sNN} = 14.5\,\mathrm{GeV}$, where the data are cited from Ref. [20]. Once again, Equation (1) fits well the data in Au-Au collisions at 14.5 GeV at the RHIC-BES.

Figures 4–6 are also the same as Figure 1, but they show the p_{T} spectra at $\sqrt{sNN = 19.6}$, 27, and 39 GeV, respectively. Once more, Equation (1) fits well the data in Au-Au collisions at other RHIC-BES energies.

It is noteworthy to point out that Equation (1) for the blast-wave model in the system is assumed to be in local thermodynamic equilibrium, and therefore, a single T_0 and β_{T} should be obtained by the weight average of different particle species. To see clearly the trends of weight average parameters, Figures 7(a) and 7(b) show the dependences of weight averages T_0 and β_{T} on $\sqrt{sNN}$ for different event centralities.

(a)   (b)   (c)
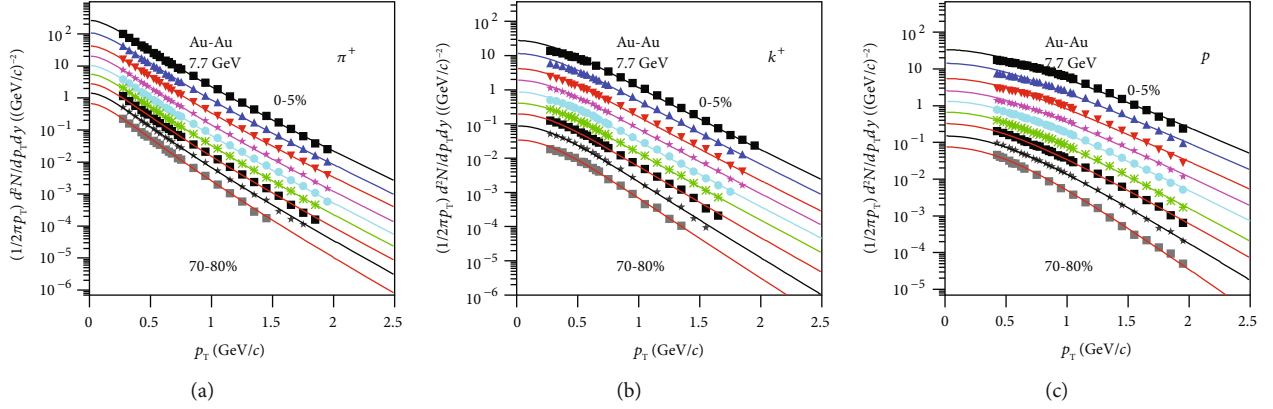
FIGURE 1: Transverse momentum spectra of (a–c) π^+, K^+, and p produced in different centrality bins in Au-Au collisions at $\sqrt{sNN} = 7.7$ GeV. The symbols represent the experimental data measured by the STAR Collaboration in the midrapidity interval $|y| < 0.1$ [19]. The curves are our fitted results by Equation (1).

The symbols represent the parameter values averaged by weighting the yields of different particles which are listed in Table 1. One can see that T_0 and β_T increase with the increase in $\sqrt{sNN}$ from 7.7 to 39 GeV. Meanwhile, T_0 and β_T increase with the increase in the event centrality from the periphery to the center.

In addition, the variation of weight averages T_0 on β_T for different collision energies and event centralities is displayed in Figure 7(c), where the symbols represent the parameter values averaged by weighting the yields of different particles. One can see that T_0 increases with the increase in β_T. At higher energy and in central collisions, one sees larger T_0 and β_T. There is a positive correlation between T_0 and β_T.

The dependences of mean transverse momentum ($\langle p_T \rangle$) and initial temperature (T_i) on $\sqrt{sNN}$ for different event centralities obtained by weighting the yields of different particles are shown in Figures 8(a) and 8(b), respectively, where $T_i = \sqrt{\langle p_T^2 \rangle / 2}$ according to the color string percolation model [51–53]. One can see that $\langle p_T \rangle$ and T_i increase with the increase in $\sqrt{sNN}$ from 7.7 to 39 GeV. Meanwhile, $\langle p_T \rangle$ and T_i increase with the increase in event centrality from the periphery to the center.

We notice that $T_i = 0.28 - 0.38$ GeV which is quite high for the considered collision energies. Because we obtain T_i from the spectra of particles with nonzero masses, it is possible to have a high value. If we obtain T_i from the spectra of photons, the value will be small. High T_i renders that the excitation degree of the emission source at the stage of the initial state is high. Meanwhile, one of the key issues is whether the transverse flow should be also considered at the initial stage. Naturally, after considering the transverse flow at the initial stage, T_i will be small. It is regretful that we have no clear idea on the extraction of transverse flow at the initial stage. As an alternative method, if we redefine $T_i = k_0 \sqrt{\langle p_T^2 \rangle / 2}$ as the initial temperature and $\beta_{Ti} = (1 - k_0) \sqrt{\langle p_T^2 \rangle / 2}$ as the initial transverse flow velocity, where $0 < k_0 < 1$ is to be determined, we may obtain a small T_i and a nonzero β_{Ti}.

The reason for the increase in T_0 and β_T with the increase in collision energy is due to the fact that more energies are deposited in collisions at higher energy in the considered RHIC-BES energy range. Meanwhile, the system size at higher energy decreases due to a relativistic constriction effect, which results in a smaller volume and then a larger energy density and larger T_0. Meanwhile, at higher energy, the squeeze is more violent, which results in a rapider expansion and larger β_T.

The reason for the increase in T_0 and β_T with the increase in event centrality is due to the fact that the central collisions contain more nucleons than the peripheral collisions; then, more energies are deposited in central collisions. Meanwhile, a rapider expansion appears due to more violent squeeze in central collisions, compared to peripheral collisions. As a result, both T_0 and β_T in central collisions are larger than those in peripheral collisions.

Because of $\langle p_T \rangle$ and T_i being positive correlation with T_0 and β_T, with increasing collision energy and event centrality, the increasing trend of T_0 and β_T results naturally in the increasing trend of $\langle p_T \rangle$ and T_i. This work shows that the two free parameters T_0 and β_T and the two derived parameters $\langle p_T \rangle$ and T_i appear to be similar law on the dependences of collision energy and event centrality. In particular, $\langle p_T \rangle$ and T_i are model-independent, though we obtain them from model-dependent free parameters T_0 and β_T in this work. In fact, $\langle p_T \rangle$ and T_i can be obtained by the p_T data themselves if the data are across the possible p_T range.

It seems that there are nonmonotonous changes at 11.5 GeV in the excitation functions of β_T, $\langle p_T \rangle$, and T_i in the most central Au-Au collisions. These nonmonotonous changes reflect the minimum or maximum point of equation of state (EoS) of the matter formed in collisions. At a few GeV to about 10 GeV, the matter formed in collisions is baryon-dominant. At above 10 GeV, the matter formed in collisions is meson-dominant. At around 10 GeV, the baryon number density is the largest [54] due to the competition between projectile/target penetrating/stopping and longitudinal contraction.

TABLE 1: Values of free parameters (T_0 and β_T), normalization constant (N_0), χ^2, and dof corresponding to the curves in Figures 1–6.

Figure	Particle	Centrality	T_0	β_T	N_0	χ^2	dof
	π^+	0–5%	0.130 ± 0.004	0.306 ± 0.006	15.00 ± 1.00	17	26
		5–10%	0.129 ± 0.005	0.305 ± 0.005	6.02 ± 0.9	14	26
		10–20%	0.128 ± 0.004	0.303 ± 0.007	2.35 ± 1.05	20	26
		20–30%	0.126 ± 0.005	0.302 ± 0.006	1.09 ± 0.60	18	26
		30–40%	0.124 ± 0.004	0.300 ± 0.006	0.54 ± 0.43	19	23
		40–50%	0.122 ± 0.003	0.297 ± 0.007	0.28 ± 0.02	13	23
		50–60%	0.120 ± 0.004	0.292 ± 0.004	0.14 ± 0.02	20	22
		60–70%	0.118 ± 0.004	0.280 ± 0.005	0.067 ± 0.001	16	21
		70–80%	0.115 ± 0.005	0.269 ± 0.007	0.030 ± 0.008	11	18
	K^+	0–5%	0.133 ± 0.005	0.305 ± 0.005	3.65 ± 0.20	99	20
		5–10%	0.131 ± 0.004	0.304 ± 0.005	1.50 ± 0.15	76	22
		10–20%	0.130 ± 0.004	0.302 ± 0.007	0.53 ± 0.05	55	22
		20–30%	0.128 ± 0.005	0.301 ± 0.007	0.24 ± 0.17	27	22
Figure 1		30–40%	0.127 ± 0.004	0.299 ± 0.009	0.11 ± 0.01	27	21
Au-Au		40–50%	0.125 ± 0.006	0.296 ± 0.008	0.050 ± 0.002	16	20
7.7 GeV		50–60%	0.123 ± 0.005	0.278 ± 0.007	0.23 ± 0.02	34	19
		60–70%	0.118 ± 0.004	0.265 ± 0.008	0.0093 ± 0.0007	34	18
		70–80%	0.116 ± 0.004	0.250 ± 0.008	0.0034 ± 0.0003	29	15
	p	0–5%	0.134 ± 0.004	0.340 ± 0.005	9.31 ± 0.60	54	29
		5–10%	0.133 ± 0.005	0.328 ± 0.006	3.90 ± 0.15	47	29
		10–20%	0.132 ± 0.006	0.318 ± 0.008	1.50 ± 0.20	46	29
		20–30%	0.130 ± 0.005	0.310 ± 0.008	0.65 ± 0.05	28	29
		30–40%	0.128 ± 0.004	0.301 ± 0.006	0.32 ± 0.04	14	25
		40–50%	0.126 ± 0.005	0.280 ± 0.007	0.15 ± 0.03	13	25
		50–60%	0.124 ± 0.004	0.271 ± 0.006	0.070 ± 0.008	7	24
		60–70%	0.122 ± 0.003	0.250 ± 0.005	0.030 ± 0.004	8	25
		70–80%	0.120 ± 0.006	0.204 ± 0.009	0.013 ± 0.001	14	18
	π^+	0–5%	0.132 ± 0.004	0.315 ± 0.005	19.11 ± 1.60	5	26
		5–10%	0.130 ± 0.005	0.313 ± 0.005	7.60 ± 1.40	16	26
		10–20%	0.129 ± 0.004	0.312 ± 0.006	2.90 ± 0.50	14	26
		20–30%	0.128 ± 0.003	0.311 ± 0.007	1.36 ± 0.10	34	26
		30–40%	0.127 ± 0.003	0.310 ± 0.008	0.38 ± 0.05	15	26
		40–50%	0.126 ± 0.006	0.307 ± 0.007	0.34 ± 0.03	16	26
		50–60%	0.124 ± 0.004	0.305 ± 0.005	0.16 ± 0.01	7	23
Figure 2		60–70%	0.121 ± 0.004	0.296 ± 0.006	0.080 ± 0.007	6	21
Au-Au		70–80%	0.119 ± 0.005	0.288 ± 0.008	0.040 ± 0.005	10	21
11.5 GeV	K^+	0–5%	0.135 ± 0.005	0.314 ± 0.009	4.23 ± 0.30	64	22
		5–10%	0.133 ± 0.004	0.312 ± 0.008	1.72 ± 0.10	62	23
		10–20%	0.132 ± 0.006	0.310 ± 0.010	0.60 ± 0.05	46	23
		20–30%	0.130 ± 0.003	0.308 ± 0.004	0.27 ± 0.02	45	23
		30–40%	0.129 ± 0.004	0.307 ± 0.006	0.13 ± 0.01	59	23
		40–50%	0.128 ± 0.005	0.306 ± 0.007	0.060 ± 0.006	11	23
		50–60%	0.126 ± 0.004	0.300 ± 0.006	0.026 ± 0.002	15	22

TABLE 1: Continued.

Figure	Particle	Centrality	T_0	β_{T}	N_0	χ^2	dof
		60–70%	0.124 ± 0.003	0.288 ± 0.005	0.011 ± 0.001	6	20
		70–80%	0.122 ± 0.004	0.264 ± 0.011	0.0050 ± 0.0003	26	19
	p	0–5%	0.136 ± 0.005	0.323 ± 0.007	7.74 ± 1.00	55	25
		5–10%	0.135 ± 0.005	0.321 ± 0.007	2.90 ± 0.25	56	26
		10–20%	0.134 ± 0.005	0.318 ± 0.006	1.12 ± 0.15	40	26
		20–30%	0.132 ± 0.004	0.311 ± 0.007	0.50 ± 0.03	24	26
		30–40%	0.130 ± 0.005	0.308 ± 0.007	0.24 ± 0.01	13	26
		40–50%	0.128 ± 0.003	0.285 ± 0.006	0.12 ± 0.01	10	25
		50–60%	0.125 ± 0.004	0.274 ± 0.008	0.55 ± 0.01	13	25
		60–70%	0.123 ± 0.00414	0.251 ± 0.006	0.024 ± 0.004	7	25
		70–80%	0.121 ± 0.004	0.231 ± 0.007	0.010 ± 0.003	23	26
	π^+	0–5%	0.135 ± 0.003	0.320 ± 0.005	22.14 ± 2.00	4	25
		5–10%	0.133 ± 0.003	0.318 ± 0.006	8.50 ± 2.00	10	25
		10–20%	0.132 ± 0.004	0.317 ± 0.006	3.50 ± 0.25	12	25
		20–30%	0.131 ± 0.004	0.315 ± 0.005	1.60 ± 0.13	15	25
		30–40%	0.130 ± 0.004	0.314 ± 0.007	0.80 ± 0.06	10	25
		40–50%	0.128 ± 0.004	0.311 ± 0.006	0.40 ± 0.03	16	25
		50–60%	0.126 ± 0.004	0.307 ± 0.007	0.19 ± 0.02	7	25
		60–70%	0.124 ± 0.004	0.299 ± 0.007	0.093 ± 0.014	8	25
		70–80%	0.120 ± 0.005	0.291 ± 0.005	0.040 ± 0.006	14	25
	K^+	0–5%	0.137 ± 0.005	0.318 ± 0.007	4.36 ± 0.40	16	23
		5–10%	0.136 ± 0.004	0.314 ± 0.008	1.86 ± 0.20	8	23
		10–20%	0.135 ± 0.005	0.313 ± 0.008	0.70 ± 0.08	21	23
Figure 3		20–30%	0.134 ± 0.004	0.312 ± 0.006	0.31 ± 0.03	15	23
Au-Au		30–40%	0.132 ± 0.004	0.310 ± 0.009	0.14 ± 0.01	9	23
14.5 GeV		40–50%	0.130 ± 0.003	0.308 ± 0.008	0.067 ± 0.006	7	21
		50–60%	0.128 ± 0.006	0.305 ± 0.010	0.025 ± 0.003	9	21
		60–70%	0.127 ± 0.004	0.294 ± 0.007	0.012 ± 0.001	3	19
		70–80%	0.125 ± 0.005	0.267 ± 0.008	0.0060 ± 0.0006	4	17
	p	0–5%	0.139 ± 0.005	0.335 ± 0.009	6.47 ± 0.70	22	23
		5–10%	0.137 ± 0.004	0.328 ± 0.008	2.90 ± 0.30	20	23
		10–20%	0.135 ± 0.003	0.326 ± 0.008	1.03 ± 0.12	18	23
		20–30%	0.134 ± 0.004	0.323 ± 0.007	0.46 ± 0.07	15	23
		30–40%	0.132 ± 0.004	0.315 ± 0.008	0.21 ± 0.03	12	23
		40–50%	0.130 ± 0.005	0.311 ± 0.007	0.096 ± 0.012	11	23
		50–60%	0.128 ± 0.005	0.294 ± 0.005	0.042 ± 0.007	13	23
		60–70%	0.126 ± 0.005	0.270 ± 0.008	0.018 ± 0.004	18	23
		70–80%	0.123 ± 0.004	0.236 ± 0.007	0.0080 ± 0.0019	26	23
	π^+	0–5%	0.138 ± 0.004	0.322 ± 0.004	24.14 ± 2.00	9	23
Figure 4		5–10%	0.137 ± 0.004	0.321 ± 0.005	9.50 ± 0.80	6	23
Au-Au		10–20%	0.135 ± 0.005	0.319 ± 0.008	3.75 ± 0.25	7	23
19.6 GeV		20–30%	0.134 ± 0.004	0.317 ± 0.005	1.97 ± 0.16	12	23
		30–40%	0.132 ± 0.003	0.315 ± 0.005	0.87 ± 0.06	18	23

Table 1: Continued.

Figure	Particle	Centrality	T_0	β_T	N_0	χ^2	dof
		40–50%	0.130 ± 0.004	0.312 ± 0.006	0.43 ± 0.04	20	23
		50–60%	0.129 ± 0.005	0.311 ± 0.008	0.22 ± 0.02	16	23
		60–70%	0.128 ± 0.004	0.308 ± 0.008	0.10 ± 0.01	16	23
		70–80%	0.125 ± 0.005	0.303 ± 0.009	0.048 ± 0.004	14	23
	K^+	0–5%	0.140 ± 0.003	0.320 ± 0.007	4.98 ± 0.30	24	23
		5–10%	0.138 ± 0.005	0.319 ± 0.009	2.00 ± 0.20	33	23
		10–20%	0.136 ± 0.005	0.318 ± 0.007	0.75 ± 0.05	33	23
		20–30%	0.135 ± 0.005	0.314 ± 0.007	0.34 ± 0.02	21	23
		30–40%	0.133 ± 0.004	0.311 ± 0.007	0.16 ± 0.03	12	23
		40–50%	0.130 ± 0.005	0.309 ± 0.009	0.075 ± 0.005	15	22
		50–60%	0.129 ± 0.004	0.307 ± 0.008	0.036 ± 0.005	8	22
		60–70%	0.128 ± 0.006	0.300 ± 0.010	0.016 ± 0.001	23	20
		70–80%	0.126 ± 0.004	0.294 ± 0.009	0.0070 ± 0.0003	25	19
	p	0–5%	0.142 ± 0.005	0.338 ± 0.006	5.84 ± 0.70	41	26
		5–10%	0.140 ± 0.006	0.336 ± 0.008	2.40 ± 0.30	28	22
		10–20%	0.138 ± 0.005	0.334 ± 0.005	0.91 ± 0.12	19	20
		20–30%	0.136 ± 0.005	0.324 ± 0.007	0.37 ± 0.06	41	20
		30–40%	0.133 ± 0.004	0.316 ± 0.005	0.18 ± 0.03	20	20
		40–50%	0.131 ± 0.006	0.312 ± 0.008	0.090 ± 0.016	8	20
		50–60%	0.129 ± 0.005	0.295 ± 0.009	0.042 ± 0.007	14	20
		60–70%	0.128 ± 0.004	0.275 ± 0.008	0.019 ± 0.003	2	20
		70–80%	0.125 ± 0.004	0.237 ± 0.007	0.0080 ± 0.0013	11	20
	π^+	0–5%	0.139 ± 0.004	0.326 ± 0.006	26.14 ± 1.80	5	23
		5–10%	0.138 ± 0.004	0.324 ± 0.008	11.07 ± 2.00	8	23
		10–20%	0.136 ± 0.005	0.323 ± 0.004	4.25 ± 0.25	10	23
		20–30%	0.135 ± 0.004	0.322 ± 0.004	1.90 ± 0.15	14	23
		30–40%	0.133 ± 0.003	0.321 ± 0.004	0.98 ± 0.10	23	23
		40–50%	0.131 ± 0.004	0.320 ± 0.006	0.50 ± 0.03	26	23
		50–60%	0.130 ± 0.005	0.318 ± 0.005	0.23 ± 0.03	19	23
		60–70%	0.129 ± 0.005	0.317 ± 0.009	0.11 ± 0.01	21	23
		70–80%	0.128 ± 0.004	0.315 ± 0.005	0.048 ± 0.005	19	23
Figure 5 Au-Au 27 GeV	K^+	0–5%	0.142 ± 0.005	0.324 ± 0.008	5.11 ± 0.60	53	23
		5–10%	0.140 ± 0.005	0.322 ± 0.007	2.15 ± 0.20	52	23
		10–20%	0.139 ± 0.003	0.321 ± 0.008	0.82 ± 0.10	55	23
		20–30%	0.137 ± 0.006	0.321 ± 0.005	0.37 ± 0.03	43	23
		30–40%	0.136 ± 0.004	0.320 ± 0.007	0.18 ± 0.01	25	23
		40–50%	0.134 ± 0.004	0.318 ± 0.008	0.86 ± 0.01	9	23
		50–60%	0.132 ± 0.005	0.316 ± 0.005	0.040 ± 0.005	8	23
		60–70%	0.130 ± 0.004	0.311 ± 0.006	0.014 ± 0.003	12	23
		70–80%	0.128 ± 0.004	0.304 ± 0.007	0.0070 ± 0.0004	27	23
	p	0–5%	0.144 ± 0.004	0.343 ± 0.007	5.31 ± 0.40	34	20
		5–10%	0.143 ± 0.004	0.341 ± 0.007	2.20 ± 0.22	27	20
		10–20%	0.141 ± 0.005	0.336 ± 0.007	0.84 ± 0.09	21	20

TABLE 1: Continued.

Figure	Particle	Centrality	T_0	β_T	N_0	χ^2	dof
		20–30%	0.139 ± 0.005	0.330 ± 0.006	0.37 ± 0.05	15	20
		30–40%	0.137 ± 0.005	0.326 ± 0.008	0.18 ± 0.03	9	20
		40–50%	0.134 ± 0.005	0.318 ± 0.005	0.090 ± 0.016	8	20
		50–60%	0.131 ± 0.004	0.300 ± 0.008	0.042 ± 0.005	3	20
		60–70%	0.129 ± 0.004	0.280 ± 0.005	0.019 ± 0.002	6	20
		70–80%	0.126 ± 0.004	0.257 ± 0.007	0.0070 ± 0.0003	9	20
	π^+	0–5%	0.141 ± 0.004	0.330 ± 0.007	27.84 ± 2.30	7	23
		5–10%	0.139 ± 0.005	0.328 ± 0.007	11.60 ± 0.70	14	23
		10–20%	0.138 ± 0.004	0.326 ± 0.006	4.50 ± 0.30	23	23
		20–30%	0.136 ± 0.004	0.325 ± 0.005	2.12 ± 0.10	38	23
		30–40%	0.135 ± 0.003	0.324 ± 0.008	1.05 ± 0.08	42	23
		40–50%	0.135 ± 0.005	0.322 ± 0.005	0.52 ± 0.02	36	23
		50–60%	0.134 ± 0.004	0.321 ± 0.008	0.27 ± 0.02	39	23
		60–70%	0.132 ± 0.004	0.320 ± 0.007	0.12 ± 0.01	36	23
		70–80%	0.130 ± 0.005	0.319 ± 0.008	0.062 ± 0.005	51	23
	K^+	0–5%	0.148 ± 0.004	0.328 ± 0.005	5.29 ± 0.40	35	23
		5–10%	0.147 ± 0.004	0.327 ± 0.006	2.30 ± 0.15	15	23
		10–20%	0.146 ± 0.005	0.328 ± 0.005	0.90 ± 0.08	29	23
Figure 6		20–30%	0.145 ± 0.006	0.324 ± 0.009	0.40 ± 0.03	19	23
Au-Au		30–40%	0.144 ± 0.005	0.323 ± 0.008	0.19 ± 0.01	12	23
39 GeV		40–50%	0.143 ± 0.005	0.321 ± 0.006	0.090 ± 0.010	10	23
		50–60%	0.142 ± 0.003	0.317 ± 0.006	0.0040 ± 0.0004	12	23
		60–70%	0.140 ± 0.004	0.316 ± 0.005	0.019 ± 0.001	15	23
		70–80%	0.138 ± 0.005	0.313 ± 0.008	0.0083 ± 0.0003	18	23
	p	0–5%	0.149 ± 0.005	0.359 ± 0.008	4.38 ± 0.50	34	19
		5–10%	0.148 ± 0.004	0.348 ± 0.006	1.94 ± 0.30	36	19
		10–20%	0.146 ± 0.005	0.346 ± 0.006	0.80 ± 0.12	22	19
		20–30%	0.145 ± 0.004	0.340 ± 0.007	0.33 ± 0.05	16	19
		30–40%	0.144 ± 0.004	0.335 ± 0.005	0.16 ± 0.03	8	19
		40–50%	0.144 ± 0.004	0.330 ± 0.006	0.078 ± 0.014	13	19
		50–60%	0.143 ± 0.004	0.300 ± 0.006	0.040 ± 0.005	1	19
		60–70%	0.139 ± 0.004	0.281 ± 0.005	0.017 ± 0.002	4	19
		70–80%	0.127 ± 0.004	0.274 ± 0.007	0.0080 ± 0.0006	10	19

It is hard to say whether the minimum or maximum point of EoS of the matter formed in the most central Au-Au collisions at 11.5 GeV is related to the search for the QCD critical end point (CEP) which is the main objective of the BES program performed by the STAR Collaboration. Generally, large nonmonotonous changes or saturations or a slight increase should appear in the excitation functions of some quantities at the critical energy which is the energy corresponding to the CEP. The excitation functions considered in this paper change slightly. Although there is no value in the energy range of less than 7.7 GeV, it is expected that the excitation function increases quickly in the energy range of a

few GeV while the onset stage of a slight increase appears at around 10 GeV in the excitation functions of $\langle p_T \rangle$ and T_i.

It should be noted that there is entanglement in the extraction of T_0 and β_T. In fact, if one uses smaller T_0 and larger β_T for central collisions, a decreasing trend for T_0 from peripheral to central collisions can be obtained. Meanwhile, a negative correlation between T_0 and β_T can also be obtained. Thus, this situation is in agreement with some current references [19, 55, 56]. If one even uses almost invariant or slightly larger T_0 and properly larger β_T for central collisions, an almost invariant or slightly increased trend for T_0 from peripheral to central collisions can be obtained [57]. To show
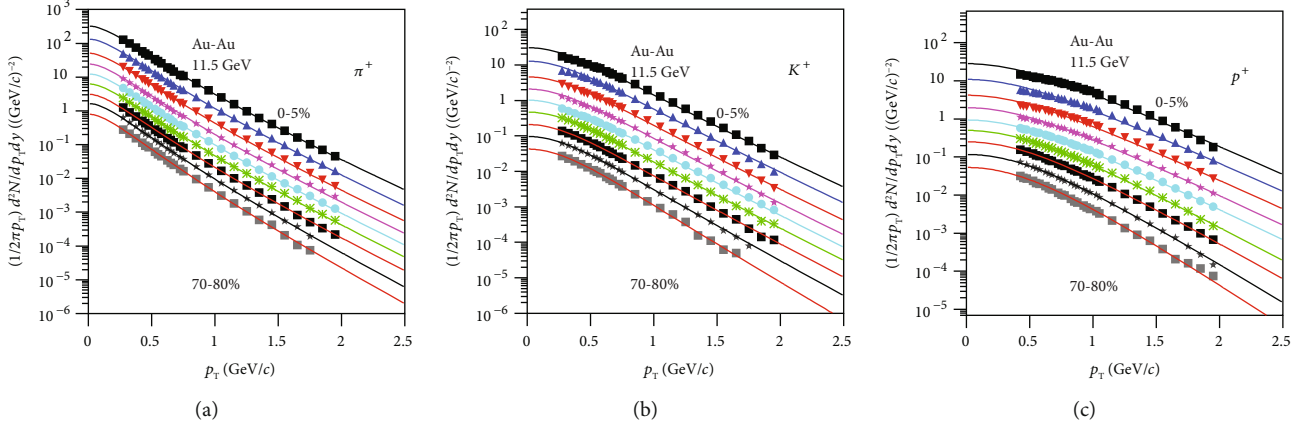
FIGURE 2: The same as Figure 1, but showing the results at $\sqrt{sNN} = 11.5$ GeV.
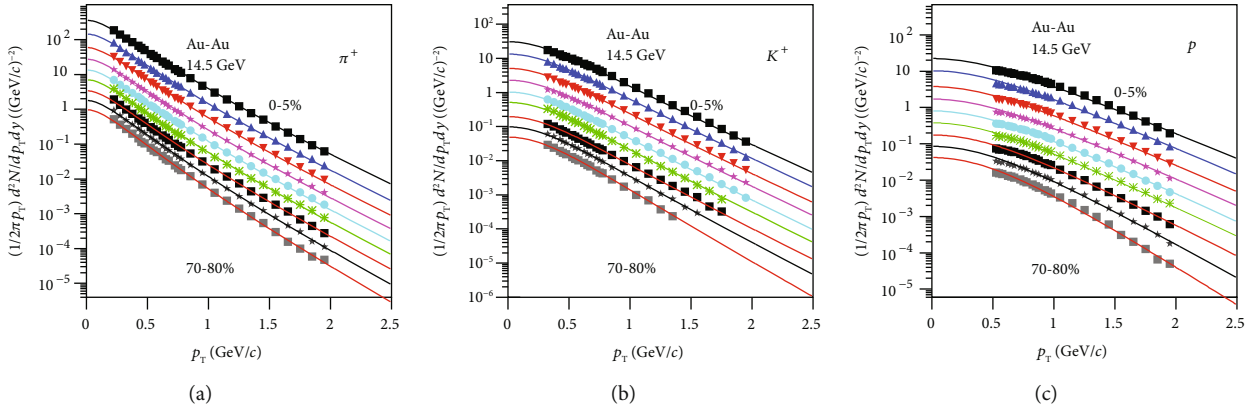
FIGURE 3: The same as Figure 1, but showing the results at $\sqrt{sNN} = 14.5$ GeV, where the data are cited from Ref. [20].
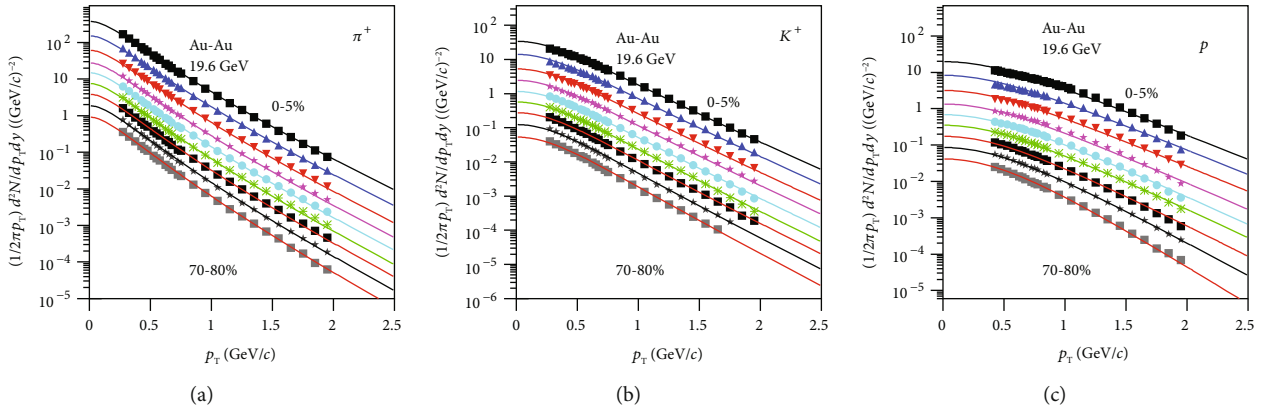
FIGURE 4: The same as Figure 1, but showing the results at $\sqrt{sNN} = 19.6$ GeV.

the flexibility in the extraction of T_0 and β_T, this work has reported an increasing trend for T_0 from peripheral to central collisions and a positive correlation between T_0 and β_T.

In addition, we have taken $n_0 = 2$ in this work, which closely resembles the hydrodynamic profile as mentioned in Ref. [21]. Although Ref. [58] shows that $n_0 = 1$ is the closest approximation to hydrodynamics at freeze-out, Ref. [36]

shows that $n_0 = 2$ or 1 does not affect obviously the fit curve and free parameters T_0 and β_T. If we consider that $\beta(r)$ decays quickly from the surface to the center of the emission source, we are inclined to use $n_0 = 2$. Anyhow, we are not inclined to regard n_0 as a free parameter which is too mutable and debatable in our opinion. In current analysis with the blast-wave model [22], not only is n_0 mutable (from $0.0 \pm$
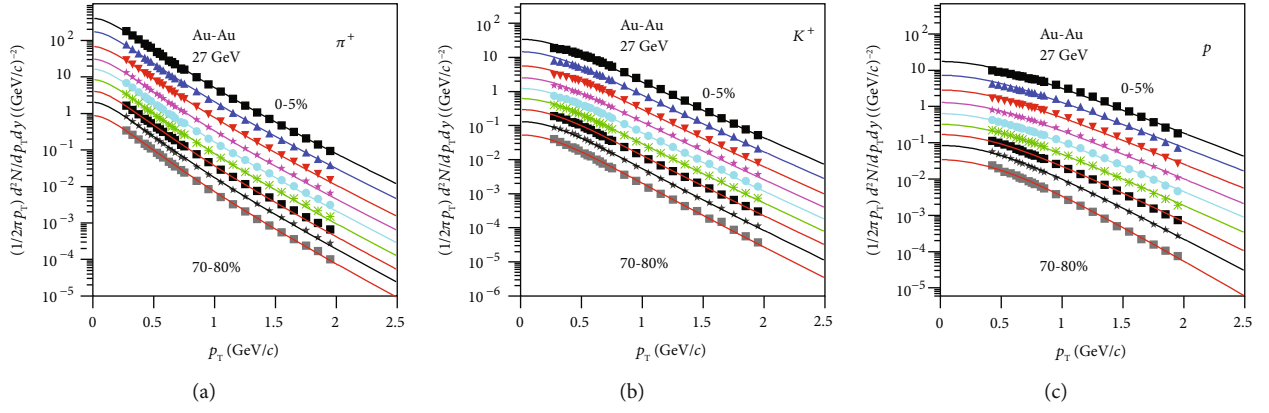
FIGURE 5: The same as Figure 1, but showing the results at $\sqrt{sNN} = 27$ GeV.
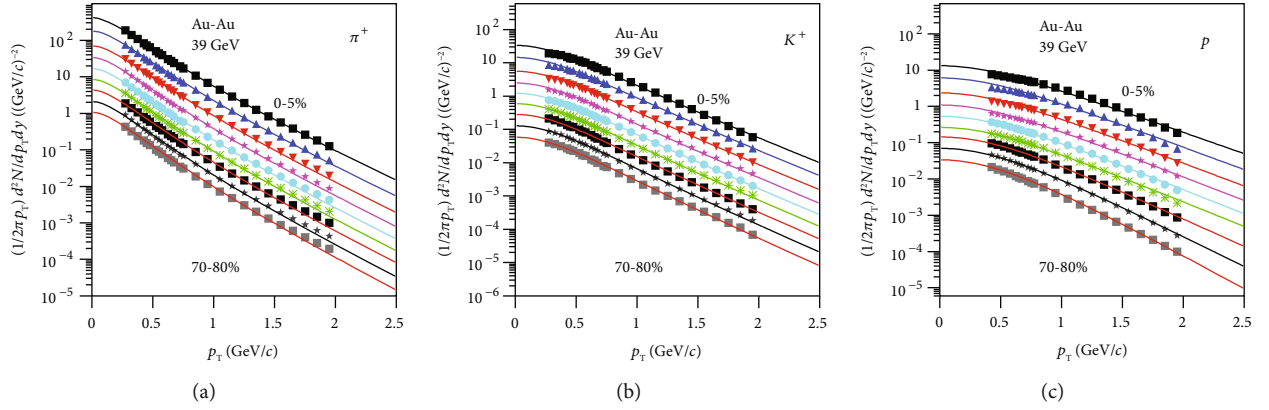
FIGURE 6: The same as Figure 1, but showing the results at $\sqrt{sNN} = 39$ GeV.
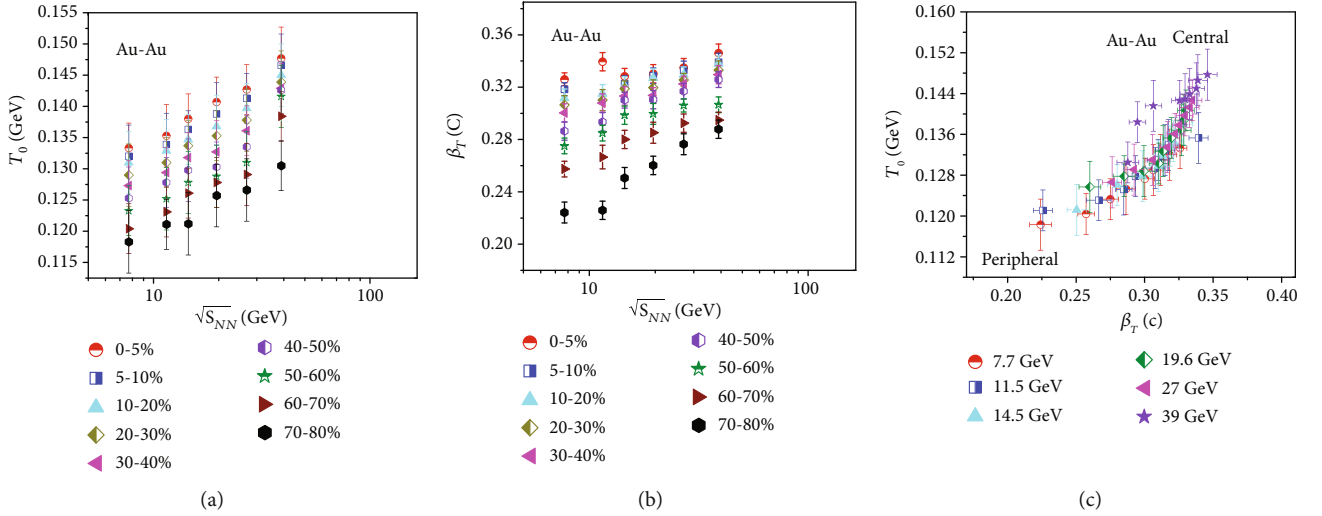
FIGURE 7: Dependences of weighted averages (a) T_0 and (b) β_T on $\sqrt{sNN}$ for different event centralities as well as (c) T_0 on β_T for different collision energies and event centralities. The different symbols display different centrality classes in (a) and (b) or different collision energies in (c), which are averaged by weighting the yields of different particles which are listed in Table 1.
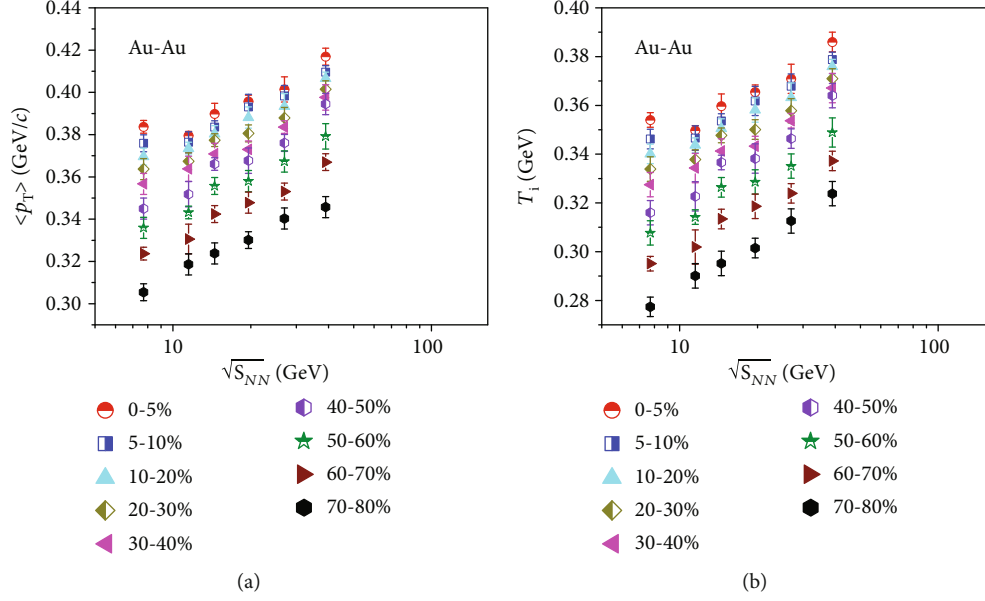
FIGURE 8: Dependences of weighted averages (a) $\langle p_T \rangle$ and (b) T_i on $\sqrt{sNN}$ for different event centralities. The different symbols display different centrality classes, which are averaged by weighting the yields of different particles which are listed in Table 1.

10.1 to 4.3 ± 1.7) but also the p_T coverage is narrow and particle-dependent ($p_T \approx 0.20 - 0.70 \, \text{GeV}/c$ for π^+, $0.25 - 0.75 \, \text{GeV}/c$ for K^+, and $0.35 - 1.15 \, \text{GeV}/c$ for p), which uses a single kinetic freeze-out scenario and results in different trends of T_0 versus β_T from this work. If we also regard n_0 as a free parameter and use narrow and particle-dependent p_T coverage, consistent result with current analysis [22] can be naturally obtained by us.

Indeed, there are too much uncertainties arising from the choice of fit function and flow profile and from the well-known ambiguity in the fit results—in a single p_T spectrum, it is always possible to trade β_T against T_0. That is, T_0 and β_T is negatively correlative for a given p_T spectrum. It is possible that we may use suitable T_0 and β_T for a set of p_T spectra and obtain a positive or negative correlation. In a positive correlation, decreasing T_0 and increasing β_T will result in a negative correlation. Contrarily, in a negative correlation, increasing T_0 and decreasing β_T will result in a positive correlation. Indeed, there is an influence if we use a changeable p_T coverage and/or n_0 choice on the extraction of the two free parameters. In our opinion, to reduce the uncertainties, one should use a fixed flow profile (n_0) and wide and fixed p_T coverage for different particles. In fact, we have used $n_0 = 2$ and $p_T < 2.5 \, \text{GeV}/c$ for different particles in this work and used a multiple freeze-out scenario such as that used in Ref. [59].

Our result (Table 1) shows that the heavier the particle is, the higher T_0 and the smaller β_T correspond. This result is in agreement with the hydrodynamic-type behavior [4]. The final T_0 and β_T are averaged by weighting different particle yields, which shows a positive correlation between T_0 and β_T (Figure 7). Our result is in agreement with the alternative method [36, 37] in which T_0 is regarded as the intercept in the linear relation of T versus m_0 and β_T is regarded as the slope in the linear relation of $\langle p_T \rangle$ versus $m_0 \bar{\gamma}$, where $\bar{\gamma}$ is

the mean Lorentz factor in the source rest frame. Our result is also in agreement with a very recent work [60] which uses the same method as ours. If the negative correlation can be explained as the result of a longer lifetime (lower excitation degree) which corresponds to lower T_0 and a quicker expansion (stronger squeeze) which corresponds to larger β_T, the positive correlation can be explained as the result of a high excitation degree which corresponds to high T_0 and quick expansion (strong squeeze) which corresponds to large β_T.

This whole phenomenal analysis results in degrees of thermal motion and collective expansion that are reflected by T_0 and β_T, respectively. With the increasing collision energy, the system may undergo different evolution processes. In the considered RHIC-BES energy range, the violent degree of collisions increases with increasing collision energy. The trends of T_0 and β_T show approximately monotonous increase in which large fluctuation does not appear, though there are nonmonotonous changes at 11.5 GeV in some cases. The evolution processes at the considered six energies show similar behaviors to each other.

4. Conclusions

The main observations and conclusions are summarized as follows.

(a) By using the method of data-driven reanalysis, the blast-wave model with the Boltzmann-Gibbs statistics is used to analyze the collision energy-dependent and event centrality-dependent double-differential transverse momentum spectra of charged particles (π^+, K^+, and p) produced in the midrapidity interval in Au-Au collisions at the RHIC-BES energies. The contribution of soft excitation is considered in this

work, but the contribution of the hard process is not excluded if available

(b) As the free parameters, the kinetic freeze-out temperature T_0 and transverse flow velocity β_T are extracted with the blast-wave model. Both T_0 and β_T increase with the increase in collision energy due to more violent collisions at higher energy. The two parameters also increase with the increase in event centrality, as the central collisions contain more nucleons which means more energy deposited and more violent collisions and squeeze, compared with peripheral collisions

(c) As the derived parameters, the mean transverse momentum $\langle p_T \rangle$ and initial temperature T_i appear to be similar law to the free parameters T_0 and β_T when we study the dependences of parameters on collision energy and event centrality. Although T_0 and β_T are model-dependent, $\langle p_T \rangle$ and T_i are generally model-independent. There is no large fluctuation in the excitation function of the considered parameters at the RHIC-BES, which means a similar collision mechanism

Data Availability

The data used to support the findings of this study are included within the article and are cited at relevant places within the text as references.

Ethical Approval

The authors declare that they are in compliance with ethical standards regarding the content of this paper.

Disclosure

The funding agencies have no role in the design of the study; in the collection, analysis, or interpretation of the data; in the writing of the manuscript; or in the decision to publish the results.

Conflicts of Interest

The authors declare that there are no conflicts of interest regarding the publication of this paper.

Acknowledgments

References

[1] S. Mukherjee and V. Skokov, "Universality driven analytic structure of QCD crossover: radius of convergence in baryon chemical potential," https://arxiv.org/abs/1909.04639.

[2] W.-J. Fu, J. M. Pawlowski, and F. Rennecke, "The QCD phase structure at finite temperature and density," https://arxiv.org/abs/1909.02991.

[3] G.-Y. Shao, W.-B. He, and X.-Y. Gao, "Deformed QCD phase structure and entropy oscillation in the presence of a magnetic background," *Physical Review D*, vol. 100, no. 1, article 014020, 2019.

[4] R. Sahoo, "Possible formation of QGP-droplets in proton-proton collisions at the CERN Large Hadron Collider," *AAPPS Bulletin*, vol. 29, no. 4, 2019.

[5] M. Gyulassy and L. McLerran, "New forms of QCD matter discovered at RHIC," *Nuclear Physics A*, vol. 750, no. 1, pp. 30–63, 2005.

[6] M. T. AlFiky, O. T. ElSherif, and A. M. Hamed, "Quark gluon plasma formation in proton-proton collisions using PYTHIA," https://arxiv.org/abs/1902.05114.

[7] F. Rennecke, W.-J. Fu, and J. M. Pawlowski, "Strangeness neutrality and the QCD phase diagram," https://arxiv.org/abs/1907.08179.

[8] A. Andronic, P. Braun-Munzinger, and J. Stachel, "Hadron production in central nucleus–nucleus collisions at chemical freeze-out," *Nuclear Physics A*, vol. 772, no. 3-4, pp. 167–199, 2006.

[9] G. Inghirami, P. Hillmann, B. Tomášik, and M. Bleicher, "Temperatures and chemical potentials at kinetic freeze-out in relativistic heavy ion collisions from coarse grained transport simulations," https://arxiv.org/abs/1909.00643.

[10] C. Yang, "The STAR detector upgrades and physics in beam energy scan phase II," *EPJ Web of Conferences*, vol. 182, article 02130, p. 02130, 2018.

[11] K. C. Meehan, "Fixed target collisions at STAR," *Nuclear Physics A*, vol. 956, pp. 878–881, 2016.

[12] X. Sun and the STAR Collaboration, "Flow in the RHIC Beam Energy Scan from STAR," *Journal of Physics: Conference Series*, vol. 535, article 012005, 2014.

[13] K. C. Meehan, "The fixed-target experiment at STAR," *Journal of Physics: Conference Series*, vol. 742, article 012022, 2016.

[14] T. Ablyazimov, A. Abuhoza, R. P. Adak et al., "Challenges in QCD matter physics – the scientific programme of the Compressed Baryonic Matter experiment at FAIR," *The European Physical Journal A*, vol. 53, p. 60, 2017.

[15] J. Chen, D. Keane, Y. G. Ma, A. Tang, and Z. Xu, "Antinuclei in heavy-ion collisions," *Physics Reports*, vol. 760, pp. 1–39, 2018.

[16] N. Xu, "An overview of STAR experimental results," *Nuclear Physics A*, vol. 931, pp. 1–12, 2014.

[17] S. Chatterjee, S. Das, L. Kumar et al., "Freeze-out parameters in heavy-ion collisions at AGS, SPS, RHIC, and LHC energies," *Advances in High Energy Physics*, vol. 2015, Article ID 349013, 20 pages, 2015.

[18] S. Uddin, I. Bashir, and R. A. Bhat, "Transverse momentum distributions of hadrons produced in Pb-Pb collisions at LHC energy $\sqrt{s_{NN}} = 2.76$ TeV," *Advances in High Energy Physics*, vol. 2015, Article ID 154853, 7 pages, 2015.

[19] L. Adamczyk, J. K. Adkins, G. Agakishiev et al., "Bulk properties of the medium produced in relativistic heavy-ion collisions

from the Beam Energy Scan program," *Physical Review C*, vol. 96, no. 4, article 044904, 2017.

[20] V. Bairathi, "Study of the bulk properties of the system formed in Au + Au collisions at $\sqrt{s_{NN}}$ = 14.5 GeV using the STAR detector at RHIC," *Nuclear Physics A*, vol. 956, pp. 292–295, 2016.

[21] E. Schnedermann, J. Sollfrank, and U. Heinz, "Thermal phenomenology of hadrons from 200A GeV S+S collisions," *Physical Review C*, vol. 48, no. 5, pp. 2462–2475, 1993.

[22] B. I. Abelev, M. M. Aggarwal, Z. Ahammed et al., "Systematic measurements of identified particle spectra in pp, d + Au, and Au+Au collisions at the STAR detector," *Physical Review C*, vol. 79, no. 3, article 034909, 2009.

[23] B. I. Abelev, M. M. Aggarwal, Z. Ahammed et al., "Identified particle production, azimuthal anisotropy, and interferometry measurements in Au + Au collisions at $\sqrt{s_{NN}}$ = 9.2 GeV," *Physical Review C*, vol. 81, no. 2, article 024911, 2010.

[24] Z. Tang, Y. Xu, L. Ruan, G. van Buren, F. Wang, and Z. Xu, "Spectra and radial flow in relativistic heavy ion collisions with Tsallis statistics in a blast-wave description," *Physical Review C*, vol. 79, no. 5, article 051901, 2009.

[25] Z.-B. Tang, L. Yi, L. J. Ruan et al., "The statistical origin of constituent-quark scaling in QGP hadronization," *Chinese Physics Letters*, vol. 30, no. 3, article 031201, 2013.

[26] K. Jiang, Y. Zhu, W. Liu et al., "Onset of radial flow in $p + p$ collisions," *Physical Review C*, vol. 91, no. 2, article 024910, 2015.

[27] S. Takeuchi, K. Murase, T. Hirano, P. Huovinen, and Y. Nara, "Effects of hadronic rescattering on multistrange hadrons in high-energy nuclear collisions," *Physical Review C*, vol. 92, no. 4, article 044907, 2015.

[28] H. Heiselberg and A.-M. Levy, "Elliptic flow and Hanbury-Brown–Twiss correlations in noncentral nuclear collisions," *Physical Review C*, vol. 59, no. 5, pp. 2716–2727, 1999.

[29] U. W. Heinz, "Hydrodynamics at RHIC: how well does it work, where and how does it break down?," *Journal of Physics G: Nuclear and Particle Physics*, vol. 31, no. 6, article S717, 2005.

[30] R. Russo, "Measurement of D+ meson production in pPb collisions with the ALICE detector," 2015, https://arxiv.org/abs/1511.04380.

[31] S. Sadhu and P. Ghosh, "Anomalous features of particle production in high-multiplicity events of pp collisions at the LHC energies," *Physical Review D*, vol. 99, no. 3, article 034020, 2019.

[32] G. Bíró, G. Barnaföldi, T. Biró, K. Ürmössy, and Á. Takács, "Systematic analysis of the non-extensive statistical approach in high energy particle collisions - experiment vs. theory," *Entropy*, vol. 19, no. 3, article e19030088, p. 88, 2017.

[33] H.-R. Wei, F.-H. Liu, and R. A. Lacey, "Disentangling random thermal motion of particles and collective expansion of source from transverse momentum spectra in high energy collisions," *Journal of Physics G: Nuclear and Particle Physics*, vol. 43, no. 12, article 125102, 2016.

[34] H.-R. Wei, F.-H. Liu, and R. A. Lacey, "Kinetic freeze-out temperature and flow velocity extracted from transverse momentum spectra of final-state light flavor particles produced in collisions at RHIC and LHC," *The European Physical Journal A*, vol. 52, no. 4, p. 102, 2016.

[35] H.-L. Lao, H.-R. Wei, F.-H. Liu, and R. A. Lacey, "An evidence of mass-dependent differential kinetic freeze-out scenario

observed in Pb-Pb collisions at 2.76 TeV," *The European Physical Journal A*, vol. 52, no. 7, p. 203, 2016.

[36] H.-L. Lao, F.-H. Liu, B.-C. Li, and M.-Y. Duan, "Kinetic freeze-out temperatures in central and peripheral collisions: which one is larger?," *Nuclear Science and Techniques*, vol. 29, no. 6, p. 82, 2018.

[37] H.-L. Lao, F.-H. Liu, B.-C. Li, M.-Y. Duan, and R. A. Lacey, "Examining the model dependence of the determination of kinetic freeze-out temperature and transverse flow velocity in small collision system," *Nuclear Science and Techniques*, vol. 29, no. 11, p. 164, 2018.

[38] J. Cleymans and D. Worku, "Relativistic thermodynamics: transverse momentum distributions in high-energy physics," *The European Physical Journal A*, vol. 48, no. 11, p. 160, 2012.

[39] H. Zheng and L. Zhu, "Comparing the Tsallis distribution with and without thermodynamical description in $p +p$ collisions," *Advances in High Energy Physics*, vol. 2016, Article ID 9632126, 10 pages, 2016.

[40] R. Hagedorn, "Multiplicities, p_T distributions and the expected hadron → quark-gluon phase transition," *La Rivista del Nuovo Cimento*, vol. 6, no. 10, pp. 1–50, 1983.

[41] ALICE Collaboration, B. Abelev, J. Adam et al., "Production of $\sum(1385)^{\pm}$ and $\Xi(1530)^0$ in proton–proton collisions at $\sqrt{s}$ = 7 TeV," *The European Physical Journal C*, vol. 75, no. 1, p. 1, 2015.

[42] R. L. Ray and A. Jentsch, "Phenomenological models of two-particle correlation distributions on transverse momentum in relativistic heavy-ion collisions," *Physical Review C*, vol. 99, no. 2, article 024911, 2019.

[43] The CMS Collaboration, S. Chatrchyan, V. Khachatryan et al., "Study of high-p_T charged particle suppression in PbPb compared to pp collisions at $\sqrt{s_{NN}}$ = 2.76 TeV," *The European Physical Journal C*, vol. 72, no. 3, 2012.

[44] C. Tsallis, "Possible generalization of Boltzmann-Gibbs statistics," *Journal of Statistical Physics*, vol. 52, no. 1-2, pp. 479–487, 1988.

[45] B. I. Abelev, J. Adams, M. M. Aggarwal et al., "Strange particle production in $p + p$ collisions at $\sqrt{s}$ = 200 GeV," *Physical Review C*, vol. 75, no. 6, article 064901, 2007.

[46] T. S. Biró, G. Purcsel, and K. Urmössy, "Non-extensive approach to quark matter," *The European Physical Journal A*, vol. 40, no. 3, p. 325, 2009.

[47] R. Odorico, "Does a transverse energy trigger actually trigger on large-P_T jets?," *Physics Letters B*, vol. 118, no. 1-3, pp. 151–154, 1982.

[48] G. Arnison, A. Astbury, B. Aubert et al., "Transverse momentum spectra for charged particles at the CERN proton-antiproton collider," *Physics Letters B*, vol. 118, no. 1-3, pp. 167–172, 1982.

[49] T. Mizoguchi, M. Biyajima, and N. Suzuki, "Analyses of whole transverse momentum distributions in $p\bar{p}$ and pp collisions by using a modified version of Hagedorn's formula," *International Journal of Modern Physics A*, vol. 32, no. 11, article 1750057, 2017.

[50] M. Suleymanov, "The meaning behind observed p_T regions at the LHC energies," *International Journal of Modern Physics E*, vol. 27, no. 1, article 1850008, 2018.

[51] L. J. Gutay, A. S. Hirsch, R. P. Scharenberg, B. K. Srivastava, and C. Pajares, "De-confinement in small systems: clustering of color sources in high multiplicity $\bar{p}p$ collisions at $\sqrt{s}$ = 1.8

TeV," *International Journal of Modern Physics E*, vol. 24, no. 12, article 1550101, 2015.

[52] A. S. Hirsch, C. Pajares, R. P. Scharenberg, and B. K. Srivastava, "De-confinement in high multiplicity proton-proton collisions at LHC energies," 2018, https://arxiv.org/abs/1803.02301.

[53] P. Sahoo, S. De, S. K. Tiwari, and R. Sahoo, "Energy and centrality dependent study of deconfinement phase transition in a color string percolation approach at RHIC energies," *The European Physical Journal A*, vol. 54, no. 8, p. 136, 2018.

[54] J. Cleymans, "The physics case for the $\sqrt{s_{NN}} \approx 10$ GeV region," 2017, http://arxiv.org/abs/1711.02882.

[55] B. Abelev, J. Adam, D. Adamová et al., "Centrality dependence of π, K, and p production in Pb-Pb collisions at $\sqrt{s_{NN}} = 2.76$ TeV," *Physical Review C*, vol. 88, no. 4, article 044910, 2013.

[56] L. Kumar, "Systematics of kinetic freeze-out properties in high energy collisions from STAR," *Nuclear Physics A*, vol. 931, pp. 1114–1119, 2014.

[57] A. Khuntia, H. Sharma, S. K. Tiwari, R. Sahoo, and J. Cleymans, "Radial flow and differential freeze-out in proton-proton collisions at $\sqrt{s} = 7$ TeV at the LHC," *The European Physical Journal A*, vol. 55, p. 3, 2019.

[58] P. F. Kolb and U. Heinz, "Hydrodynamic description of ultrarelativistic heavy-ion collisions," in *Quark-Gluon Plasma 3*, R. C. Hwa and X.-N. Wang, Eds., p. 788, World Scientific, Singapore, 2004.

[59] D. Thakur, S. Tripathy, P. Garg, R. Sahoo, and J. Cleymans, "Indication of a differential freeze-out in proton-proton and heavy-ion collisions at RHIC and LHC energies," *Advances in High Energy Physics*, vol. 2016, Article ID 4149352, 13 pages, 2016.

[60] P.-P. Yang, M.-Y. Duan, F.-H. Liu, and R. Sahoo, "Multiparticle production and initial quasi-temperature from proton induced carbon collisions at $p_{Lab} = 31$ GeV/c," https://arxiv.org/abs/1903.04008.

Research Article

Centrality Dependence of Multiplicity Fluctuations in Ion-Ion Collisions from the Beam Energy Scan at FAIR

Anuj Chandra (iD)**, Bushra Ali, and Shakeel Ahmad** (iD)

Department of Physics, Aligarh Muslim University, Aligarh 202002, India

Correspondence should be addressed to Shakeel Ahmad; shakeel.ahmad@cern.ch

Multiplicity distributions and event-by-event multiplicity fluctuations in AuAu collisions at energies in future heavy-ion experiment at the Facility for Anti-proton and Ion Research (FAIR) are investigated. Events corresponding to FAIR energies are simulated in the frame work of Ultra Relativistic Quantum Molecular Dynamics (URQMD) model. It is observed that the mean and the width of multiplicity distributions monotonically increase with beam energy. The trend of variations of dispersion with mean number of participating nucleons for the centrality-bin width of 5% are in accord with the Central Limit Theorem. The multiplicity distributions in various centrality bins as well as for full event samples are observed to obey Koba, Nielsen and Olesen (KNO) scaling. The trends of variations of scaled variance with beam energy are also found to support the KNO scaling predictions for larger collision centrality. The findings also reveal that the statistical fluctuations in 5% centrality-bin width appear to be under control.

1. Introduction

Any physical quantity measured in an experiment is subject to fluctuations. These fluctuations depend on the property of the system and are expected to provide important information about the nature of the system under study [1, 2]. As regards relativistic heavy-ion (AA) collisions, the system so created is a dense and hot fireball consisting of partonic and (or) hadronic matter [1, 2]. To investigate the existence of partonic matter in the early life of fireball is one of the main goals of AA collisions. Study of fluctuations in AA collisions would help to check the idea that fluctuations of a thermal system are directly related to various susceptibilities and could be an indicator for the possible phase transitions [1–3]. Fluctuations in experimental observables, such as charged particle multiplicity, particle ratios, mean transverse momentum, and other global observables are related to the thermodynamic properties of the system, like, entropy, specific heat, chemical potential, etc. [4–7]. Event-by-event (ebe) fluctuations of these quantities are regarded as an important mean to understand the particle production dynamics which, in turn, would lead to understand the nature of phase transition and the critical fluctuations at the QCD phase boundary. A non-monotonic behavior of the fluctuations as a function of collision centrality and

energy of the colliding beam may signal the onset of confinement and may be used to probe the critical point in the QCD phase diagram [7]. The multiplicity of charged particles produced in heavy-ion collisions is the simplest and day-one observable, which provides a mean to investigate the dynamics of highly excited multi-hadron system. Studies involving multiplicity distributions (MDs) of the relativistic charged particles produced would allow finding the deviations from a simple superposition of multiple independent nucleon–nucleon (nn) collisions. Such studies, if carried out in limited rapidity space are envisaged to provide useful information on dynamical fluctuations [8–11]. It has been stressed that moments of MDs in full and limited rapidity bins would lead to make some interesting remarks about the production mechanisms involved. Dependence of MDs and their moments on collision centrality is also expected to lead to some interesting conclusions because of the fact that in narrow centrality windows the geometrical fluctuations may be treated as under control, whereas, such windows, if correspond to most central collisions, may be of additional importance because of the extreme conditions of temperature and excitation energy [7]. An attempt is, therefore, made to study the multiplicity fluctuations in the narrow centrality windows in AuAu collisions for the Beam Energy Scan (BES) at FAIR energies (for E_{lab} =10, 20, 30 and 40A GeV) in the frame

TABLE 1: Values of $\langle N_{\text{part}} \rangle$, $\langle N_{\text{ch}} \rangle$, dispersion ($\sigma$) and scaled variance ($\omega$) in various centrality bins at $E_{\text{lab}} = 10\text{A GeV/c}$.

Centrality (%)	$\langle N_{\text{part}} \rangle$	$\langle N_{\text{ch}} \rangle$	σ	ω
5	348.00 ± 0.0020	231.03 ± 0.07	25.07 ± 0.05	2.7198 ± 0.0009
10	289.90 ± 0.0020	182.37 ± 0.06	21.63 ± 0.05	2.5650 ± 0.0009
15	238.45 ± 0.0020	144.36 ± 0.05	19.34 ± 0.05	2.5898 ± 0.0010
20	195.27 ± 0.0020	113.62 ± 0.04	17.26 ± 0.05	2.6214 ± 0.0012
25	159.21 ± 0.0020	89.70 ± 0.04	15.19 ± 0.05	2.5727 ± 0.0013
30	127.17 ± 0.0020	70.10 ± 0.04	13.85 ± 0.05	2.7352 ± 0.0016
35	100.08 ± 0.0020	53.49 ± 0.03	12.18 ± 0.05	2.7734 ± 0.0019
40	77.97 ± 0.0010	39.72 ± 0.03	10.76 ± 0.05	2.9171 ± 0.0022
45	58.89 ± 0.0010	28.99 ± 0.02	9.22 ± 0.05	2.9297 ± 0.0027
50	44.44 ± 0.0010	20.62 ± 0.02	7.84 ± 0.05	2.9803 ± 0.0032
55	31.99 ± 0.0010	13.86 ± 0.02	6.46 ± 0.05	3.0073 ± 0.0039
60	22.27 ± 0.0010	9.13 ± 0.01	5.17 ± 0.05	2.9287 ± 0.0049
65	14.83 ± 0.0010	5.95 ± 0.01	4.14 ± 0.05	2.8798 ± 0.0059
70	10.15 ± 0.0010	3.67 ± 0.01	3.21 ± 0.05	2.8056 ± 0.0071
75	7.06 ± 0.0020	2.17 ± 0.01	2.42 ± 0.05	2.6991 ± 0.0089
80	5.53 ± 0.0050	1.20 ± 0.00	1.77 ± 0.05	2.6062 ± 0.0111

work of URQMD model, using the code, urqmd-v3.4 [12, 13]. The number of events simulated at these energies are 2.3, 2.3, 2.1, and 2.2M ($M = 10^6$) respectively. The analysis is carried out in the pseudorapidity (η) and transverse momentum (p_T) intervals: $-1.0 < \eta < 1.0$ and $0.2 < p_T < 5.0 \text{GeV/c}$ respectively.

2. The URQMD Model

Multiparticle production in relativistic collisions have been described earlier within the hydrodynamic approach [14]. At a later stage, the Regge theory [15] and multiperipheral models were developed [15, 16]. Although the difficulties attributed to the statistical models were overcome in these models, yet the inconvenience of this approach is the large number of free parameters which are to be fixed by comparison with the experiments. Subsequently various quark-parton models motivated by QCD were introduced and as a consequence a large variety of models for hadronic and heavy-ion collisions were proposed. These models may be classified into macroscopic (statistical and thermodynamic) models [17] and microscopic (string, transport, cascade, etc.) models, like URQMD, VENUS, RQMD, etc. The microscopic models describe the individual hadron-hadron collisions.

URQMD model is based on the covariant propagation of constituent quarks and di-quarks but has been accompanied by baryonic and mesonic degrees of freedom. At low energies, $\sqrt{s_{\text{NN}}} < 5 \text{GeV}$, the collisions are described in terms of interactions between hadrons and their excited states [17], whereas at higher energies (>5 GeV), the quark and gluon degrees of freedom are considered and the concept of color string excitation is introduced with their subsequent fragmentation into hadrons [13]. In a transport model, AA collisions are considered as the superposition of all possible binary nn collisions. Every nn collision corresponding to the impact parameter, $b \leq \sqrt{\sigma_{\text{tot}}/\pi}$ is considered, where σ_{tot} represents the total cross section. The two colliding nuclei are described by Fermi gas model [17] and hence the initial momentum of each nucleon is taken at random between zero and Thomas-Fermi momentum. The interaction term includes more

than 50 baryon and 45 meson species. The model can treat the intermediate fireball both in and out of a local thermal and chemical equilibria. The URQMD model, thus, provides an ideal framework to study heavy-ion collisions. Although, the phase transition from a hadronic to partonic phase are not explicitly included in the model, thus a clear suggestion about the location of critical point can not be made. The study, however, might help in the interpretation of the experimental data since it will permit subtraction of simple dynamical and geometrical effects from the expected Quark Gluon Plasma (QGP) signals [18].

3. Results and Discussion

The URQMD model gives the value of impact parameter, b on ebe basis which allows to determine the collision centrality and mean number of participating nucleons, $\langle N_{\text{part}} \rangle$ using the Glauber model [7, 19]. Values of number of participating nucleons, mean charged particle multiplicities and dispersion of MDs (σ) for various collision centralities at the four energies are estimated and listed in Tables 1–4. The centrality selection is made from the MDs of charged particles for the minimum bias events in the considered η and p_T ranges. This is illustrated in Figure 1, where the multiplicity distribution of minimum bias events for $E_{\text{lab}} = 40 \text{A GeV}$ is displayed. The shaded regions show 10% centrality cross-section bins. Variations of $\langle N_{\text{ch}} \rangle$ and σ with $\langle N_{\text{part}} \rangle$ for the centrality bin width = 2, 5 and 10% are presented in Figures 2 and 3. The statistical errors associated with these parameters are too small to be noticed in the figures. It may be noted from these figures that $\langle N_{\text{ch}} \rangle$ and σ increase smoothly with $\langle N_{\text{part}} \rangle$ or collision centrality. The lines in Figure 2 are due to the best fits to the data obtained using the equation

$$\langle N_{\text{ch}} \rangle = a + b \langle N_{\text{part}} \rangle + c \langle N_{\text{part}} \rangle^2, \tag{1}$$

whereas, in Figure 3 the lines are due to the least square fits to the data of the form

$$\sigma = p + q \sqrt{\langle N_{\text{part}} \rangle}. \tag{2}$$

TABLE 2: Values of the same variables, as in Table 1, but for E_{lab} = 20A GeV/c.

Centrality (%)	$\langle N_{part} \rangle$	$\langle N_{ch} \rangle$	σ	ω
5	348.00 ± 0.0020	288.81 ± 0.07	27.91 ± 0.05	2.6980 ± 0.0008
10	289.90 ± 0.0020	227.70 ± 0.06	24.58 ± 0.05	2.6535 ± 0.0008
15	238.45 ± 0.0020	179.76 ± 0.06	22.37 ± 0.04	2.7839 ± 0.0010
20	195.27 ± 0.0020	141.24 ± 0.05	20.27 ± 0.04	2.9100 ± 0.0012
25	159.21 ± 0.0020	111.38 ± 0.05	18.10 ± 0.03	2.9414 ± 0.0014
30	127.17 ± 0.0020	86.96 ± 0.04	16.52 ± 0.03	3.1384 ± 0.0017
35	100.08 ± 0.0020	66.34 ± 0.04	14.62 ± 0.03	3.2211 ± 0.0020
40	77.97 ± 0.0010	49.44 ± 0.03	12.90 ± 0.02	3.3637 ± 0.0024
45	58.89 ± 0.0010	36.03 ± 0.03	11.05 ± 0.02	3.3876 ± 0.0030
50	44.44 ± 0.0010	25.75 ± 0.02	9.49 ± 0.02	3.4943 ± 0.0035
55	31.99 ± 0.0010	17.36 ± 0.02	7.80 ± 0.01	3.5043 ± 0.0042
60	22.27 ± 0.0010	11.53 ± 0.02	6.32 ± 0.01	3.4638 ± 0.0055
65	14.83 ± 0.0010	7.55 ± 0.01	5.11 ± 0.01	3.4627 ± 0.0066
70	10.15 ± 0.0010	4.71 ± 0.01	4.00 ± 0.01	3.4008 ± 0.0080
75	7.06 ± 0.0020	2.79 ± 0.01	3.06 ± 0.01	3.3583 ± 0.0100
80	5.53 ± 0.0050	2.25 ± 0.21	2.62 ± 0.15	3.0484 ± 0.3079

TABLE 3: Values of the same variables, as in Table 1, but for E_{lab} = 30A GeV/c.

Centrality (%)	$\langle N_{part} \rangle$	$\langle N_{ch} \rangle$	σ	ω
5	348.00 ± 0.0020	327.23 ± 0.09	31.63 ± 0.06	3.0566 ± 0.0009
10	289.90 ± 0.0020	257.60 ± 0.08	27.73 ± 0.05	2.9857 ± 0.0010
15	238.45 ± 0.0020	203.53 ± 0.07	25.22 ± 0.05	3.1245 ± 0.0011
20	195.27 ± 0.0020	159.94 ± 0.06	22.70 ± 0.04	3.2205 ± 0.0013
25	159.21 ± 0.0020	126.11 ± 0.06	20.26 ± 0.04	3.2551 ± 0.0016
30	127.17 ± 0.0020	98.62 ± 0.05	18.56 ± 0.03	3.4930 ± 0.0019
35	100.08 ± 0.0020	75.28 ± 0.04	16.47 ± 0.03	3.6032 ± 0.0023
40	77.97 ± 0.0010	56.15 ± 0.04	14.48 ± 0.03	3.7316 ± 0.0027
45	58.89 ± 0.0010	40.95 ± 0.03	12.40 ± 0.02	3.7530 ± 0.0033
50	44.44 ± 0.0010	29.36 ± 0.03	10.63 ± 0.02	3.8484 ± 0.0040
55	31.99 ± 0.0010	19.87 ± 0.02	8.83 ± 0.02	3.9211 ± 0.0048
60	22.27 ± 0.0010	13.20 ± 0.02	7.19 ± 0.01	3.9103 ± 0.0063
65	14.83 ± 0.0010	8.68 ± 0.02	5.81 ± 0.01	3.8935 ± 0.0076
70	10.15 ± 0.0010	5.44 ± 0.01	4.60 ± 0.01	3.8949 ± 0.0094
75	7.06 ± 0.0020	3.23 ± 0.01	3.51 ± 0.01	3.8103 ± 0.0116
80	5.53 ± 0.0050	3.01 ± 0.25	3.13 ± 0.18	3.2661 ± 0.2933

The values of coefficients, occurring in equations (1) and (2) are listed in Tables 5 and 6 respectively. As described in ref. [7], the centrality dependence of the moments may be understood by the Central Limit Theorem (CLT), according to which, $\langle N_{ch} \rangle \propto N_{part}$ and $\sigma \propto \sqrt{N_{part}}$. However, in the present study the mean multiplicity is observed to grow with $\langle N_{part} \rangle$, as given by equation (1), i.e. a slight deviation from linearity is exhibited by the data irrespective of the fact that how large or small the centrality bins are chosen. The variations of σ with $\langle N_{part} \rangle$, shown in Figure 3, are seen to be nicely fitted by equation (2) for 5% centrality bin width, while for the centrality bin widths of 2% and 10% the data are seen to be fitted only for centrality >20%, as indicated by the lines in this figure; the lines are drawn for the range of

centrality for which the fits of the data have been performed. Similar deviations from CLT have also been observed in AuAu collisions at RHIC and lower energies [7]. In order to extract information regarding dynamical fluctuations arising from physical processes, fluctuations in mean number of participating nucleons are to be minimized. To achieve the same, centrality bins considered should be kept narrow because the fluctuations in the particle multiplicities are directly related to the fluctuations in the mean number of participating nucleons. The inherent fluctuations may be reduced by choosing narrow centrality bins; the inherent fluctuations are the fluctuations which arise due to the difference in the geometry even within the selected centrality bin. A very narrow centrality bin, if considered, would,

TABLE 4: Values of the same variables, as in Table 1, but for E_{lab} = 40A GeV/c.

Centrality (%)	$\langle N_{\text{part}}\rangle$	$\langle N_{\text{ch}}\rangle$	σ	ω
5	348.00 ± 0.0020	353.86 ± 0.10	35.23 ± 0.07	3.5065 ± 0.0010
10	289.90 ± 0.0020	278.50 ± 0.08	30.55 ± 0.06	3.3503 ± 0.0011
15	238.45 ± 0.0020	219.93 ± 0.07	27.86 ± 0.05	3.5289 ± 0.0013
20	195.27 ± 0.0020	172.92 ± 0.07	24.98 ± 0.05	3.6082 ± 0.0015
25	159.21 ± 0.0020	136.43 ± 0.06	22.09 ± 0.04	3.5766 ± 0.0017
30	127.17 ± 0.0020	106.50 ± 0.05	20.16 ± 0.04	3.8159 ± 0.0020
35	100.08 ± 0.0020	81.49 ± 0.05	17.75 ± 0.03	3.8673 ± 0.0024
40	77.97 ± 0.0010	60.80 ± 0.04	15.78 ± 0.03	4.0966 ± 0.0029
45	58.89 ± 0.0010	44.31 ± 0.04	13.50 ± 0.03	4.1148 ± 0.0036
50	44.44 ± 0.0010	31.76 ± 0.03	11.55 ± 0.02	4.1974 ± 0.0042
55	31.99 ± 0.0010	21.58 ± 0.02	9.61 ± 0.02	4.2835 ± 0.0051
60	22.27 ± 0.0010	14.31 ± 0.02	7.78 ± 0.01	4.2327 ± 0.0066
65	14.83 ± 0.0010	9.43 ± 0.02	6.28 ± 0.01	4.1880 ± 0.0079
70	10.15 ± 0.0010	5.90 ± 0.01	4.95 ± 0.01	4.1634 ± 0.0097
75	7.06 ± 0.0020	3.50 ± 0.01	3.77 ± 0.01	4.0707 ± 0.0120
80	5.53 ± 0.0050	2.04 ± 0.03	2.97 ± 0.02	4.3207 ± 0.0620

TABLE 5: Values of parameters, a, b, and c, occurring in equation (1) at different energies.

E_{lab}	Fit Par.	Centrality 10%	Centrality 5%	Centrality 2%
	$a \times 10^{-1}$	−17.425 ± 0.032	−19.211 ± 0.071	−13.718 ± 0.004
10A GeV	$b \times 10^{-2}$	49.595 ± 0.018	49.581 ± 0.020	43.791 ± 0.015
	$c \times 10^{-4}$	4.895 ± 0.008	4.452 ± 0.007	5.350 ± 0.005
	$a \times 10^{-1}$	−15.317 ± 0.051	−18.215 ± 0.063	−17.031 ± 0.045
20A GeV	$b \times 10^{-2}$	60.103 ± 0.024	60.250 ± 0.021	53.923 ± 0.017
	$c \times 10^{-4}$	6.668 ± 0.010	6.670 ± 0.007	6.900 ± 0.006
	$a \times 10^{-1}$	−16.633 ± 0.061	−18.670 ± 0.066	−17.852 ± 0.050
30A GeV	$b \times 10^{-2}$	68.297 ± 0.029	68.483 ± 0.024	60.889 ± 0.019
	$c \times 10^{-4}$	7.458 ± 0.012	7.428 ± 0.008	7.872 ± 0.007
	$a \times 10^{-1}$	−18.499 ± 0.063	−19.733 ± 0.065	−18.947 ± 0.049
40A GeV	$b \times 10^{-2}$	74.059 ± 0.030	73.900 ± 0.026	65.885 ± 0.020
	$c \times 10^{-4}$	7.986 ± 0.013	8.080 ± 0.010	8.468 ± 0.007

TABLE 6: Values of parameters, p and q, occurring in equation (2) at different energies.

E_{lab}	Fit Par.	Centrality 10%	Centrality 5%	Centrality 2%
10A GeV	$P \times 10^{-1}$	−21.171 ± 0.061	−10.181 ± 0.087	8.087 ± 0.055
	$q \times 10^{-1}$	16.436 ± 0.017	13.244 ± 0.001	11.704 ± 0.011
20A GeV	$p \times 10^{-1}$	−19.790 ± 0.082	−8.694 ± 0.008	−6.706 ± 0.067
	$q \times 10^{-1}$	−19.050 ± 0.019	15.308 ± 0.001	13.634 ± 0.013
30A GeV	$p \times 10^{-1}$	−21.280 ± 0.097	−8.795 ± 0.008	−6.936 ± 0.073
	$q \times 10^{-1}$	21.334 ± 0.023	17.131 ± 0.002	15.295 ± 0.015
40A GeV	$p \times 10^{-1}$	-22.988 ± 0.101	-11.275 ± 0.008	-8.658 ± 0.075
	$q \times 10^{-1}$	23.292 ± 0.026	18.901 ± 0.002	16.814 ± 0.016

therefore, minimize this effect but may cause additional fluctuations due to statistics. Centrality resolution of the detectors also demands that the chosen centrality bins should not be too narrow. Thus, our observations from Figure 3, tend to suggest that fluctuation effects dominate if the centrality bin width is somewhat larger or quite small.

Multiplicity distributions of relativistic charged particles for minimum bias events for $|\eta| < 1.0$ and $p_T = 0.2 - 5.0$ GeV/c
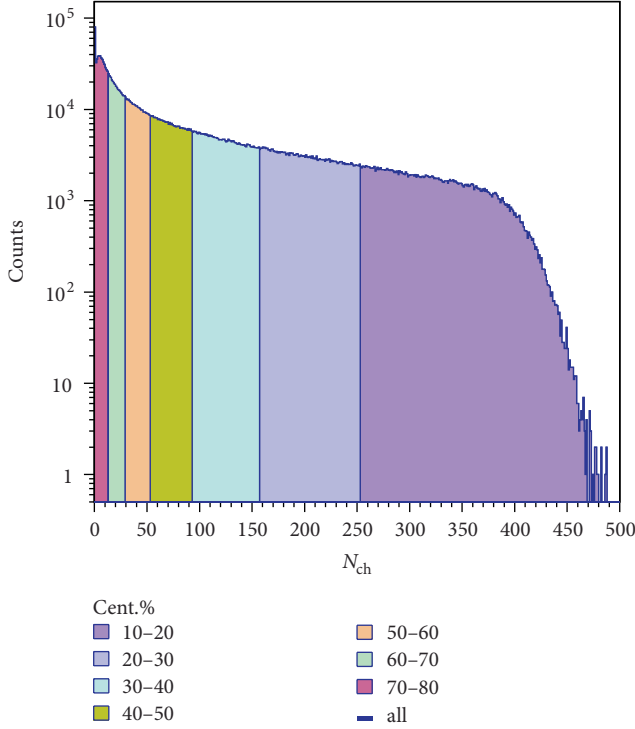
FIGURE 1: An example of centrality selection from the multiplicity distribution of minimum bias simulated events at $E_{lab} = 40A$ GeV.

FIGURE 2: Variations of mean multiplicity with mean number of participating nucleons. The lines are due to fits obtained using equation (1).

are displayed in Figure 4. It may be noted from the figure that MDs at the four beam energies considered, acquire nearly similar shapes and it is expected that the maximum values of N_{ch} become higher with increasing energies. Similar trends in MDs have also been reported by Ghosh et al. [17] at the same beam energies predicted by URQMD model. MDs of relativistic charged particles for various centrality groups at the four beam energies have also been examined. Distributions for $E_{lab} = 40A$ GeV are presented in Figure 5 along-with the distribution of full sample of events (minimum bias). It is evidently clear from the figure that MD of minimum bias sample is a convolution of MDs with different centrality classes.

Yet another way to examine and predict the MDs, is to plot MDs in terms of KNO scaling variable Z ($=N_{ch}/\langle N_{ch} \rangle$). It has been observed that MDs in hadron-hadron collisions exhibit a universal behaviour in a wide range of incident energies if plotted as $\langle N_{ch} \rangle P(N_{ch})$ against the variable Z [20–25]. It was shown that MDs corresponding to pp collisions in the energy range ~ (50–303) GeV are nicely reproduced by the functional form given by Slattery [22]. MDs in pp collisions, for non single diffractive events at ISR energies have also been observed to exhibit KNO scaling [26]. Since the width of MDs for a given centrality gives the extent of fluctuations, the origin of the fluctuations are, thus, inherent in the width of MDs. To understand this behaviour, MDs should be plotted for different centrality bins in terms of KNO scaling variable. MDs for 10, 30, and 50% centrality are plotted in terms of KNO scaling variable in Figure 6. For clarity sake, each next distribution is shifted upwards on y-scale by a factor of 10. It is observed that the distributions become wider with increasing collision
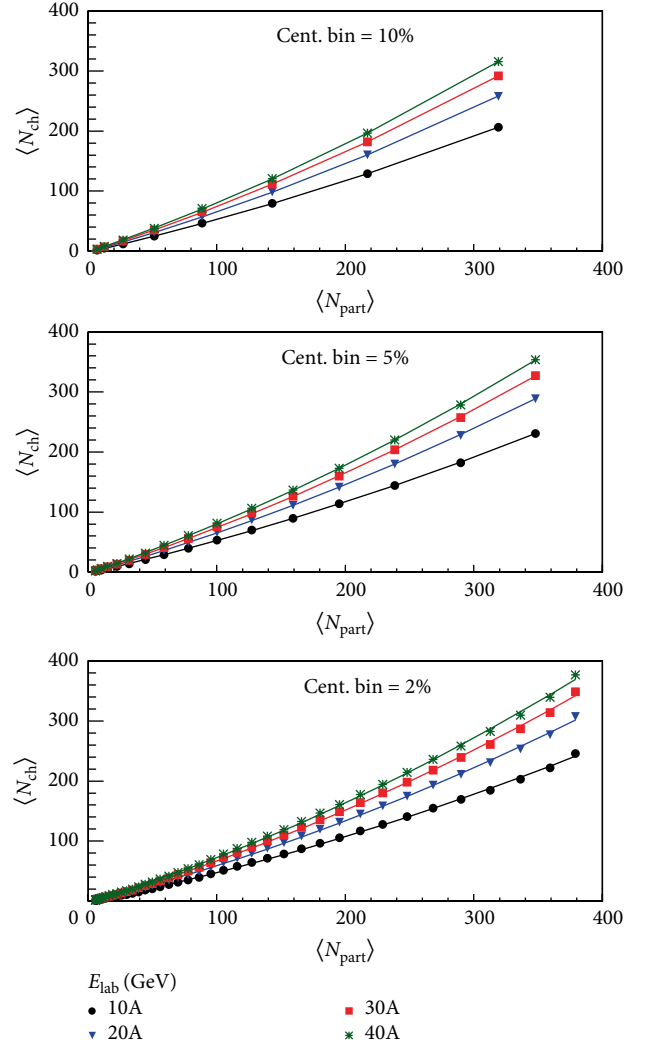
centrality, but exhibits a perfect scaling behavior. MDs, plotted in terms of KNO variable for full event sample in Figure 7, are also noticed to show a perfect KNO scaling.

The scaled variance, ω of the MDs defined as,

$$\omega = \frac{\sigma^2}{\langle N_{ch} \rangle}, \tag{3}$$

here ω is regarded as a quantitative measure of the particle number fluctuations [7, 18, 27–29]. The scaled variance, ω is an intensive quantity which does not depend on the volume of the system within the grand canonical ensemble (GCE) of statistical mechanics or on the number of sources within models of independent source, like wounded nucleon model. The value of scaled variance will be zero in the absence of fluctuations in MDs and unity for Poisson MDs. Since the volume of the system created in AA collisions fluctuates from event to event, and ω would depend on volume fluctuations, it becomes important to reduce the fluctuation effects in
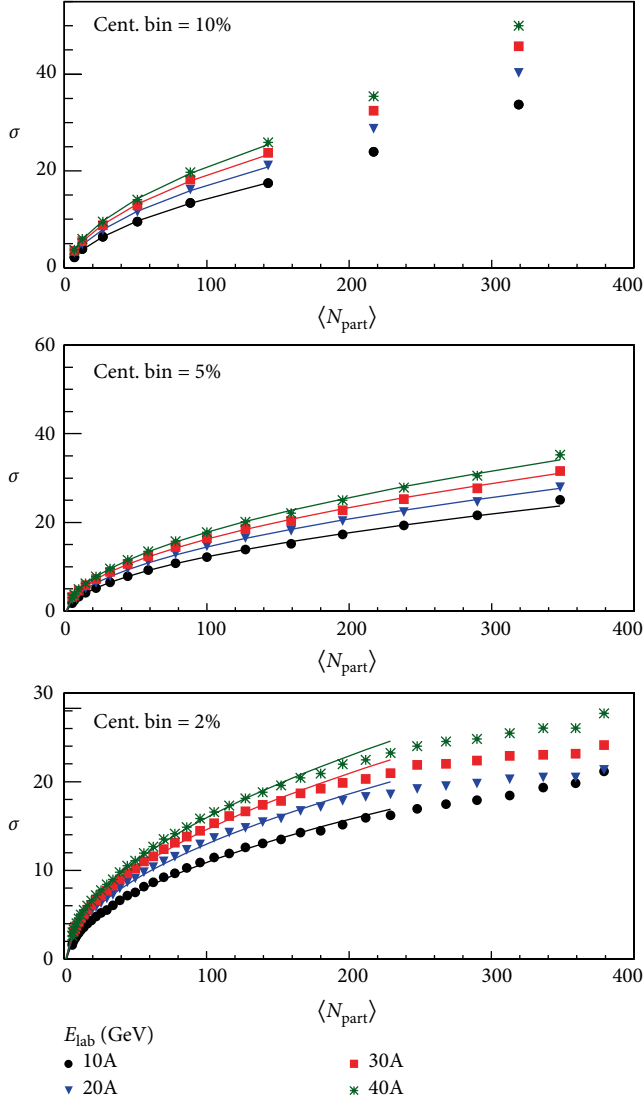
FIGURE 3: Variations of dispersion with mean number of participating nucleons. The lines are due to fits obtained using equation (2).

Energy (GeV)
- 10A
- 20A
- 30A
- 40A

FIGURE 4: Multiplicity distributions of charged particles for AuAu collisions at 10A, 20A, 30A, and 40A GeV in the range $p_T = 0.2 - 5.0$ GeV/c and $|\eta| = 1.0$.

Cent.%
- 10–20
- 20–30
- 30–40
- 40–50
- 50–60
- 60–70
- 70–80
- all
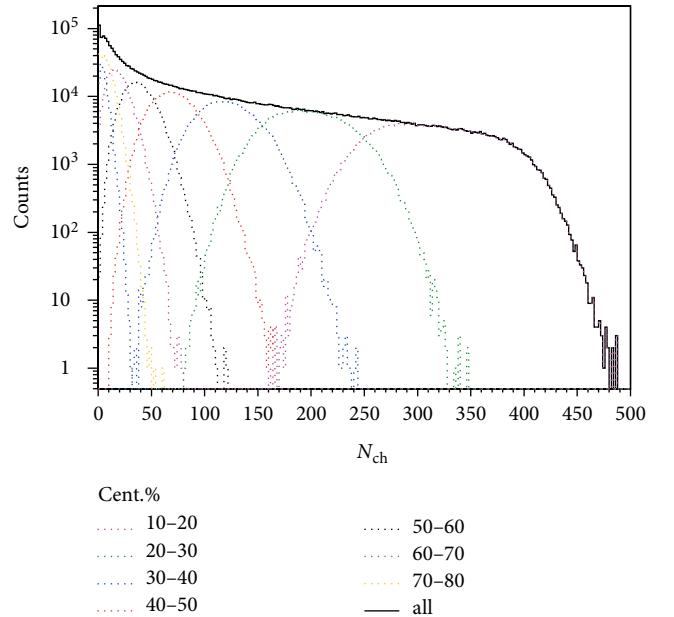
FIGURE 5: Multiplicity distributions of relativistic charged particles for various centrality classes at 40A GeV in the range $p_T = 0.2 - 5.0$ GeV/c and $|\eta| = 1.0$.

fluctuation studies [28]. As mentioned earlier, one way to reduce the fluctuation effects is to reduce the number of participating nucleons by selecting the narrow centrality bins. However, the choices of centrality should be such that it does not introduce additional fluctuations due to finite multiplicity and detector resolutions. Once the statistical fluctuation part is under control, the fluctuation effects present will be mostly of dynamical origin, which may contain interesting physics associated with the collisions, like hydrodynamic expansion, hadronization at freeze-out, etc.

Variation of scaled variance with center of mass (c.m.) energy for different centrality bins are plotted in Figure 8. It may be noted from the figure that ω increases with beam energy as well as in centrality bin widths. It may also be noted that increase of ω with c.m. energy becomes linear for the centrality classes 35% and above. If the data obey the KNO scaling [21], it is predicted that ω should increase linearly with mean charge multiplicity [29]. It may also be noticed in

Figure 8 that increase of ω with beam energy is somewhat weaker for the central collisions. Similar trends of variations of ω with energy have also been reported in pp collisions by NA61 collaboration [29].
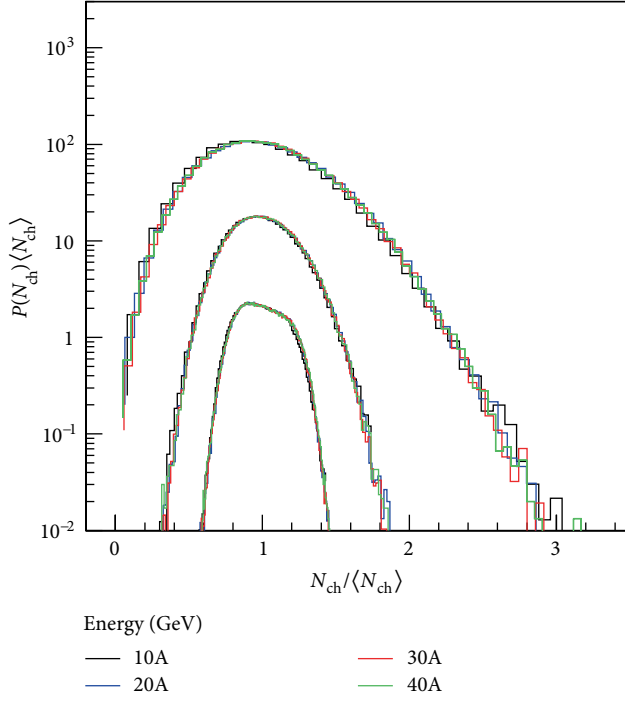
FIGURE 6: Scaled Multiplicity distributions of relativistic charged particles for the centrality bins 0–10%, 30–40% and 50–60%. Distributions corresponding to 30–40% and 50–60% are shifted upwards on the y-scale by factors 10 and 100 for clarity sake only.
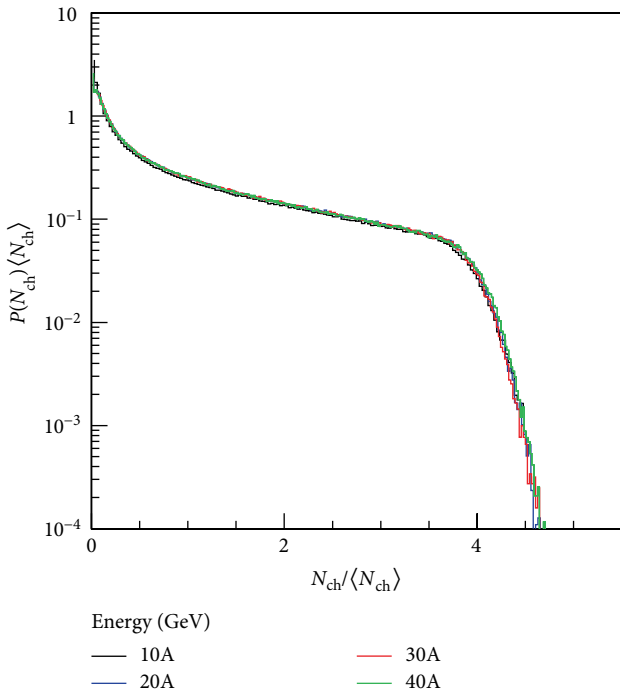
FIGURE 7: Scaled Multiplicity distributions of relativistic charged particles for the minimum bias events at the four beam energies considered.
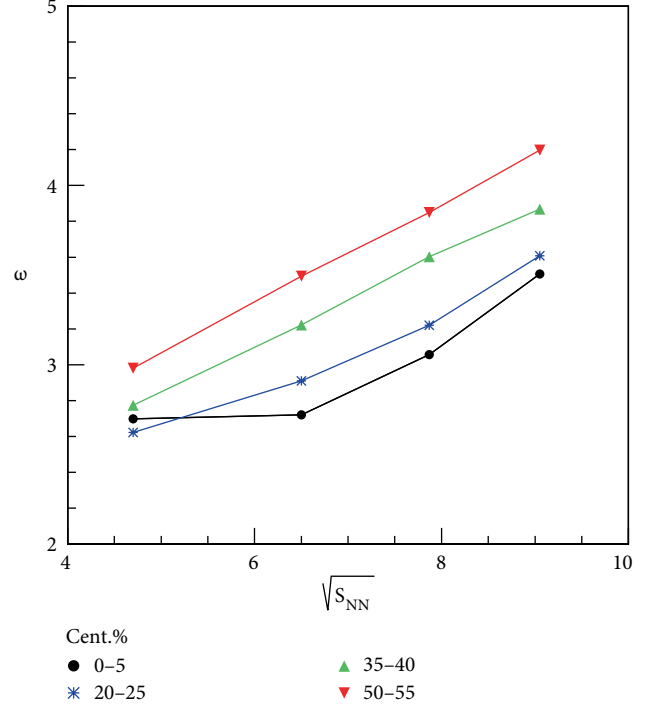
FIGURE 8: Dependence of scaled variance, ω on beam energy.

Centrality dependence of scaled variance at the four incident energies is exhibited in Figure 9. It is observed that for 10% centrality bins ω increases with centrality bin widths, whereas for 5% and 2% this parameter slowly decreases with increasing centrality and thereafter tends to acquire nearly constant values. This observation, thus, supports that statistical fluctuations arising due to fluctuations in N_{part} becomes visible if the centrality bin width is 10% or more and hence considering a bin as wide as 5%, would help to arrive at some meaningful conclusions on dynamical fluctuations, if present.

4. Conclusions

MDs and ebe multiplicity fluctuations in AuAu collisions from the beam energy scan in future heavy-ion experiment at the Facility for Antiproton and Ion Research (FAIR) are examined in the frame work of Ultra-Relativistic Quantum Molecular Dynamics model, URQMD. The mean values of MDs are observed to shift towards the higher multiplicity and the width of the distributions are found to become wider from central to peripheral collisions. The MDs are also observed to obey KNO scaling in various centrality windows as well as for full event (minimum bias) samples. Centrality-bin width dependence of the 2nd moments and scaled variance gives the idea of bin width effect and centrality window-width selection, where the statistical fluctuations may be treated as under control.
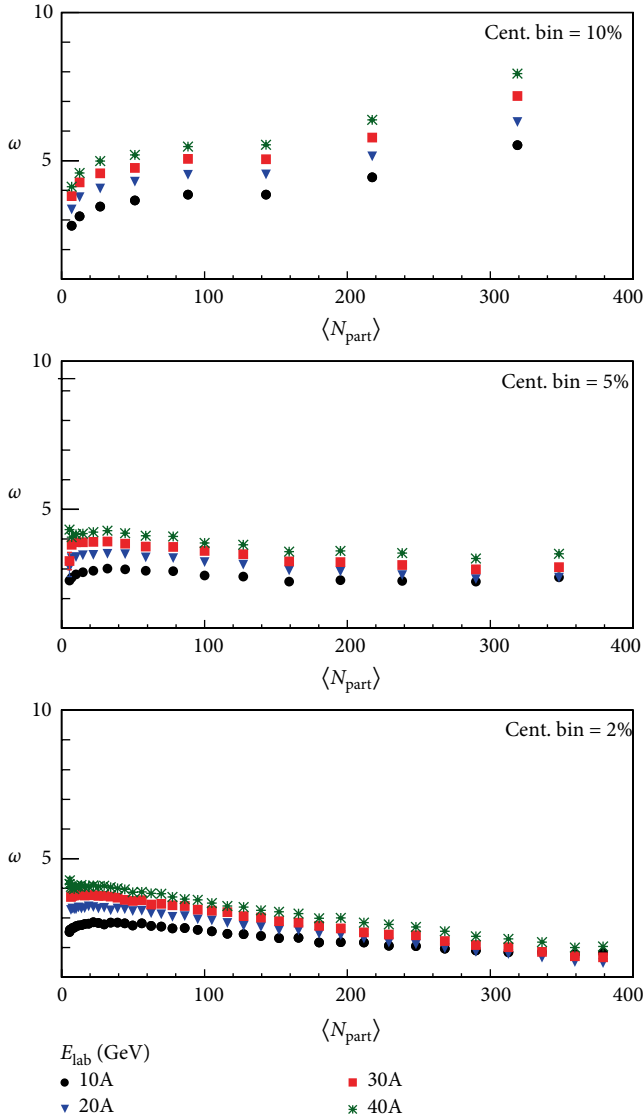
Figure 9: Dependence of scaled variance, ω on $\langle N_{part} \rangle$ in different centrality-bin widths.

Data availability

The data used to support the findings of this study are available with the corresponding author and may be provided on request.

Conflicts of Interest

The authors declare that there are no conflicts of interest.

References

[1] S. A. Voloshin, V. Koch, and H. G. Ritter, "Event-by-event fluctuations in collective quantities," *Physical Review C*, vol. 60, no. 2, p. 024091, 1999.

[2] S. Ahmad, M. M. Khan, S. Khan, A. Khatun, and M. Irfan, "A study of event-by-event fluctuations in relativistic heavy-ion collisions," *International Journal of Modern Physics E*, vol. 23, no. 11, p. 1450065, 2014.

[3] J. L. Albacete, A. Dumitru, and C. Marquet, "The initial state of heavy ion collisions," *International Journal of Modern Physics A*, vol. 28, no. 11, p. 1340010, 2013.

[4] M. Stephanov, K. Rajagopal, and E. Shuryak, "Event-by-event fluctuations in heavy ion collisions and the QCD critical point," *Physical Review D*, vol. 60, no. 11, p. 114028, 1999.

[5] M. Stephanov, K. Rajagopal, and E. Shuryak, "Signatures of the tri-critical point in QCD," *Physical Review Letters*, vol. 81, no. 22, pp. 4816–4819, 1998.

[6] M. A. Stephanov, "QCD phase diagram and the critical point," *International Journal of Modern Physics A*, vol. 20, no. 19, pp. 4387–4392, 2005.

[7] M. Mukherjee, S. Basu, S. Choudhury, and T. K. Nayak, "Fluctuations in charged particle multiplicities in relativistic heavy-ion collisions," *Journal of Physics G: Nuclear and Particle Physics*, vol. 43, no. 8, p. 085102, 2016, https://arxiv.org/abs/1603.02083v3

[8] J. Bächler, J. Bartke, H. Białkowska et al., "Fluctuations of multiplicities in rapidity windows in sulphur-sulphur collisions at 200A GeV," *Zeitschrift für Physik C Particles and Fields*, vol. 56, no. 3, pp. 347–354, 1992.

[9] A. Bialas and R. Peschanski, "Moments of rapidity distributions as a measure of short-range fluctuations in high-energy collisions," *Nuclear Physics B*, vol. 273, no. 3-4, pp. 703–718, 1986.

[10] R. C. Hwa, "A proposed analysis of multiplicity fluctuations in high-energy heavy-ion collisions," *Physics Letters B*, vol. 201, no. 1, pp. 165–168, 1988.

[11] R. C. Hwa, "Enhanced multiplicity fluctuation as a possible signature of quark matter," *Progress in Particle and Nuclear Physics*, vol. 41, pp. 277–281, 1988.

[12] S. A. Bass, M. Belkacem, M. Bleicher et al., "Microscopic models for ultrarelativistic heavy ion collisions," *Progress in Particle and Nuclear Physics*, vol. 41, pp. 255–370, 1998, https://arxiv.org/abs/nucl-th/9803035v2.

[13] M. Bleicher, E. Zabrodin, C. Spieles et al., "Relativistic hadron-hadron collisions in the ultra-relativistic quantum molecular dynamics model," *Journal of Physics G: Nuclear and Particle Physics*, vol. 25, no. 9, pp. 1859–1896, 1999, https://arxiv.org/abs/hep-ph/9909407v1.

[14] S. Z. Belen'kji and L. D. Landau, "Hydrodynamic theory of multiple production of particles," *Il Nuovo Cimento*, vol. 3, no. S1, pp. 15–31, 1956.

[15] T. Regge, "Introduction to complex orbital momenta," *Il Nuovo Cimento*, vol. 14, no. 5, pp. 951–976, 1959.

[16] H. Stöcker and W. Greiner, "High energy heavy ion collisions–probing the equation of state of highly excited hardronic matter," *Physics Reports*, vol. 137, no. 5-6, pp. 277–392, 1986.

[17] S. Ghosh, P. Mali, and A. Mukhopadhyay, "Net-charge fluctuation in Au+Au collisions at energies available at the facility for antiproton and ion research using the UrQMD model," *Physical Review C*, vol. 96, no. 2, p. 024912, 2017.

[18] V. P. Konchakovski, B. Lungwitz, M. I. Gorenstein, and E. L. Bratkovskaya, "Multiplicity fluctuations in nucleus-nucleus collisions: dependence on energy and atomic number," *Physical Review C*, vol. 76, no. 2, p. 024906, 2008, https://arxiv.org/abs/0712.2044v2.

[19] M. L. Miller, K. Reygers, S. J. Sanders, and P. Steinberg, "Glauber modeling in high-energy nuclear collisions," *Annual Review of Nuclear and Particle Science*, vol. 57, no. 1, pp. 205–243, 2007.

[20] A. Shakeel, H. Khushnood, M. Irfan, U. Ali, A. Ahmad, and M. Shafi, "Scaling of multiplicity distribution of charged shower particles in proton-nucleus interactions at 400 GeV," *Physica Scripta*, vol. 29, no. 5, pp. 435–437, 1984.

[21] Z. Koba, H. B. Neclson, and P. Olesen, "Scaling of multiplicity distributions in high energy hadron collisions," *Nuclear Physics B*, vol. 40, pp. 317–334, 1972.

[22] P. Slattery, "Evidence for the onset of semi-inclusive scaling in proton-proton collisions in the 50–300 GeV/c momentum range," *Physical Review Letters*, vol. 29, no. 24, pp. 1624–1627, 1972.

[23] J. W. Martin, J. R. Florian, L. D. Kirkpatrick, J. J. Lord, and R. E. Gibbs, "Scaling of multiplicity and angular distributions in p-emulsion interactions at 30, 67 and 200 GeV," *II Nuovo Cimento A*, vol. 25, no. 3, pp. 447–452, 1975.

[24] P. Olesen, "The 200 GeV multiplicity distribution and scaling," *Physics Letters B*, vol. 41, no. 5, pp. 602–604, 1972.

[25] A. J. Buras, J. Dias de Deus, and R. Møller, "Multiplicity scaling at low energies, a generalized Wroblewski-formula and the leading particle effect," *Physics Letters B*, vol. 47, no. 3, pp. 251–254, 1973.

[26] A. Breakstone, R. Campanini, H. B. Crawley et al., "Charged multiplicity distribution in pp interactions at CERN ISR energies," *Physical Review D*, vol. 30, no. 3, pp. 528–535, 1984.

[27] M. Mukherjee, "Multiplicity distributions and fluctuations in proton-proton and heavy-ion collisions," *EPJ Web of Conferences*, vol. 112, p. 04004, 2016.

[28] A. Seryakov, "Rapid change of multiplicity fluctuations in system size dependence at SPS energies," *KnE Energy and Physics*, pp. 170–177, 2018, https://arxiv.org/abs/1712.03014v1, ICPPA 2017, 3rd International Conference on Particle Physics and Astrophysics.

[29] M. Mackowiak-Pawlowska, A. Wilczek, and NA61 Coll., "Multiplicity fluctuations of identified hadrons in p+p interactions at SPS energies," *Journal of Physics: Conference Series*, vol. 509, p. 012044, 2014, https://arxiv.org/abs/1402.0707v1.

Research Article

Contributions of Jets in Net Charge Fluctuations from the Beam Energy Scan at RHIC and LHC

Bushra Ali, Shaista Khan, and Shakeel Ahmad (iD)

Department of Physics, Aligarh Muslim University, Aligarh 202 002, India

Correspondence should be addressed to Shakeel Ahmad; shakeel.ahmad@cern.ch

Received 18 March 2019; Accepted 13 June 2019; Published 14 July 2019

Academic Editor: Fu-Hu Liu

Dynamical net charge fluctuations have been studied in ultrarelativistic heavy-ion collisions from the beam energy scan at RHIC and LHC energies by carrying out the hadronic model simulation. Monte Carlo model, HIJING, is used to generate events in two different modes, HIJING-default with jet quenching switched off and jet/minijet production switched off. A popular variable, $\nu_{[+-,dyn]}$, is used to study the net charge fluctuations in different centrality bins and the findings are compared with the available experimental values reported earlier. Although the broad features of net charge fluctuations are reproduced by the HIJING, the model predicts the larger magnitude of fluctuations as compared to the one observed in experiments. The role of jets/minijets production in reducing the net charge fluctuations is, however, distinctly visible from the analysis of the two types of HIJING events. Furthermore, $dN_{ch}/d\eta$ and $1/N$ scaling is partially exhibited, which is due to the fact that, in HIJING, nucleus-nucleus collisions are treated as multiple independent nucleon-nucleon collisions.

1. Introduction

The interest in the studies involving event-by-event fluctuations in hadronic (hh) and heavy-ion (AA) collisions is primarily connected to the idea that the correlations and fluctuations of dynamical origin are associated with the critical phenomena of phase transitions and leads to the local and global differences between the events produced under similar initial conditions [1, 2]. Several different approaches have been made to investigate the event-by-event fluctuations in hh and AA collisions at widely different energies, for example, multifractals [3–5], normalized factorial moments [6], erraticity [4, 7], k-order pseudorapidity spacing [8, 9], and transverse momentum(p_T) spectra. Furthermore, event-by-event fluctuations in the conserved quantities, like strangeness, baryon number, and electric charge, have emerged as new tools to estimate the degree of equilibration and criticality of the measured system [10]. Experiments such as RHIC and LHC are well suited for the study of these observables [10, 11].

Event-by-event fluctuations of net charge of the produced relativistic charged particles serve as an important tool to investigate the composition of hot and dense matter prevailing in the "fireball", created during the intermediate stage of AA collisions, which, in principle, can be characterized in the framework of QCD [11]. It has been argued that a phase transition from QGP to normal hadronic state is an entropy conserving process [12] and, therefore, the fluctuations in net electric charge will be significantly reduced in the final state in comparison to what is envisaged to be observed from a hadron gas system [13, 14]. This is expected because the magnitude of charge fluctuations is proportional to the square of the number of charges present in the system which depends on the state from which charges originate. In a system passing through QGP phase, quarks are the charge carriers, whereas in the case of hadron gas, the charge carriers are hadrons. This suggests that the charge fluctuations observed in the case of QGP with fractional charges would be smaller than those in hadron gas with integral charges [10, 15, 16]. A reduction in the fluctuations of net charge in Pb-Pb collision at $\sqrt{s_{NN}}$ = 2.76 TeV in comparison to that observed at RHIC has been reported by ALICE collaboration [17]. A question arises here whether the fluctuations arising from QGP or from hadron gas would survive during the evaluation

of the system [10, 18–21]. The fluctuations observed at the freeze-out depend crucially on the equation of state of the system and final effects. It has been shown [22] that large charge fluctuations survive, if they are accompanied by large temperature fluctuations at freeze-out in context to the experiments. Measurement of charge fluctuations depends on the observation window, which is so selected that the majority of the fluctuations are captured without being affected by the conservation limits [19–21].

An attempt is, therefore, made to carry out a systematic study of dynamical net charge fluctuations from beam energy scan at RHIC and LHC energies using the Monte Carlo model, HIJING, and the findings are compared with those obtained with the real data and other MC models. The reason for using the code HIJING is that it gives an opportunity to study the effect of jets and jet-quenching. HIJING events are generated at various beam energies corresponding to RHIC and LHC which cover an energy range from $\sqrt{s_{NN}}$ = 62.4 GeV to 5.02 TeV. Two sets of events, (i) HIJING-default with jets and minijets and (ii) HIJING with no jet/minijet production, are generated for each of the incident energies considered.

2. Formalism

The charge fluctuations are usually studied in terms of two types of measures [23]. The first one is D, which is the direct measure of the variance of event-by-event net charge $\langle \delta Q^2 \rangle = \langle Q^2 \rangle - \langle Q \rangle^2$, where $Q = N_+ - N_-$; N_+ and N_-, respectively, denote the multiplicities of positively and negatively charged particles produced in an event in the considered phase space. Since the net charge fluctuations may get affected by the uncertainties arising out of volume fluctuations, the fluctuations in the ratio $R = N_+/N_-$ are taken as the other suitable parameter. R is related to the net charge fluctuations via the parameter D as [13, 15–17]

$$D = \langle N_{ch} \rangle \delta R^2 \simeq 4 \frac{\langle \delta Q^2 \rangle}{\langle N_{ch} \rangle} \tag{1}$$

which gives a measure of charge fluctuations per unit entropy. It has been shown that D acquires a value ~4 for an uncorrelated pion gas which decreases to ~3 after taking into account the resonance yields [15]. For QGP, the value of D has been reduced to ~ 1 − 1.5, where the uncertainty arises due to the uncertainties involved in relating the entropy to the multiplicity of the charged hadrons in the final state [24]. The parameter D, thus, may be taken as an efficient probe for distinguishing between the hadron gas and QGP phases. These fluctuations are, however, envisaged to be diluted in the rapidly expanding medium due to the diffusion of particles in rapidity space [19, 20]. Resonance decays, collision dynamics, radial flow, and final state interactions may also affect the amount of fluctuations measured [15, 25–27]. The first results on net charge fluctuations at RHIC were presented by PHENIX [28] in terms of reduced variance $\omega_d = \langle \delta Q^2 \rangle / N_{ch}$, while STAR [27] results were based on a dynamical net charge fluctuations measure, $\nu_{[+-,dyn]}$, and were treated as a rather reliable measure of the net

charge fluctuations as $\nu_{[+-,dyn]}$ was found to be robust against detection efficiency.

Furthermore, the contributions from statistical fluctuations would also be present if net charge fluctuations are studied in terms of parameter D and it will be difficult to extract the contribution due to fluctuations of dynamical origin. The novel method of estimating the net charge fluctuations takes into account the correlation strength between + +, - -, and + - charge particle pairs [10, 29]. The difference between the relative multiplicities of positively and negatively charged particles is given as

$$\nu_{+-} = \left\langle \left(\frac{N_+}{\langle N_+ \rangle} - \frac{N_-}{\langle N_- \rangle} \right)^2 \right\rangle \tag{2}$$

where the angular brackets represent the mean value over the entire sample of events. The Poisson limit of this quantity is expressed as [27]

$$\nu_{[+-,stat]} = \frac{1}{\langle N_+ \rangle} + \frac{1}{\langle N_- \rangle} \tag{3}$$

The dynamical net charge fluctuations may, therefore, be written as the difference of these two quantities:

$$\nu_{[+-,dyn]} = \nu_{[+-]} - \nu_{[+-,stat]} \tag{4}$$

$$\nu_{[+-,dyn]} = \frac{\langle N_+ (N_+ - 1) \rangle}{\langle N_+ \rangle^2} + \frac{\langle N_- (N_- - 1) \rangle}{\langle N_- \rangle^2} - 2 \frac{\langle N_+ N_- \rangle}{\langle N_+ \rangle \langle N_- \rangle} \tag{5}$$

From the theoretical point of view, $\nu_{[+-,dyn]}$ can be expressed in terms of two particle integral correlation functions as

$$\nu_{[+-,dyn]} = R_{++} + R_{--} - 2R_{+-} \tag{6}$$

where the term $R_{\alpha\beta}$ gives the ratio of integrals of two- and single-particle pseudorapidity density function, defined as

$$R_{\alpha\beta} = \frac{\int dn_\alpha dn_\beta \left(dN/dn_\alpha dn_\beta \right)}{\int dn_\alpha \left(dN/dn_\alpha \right) \int dn_\beta \left(dN/dn_\beta \right)} \tag{7}$$

The variable $\nu_{[+-,dyn]}$ is, thus, basically a measure of relative correlation strength of + +, - -, and + - charged hadron pairs. For independent emission of particles, these correlations should be ideally zero. However, in practice, a partial correlation is observed due to string and jet-fragmentation, resonance decays, and so forth. The strengths of R_{++}, R_{--}, and R_{+-} are expected to vary with system size and beam energy. Moreover, as the charge conservation, + - pair are expected to be rather strongly correlated as compared to like sign charge pairs and hence $2R_{+-}$ in (6) is envisaged to be larger than the sum of the other two terms [27] giving $\nu_{[+-,dyn]}$ values less than zero, which is evident from the results based on pp and $\bar{p}p$ collisions at CERN ISR and FNAL and later on in heavy-ion collisions at RHIC [27, 29–32] and LHC energies [17, 27].
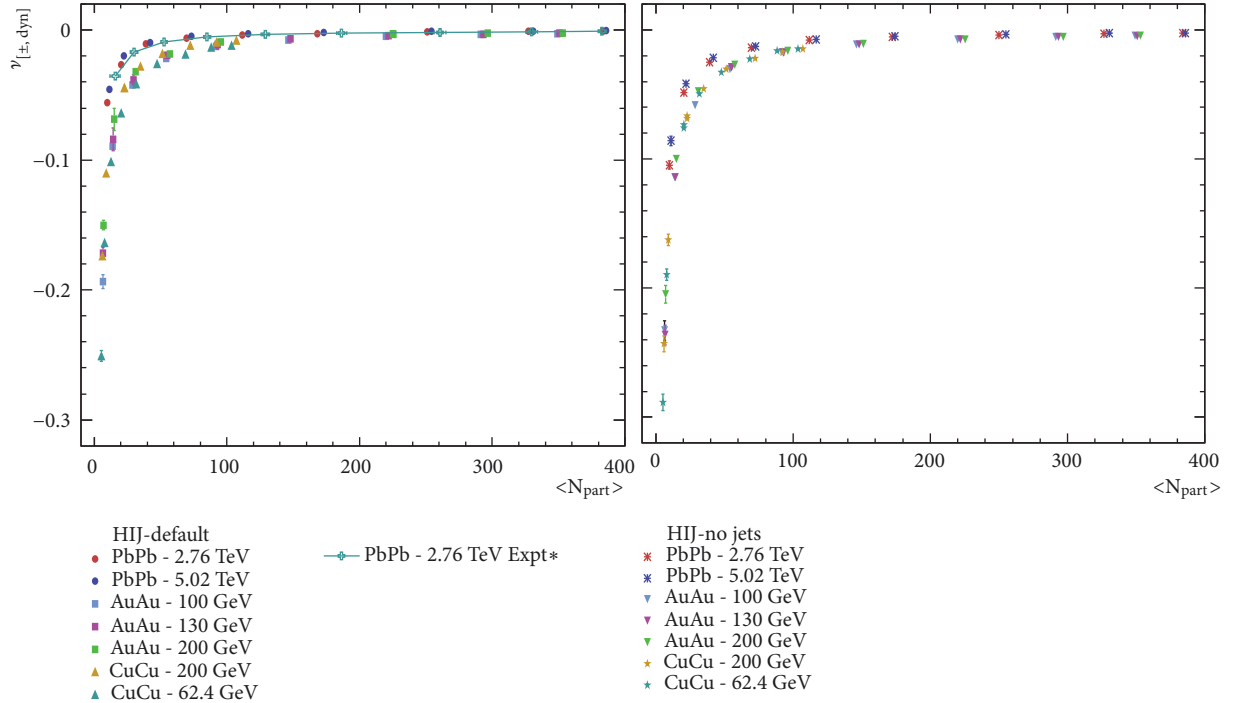
FIGURE 1: Dependence of net charge fluctuations $\nu_{[+-,dyn]}$ on the number of participating nucleons, N_{part}, for the HIJING events with jets/minijets on and off. Experimental results for Pb-Pb collisions at 2.76 TeV are also shown [data from [17]].

TABLE 1: Details of events selected for analysis.

Energy (GeV)	Type of collision	No. of events ($\times 10^6$)
5020	Pb-Pb	0.6
2760	Pb-Pb	0.6
200	Au-Au	0.6
130	Au-Au	0.6
100	Au-Au	0.6
200	Cu-Cu	1.0
62.4	Cu-Cu	1.0

3. Results and Discussion

Several sets of MC events corresponding to different collision systems in a wide range of beam energies are generated using the code HIJING-1.37 [33] for the present analysis. The details of the events simulated are listed in Table 1. Two sets of events for each beam energy and colliding nuclei, HIJING-default with jet-quenching off and with jet/minijet production switched off, are simulated and analyzed. It has been argued [34, 35] that the minijets (semihard parton scattering with few GeV/c momentum transfer) are copiously produced in the early state of AA collisions at RHIC and higher energies. In a QGP medium, if present, the jets/minijets will lose energy through induced gluon radiation [36], a process referred to as jet-quenching in the case of higher p_T partons. The properties of the dissipative medium would determine the extent of energy loss of jets and minijets. The influence of the production of jets/minijets in AA collisions in the produced medium on the net charged fluctuations may be

investigated by comparing the findings due to the two types of HIJING simulated events. The analysis has been carried out by considering the particles having their pseudorapidity values $|\eta| < 1.0$ and p_T values in the range 0.2 GeV/c $< p_T <$ 5.0 GeV/c. These η and p_T cuts have been applied to facilitate the comparison of the findings with the experimental result having similar cuts.

Values of $\nu_{[+-,dyn]}$ for different collision centralities are estimated for various data sets and are listed in Tables 2–5 along with the corresponding values of number of participating nucleons, N_{part}. Variations of $\nu_{[+-,dyn]}$ with mean number of participating nucleons, N_{part}, for various data sets are exhibited in Figure 1. Such dependencies observed in experiments STAR [27] and ALICE [17, 32] are also displayed in the same figure. A monotonic dependence of $\nu_{[+-,dyn]}$ on N_{part} is seen in the figure. It may be of interest to note that, for a given N_{part}, the magnitude of $\nu_{[+-,dyn]}$ decreases with increasing beam energy and this difference becomes more and more pronounced on moving from most central (5%) to the peripheral (70 − 80%) collisions. It is also interesting to note in the figure that the HIJING predicted values (for HIJING-default events) are quite close to the experimental values. However, the corresponding $\nu_{[+-,dyn]}$ values for the events with jets/minijets off are somewhat larger. The jets-off multiplicities reflect the soft processes, whereas the jets-on multiplicities include the contributions from the jets and minijets [32]. This may cause the reduction in the contributions coming from the third term of (5), which represents the correlations between + - pairs. This is expected to occur at these energies, as the events have high multiplicities and are dominated by multiple minijet productions, which might

TABLE 2: Values of N_{part}, $\nu_{[+-,dyn]}$ and $\nu_{[+-,dyn]}^{corr}$ for various centrality classes in $|\eta| < 1$ for events corresponding to $^{197}Au - ^{197}Au$ collisions.

cent.%	HIJING-default			HIJING-no jets		
	N_{part}	$\nu_{[+-,dyn]}$	$\nu_{[+-,dyn]}^{corr}$	N_{part}	$\nu_{[+-,dyn]}$	$\nu_{[+-,dyn]}^{corr}$
			Au-Au at 100 GeV errors are in units of $\times10^{-3}$			
5	349.19±0.10	-0.00279±0.06	-0.00134±0.67	349.36±0.10	-0.00450±0.11	-0.00247±1.23
10	291.43±0.10	-0.00339±0.07	-0.00162±0.81	291.54±0.10	-0.00523±0.14	-0.00278±1.39
20	219.88±0.10	-0.00469±0.07	-0.00228±1.14	219.95±0.10	-0.00743±0.15	-0.00418±2.09
30	146.36±0.08	-0.00742±0.12	-0.00373±1.87	146.21±0.08	-0.01137±0.21	-0.00647±3.24
40	91.66±0.07	-0.01252±0.22	-0.00643±3.22	91.79±0.07	-0.01735±0.41	-0.00955±4.78
50	54.16±0.05	-0.02176±0.35	-0.01126±5.63	54.00±0.05	-0.03048±0.56	-0.01725±8.63
60	28.81±0.04	-0.04201±0.82	-0.02183±10.9	28.72±0.04	-0.05813±1.06	-0.03342±16.72
70	13.73±0.02	-0.08949±1.37	-0.04683±23.42	13.76±0.02	-0.11431±2.79	-0.06308±31.58
80	6.51±0.02	-0.19365±5.40	-0.10322±51.69	6.48±0.02	-0.23294±7.70	-0.12489±62.58
			Au-Au at 130 GeV errors are in units of $\times10^{-3}$			
5	350.57±0.10	-0.00238±0.06	-0.00116±0.58	350.56±0.10	-0.00466±0.10	-0.00276±1.38
10	293.23±0.10	-0.00306±0.06	-0.00156±0.78	293.29±0.10	-0.00531±0.16	-0.00303±1.52
20	221.67±0.10	-0.00424±0.61	-0.00219±1.14	222.00±0.10	-0.00722±0.19	-0.00420±2.10
30	147.80±0.08	-0.00666±0.77	-0.00351±1.80	147.97±0.08	-0.01109±0.20	-0.00657±3.28
40	93.12±0.07	-0.01093±3.68	-0.00571±3.44	93.16±0.07	-0.01741±0.38	-0.01025±5.13
50	55.14±0.05	-0.01936±2.35	-0.01030±5.30	55.08±0.05	-0.02889±0.61	-0.01683±8.42
60	29.49±0.04	-0.03832±3.89	-0.02091±10.66	50.10±0.05	-0.02884±0.70	-0.01683±8.43
70	14.14±0.03	-0.08413±8.79	-0.04713±24.07	14.23±0.03	-0.11416±2.80	-0.06826±34.17
80	6.71±0.02	-0.17158±4.41	-0.09314±46.63	6.74±0.02	-0.23619±7.59	-0.13987±70.08
			Au-Au at 200 GeV errors are in units of $\times10^{-3}$			
5	353.05±0.09	-0.00216±0.05	-0.00120±0.60	353.17±0.09	-0.00452±0.11	-0.00279±1.39
10	296.71±0.10	-0.00255±0.04	-0.00138±0.69	296.84±0.10	-0.00544±0.14	-0.00337±1.69
20	225.37±0.10	-0.00317±0.31	-0.00160±0.81	225.55±0.10	-0.00723±0.12	-0.00450±2.25
30	155.03±0.10	-0.00557±0.42	-0.00100±0.52	151.28±0.08	-0.01067±0.18	-0.00662±3.31
40	95.63±0.07	-0.00917±1.00	-0.00505±2.58	96.00±0.07	-0.01630±0.28	-0.00993±4.97
50	56.92±0.05	-0.01855±2.54	-0.01129±5.85	57.39±0.05	-0.02718±0.52	-0.01657±8.29
60	31.07±0.04	-0.03223±6.21	-0.01850±9.26	31.16±0.04	-0.04752±0.99	-0.028104±14.06
70	14.93±0.03	-0.06861±8.52	-0.03957±20.38	15.12±0.03	-0.09972±2.23	-0.059954±30.00
80	7.16±0.02	-0.15018±3.64	-0.08783±43.97	7.18±0.02	-0.20465±6.96	-0.121323±60.80

TABLE 3: Values of N_{part}, $v_{[+-,dyn]}$, and $v_{[+-,dyn]}^{corr}$ for different centrality bins in $|\eta| < 1.0$ simulated for $^{64}Cu - ^{64}Cu$ interactions at 62.4 and 200 GeV.

cent.%	HIJING-default			HIJING-no jets		
	N_{part}	$v_{[+-,dyn]}$	$v_{[+-,dyn]}^{corr}$	N_{part}	$v_{[+-,dyn]}$	$v_{[+-,dyn]}^{corr}$
	Cu-Cu at 62.4 GeV errors are in units of $\times 10^{-3}$					
5	103.68±0.03	-0.011595±0.26	-0.00519±2.60	103.73±0.03	-0.01479±0.36	-0.00725±3.62
10	88.36±0.04	-0.01314±0.23	-0.00556±2.78	88.45±0.04	-0.01631±0.43	-0.00743±3.72
20	68.59±0.04	-0.01813±0.31	-0.00825±4.12	68.35±0.04	-0.02268±0.37	-0.01115±5.57
30	47.57±0.03	-0.02577±0.44	-0.01134±5.67	47.61±0.03	-0.03284±0.48	-0.01623±8.12
40	31.62±0.03	-0.04126±0.52	-0.01937±9.69	31.58±0.03	-0.04972±0.75	-0.02466±12.34
50	20.45±0.02	-0.06349±1.16	-0.02943±14.72	20.42±0.02	-0.07580±1.09	-0.03711±18.56
60	12.67±0.02	-0.10112±2.01	-0.04593±22.98	19.33±0.02	-0.07352±1.31	-0.03464±17.33
70	7.92±0.01	-0.16345±2.73	-0.07501±37.53	7.91±0.01	-0.18968±4.29	-0.09017±45.13
80	5.26±0.01	-0.25073±4.09	-0.11766±58.86	5.28±0.01	-0.28850±6.42	-0.13992±70.03
	Cu-Cu at 200 GeV errors are in units of $\times 10^{-3}$					
5	107.26±0.03	-0.00756±0.16	-0.00423±2.12	107.09±0.03	-0.01468±0.45	-0.00905±4.53
10	92.39±0.04	-0.00911±0.17	-0.00517±2.58	92.31±0.04	-0.01728±0.43	-0.01073±5.37
20	72.41±0.04	-0.01174±0.18	-0.00648±3.24	72.54±0.04	-0.02189±0.46	-0.01355±6.78
30	51.26±0.03	-0.01766±0.25	-0.00997±4.98	51.31±0.03	-0.03018±0.56	-0.01839±9.20
40	34.79±0.03	-0.02786±0.39	-0.01613±8.06	34.82±0.03	-0.04548±0.96	-0.02814±14.08
50	22.92±0.03	-0.04417±0.77	-0.02579±12.90	22.88±0.03	-0.06879±1.45	-0.04248±20.12
60	20.93±0.03	-0.04410±0.64	-0.02579±12.90	20.91±0.03	-0.06650±1.33	-0.04027±21.01
70	9.11±0.02	-0.10984±2.26	-0.06197±31.01	9.13±0.02	-0.16262±4.29	-0.09710±48.62
80	5.99±0.01	-0.17367±2.84	-0.10029±50.17	5.98±0.01	-0.24322±6.05	-0.14339±71.78

TABLE 4: Values of N_{part}, $v_{[+-,dyn]}$ and $v_{[+-,dyn]}^{corr}$ for different centrality bins in $|\eta| < 1.0$ simulated for $^{208}Pb - {}^{208}Pb$ collisions at 2.76 and 5.02 TeV.

cent.%	HIJING-default				HIJING-no jets	
	N_{part}	$v_{[+-,dyn]}$	$v_{[+-,dyn]}^{corr}$	N_{part}	$v_{[+-,dyn]}$	$v_{[+-,dyn]}^{corr}$
Pb-Pb at 2760 GeV errors are in units of $\times 10^{-3}$						
5	383.54±0.09	-0.00077±0.01	-0.00055±0.27	383.75±0.09	-0.00227±0.06	-0.00160±0.80
10	327.34±0.11	-0.00091±0.02	-0.00062±0.31	333.39±1.77	-0.00279±0.06	-0.00200±1.00
20	250.99±0.11	-0.00124±0.01	-0.00085±0.42	249.97±0.11	-0.00385±0.05	-0.00282±1.41
30	168.17±0.09	-0.00269±0.03	-0.00196±0.98	172.23±0.09	-0.00517±0.10	-0.00367±1.83
40	115.74±0.08	-0.00354±0.04	-0.00251±1.25	111.91±0.08	-0.00803±0.15	-0.00571±2.85
50	69.43±0.09	-0.00640±0.14	-0.00461±2.30	69.52±0.06	-0.01373±0.26	-0.00997±4.99
60	31.13±0.04	-0.01060±0.62	-0.00722±3.63	39.36±0.05	-0.02487±0.38	-0.01815±9.08
70	22.33±0.04	-0.02685±0.31	-0.01943±9.71	20.33±0.03	-0.04836±0.93	-0.03506±17.54
80	11.25±0.04	-0.05571±0.87	-0.03928±19.65	9.99±0.03	-0.10468±3.34	-0.07691±38.53
Pb-Pb at 5020 GeV errors are in units of $\times 10^{-3}$						
5	385.67±0.09	-0.00056±0.01	-0.00040±0.20	386.00±0.09	-0.00225±0.06	-0.00167±0.83
10	331.10±0.11	-0.00077±0.01	-0.00057±0.28	330.62±0.11	-0.00257±0.06	-0.00189±0.94
20	254.11±0.11	-0.00093±0.01	-0.00064±0.32	255.20±0.11	-0.00355±0.06	-0.00267±1.33
30	173.09±0.12	-0.00164±0.01	-0.00129±0.64	174.31±0.09	-0.00515±0.07	-0.00385±1.92
40	116.08±0.08	-0.00277±0.03	-0.00205±1.02	116.85±0.08	-0.00755±0.13	-0.00561±2.80
50	73.34±0.06	-0.00461±0.06	-0.00339±1.69	72.65±0.06	-0.01261±0.22	-0.00947±4.73
60	42.17±0.05	-0.00941±0.12	-0.00702±3.51	42.02±0.05	-0.02167±0.43	-0.01617±8.09
70	22.33±0.04	-0.01991±0.31	-0.01482±7.41	22.13±0.04	-0.04158±1.20	-0.03094±15.49
80	11.25±0.04	-0.04568±0.87	-0.03465±17.34	11.05±0.03	-0.08586±3.72	-0.0639±32.10

TABLE 5: Values of N_{part}, $\nu_{[+-,dyn]}$, and $\nu^{corr}_{[+-,dyn]}$ for $^{208}Pb - {}^{208}Pb$ collisions at 2.76 TeV [data from [17]].

| cent.%	N_{part}	$\nu_{[+-,dyn]}$	$\nu^{corr}_{[+-,dyn]}$
5	382.80±3.1	-0.00104±0.00001	-0.00093±0.00001
10	329.70±4.6	-0.00126±0.00001	-0.00113±0.00002
20	260.50±4.4	-0.00165±0.00001	-0.00148±0.00001
30	186.40±3.9	-0.00236±0.00001	-0.00211±0.00002
40	128.90±3.3	-0.00348±0.00008	-0.00311±0.00008
50	85.00±2.6	-0.00541±0.00004	-0.00483±0.00004
60	52.80±2.0	-0.00903±0.00007	-0.00802±0.00007
70	30.00±2.8	-0.01675±0.00017	-0.01482±0.00017
80	15.80±3.8	-0.03547±0.00041	-0.03144±0.00041
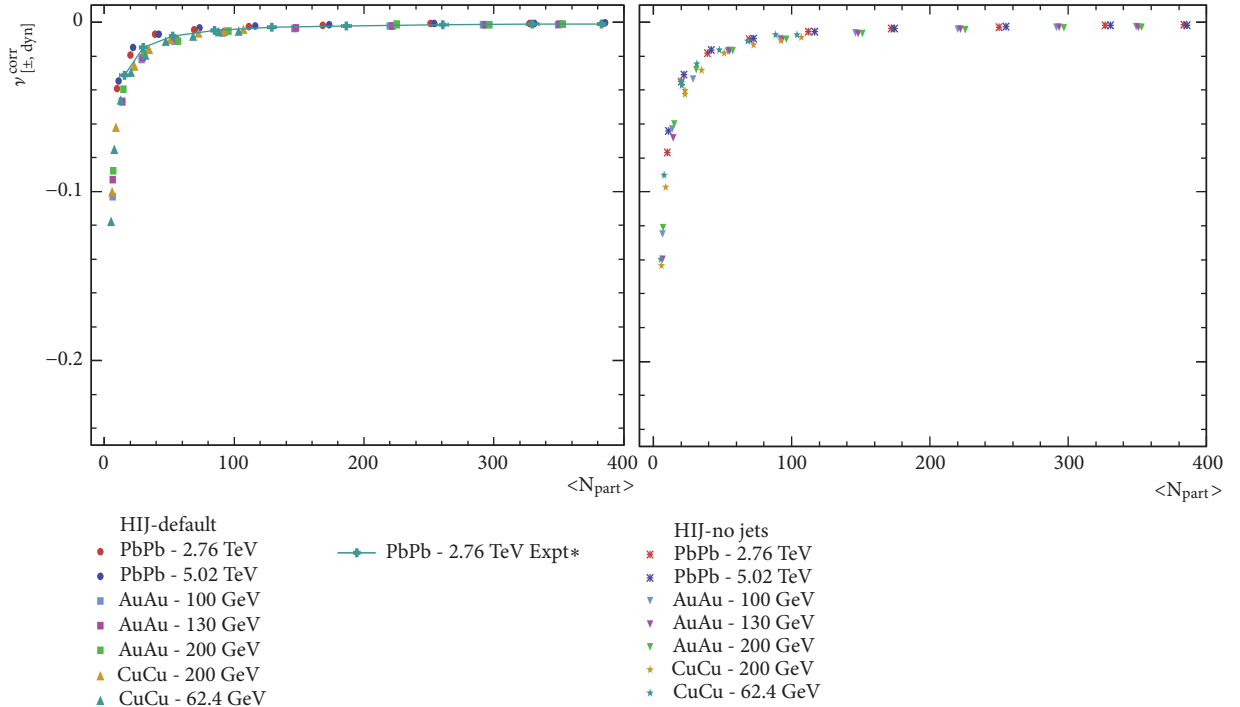
FIGURE 2: The same plot as Figure 1 but for corrected versions of net charge fluctuations.

cause the reduction in the strengths of correlations and fluctuations [37].

The parameter D and $\nu_{[+-,dyn]}$ are related to each other as per the relation

$$\langle N_{ch} \rangle \nu_{[+-,dyn]} = D - 4 \tag{8}$$

The magnitude of net charge fluctuations is limited by the global charge conservation of the produced particles [29]. Considering the effect of global charge conservation, the dynamical fluctuations need to be corrected by a factor of $-4/\langle N_{total} \rangle$, where N_{total} denotes the total charged particle multiplicity of an event in full phase space. Taking into account the global charge conservation and finite acceptance, the corrected value of $\nu_{[+-,dyn]}$ is given by

$$\nu^{corr}_{[+-,dyn]} = \nu_{[+-,dyn]} + \frac{4}{\langle N_{total} \rangle} \tag{9}$$

Values of $\nu^{corr}_{[+-,dyn]}$ for various data sets are presented in the last column of Tables 2–4, whereas variations of $\nu^{corr}_{[+-,dyn]}$ with N_{part} for these data sets are displayed in Figure 2. Although the trends of variations of $\nu_{[+-,dyn]}$ and $\nu^{corr}_{[+-,dyn]}$ with N_{part} for both types of HIJING events are similar, it might be noticed that the data points corresponding to various energies lie rather close to each other in the semicentral and peripheral collision regions. This weakening of energy dependence is observed for both types of HIJING samples considered.

The observed dependence of $\nu_{[+-,dyn]}$ or its corrected form $\nu^{corr}_{[+-,dyn]}$ on N_{part} or collision centrality indicates the weakening of correlations among the produced hadrons, as one moves from central to peripheral collisions, and nearly matches with the experimental results. These findings, thus, tend to suggest that $\nu_{[+-,dyn]}$ should be proportional to the centrality of collisions or charged particle multiplicity, if AA
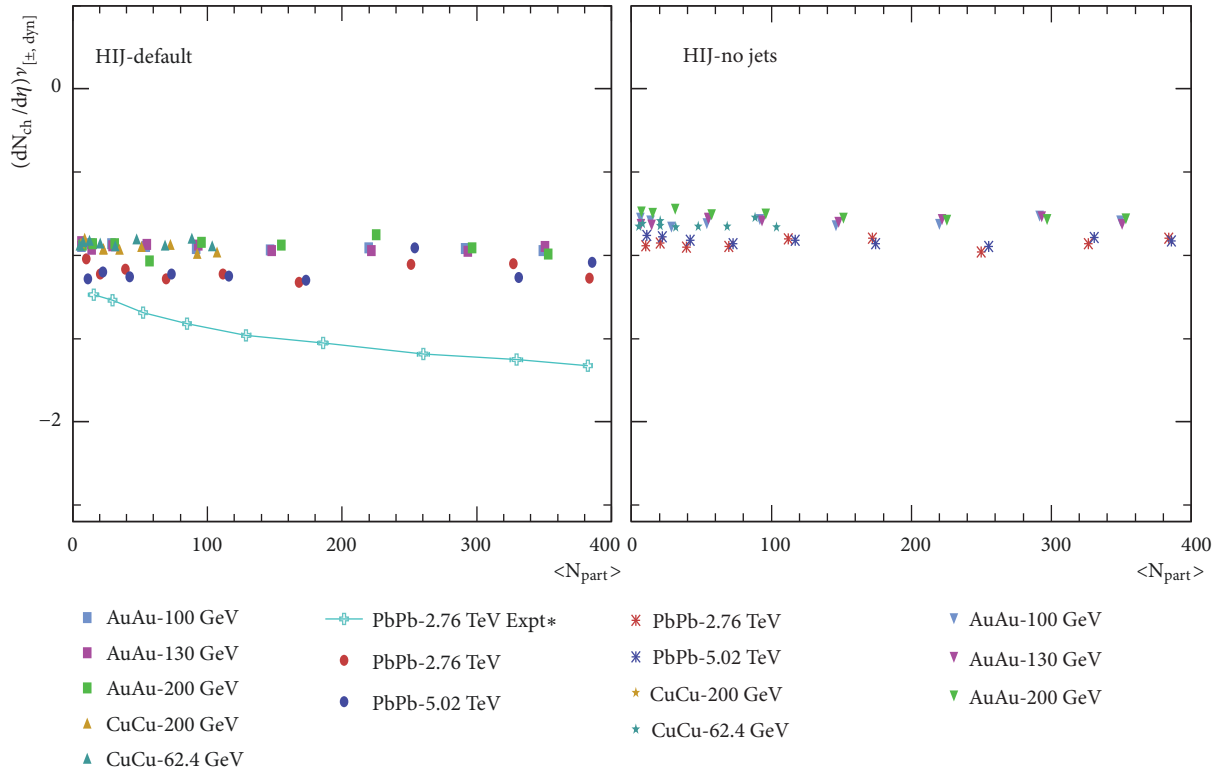
FIGURE 3: $(dN_{ch}/d\eta)\nu_{[+-,dyn]}$ plotted against N_{part} for HIJING default with jet production on (left panel) and jet production off (right panel). The line represents the Pb-Pb data from [17].

collisions are taken as the superpositions of independent nucleon-nucleon (nn) collisions with negligible rescattering effects (which is the basic property of HIJING model). This may be tested by scaling $\nu_{[+-,dyn]}$ by charged particle density $dN_{ch}/d\eta$ and plotting against N_{part}. These plots are displayed in Figures 3 and 4. It may be observed from these figures that the data at different energies show the same qualitative behavior. The values of product $(dN_{ch}/d\eta)\nu_{[+-,dyn]}$ are noticed to be minimum for peripheral collisions and gradually increase to their maximum for the most central collisions; the rise from minimum to maximum is about ~35 - 40 % for various data sets. An increase of 50% has been observed [36] in STAR Au-Au collisions. Such an increase in $(dN_{ch}/d\eta)\nu_{[+-,dyn]}$ values with N_{part} may be accounted to the increase in the particle multiplicity per participant. Data from UA1 and PHOBOS show that, for pp and Au-Au collisions at 200 GeV, $dN_{ch}/d\eta$ increases from 2.4 to 3.9 for most central collisions, thus giving an increase of about 60% [38]

The scaling of $\nu_{[+-,dyn]}$ with N_{part} has also been checked and the plots are shown in Figure 5, whereas after applying the corrections to $\nu_{[+-,dyn]}$ the values of the products are plotted against N_{part} in Figure 6. It is observed from these figures that, with increasing N_{part}, $N_{part}\nu_{[+-,dyn]}$ values gradually decrease for all the data sets. Moreover, for a given N_{part}, the values of product $N_{part}\nu_{[+-,dyn]}$ decrease with the beam energy. It is interesting to note that the difference in the values observed at RHIC and LHC energies, after applying

the corrections to $\nu_{[+-,dyn]}$ values, almost vanishes. It is also interesting to note that the HIJING simulated data points lie closer to the corresponding ones reported earlier using the ALICE data [17]. The decreasing trends of $N_{part}\nu_{[+-,dyn]}$ (or $N_{part}\nu_{[+-,dyn]}^{corr}$) from peripheral to most central collisions observed in STAR are in contrast to what is observed in the present study using the HIJING data at RHIC and higher energies. Furthermore, the lower values of product $(dN_{ch}/d\eta)\nu_{[+-,dyn]}$ or $N_{part}\nu_{[+-,dyn]}$, as shown in Figures 4 and 6 predicted by the HIJING with no jets in comparison to those predicted by HIJING-default, indicate the reduction in magnitude of $\nu_{[+-,dyn]}$ due to the productions of jets and minijets.

The variations of $\nu_{[+-,dyn]}$ and $\nu_{[+-,dyn]}^{corr}$ with charged particle density $dN_{ch}/d\eta$ for the two sets of HIJING events are shown in Figure 7. Results based on Pb-Pb 2.76 TeV experimental data [17] for the same η and p_T cuts are also presented in the same figure. It is worthwhile to note in these figures that HIJING-default predicted values for 2.76 TeV data are quite close to the corresponding experimental values. Although the magnitude of $\nu_{[+-,dyn]}$ or $\nu_{[+-,dyn]}^{corr}$ exhibits an energy dependence, which becomes more pronounced as the $dN_{ch}/d\eta$ values decrease, that is, from semicentral to peripheral collisions, the data points for various event samples tend to fall on a single curve. Data for the events with no jets exhibit almost similar behavior except for Pb-Pb data at 2.76 and 5.02 TeV without jet production. This may lead to the conclusion that as one moves from RHIC
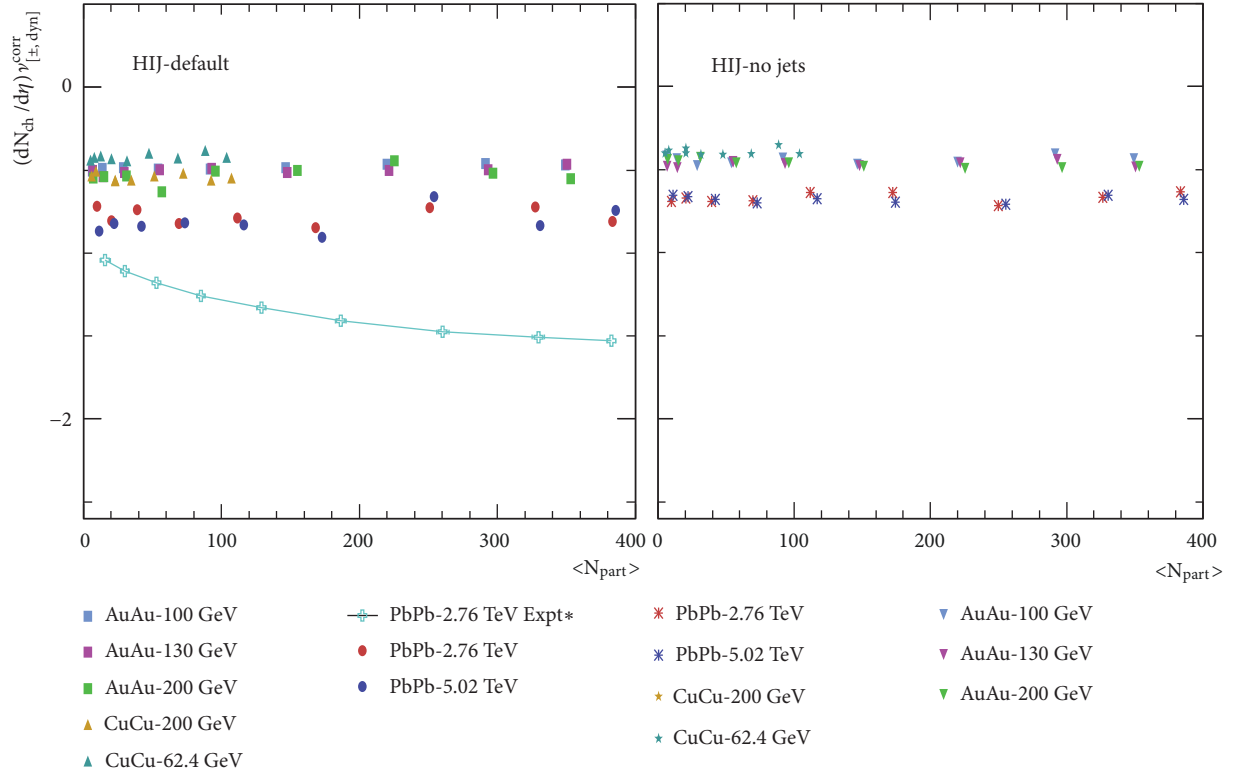
FIGURE 4: The same plot as Figure 3 but for corrected net charge fluctuations, $\nu^{corr}_{[+-,dyn]}$.
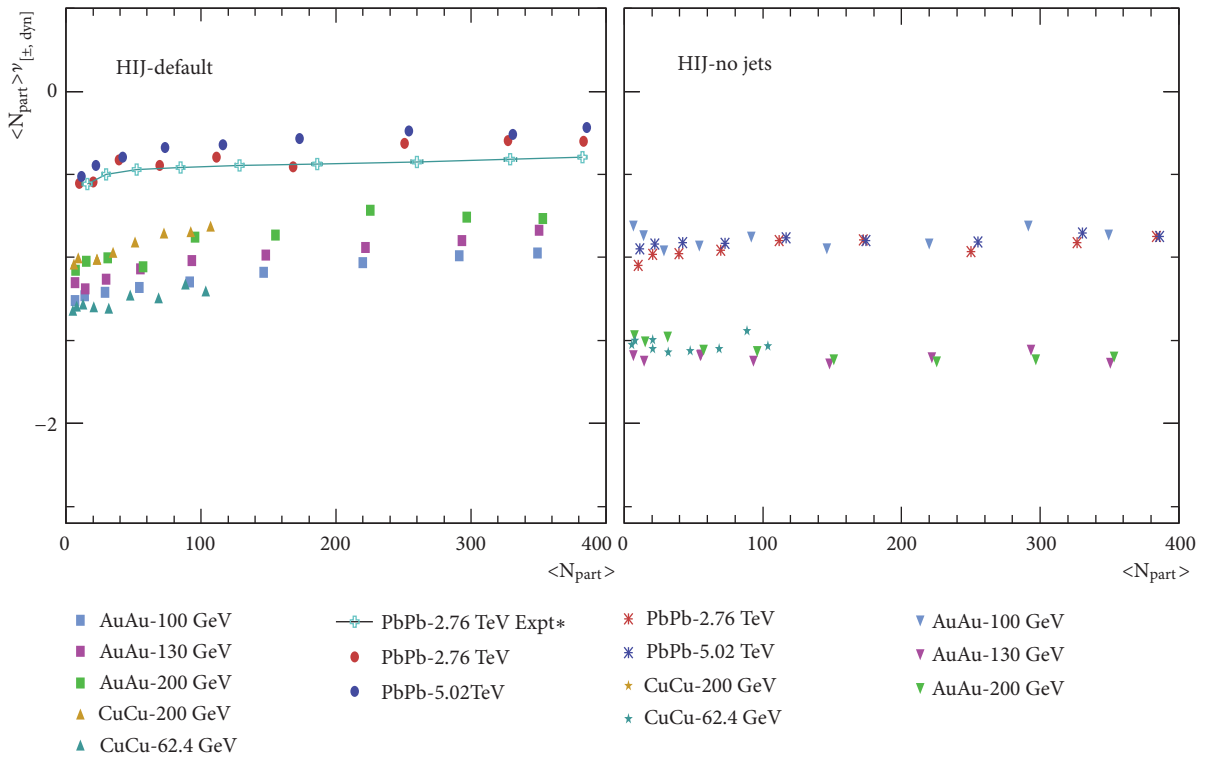

FIGURE 5: Dependence of product of N_{part} and $\nu_{[+-,dyn]}$ on centrality for the two sets of HIJING events at different energies. The line represents the experimental result reported in [17] for $\sqrt{s_{NN}} = 2.76$ TeV Pb-Pb collisions.
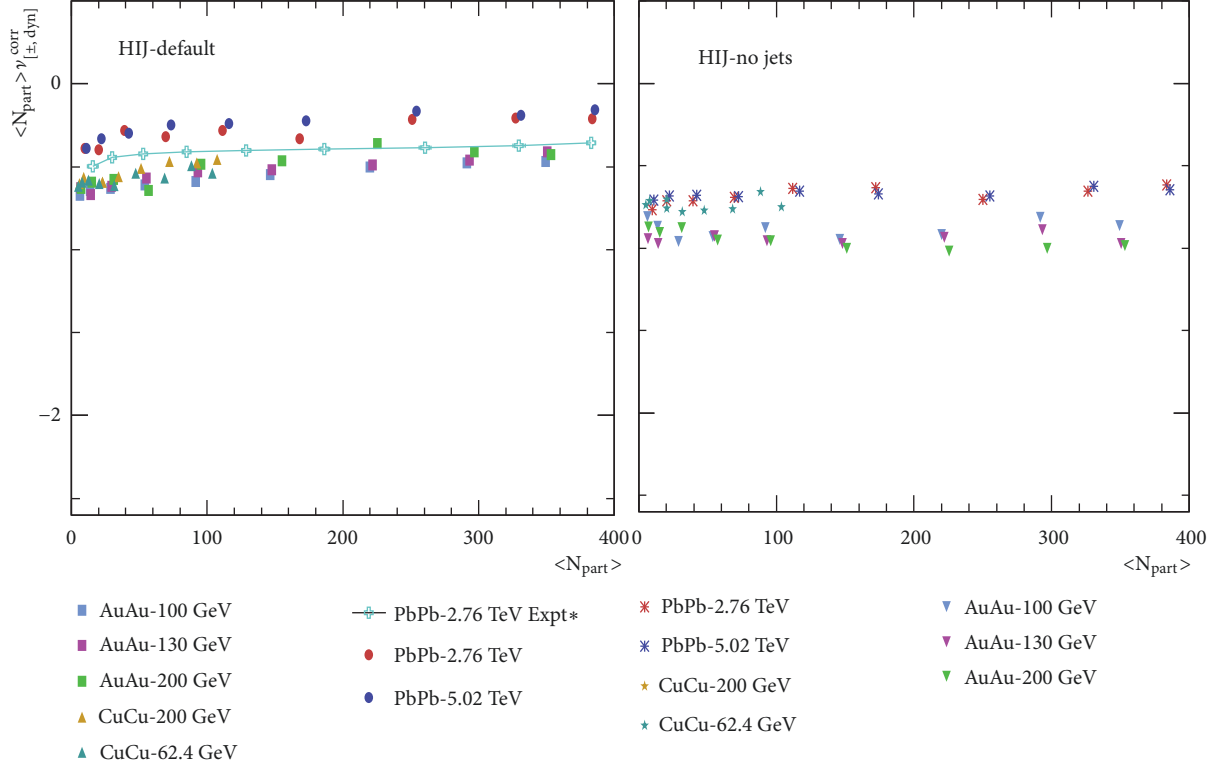
FIGURE 6: Variations of $(N_{part})v^{corr}_{[+-,dyn]}$ with N_{part} for the two sets of HIJING events.

to LHC energies, contributions to the particle multiplicity coming from the jet/minijet production cause the reduction in the magnitude of charge fluctuations.

As mentioned earlier, if AA collisions are the superpositions of m number of nn collisions the single particle density for nn and AA collisions would be written as $\rho_1^n n(\eta) = dN_{ch}/d\eta$ and $\rho_1^A A(\eta) = m\rho_1^{nn}\eta$. In such a scenario, the invariant cross section is proportional to the number of nn collisions, m, and the quantity $(dN_{ch}/d\eta)v_{[+-,dyn]}$ is independent of centrality of collision and the system size [12]. STAR results, however, give ~40% increase in $(dN_{ch}/d\eta)v_{[+-,dyn]}$ values for Au-Au and Cu-Cu collisions. The product $(dN_{ch}/d\eta)v_{[+-,dyn]}$ is plotted against $dN_{ch}/d\eta$ for the two types of event sample in Figure 8. Similar plots for $v^{corr}_{[+-,dyn]}$ are also shown in Figure 9. The scaled values of $v_{[+-,dyn]}$ and $v^{corr}_{[+-,dyn]}$ are observed to increase with increasing $dN_{ch}/d\eta$ values in almost similar fashion. Furthermore, for a given $dN_{ch}/d\eta$ the scaled values of $v_{[+-,dyn]}$ or its corrected version are noticed to increase with increasing energy. It is also observed that for a particular set of events (HIJING-default and jets off) the values of $v_{[+-,dyn]}$ and $v^{corr}_{[+-,dyn]}$ are somewhat larger when jet/minijet production is switched off.

It has been suggested [39] that any multiplicity scaling should be based on the mean multiplicities of charged particles. In the model-independent sources [40], mean particle multiplicity is taken to be proportional to the number of sources, $\langle N_s \rangle$, which changes from event to event. The multiplicity of positively and negatively charged particles may be expressed as

$$\langle N_+ \rangle = \alpha_1 + \alpha_2 + \cdots + \alpha_{N_s} \tag{10}$$

$$\langle N_- \rangle = \beta_1 + \beta_2 + \cdots + \beta_{N_s} \tag{11}$$

where α_i and β_i represent the contributions from i^{th} source. The first and second moments of multiplicity distributions are written as

$$\langle N_a \rangle = \langle \alpha \rangle \langle N_s \rangle \tag{12}$$

$$\langle N_b \rangle = \langle \beta \rangle \langle N_s \rangle \tag{13}$$

$$\langle N_a^2 \rangle = \langle \alpha^2 \rangle \langle N_s \rangle + \langle \alpha \rangle^2 \left[\langle N_s^2 \rangle - \langle N_s \rangle \right] \tag{14}$$

$$\langle N_b^2 \rangle = \langle \beta^2 \rangle \langle N_s \rangle + \langle \beta \rangle^2 \left[\langle N_s^2 \rangle - \langle N_s \rangle \right] \tag{15}$$

$$\langle N_a N_b \rangle = \langle \alpha\beta \rangle \langle N_s \rangle + \langle \alpha \rangle \langle \beta \rangle \langle N_s^2 \rangle - \langle N_s \rangle \right] \tag{16}$$

and here $\langle \alpha \rangle$ and $\langle \beta \rangle$ and $\langle \alpha^1 \rangle$, $\langle \beta^1 \rangle$, and $\langle \alpha\beta \rangle$ are the first and second moments of the probability distributions $P(\alpha, \beta)$ for a single source.
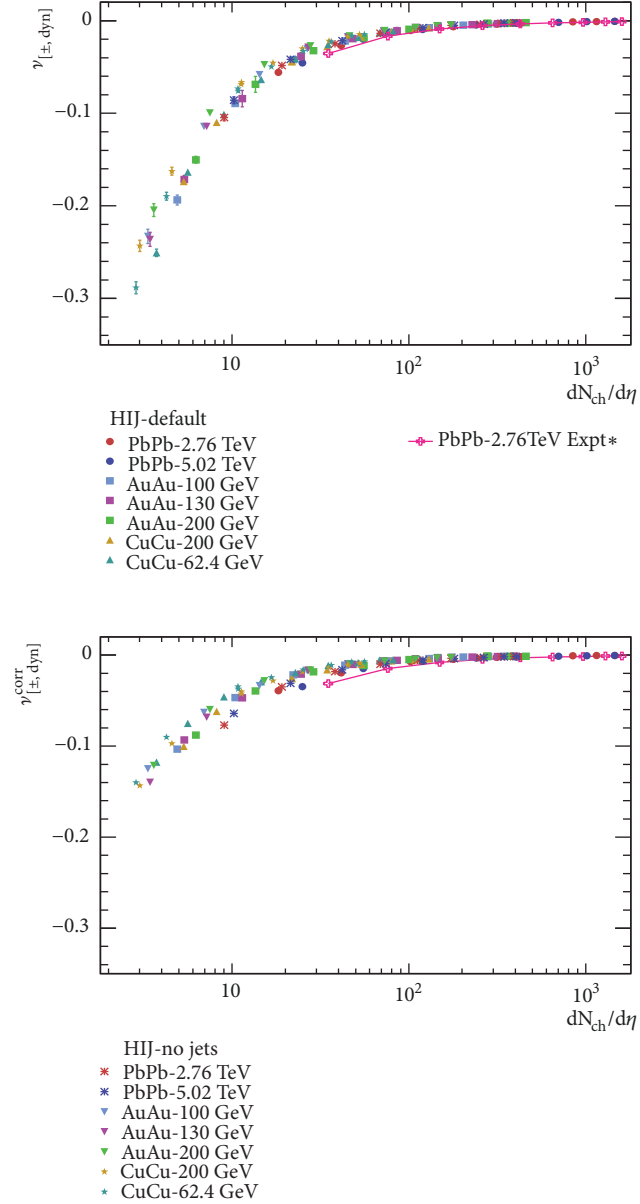
FIGURE 7: Variations of net charge fluctuations $\nu_{[+-,dyn]}$ and their corrected version, $\nu_{[+-,dyn]}^{corr}$, with charged particle density, $dN_{ch}/d\eta$, for the two sets of HIJING events. The lines are due to the 2.76 TeV Pb-Pb values taken from [17].

Following the details as given in [40] and using the equation

$$\nu_{dyn}[a,b] = \frac{\langle N_a^2 \rangle}{\langle N_a \rangle^2} + \frac{\langle N_b^2 \rangle}{\langle N_b \rangle^2} - 2\frac{\langle N_a N_b \rangle}{\langle N_a \rangle \langle N_b \rangle}$$

$$- \left(\frac{1}{\langle N_a \rangle} + \frac{1}{\langle N_b \rangle} \right) \tag{17}$$

the following form of ν_{dyn} may be obtained [41]:

$$\nu_{dyn}[a,b] = \frac{1}{\langle N_s \rangle}\left[\frac{\langle \alpha^2 \rangle}{\langle \alpha \rangle^2} + \frac{\langle \beta^2 \rangle}{\langle \beta \rangle^2} - 2\frac{\langle \alpha\beta \rangle}{\langle \alpha \rangle \langle \beta \rangle} \right.$$

$$\left. - \left(\frac{1}{\langle \alpha \rangle} + \frac{1}{\langle \beta \rangle} \right) \right] \simeq \frac{1}{\langle N_s \rangle} \nu^*[\alpha, \beta] \tag{18}$$

where $\nu^*[\alpha, \beta]$ is the quantity of the multiplicities of types a and b for each source. This gives $\nu_{a,b}$ to be inversely proportional to the size of the colliding nuclei. On the other hand, as the term $\langle N_s^2 \rangle - \langle N_s \rangle$ is canceled out by construction, ν_{dyn} is independent of the system size but requires an additional scaling due to the remaining term, $1/\langle N_s \rangle$. If $1/(1/\langle N_a \rangle + 1/\langle N_b \rangle)$ type of scaling is used, then, substituting (12) and (13) in (17), the term $1/\langle N_s \rangle$ vanishes and the following form of the scaling is obtained:

$$\frac{\nu_{dyn}[a,b]}{1/\langle N_a \rangle + 1/\langle N_b \rangle} = \frac{\nu_{dyn}[\alpha, \beta]}{1/\langle \alpha \rangle + 1/\langle \beta \rangle} \tag{19}$$

The scaling of this type has been tested and the results for the various data sets are shown in Figures 10 and 11. It may be seen in these figures that the scaled $\nu_{[+-,dyn]}$ values for a given energy are nearly independent of charged particle density. It is further observed that the magnitude of scaled $\nu_{[+-,dyn]}$ values increases as one moves from RHIC to LHC energies. The magnitude of $\nu_{[+-,dyn]}$ is observed to be inversely proportional to the number of subcollisions leading to the particle production. If number of particles produced in each subcollision is independent of collision centrality, $\nu_{[+-,dyn]}$ would exhibit $1/N$ scaling [42]. It has been reported [42] that in Au-Au collisions at 130 GeV $1/N$ scaling is clearly noted by the data. HIJING simulated data, however, supports such scaling. In contrast to this, findings from URQMD simulations do not support $1/N$ scaling, which maybe because in URQMD rescattering effects are included which would reduce the magnitude of $N\nu_{[+-,dyn]}$ for central collisions [42]. On the basis of various types of scaling of $\nu_{[+-,dyn]}$ tested in the present study and also the ones by other workers, it may be concluded here that $1/(1/\langle N_a \rangle + 1/\langle N_b \rangle)$ scaling of $\nu_{[+-,dyn]}$ is relatively a better scaling as compared to other scalings.

4. Conclusions

A systematic study of various aspects of net charge fluctuations has been looked into by simulating the Monte Carlo events using the HIJING generator in two different modes, (i) HIJING-default with jet-quenching turned off and (ii) production of jets and minijets turned off. Although both types of events exhibit almost similar dependence of $\nu_{[+-,dyn]}$ on collision centrality and charged particle density, the observed difference in the magnitude of fluctuations clearly reflects the role of jets and minijets in reduction of net charge fluctuations. The trend of energy dependence of ν_{dyn}, for various centrality bins, exhibited by the MC data used in the present study, matches with STAR and ALICE results. N_{part} and $dN_{ch}/d\eta$ scalings of $\nu_{[+-,dyn]}$ after applying the correction for global charge conservation are approximately exhibited by both types of event samples used. This is expected as, in HIJING case, AA collisions are treated as the superpositions
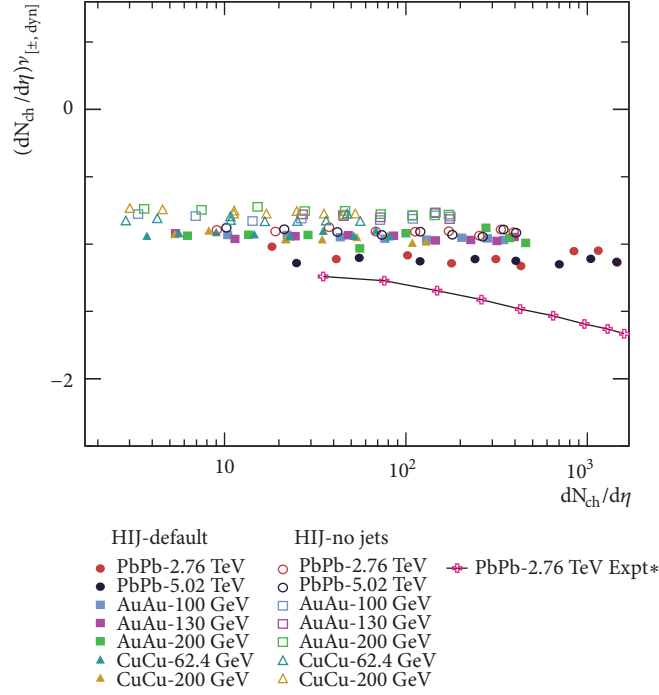
FIGURE 8: Scaling of $\nu_{[+-,dyn]}$ with $dN_{ch}/d\eta$ for various MC data samples at different energies.
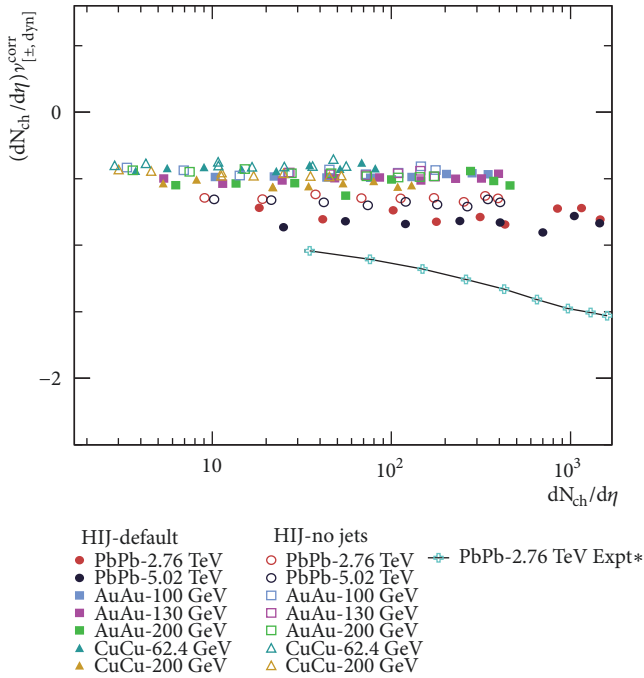
FIGURE 9: The same plot as in Figure 8 but after applying corrections to $\nu_{[+-,dyn]}$ values.
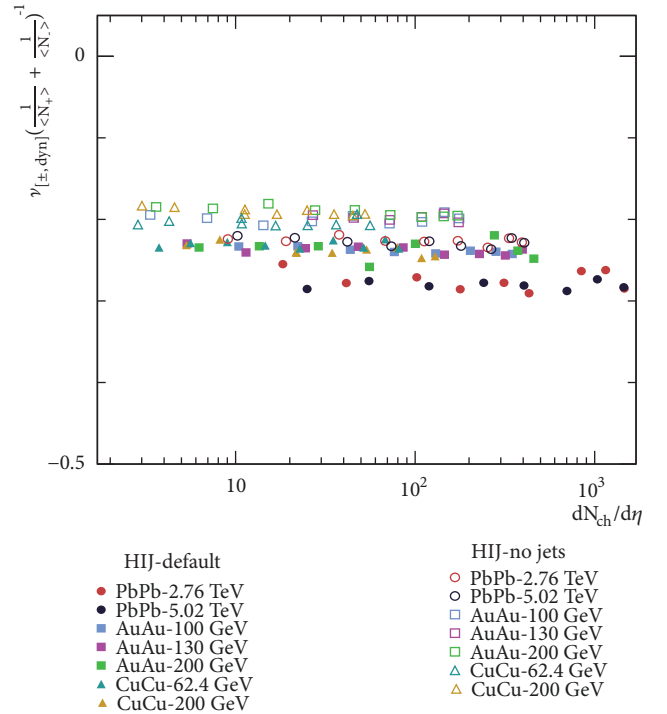
FIGURE 10: $1/(1/\langle N_+ \rangle + 1/\langle N_- \rangle)$ scaling of net charge fluctuations at different energies for the two sets of HIJING events.

of multiple nucleon-nucleon collisions. The findings also reveal that the production of jets and minijets plays dominant role in reducing the strength of particle correlations and fluctuations.

Data Availability

The data used to support the findings of this study are available from the corresponding author upon request.

FIGURE 11: $1/(1/\langle N_+ \rangle + 1/\langle N_- \rangle)$ scaling of corrected net charge fluctuations for two types of HIJING events at different energies.

Conflicts of Interest

The authors declare that there are no conflicts of interest.

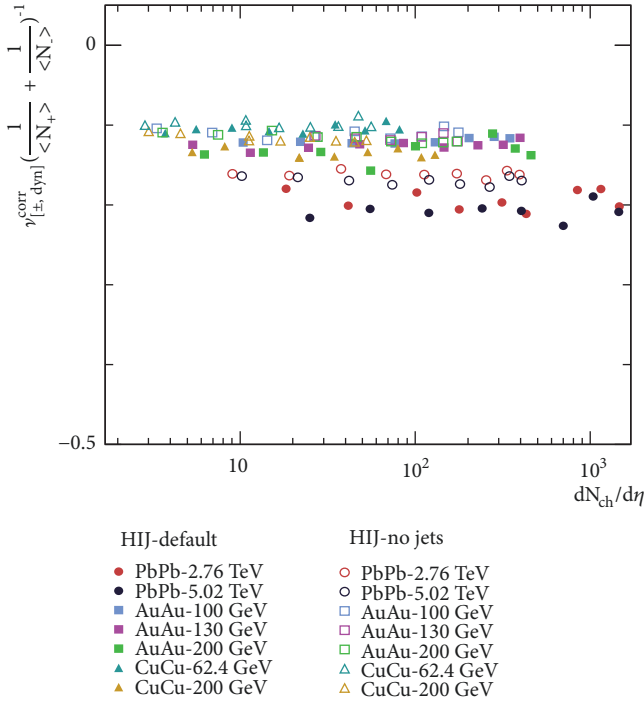## References

[1] E. A. De Wolf, I. M. Dremin, and W. Kittel, "Scaling laws for density correlations and fluctuations in multiparticle dynamics," *Physics Reports*, vol. 270, pp. 1–141, 1996.

[2] S. Ahmad, S. Khan, A. Kumar, A. Singh, A. Ahmad, and B. K. Singh, "Correlations and event-by-event fluctuations in high multiplicity events produced in ^{208}Pb-^{208}Pb collisions," *Advances in High Energy Physics*, vol. 2018, Article ID 6914627, 11 pages, 2018.

[3] R. C. Hwa, "Fractal measures in multiparticle production," *Physical Review D*, vol. 41, no. 5, p. 1456, 1990.

[4] S. Ahmad, A. R. Khan, M. Zafar, and M. Irfan, "On multifractality and multifractal specific heat in ion-ion collisions," *Chaos, Solitons & Fractals*, vol. 42, no. 1, pp. 538–547, 2009.

[5] S. Khan and S. Ahmad, "Multifractal characteristics of multiparticle production in heavy-ion collisions at SPS energies," *International Journal of Modern Physics E*, vol. 27, no. 1, Article ID 1850004, 2018.

[6] A. Bialas and R. Peschanski, "Moments of rapidity distributions as a measure of short-range fluctuations in high-energy collisions," *Nuclear Physics B*, vol. 273, no. 3-4, pp. 703–718, 1986.

[7] R. C. Hwa, "Beyond intermittency: erraticity," *Acta Physica Polonica B*, vol. 27, pp. 1789–1800, 1996.

[8] M. L. Cherry and KLM Collaboration, "Event-by-event analysis of high multiplicity Pb (158-GeV/nucleon) Ag/Br collisions," *Acta Physica Polonica B*, vol. 29, pp. 2129–2146, 1998.

[9] K. Fialkowski and R. Wit, "Event-by-event cluster analysis of final states from heavy ion collisions," *Acta Physica Polonica B*, vol. 30, pp. 2759–2765, 1999.

[10] B. Sharma, M. M. Aggarwal, N. R. Sahoo, and T. K. Nayak, "Dynamical charge fluctuations in the hadronic medium," *Physical Review C*, vol. 91, no. 2, Article ID 024909, 2015.

[11] M. Mukherjee, S. Basu, S. Choudhury, and T. K. Nayak, "Fluctuations in charged particle multiplicities in relativistic heavy-ion collisions," *Journal of Physics G: Nuclear and Particle Physics*, vol. 43, no. 8, Article ID 085102, 2016.

[12] S. Gosh, P. Mali, and A. Mukhopadhyay, "Net-charge fluctuation in Au+Au collisions at energies available at the facility for antiproton and Ion Research using the UrQMD model," *Physical Review C*, vol. 96, no. 2, Article ID 024912, 2017.

[13] S. Jeon and V. Koch, "Fluctuations of particle ratios and the abundance of hadronic resonances," *Physical Review Letters*, vol. 83, no. 26, p. 5435, 1999.

[14] H. Heiselberg and A. D. Jackson, "Anomalous multiplicity fluctuations from phase transitions in heavy ion collisions," *Physical Review C: Nuclear Physics*, vol. 63, Article ID 064904, 2001.

[15] S. Jeon and V. Koch, "Charged particle ratio fluctuation as a signal for quark-gluon plasma," *Physical Review Letters*, vol. 85, no. 10, p. 2076, 2000.

[16] M. Bleicher, S. Jeon, and V. Koch, "Event-by-event fluctuations of the charged particle ratio from nonequilibrium transport theory," *Physical Review C*, vol. 62, no. 6, Article ID 061902, 2000.

[17] B. Abelev and ALICE Collaboration, "Net-charge fluctuations in Pb-Pb collisions at $\sqrt{s_{NN}}$ = 2.76 TeV," *Physical Review Letters*, vol. 110, no. 15, Article ID 1523201, 2013.

[18] B. Mohanty, J. Alam, and T. K. Nayak, "Evolution of fluctuation in relativistic heavy-ion collisions," *Physical Review C: Nuclear Physics*, vol. 67, no. 2, Article ID 024904, 2003.

[19] E. V. Shuryak and M. A. stephanov, "Long-range charge fluctuations and search for a quark-gluon plasma signal," *Physical Review C*, vol. 63, no. 6, Article ID 064903, 2001.

[20] M. A. Aziz and S. Gavin, "Causal diffusion and the survival of charge fluctuations in nuclear collisions," *Physical Review C: Nuclear Physics*, vol. 70, Article ID 034905, 2004.

[21] M. Sakaida, M. Asakawa, and M. Kitazawa, "Effects of global charge conservation on time evolution of cumulants of conserved charges in relativistic heavy ion collisions," *Physical Review C*, vol. 90, no. 6, Article ID 064911, 2014.

[22] M. Prakash, R. Rapp, J. Wambach, and I. Zahed, "Isospin fluctuations in QCD and relativistic heavy-ion collisions," *Physical Review C*, vol. 65, no. 3, Article ID 034906, 2002.

[23] M. R. Atayan, B. Yuting, E. A. De Wolf et al. et al., "Charge fluctuations in π^+p and K$^+$p collisions at 250 GeV/c," *Physical Review D: Particles, Fields, Gravitation and Cosmology*, vol. 71, no. 1, Article ID 012002, 2005.

[24] S. Jeon and V. Koch, "Event-by-event fluctuations," in *Koch in Quark-Gluon Plasma3*, R. C. Hwa and X. N. Wang, Eds., p. 430, World Scientific, Singapore, 2004, https://arxiv.org/abs/hep-ph/0304012.

[25] S. A. Voloshin, "Transverse radial expansion in nuclear collisions and two particle correlations," *Physics Letters B*, vol. 632, no. 4, pp. 490–494, 2006.

[26] J. Zarnek, "Measures of charge fluctuations in nuclear collisions," *Physical Review C*, vol. 66, no. 2, Article ID 024905, 2002.

[27] B. J. Abelev and STAR Collaboration, "Beam-energy and system-size dependence of dynamical net charge fluctuations," *Physical Review C*, vol. 79, no. 2, Article ID 024906, 2009.

[28] K. Adox and PHENIX Collaboration, "Net charge fluctuations in Au + Au interactions at $\sqrt{sNN}$ = 130 GeV," *Physical Review Letters*, vol. 89, no. 8, Article ID 082301, 2002.

[29] C. A. Pruneau, S. Gavin, and S. Voloshin, "Methods for the study of particle production fluctuations," *Physical Review C*, vol. 66, no. 4, Article ID 0444904, 2002.

[30] L. Foà, "Inclusive study of high-energy multiparticle production and two-body correlations," *Physics Reports*, vol. 22, no. 1, pp. 1–56, 1975.

[31] J. Adamus and STAR Collaboration, "Net charge fluctuations in Au + Au collisions at $\sqrt{sNN}$ = 130 GeV," *Physical Review C*, vol. 68, no. 4, Article ID 044905, 2003.

[32] Z. You, W. Ke-Jun, and L. Feng, "Charged particle fluctuation in Au+Au collision," *Chinese Physics C*, vol. 34, no. 9, pp. 1436–1439, 2018.

[33] M. Gyulassy and X. N. Wang, "HIJING 1.0: a Monte Carlo program for parton and particle production in high energy hadronic and nuclear collisions," *Computer Physics Communications*, vol. 83, no. 2-3, pp. 307–331, 1994.

[34] Q. Liu and T. A. Trainor, "Jet quenching and event-wise mean-p_t fluctuations in Au-Au collisions at $\sqrt{sNN}$ = 200 GeV in Hijing-1.37," *Physics Letters B*, vol. 567, no. 3-4, pp. 184–188, 2003.

[35] K. Kajantie, P. V. Landshoff, and J. Lindfors, "Minijet production in high-energy nucleus-nucleus collisions," *Physical Review Letters*, vol. 59, no. 22, p. 2527, 1987.

[36] M. Gyulassy and M. Plumer, "Jet quenching in dense matter," *Physics Letters B*, vol. 243, no. 4, pp. 432–438, 1990.

[37] X. N. Wang, "Mini-jets and multiplicity fluctuation in small rapidity intervals," *Physics Letters B*, vol. 248, no. 3-4, pp. 447–452, 1990.

[38] C. A. Pruneau and STAR Collaboration, "Net charge fluctuations at RHIC," *Acta Physica Hungarica A*, vol. 25, no. 2-4, pp. 401–408, 2006.

[39] V. Koch and T. Schuster, "Energy dependence of K/π fluctuations in relativistic heavy-ion collisions," *Physical Review C: Nuclear Physics*, vol. 81, Article ID 034910, 2010.

[40] A. Biallas, M. Bleszynski, and W. Czyz, "Multiplicity distributions in nucleus-nucleus collisions at high energies," *Nuclear Physics B*, vol. 111, pp. 461–476, 1976.

[41] M. Arslandok and ALICE Collaboration, "Event-by-event identified particle ratio fluctuations in Pb–Pb collisions with alice using the identity method," *Nuclear Physics A*, vol. 956, pp. 870–873, 2016.

[42] C. A. Pruneau and STAR Collaboration, "Event by event net charge fluctuations," *Acta Physica Hungarica A. Heavy Ion Physics*, vol. 21, no. 2–4, pp. 261–266, 2004.

Research Article

Out-Of-Equilibrium Transverse Momentum Spectra of Pions at LHC Energies

Abdel Nasser Tawfik [1,2]

[1] *Nile University, Egyptian Center for Theoretical Physics, Juhayna Square of 26th-July-Corridor, 12588 Giza, Egypt*
[2] *World Laboratory for Cosmology And Particle Physics (WLCAPP), 11571 Cairo, Egypt*

Correspondence should be addressed to Abdel Nasser Tawfik; atawfik@nu.edu.eg

In order to characterize the transverse momentum spectra (p_T) of positive pions measured in the ALICE experiment, two thermal approaches are utilized; one is based on degeneracy of nonperfect Bose-Einstein gas and the other imposes an *ad hoc* finite pion chemical potential. The inclusion of missing hadron states and the out-of-equilibrium contribute greatly to the excellent characterization of pion production. An excellent reproduction of these p_T-spectra is achieved at $\mu_\pi = 0.12$ GeV and this covers the entire range of p_T. The excellent agreement with the experimental results can be understood as a manifestation of not-yet-regarded anomalous pion production, which likely contributes to the long-standing debate on "*anomalous*" proton-to-pion ratios at top RHIC and LHC energies.

1. Introduction

The collective properties of strongly interacting matter (radial flow, for instance) and dynamics of colliding hadrons can be explored from the study of transverse momentum distributions (p_T) of produced particles. RHIC results on well-identified particles produced at low p_T, especially pions, have shown that the bulk matter created can be well described by hydrodynamics [1]. It should be emphasized that the high-p_T spectra, especially for the lowest-lying Nambu-Goldstone bosons, pions, likely manifest dynamics and interactions of partons and jets created in the earliest stage of nuclear collisions [2]. For instance, the collective expansion in form of radial flow might be caused by internal pressure gradients. Furthermore, the p_T-distributions are assumed to determine conditions, such as temperature and flow velocity, gaining dominance during the late eras of the evolution of the high-energy collision which is generically well-described as kinetic freeze-out, where the elastic interactions are ceased, conclusively.

From the theoretical point of view, the p_T-spectra are excellent measurements enabling us a better understanding of the QCD interactions. Soft nonperturbative QCD can be well applied to low p_T-regime (below a few GeV/c) [3]. Fragmentation of QCD string [4], parton wave functions in flux tube [5], parton thermodynamics [6], and parton recombination [7] are examples on underlying physics. At high-p_T, hard-scattering cross-section from QCD perturbative calculations, parton distribution functions, and parton-to-hadron fragmentation functions have been successfully utilized in reproducing p_T-spectra of various produced particles [8].

It is worth mentioning that there is no well-defined line separating nonperturbative from perturbative p_T-regimes [3]. Even the various theoretical studies are not distinguishing sharply between both of them. For instance, when constructing partition functions, extensive and nonextensive statistical approaches are frequently misconducted [9–11]. For instance, the claim that high p_T-spectra of different produced particles are to be reproduced by Tsallis statistics seems being incomplete [11, 12]. This simply inspires a great contradiction between nonperturbative and perturbative QCD [12]. The statistical cluster decay could be scaled as power laws very similar to the ones of Tsallis statistics. The earlier is conjectured to cover a wide range of p_T, while the latter is limited to a certain p_T-regime. This would lead to an undesired mixing up that the observed power laws might be stemming from

the statistical cluster decay and interpreted as a Tsallis-type of nonextensivity.

In addition to the proposal of utilizing a generic (non)extensive statistical approach [9–11], we want here to recall another theoretical framework based on an *ad hoc* physically motivated assumption that the pion production might be interpreted due an out-of-equilibrium process [13]. Such an approach is stemming from the pioneering works of Bogolubov devoted to an explanation for the phenomenon of superfluidity on the basis of degeneracy of a non-perfect Bose-Einstein gas [14] and determining the general form of the energy spectrum, an ingenious application of the second quantization [15]. Finite pion chemical potential recalls Bogolubov dispersion relation for low-lying elementary excitations of pion fluid. In this case, degenerate state of statistical equilibrium is removed through inserting a noninvariant term to the Hamiltonian, e.g., pion chemical potential.

After a short review of the thermal approach, the Hadron Resonance Gas (HRG) model in equilibrium is introduced in Section 2. A discussion on how to drive it towards nonequilibrium through inclusion of repulsive interactions is added. In Section 3, we elaborate modifications carried out towards implementing nonperfect Bose-Einstein gas based on a proposal of pion superfluidity. Another out-of-equilibrium thermal approach is outlined in Section 4, where finite pion chemical potential is *ad hoc* imposed. The results shall be discussed in Section 5. The conclusions are given in Section 6.

2. A Short Review on Equilibrium Resonance Gas with Van der Waals

The hadron resonances treated as a noninteracting gas [16–22] are conjectured to determine the equilibrium thermodynamic pressure of QCD matter below chiral and deconfinement *critical* temperature, i.e., hadron phase. It has been shown that the thermodynamics of a strongly interacting system can also be approximated as an ideal gas composed of hadron resonances with masses ≤ 2 GeV [19, 23]. Interested readers are kindly advised to consult the most recent review article [24]. The resonances added in contribution with the degrees of freedom needed to characterize the hadron phase.

The grand canonical partition function can be constructed as

$$Z\left(T, \mu, V\right) = \text{Tr}\left[\exp^{(\mu \mathbf{N} - \mathbf{H})/\mathbf{T}}\right], \qquad (1)$$

where H, T, and μ are the Hamiltonian, the temperature, and the chemical potential of the system, respectively. The Hamiltonian can be given by as summation of the kinetic energies of relativistic Fermi and Bose particles including the relevant degrees of freedom and the interactions resulting in formation of resonances and well describing the particle production in high-energy collisions. Under these assumptions, the sum over the *single-particle partition* functions Z_h^1

of existing hadrons and their resonances introduces dynamics to the partition function,

$$\ln Z\left(T, \mu_h, V\right)$$
$$= V \sum_h \pm \frac{g_h}{2\pi^2} \int_0^\infty k^2 dk \ln\left\{1 \pm \exp\left[\frac{\mu_h - \varepsilon_h}{T}\right]\right\}, \qquad (2)$$

where $\varepsilon_h = (k^2 + m_h^2)^{1/2}$ is the dispersion relation of h-th particle, g_h is spin-isospin degeneracy factor, and $\pm$ stands for fermions and bosons, respectively.

In the present work, we include hadron resonances with masses ≤ 2 GeV compiling by the particle data group (PDG) 2018 [25]. This mass cut-off is assumed to define the validity of the HRG model in characterizing the hadron phase [26, 27]. The inclusion of hadron resonances with heavier masses leads to divergences in all thermodynamic quantities expected at temperatures larger than the Hagedorn temperature [16, 17]. In addition to these aspects, there are fundamental reasons (will be elaborated in forthcoming sections) favoring the utilization of even *ideal* HRG model in predicting the hadron abundances and their thermodynamics. For the sake of completeness, we highlight that the hadronic resonances which are not yet measured, including missing ones, can be parameterized as a spectral function [28].

As given earlier, we assume that the constituents of the HRG are free (collisionless) particles. Some authors prefer taking into account the repulsive (*electromagnetic*) van der Waals interactions in order to partly compensate strong interactions in the hadronic medium [29] and/or to drift the system towards even partial nonequilibrium. Accordingly, each constituent is allowed to have an *eigen*volume and the hadronic system of interest becomes thermodynamically partially out-of-equilibrium (how does a statistical thermal system, like HRG, become out-of-equilibrium? To answer this question, one might need to recall the main parameters describing particle production in equilibrium. These are T, μ_h, and V [30]. In the present work, we first focus on the third parameter and therefore describe this as a partial out-of-equilibrium process. The volume V, the normalization parameter typically constrained by pions, becomes a subject of modification through van der Waals repulsive interactions, for instance. Furthermore, it should be also noticed that the chemical potentials μ_h should be modified, as well, at least in connection with the modification in V. This would explain that taking into account van der Waals repulsive interactions, known as excluded volume corrections, contributes to deriving the system of interest towards nonequilibrium.). Thus, the total volume of HRG constituents should be subtracted from the fireball volume or that of heat bath. Considerable modifications in thermodynamics of HRG including energy, entropy, and number densities should be taken into consideration. It should be highlighted that the hard-core radius of hadron nuclei can be related to the multiplicity fluctuations.

How large can be the modification in V? The answer to this question is conditioned, for instance, to the capability of the HRG model with finite-volumed constituents to reproduce first-principle lattice QCD simulations. At radius $r > 0.2$ fm, it was found that the disagreement with reliable

lattice QCD calculations becomes more and more larger [29]. It was concluded that such an excluded volume-correction becomes practically irrelevant, as it causes negligible effects at low temperatures [29]. But on the other hand, a remarkable deviation from the lattice QCD calculations is noticed at high T.

The repulsive interactions between hadrons are considered as a phenomenological extension of the HRG model. Exclusively, this is based on van der Waals excluded volume [31–34]. Intensive theoretical works have been devoted to the estimation of the excluded volume and its effects on the particle production and the fluctuations [35], for instance. It is conjectured that the hard-core radius of the hadrons can be related to the multiplicity fluctuations of the produced particles [36]. In the present work, we simply assume that the hadrons are spheres and all have the same radius. On the other hand, the assumption that the radii would be depending on the hadron masses and sizes could come up with a very small improvement. Various types of interactions have been assumed, as well [37, 38]. For the sake of possible comparison with existing literature, we focus on the van der Waals repulsive interaction. By replacing the system volume V by the actual one, V_{act}, the van der Waals excluded volume can be deduced [31]

$$V_{act} = V - \sum_h v_h N_h, \tag{3}$$

where $v_h = 4 \, (4\pi r_h^3/3)$ is volume and N_h is the number of each constituent hadron. r_h is the corresponding hard sphere radius of h-th particle. The procedure encoded in (3) leads to modification in the chemical potentials $\tilde{\mu}_h = \mu_h - v_h \, p$, where the thermodynamic pressure p is self-consistently expressed as $\sum_h p_h^{id}(T, \tilde{\mu}_h)$ and

$$n = \frac{\sum_h n_h^{id}\,(T, \tilde{\mu}_h)}{1 + \sum_h v_h n_h^{id}\,(T, \tilde{\mu}_h)}, \tag{4}$$

$$\epsilon = \frac{\sum_h \epsilon_h^{id}\,(T, \tilde{\mu}_h)}{1 + \sum_h v_h n_h^{id}\,(T, \tilde{\mu}_h)}, \tag{5}$$

$$s = \frac{\sum_h s_h^{id}\,(T, \tilde{\mu}_h)}{1 + \sum_h v_h n_h^{id}\,(T, \tilde{\mu}_h)}, \tag{6}$$

where the superscript *id* refers to thermodynamic quantities calculated in HRG model with point-like constituents, i.e., ideal gas.

In the section that follows, we work out out-of-equilibrium p_T spectra of the positive pions, where finite pion chemical potential shall be *ad hoc* inserted in.

3. Out-of-Equilibrium p_T-Spectra of Pions

In U(1) global symmetry, where the scalar field $\phi(x)$ has a unitary transformation by the phase factor $\exp(-i\alpha)$,

the Bose-Einstein condensation of lowest-lying Nambu-Goldstone bosons could be studied from the partition function [39]

$$\ln z\,(T, \mu_\pi) = \frac{V}{T}\left(\mu_\pi^2 - m^2\right)\xi^2 - V\int \frac{d^3 p}{(2\pi)^3}$$
$$\cdot \left[\frac{\varepsilon}{T} + \ln\left(1 - e^{-(\varepsilon - \mu_\pi)/T}\right) + \ln\left(1 - e^{-(\varepsilon + \mu_\pi)/T}\right)\right], \tag{7}$$

where ξ is a parameter carrying full infrared characters of the scalar field. This can be treated as a variational parameter relating to the charge of condensed boson particle. At $|\mu_\pi| < m$, (2) can obviously be recovered. When the volume element $d^3 p$ is expressed in p_T, rapidity y and azimuthal angle ϕ as $d^3 p = p_T m_T \cosh(y) dp_T \, dy \, d\phi$ and the energy becomes $\varepsilon = m_T \cosh(y)$, then at $\mu_\pi \longrightarrow m$, where $m_T = (p_T^2 + m^2)^{1/2}$ is the pion transverse mass, the transverse momentum spectrum of pions is given as

$$\frac{1}{2\pi p_T}\frac{d^2 N_\pi}{dp_y dy} = V$$
$$\cdot \frac{m_T^{(\pi)}\cosh(y)}{(2\pi)^3}\left\{\exp\left[\frac{m_T^{(\pi)}\cosh(y) - \mu_\pi}{T}\right]\right.$$
$$\left. - 1\right\}^{-1} + \sum_{\text{reson.}\longrightarrow\pi} V \tag{8}$$
$$\cdot \frac{m_T^{(reson.)}\cosh(y)}{(2\pi)^3}\left\{\exp\left[\frac{m_T^{(reson.)}\cosh(y) - \mu_\pi}{T}\right]\right.$$
$$\left. - 1\right\}^{-1} \times b_{\text{reson.}\longrightarrow\pi},$$

where $b_{\text{reson.}\longrightarrow\pi}$ is the branching ratio of resonances decaying into pions.

The pion p_T-spectrum is calculated from direct pions plus all contributions stemming from the heavier hadron resonances decaying into pions, in which the corresponding branching ratio should be taken into consideration (8)

$$\frac{1}{2\pi p_T}\frac{d^2 N_\pi}{dp_y dy}\bigg|_\pi^{\text{total}}$$
$$= \frac{1}{2\pi p_T}\frac{d^2 N_\pi}{dp_y dy}\bigg|_\pi \tag{9}$$
$$+ \sum_{\text{reson.}\longrightarrow\pi}\frac{1}{2\pi p_T}\frac{d^2 N_{\text{reson.}}}{dp_y dy}\bigg|_{\text{reson.}\longrightarrow\pi}$$
$$\times b_{\text{reson.}\longrightarrow\pi}.$$

In the results shown in Figure 1, we distinguish between the hadron resonances with the given mass cut-off and that without sigma states. In both cases, we also distinguish between results at chemical equilibrium of pion production, i.e., $\mu_\pi = 0$, and that at out-of-equilibrium, i.e., $\mu_\pi \neq 0$.
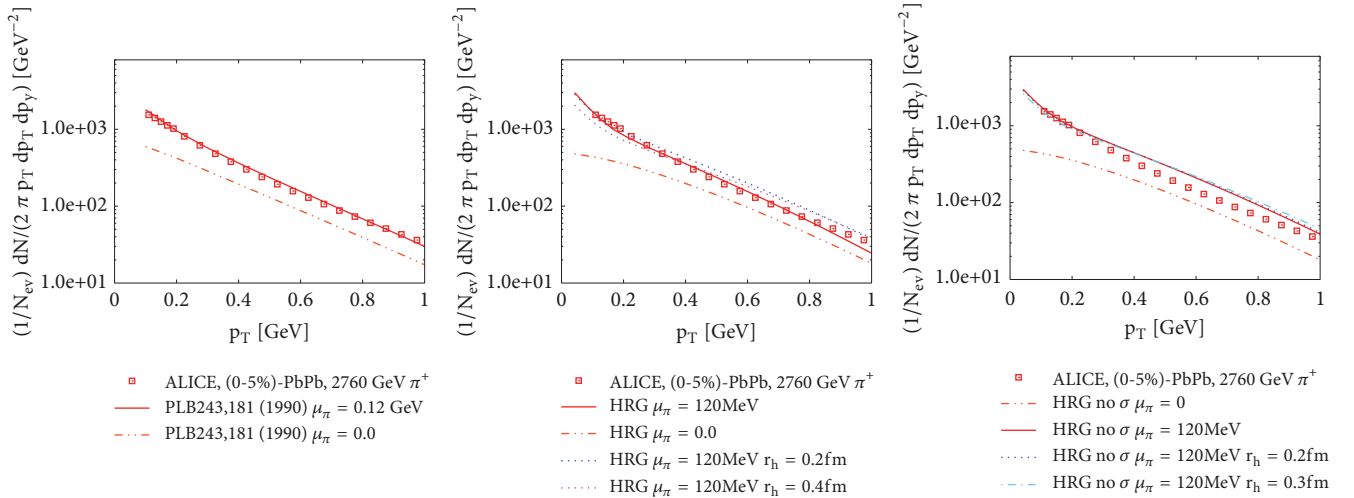
FIGURE 1: Number of positive pions per transverse momentum per rapidity is given dependent on the transverse momentum. The symbols refer to the ALICE measurements in the most central $(0 − 5\%)$ Pb+Pb collisions at 2.67 TeV. The left-hand panel shows a comparison with (10) at vanishing $\mu_\pi = 0$ and finite $\mu_\pi = 0.12$ GeV [41]. In middle and right-hand panels, HRG calculations (10), with and without scalar σ states and excluded volume corrections are confronted to the experimental measurements, as well.

4. Out-of-Equilibrium Thermal Distribution

In this section, we recall another thermal distribution at out-of-equilibrium [13], inspired by the proposal of Bogolubov to explaining the phenomenon of superfluidity as degeneracy of a nonperfect Bose-Einstein gas and determine a general form of energy spectra, a kind of ingenious application of second quantization.

In the approach introduced in [13], the p_T-spectra of *negatively* charged bosons measured from 200 A GeV O+Au and S+S collisions by NA35 experiment have been successfully reproduced. It was assumed that a cylindrical tube of matter with radius R expands, longitudinally, but without transverse flow $v_z = z/t$. When replacing ε in (2), for instance, by the azimuthal angle ϕ and the covariant form $p_\mu u^\mu$ (four-momentum and velocity) and then integrating over the freeze-out time $\tau_{fo} = \tau$, the p_T-distribution could be determined.

Then, at finite rapidity $y \neq 0$, the pion p_T-spectrum reads

$$
\frac{1}{2\pi p_T} \frac{d^2 N_\pi}{dp_y dy} = \left(\pi R^2 \tau_{fo}\right) \frac{m_T \cosh(y)}{(2\pi)^3}
$$
$$
\cdot \sum_{n=1}^{\infty} (\pm)^{n+1} \exp\left(n\frac{\mu_\pi}{T}\right) K_1\left[n\frac{m_T}{T}\cosh(y)\right].
$$

(10)

The contributions likely added by heavy resonances are contributing straightforwardly to (10). In Figure 1, we distinguish between results at chemical equilibrium of pion production, i.e., $\mu_\pi = 0$ and that at out-of-equilibrium, i.e., $\mu_\pi \neq 0$. Accordingly, we can examine the possibility of proposing a plausible explanation for the long-standing baryon-to-meson ratios, such as proton-to-pion ratios, especially at top RHIC and LHC energies [40]. We propose that this would be due to anomaly in the pion production.

5. Results

Figure 1 shows p_T-spectra of positive pions in dependence on the transverse momentum. The symbols refer to the ALICE measurements in the most central $(0 − 1\%)$ Pb+Pb collisions at 2.67 TeV [41]. The curves represent the present calculations.

The calculations from (10) at vanishing (dash-double-dotted curve) and finite $\mu_\pi = 0.12$ GeV (solid curve) are depicted in the left panel. It is obvious that finite μ_π leads to excellent agreement with the experimental results. The middle and right panels show the impacts for the excluded volume corrections and the scalar sigma states, respectively.

As done in the left panel, the contributions added by finite μ_π are examined in the middle panel. We find that the results from ideal HRG model at vanishing μ_π underestimate the experimental results. Finite μ_π and finite r_h improve the reproduction of the experimental results.

It intends to investigate the importance of these sigma states in reproducing p_T-spectra of pions at LHC energies, right panel. Various sigma states are to be in(ex)cluded: $I = 1/2$, $K_0^*(800)$ known as κ, which was excluded from 2014 particle data group and from our calculations as well, and $K_0^*(1430)$, $I = 1$, $a_0(980)$ and $a_0(1450)$ and $I = 0$, $f_0(500)$ widely known as σ, $f_0(980)$, $f_0(1370)$, $f_0(1500)$, and $f_0(1710)$.

The HRG calculations (8) with and without sigma states are presented in the right panels. Also, here we distinguish between vanishing (dash-double-dotted curve) and finite $\mu_\pi = 0.12$ GeV (solid curve). As the case with out-of-equilibrium thermal distributions, almost the same conclusion can be drawn here. Furthermore, the impacts of the inclusion of scalar sigma states are analyzed. It is obvious that these states seem to enhance the out-of-equilibrium, especially at large p_T. The excluded volume corrections are taken into consideration in the way that all stable hadrons and resonances with masses < 2 GeV are assumed to equally

have finite volume, r_h. As discussed earlier, at $r_h = 0.2$ fm, the corrections seem very small. There is no such a large variety to increase r_h and simultaneously conserve the thermodynamics consistency. A systematic analysis has been discussed in [29]; see Figure 1 and the related text.

The small difference when r_h is increased from 0.2 to 0.4 fm can basically be understood from the corresponding freeze-out temperature, with the inclusion of scalar sigma states $T_{ch} \simeq 151$ MeV, at $r_h = 0.2$ fm. But at $r_h = 0.4$ fm, T_{ch} becomes $\simeq 167$ MeV. These results are confirmed when scalar sigma states are removed, $T_{ch} \simeq 159$ MeV at $r_h = 0.2$ fm. Here, it was not possible to increase r_h to 0.4 fm due to divergence in the thermodynamic quantities, at the chemical freeze-out, for instance, T_{ch} should jump to ~ 1 GeV to fulfill the freeze-out conditions [20–22]! Therefore we have checked $r_h = 0.3$ fm. The corresponding $T_{ch} \simeq 164$ MeV. It seems in order to highlight that these results are limited to the validity of the approximation that all hadrons are conjectured to have the same radius, $r_h = 0.3$ fm.

We find that at vanishing μ_π, the results from (8) with and without scalar sigma states are almost identical. But at finite μ_π, the HRG calculations with and without scalar sigma states become distinguishable. This can be understood due to the remarkable characteristics and the great experimental abundances of the sigma states, which would appear as two-pion scalar-isoscalar resonances and are regarded as excitations of the scalar condensates, i.e., playing similar roles as the Higgs boson does for strong interactions [42]. Their $\bar{q}q$-channel interaction is a maximally attractive one. This could be so strong that it breaks spontaneously the chiral symmetry and produces a quark condensate. Instanton-induced 't Hooft interaction is also conjectured as a mechanism for that attraction [42].

In order to elaborate more about the reasons why we have chosen another alternative and thought of confronting measured p_T-spectra of pions to Bogolubov superfluidity of Bose-Einstein gas and/or a thermal approach for out-of-equilibrium production of pions, i.e., finite μ_π, some remarks are now in order. Interpreting out-of-equilibrium in heavy-ion collisions at LHC in terms of the nonextensive Tsallis statistics [43] should be a subject of a fundamental revision. This has been discussed in great detail in [9–11]. On the one hand, the basic idea behind the thermal approach such as the HRG model is apparently additivity. Obviously, the Tsallis-type approach applies extensive statistics to the *additive* HRG, where both exponential and logarithm functions are merely replaced with the corresponding Tsallis counterpart function. On the other hand, the p_T-spectra of positive pions from the most central (0 – 5%) Pb+Pb collisions at 2.67 TeV are not reproducible by (20) in [43] (not drawn in Figure 1). But an excellent reproduction of these p_T-spectra is achieved at $\mu_\pi = 0.12$ GeV, Section 4. The excellent agreement apparently covers the entire range of p_T, left panel of Figure 1.

6. Conclusions and Outlook

The standard statistical thermal approach was reported as not being able to reproduce various baryon-to-boson ratios, especially at top RHIC and LHC energies [40]. In reproducing the measured p_T-spectra of positive pions at LHC energies, we have decided in favor for another alternative thermal approach assuming an out-of-equilibrium production of pions, ($\mu_\pi \neq 0$). In addition to this, we have introduced out-of-equilibrium production of pions to the well-known HRG model. In ancillary to the baryon, the strangeness chemical potential and the electric charge potential, we have imposed $\mu_\pi \neq 0$, as well.

We have shortly highlighted the incompleteness of nonextensive Tsallis statistics, especially when confronted to bulk matter created at relativistic energies. The basic idea of implementing an *additive* resonance gas even with Tsallis algebra, where both exponential and logarithm functions are properly replaced by Tsallis algebra, seems not at all modifying the extensivity. The latter obviously contradicts the intention of taking into account out-of-equilibrium particle production.

We conclude that p_T-spectra of positive pions produced in most central (0 – 5%) Pb+Pb collisions at 2.67 TeV are well reproduced at $\mu_\pi = 0.12$ GeV. This is the case in two different thermal approaches. The first one is based on degeneracy of a nonperfect Bose-Einstein gas or an ingenious application of second quantization known as Bogolubov superfluidity. The second one is the well-known HRG model, in which $\mu_\pi \neq 0$ was *ad hoc* introduced. The baryon, strangeness, and electric charge chemical potentials, etc. can also be taken into consideration. This approach seems being successful in reproducing p_T-spectra of positive pions, at LHC energies, when PDG sigma states are taken into account.

Future works shall be devoted to a systematic comparison with other approaches and to investigating the impacts that the PDG sigma states in reproducing p_T-spectra of other hadrons. Furthermore, p_T-spectra of other bosons shall be extended to understand whether they require out-of-equilibrium processes, as the positive pions do. The behavior of the pion production at high energies, where the production of kaons, protons, and antiprotons seem requiring anomalously large contributions from the exponential term to describe the shape of their transverse momenta, could be a subject of a similar out-of-equilibrium analysis, as well.

Data Availability

The availability data are available.

Conflicts of Interest

The author declares that he has no conflicts of interest.

Acknowledgments

References

[1] N. Gyulassy and L. McLerran, "New forms of QCD matter discovered at RHIC," *Nuclear Physics A*, vol. 750, no. 1, pp. 30–63, 2005.

[2] W. Bauer and G. D. Westfall, *Advances in Nuclear Dynamics 5*, Springer, New York, NY, USA, 1999.

[3] C. Y. Wong and G. Wilk, "Tsallis fits to p_T spectra and multiple hard scattering in pp collisions at the LHC," *Physical Review D: Particles, Fields, Gravitation and Cosmology*, vol. 87, Article ID 114007, 2013.

[4] B. Andersson, G. Gustafson, and B. Nilsson-Almqvist, "A model for low-pT hadronic reactions with generalizations to hadron-nucleus and nucleus-nucleus collisions," *Nuclear Physics B*, vol. 281, no. 1-2, pp. 289–309, 1987.

[5] C.-Y. Wong and G. Gatoff, "The transverse profile of a color flux tube," *Physics Reports*, vol. 242, no. 4-6, pp. 489–494, 1994.

[6] I. Kraus, J. Cleymans, H. Oeschler, and K. Redlich, "Particle production in p–p collisions and predictions for √s=14 TeV at the CERN Large Hadron Collider (LHC)," *Physical Review C: Nuclear Physics*, vol. 79, no. 1, Article ID 014901, 2009.

[7] T. Wibig, "Journal of Physics G: Nuclear and Particle PhysicsThe non-extensivity parameter of a thermodynamical model of hadronic interactions at LHC energies," *Journal of Physics G: Nuclear and Particle Physics*, vol. 37, no. 11, Article ID 115009, 2010.

[8] S. J. Brodsky, G. de Téramond, and M. Karliner, "Puzzles in hadronic physics and novel quantum chromodynamics phenomenology," *Annual Review of Nuclear and Particle Science*, vol. 62, pp. 1–35, 2012.

[9] A. Tawfik, H. Yassin, and E. R. Abo Elyazeed, "Chemical freeze-out parameters within generic nonextensive statistics," *Indian Journal of Physics*, vol. 92, no. 10, pp. 1325–1335, 2018.

[10] A. N. Tawfik, "Lattice QCD thermodynamics and RHIC-BES particle production within generic nonextensive statistics," *Physics of Particles and Nuclei Letters*, vol. 15, no. 3, pp. 199–209, 2018.

[11] A. N. Tawfik, "Axiomatic nonextensive statistics at NICA energies," *The European Physical Journal A*, vol. 52, p. 253, 2016.

[12] A. Bialas, "Tsallis p⊥ distribution from statistical clusters," *Physics Letters B*, vol. 747, pp. 190–192, 2015.

[13] M. Kataja and P. V. Ruuskanen, "Non-zero chemical potential and the shape of the pT-distribution of hadrons in heavy-ion collisions," *Physics Letters B*, vol. 243, no. 3, pp. 181–184, 1990.

[14] N. Bogolubov, "On the theory of superfluidity," *Journal of Physics*, vol. XI, no. 1, p. 23, 1947.

[15] L. Landau, "On the theory of superfluidity," *Physical Review A: Atomic, Molecular and Optical Physics*, vol. 75, no. 5, pp. 884–885, 1949.

[16] F. Karsch, K. Redlich, and A. Tawfik, "Hadron resonance mass spectrum and lattice QCD thermodynamics," *The European Physical Journal C*, vol. 29, no. 4, pp. 549–556, 2003.

[17] F. Karsch, K. Redlich, and A. Tawfik, "Thermodynamics at non-zero Baryon number density: a comparison of lattice and Hadron resonance gas model calculations," *Physics Letters B*, vol. 571, no. 1-2, pp. 67–74, 2003.

[18] K. Redlich, F. Karsch, and A. Tawfik, "Heavy-ion collisions and lattice QCD at finite baryon density," *Journal of Physics G: Nuclear and Particle Physics*, vol. 30, no. 8, p. S1271, 2004.

[19] A. Tawfik, "QCD phase diagram: a comparison of lattice and hadron resonance gas model calculations," *Physical Review D: Particles, Fields, Gravitation and Cosmology*, vol. 71, Article ID 054502, 2005.

[20] A. Tawfik, "A universal description for the freezeout parameters in heavy-ion collisions," *Nuclear Physics A*, vol. 764, pp. 387–392, 2006.

[21] A. Tawfik, "Condition driving chemical freeze-out," *Europhysics Letters*, vol. 75, no. 3, p. 420, 2006.

[22] A. Tawfik, "Influence of strange quarks on the QCD phase diagram and chemical freeze-out," *Journal of Physics G: Nuclear and Particle Physics*, vol. 31, no. 6, pp. S1105–S1110, 2005.

[23] R. Venugopalan and M. Prakash, "Thermal properties of interacting hadrons," *Nuclear Physics A*, vol. 546, no. 4, pp. 718–760, 1992.

[24] A. N. Tawfik, "Equilibrium statistical-thermal models in high-energy physics," *International Journal of Modern Physics A*, vol. 29, no. 17, Article ID 1430021, 2014.

[25] M. Tanabashi, K. Hagiwara, K. Hikasa et al., "Review of particle physics," *Physical Review D: Particles, Fields, Gravitation and Cosmology*, vol. 98, Article ID 030001, 2018.

[26] R. Hagedorn, "Statistical thermodynamics of strong interactions at high energies," *Nuovo Cimento Supplemento*, vol. 3, pp. 147–186, 1965.

[27] R. Hagedorn, "Large-angle cross-section $p+p{\longrightarrow}A+B$ and $\pi+p{\longrightarrow}A+B$ at high energies predicted by the statistical model," *Nuovo Cimento Supplemento*, vol. 35, pp. 216–226, 1965.

[28] A. Majumder and B. Müller, "Hadron mass spectrum from lattice QCD," *Physical Review Letters*, vol. 105, Article ID 252002, p. 25, 2002.

[29] A. Tawfik, "Constant-trace anomaly as a universal condition for the chemical freeze-out," *Physical Review C*, vol. 88, Article ID 035203, 2013.

[30] M. Floris, "Hadron yields and the phase diagram of strongly interacting matter," *Nuclear Physics A*, vol. 931, pp. 103–112, 2014.

[31] D. H. Rischke, M. I. Gorenstein, H. Stöcker, and W. Greiner, "Excluded volume effect for the nuclear matter equation of state," *Zeitschrift für Physik C Particles and Fields*, vol. 51, no. 3, pp. 485–489, 1991.

[32] J. Cleymans, M. I. Gorenstein, J. Stalnacke, and E. Suhonen, "The hadronisation of a quark-gluon plasma," *Zeitschrift für Physik C Particles and Fields*, vol. 58, no. 2, pp. 347–355, 1993.

[33] G. D. Yen, M. I. Gorenstein, W. Greiner, and S. N. Yang, "Excluded volume hadron gas model for particle number ratios in A + A collisions," *Physical Review C: Nuclear Physics*, vol. 56, no. 4, pp. 2210–2218, 1997.

[34] M. I. Gorenstein, M. Gaździcki, and W. Greiner, "Critical line of the deconfinement phase transitions," *Physical Review C: Nuclear Physics*, vol. 72, no. 2, Article ID 024909, 2005.

[35] M. I. Gorenstein, M. Hauer, and D. O. Nikolajenko, "Particle number fluctuations in nuclear collisions within an excluded volume hadron gas model," *Physical Review C: Nuclear Physics*, vol. 76, no. 2, Article ID 024901, 2007.

[36] M. I. Gorenstein, M. Hauer, and O. N. Moroz, "Viscosity in the excluded volume hadron gas model," *Physical Review C: Nuclear Physics*, vol. 77, no. 2, Article ID 024911, 2008.

[37] V. Vovchenko, M. I. Gorenstein, and H. Stoecker, "Modeling baryonic interactions with the Clausius-type equation of state," *The European Physical Journal A*, vol. 54, p. 16, 2018.

[38] V. Vovchenko, M. I. Gorenstein, and H. Stoecker, "van der Waals interactions in hadron resonance gas: from nuclear matter to lattice QCD," *Physical Review Letters*, vol. 118, no. 18, Article ID 182301, 2017.

[39] J. I. Kapusta, *Finite-Temperature Field Theory*, Cambridge Monographs on Mathematical Physics, Cambridge University Press, Cambridge, UK, 1989.

[40] B. Abelev, J. Adam, D. Adamová et al., "Production of charged pions, kaons and protons at large transverse momenta in pp and Pb–Pb collisions at $\sqrt{s_{NN}}$=2.76 TeV," *Physics Letters B*, vol. 736, pp. 196–207, 2014.

[41] B. Abelev, J. Adam, D. Adamová et al., "Centrality dependence of π, K, and p production in Pb-Pb collisions at $\sqrt{s_{NN}}$ = 2.76 TeV," *Physical Review C*, vol. 88, Article ID 044910, 2013.

[42] V. V. Flambaum and E. V. Shuryak, "Dependence of hadronic properties on quark masses and constraints on their cosmological variation," *Physical Review D*, vol. 67, Article ID 083507, 2003.

[43] M. D. Azmi and J. Cleymans, "Transverse momentum distributions in proton-proton collisions at LHC energies and Tsallis thermodynamics," *Journal of Physics G: Nuclear and Particle Physics*, vol. 41, no. 6, Article ID 065001, 2014.

Research Article

A Description of Transverse Momentum Distributions in $p + p$ Collisions at RHIC and LHC Energies

Jia-Qi Hui and Zhi-Jin Jiang (iD)

College of Science, University of Shanghai for Science and Technology, Shanghai 200093, China

Correspondence should be addressed to Zhi-Jin Jiang; jzj265@163.com

It has long been debated whether the hydrodynamics is suitable for the smaller colliding systems such as $p + p$ collisions. In this paper, by assuming the existence of longitudinal collective motion and long-range interactions in the hot and dense matter created in $p + p$ collisions, the relativistic hydrodynamics incorporating with the nonextensive statistics is used to analyze the transverse momentum distributions of the particles. The investigations of the present paper show that the hybrid model can give a good description of the currently available experimental data obtained in $p + p$ collisions at RHIC and LHC energies, except for p and $\overline{p}$ produced in the range of $p_T > 3.0$ GeV/c at $\sqrt{s} = 200$ GeV.

1. Introduction

In the past decade, the experimental results of heavy ion collisions at both RHIC and LHC energies have been extensively studied. These studies have shown that the strongly coupled quark-gluon plasma (sQGP) might be created in these collisions [1–9], which exhibits a clear collective behavior almost like a perfect fluid with very low viscosity [10–28]. Therefore, the evolution of sQGP can be described in the scope of relativistic hydrodynamics. However, unlike heavy ion collisions, $p + p$ collisions are a relatively smaller system with lower multiplicity, larger viscosity, and larger fluctuation [29]. The reasonableness of applying relativistic hydrodynamics in depicting the evolution of sQGP created in $p + p$ collisions has undergone an endless debate.

In this paper, by supposing the existence of collective flow in $p + p$ colliding direction, the relativistic hydrodynamics including phase transition is introduced to describe the longitudinal expansion of sQGP. Besides the collective flow, the thermal motion also exists in sQGP. The evolution of sQGP is therefore the superposition of collective flow and thermal motion. Known from the investigations of [30, 31], the long-range interactions and memory effects might appear in sQGP. This guarantees the reasonableness of nonextensive

statistics in describing the thermodynamic aspects of sQGP. Hence, in this paper, we will use the nonextensive statistics instead of conventional statistics to characterize the thermal motion of the matter created in $p + p$ collisions.

The nonextensive statistics, *i.e.*, Tsallis nonextensive thermostatistics, is the generalization of conventional Boltzmann-Gibbs statistics, which is proposed by C. Tsallis in his pioneer work of [32]. This statistical theory overcomes the inabilities of the conventional statistical mechanics by assuming the existence of long-range interactions, long-range microscopic memory, or fractal space-time constraints in the thermodynamic system. It has a wide range of applications in cosmology [33], phase shift analyses for the pion-nucleus scattering [34], dynamical linear response theory, and variational methods [35]. It has achieved a great success in solving many physical problems, such as the solar neutrino problems [36], many-body problems, the problems in astrophysical self-gravitating systems [37], and the transverse momentum spectra [38–40].

The article is organized as follows. In Section 2, a brief description is given about the employed hydrodynamics, presenting its analytical solutions. The solutions are then used in Section 3 to formulate the transverse momentum distributions of the particles produced in $p + p$ collisions in

the light of Cooper-Frye prescription. The last Section 4 is about conclusions.

2. A Brief Introduction to the Hydrodynamic Model

The main content of the relativistic hydrodynamic model [15, 41] used in this paper is as follows.

The expansion of fluid obeys the continuity equation

$$\partial_\mu T^{\mu\nu} = 0, \quad \mu, \nu = 0, 1, \tag{1}$$

where

$$T^{\mu\nu} = (\varepsilon + p) u^\mu u^\nu - p g^{\mu\nu} \tag{2}$$

is the energy-momentum tensor of fluid and $g^{\mu\nu} = \text{diag}(1, -1)$ is the metric tensor. The four-velocity of fluid $u^\mu = (u^0, u^1) = (\cosh y_F, \sinh y_F)$, where y_F is the rapidity of fluid. ε and p in Equation (2) are the energy density and pressure of fluid, respectively, which are related by the sound speed c_s of fluid *via* the equation of state

$$\frac{dp}{d\varepsilon} = \frac{s dT}{T ds} = c_s^2, \tag{3}$$

where T and s are the temperature and entropy density of fluid, respectively.

The projection of Equation (1) to the direction of u_μ leads to the continuity equation for entropy conservation

$$\partial_\nu (s u^\nu) = 0. \tag{4}$$

The projection of Equation (1) to the direction perpendicular to u_μ gives equation

$$\frac{\partial (T \sinh y_F)}{\partial t} + \frac{\partial (T \cosh y_F)}{\partial z} = 0, \tag{5}$$

which means the existence of a scalar function ϕ satisfying

$$\frac{\partial \phi}{\partial t} = T \cosh y_F,$$
$$\frac{\partial \phi}{\partial z} = -T \sinh y_F. \tag{6}$$

By using ϕ and Legendre transformation, Khalatnikov potential χ can be introduced *via* relation

$$\chi = \phi - tT \cosh y_F + zT \sinh y_F, \tag{7}$$

which changes the coordinate base of (t, z) to that of (ω, y_F)

$$t = \frac{e^\omega}{T_0} \left(\frac{\partial \chi}{\partial \omega} \cosh y_F + \frac{\partial \chi}{\partial y_F} \sinh y_F \right), \tag{8}$$

$$z = \frac{e^\omega}{T_0} \left(\frac{\partial \chi}{\partial \omega} \sinh y_F + \frac{\partial \chi}{\partial y_F} \cosh y_F \right), \tag{9}$$

where T_0 is the initial temperature of sQGP, and $\omega = -\ln(T / T_0)$. In terms of χ, Equation (4) can be rewritten as the so-called equation of telegraphy

$$\frac{\partial^2 \chi}{\partial \omega^2} - 2\beta \frac{\partial \chi}{\partial \omega} - \frac{1}{c_s^2} \frac{\partial^2 \chi}{\partial y_F^2} = 0, \quad \beta = \frac{1 - c_s^2}{2 c_s^2}. \tag{10}$$

With the expansion of created matter, its temperature becomes lower and lower. When the temperature drops from the initial temperature T_0 to the critical temperature T_c, phase transition occurs. This will modify the value of sound speed of fluid. In sQGP, $c_s = c_0 = 1 / \sqrt{3}$, which is the sound speed of a massless perfect fluid, being the maximum of c_s. In the hadronic state, $0 < c_s = c_h \leq c_0$. At the point of phase transition, c_s is discontinuous.

The solutions of Equation (10) for sQGP and hadronic state are, respectively [15],

$$\chi_0 (\omega, y_F) = \frac{Q_0 c_0}{2} e^{\beta_0 \omega} I_0 \left(\beta_0 \sqrt{\omega^2 - c_0^2 y_F^2} \right), \tag{11}$$

$$\chi_h (\omega, y_F) = \frac{Q_0 c_0}{2} S(\omega) I_0 [\lambda (\omega, y_F)], \tag{12}$$

where I_0 is the 0th order modified Bessel function, and

$$\beta_0 = \frac{\left(1 - c_0^2 \right)}{2 c_0^2} = 1,$$

$$S(\omega) = e^{\beta_h (\omega - \omega_c) + \beta_0 \omega_c}, \tag{13}$$

$$\lambda (\omega, y_F) = \beta_h c_h \sqrt{y_h^2 (\omega) - y_F^2},$$

where $\beta_h = (1 - c_h^2) / 2 c_h^2$, $\omega_c = -\ln(T_c / T_0)$, and $y_h(\omega) = [(\omega - \omega_c) / c_h] + (\omega_c / c_0)$. The Q_0 in Equations (11) and (12) is a free parameter determined by fitting the theoretical results with experimental data.

3. The Transverse Momentum Distributions of the Particles Produced in $p+p$ Collisions

3.1. The Energy of Quantum of Produced Matter. The nonextensive statistics is based on the following two postulations [32, 36].

(a) The entropy of a statistical system possesses the form of

$$s_q = \frac{1}{q - 1} \left(1 - \sum_{i=1}^{\Omega} p_i^q \right), \tag{14}$$

where p_i is the probability of a given microstate among Ω ones and q is a fixed real parameter. The defined entropy has the usual properties of positivity, equiprobability, and irreversibility, and, in the limit of $q \longrightarrow 1$, it reduces to the conventional Boltzmann-Gibbs entropy

$$s = -\sum_i p_i \ln p_i. \tag{15}$$

(b) The mean value of an observable $\mathcal{O}$ is defined as

$$\overline{\mathcal{O}}_q = \sum_{i=1}^{\Omega} p_i^q \mathcal{O}_i, \tag{16}$$

where $\mathcal{O}_i$ is the value of an observable $\mathcal{O}$ in the microstate i.

From the above two postulations, the average occupational number of quantum in the state with temperature T can be written in a simple analytical form [42]

$$\overline{n}_q = \frac{1}{\left[1 + (q-1)\left(E - \mu_B\right)/T\right]^{1/(q-1)} + \delta}. \tag{17}$$

Here, as usual, E is the energy of quantum, and μ_B is its baryochemical potential. For baryons $\delta = 1$ and for mesons $\delta = -1$. In the limit of $q \longrightarrow 1$, it reduces to the conventional Fermi-Dirac or Bose-Einstein distributions. Hence, the value of q in the nonextensive statistics represents the degree of deviation from the conventional statistics. Known from Equation (17), the average energy of quantum in the state with temperature T reads

$$\overline{E}_q$$
$$= \frac{m_T \cosh\left(y - y_F\right)}{\left\{1 + \left[(q-1)\left(m_T \cosh\left(y - y_F\right) - \mu_B\right)\right]/T\right\}^{1/(q-1)} + \delta}, \tag{18}$$

where y is the rapidity of quantum and $m_T = \sqrt{p_T^2 + m^2}$ is its transverse mass with rest mass m and transverse momentum p_T.

3.2. The Transverse Momentum Distributions of the Particles Produced in $p + p$ Collisions.

With the expansion of hadronic matter, its temperature becomes even lower. As the temperature drops to the so-called kinetic freeze-out temperature T_f, the inelastic collisions among hadronic matter stop. The yields of produced particles remain unchanged, becoming the measured results. According to Cooper-Frye scheme [43], the invariant multiplicity distributions of produced particles take the form [15, 43]

$$\frac{d^2 N}{2\pi p_T dy \, dp_T} = \frac{A}{(2\pi)^3}$$
$$\cdot \int_{-y_h(\omega_f)}^{y_h(\omega_f)} \left(\cosh y \frac{dz}{dy_F} - \sinh y \frac{dt}{dy_F}\right) \overline{E}_q \Big|_{T=T_f} dy_F, \tag{19}$$

where A is the area of overlap region of collisions, $\omega_f = -\ln(T_f / T_0)$, and the integrand takes values at the moment of $T = T_f$. The meaning of Equation (19) is evident. The part of integrand in the round brackets is proportional to the rapidity density of fluid [43]. Hence, Equation (19) is the convolution

of rapidity of fluid with the energy of the particles in the state with temperature T. From Equations (8) and (9)

$$\cosh y \frac{dz}{dy_F} - \sinh y \frac{dt}{dy_F}$$
$$= \frac{1}{T} c_s^2 \frac{\partial}{\partial \omega} \left(\chi + \frac{\partial \chi}{\partial \omega}\right) \cosh\left(y - y_F\right) \tag{20}$$
$$- \frac{1}{T} \frac{\partial}{\partial y_F} \left(\chi + \frac{\partial \chi}{\partial \omega}\right) \sinh\left(y - y_F\right).$$

Substituting χ in Equation (20) by the χ_h of Equation (12) and taking the values at the moment of $T = T_f$, it becomes

$$\left(\cosh y \frac{dz}{dy_F} - \sinh y \frac{dt}{dy_F}\right)\Big|_{T=T_f} = \frac{Q_0 c_0}{T_f} \left(\beta_h c_h\right)^2$$
$$\cdot S\left(\omega_f\right) \left[B\left(\omega_f, y_F\right) \sinh\left(y - y_F\right) \right. \tag{21}$$
$$\left. + C\left(\omega_f, y_F\right) \cosh\left(y - y_F\right)\right],$$

where

$$B\left(\omega_f, y_F\right)$$
$$= \frac{\beta_h y_F}{\lambda\left(\omega_f, y_F\right)} \left\{\frac{\beta_h c_h y_h\left(\omega_f\right)}{\lambda\left(\omega_f, y_F\right)} I_0\left[\lambda\left(\omega_f, y_F\right)\right] \right. \tag{22}$$
$$\left. + \left[\frac{\beta_h + 1}{\beta_h} - \frac{2\beta_h c_h y_h\left(\omega_f\right)}{\lambda^2\left(\omega_f, y_F\right)}\right] I_1\left[\lambda\left(\omega_f, y_F\right)\right]\right\},$$

$$C\left(\omega_f, y_F\right) = \left\{\frac{\beta_h + 1}{\beta_h} + \frac{\left[\beta_h c_h y_h\left(\omega_f\right)\right]^2}{\lambda^2\left(\omega_f, y_F\right)}\right\}$$
$$\cdot I_0\left[\lambda\left(\omega_f, y_F\right)\right] + \frac{1}{\lambda\left(\omega_f, y_F\right)} \left\{\frac{y_h\left(\omega_f\right)}{c_h} + 1 \right. \tag{23}$$
$$\left. - \frac{2\left[\beta_h c_h y_h\left(\omega_f\right)\right]^2}{\lambda^2\left(\omega_f, y_F\right)}\right\} I_1\left[\lambda\left(\omega_f, y_F\right)\right],$$

where $\lambda(\omega_f, y_F) = \beta_h c_h \sqrt{y_h^2(\omega_f) - y_F^2}$, I_1 is the 1st order modified Bessel function.

By using Equations (19) and (21)-(23), we can obtain the transverse momentum distributions of produced particles as shown in Figures 1, 2, 3, and 4.

Figure 1 shows the transverse momentum spectra of K_S^0, $K^+, K^-, \Lambda, \overline{\Lambda}, \Xi^-, \overline{\Xi}^+$, and $\Omega^- + \overline{\Omega}^+$ produced in $p+p$ collisions at $\sqrt{s} = 200$ GeV. The solid dots, circles, and solid triangles represent the experimental data of the STAR Collaboration [44]. The solid curves are the results calculated from Equation (19). The values of free parameters q, Q_0, and χ^2/NDF are listed in Table 1. It can be seen that the present model can give a good description of the transverse momentum distributions of strange particles. Since strangeness enhancement is originally proposed as a signature of sQGP produced in nuclear
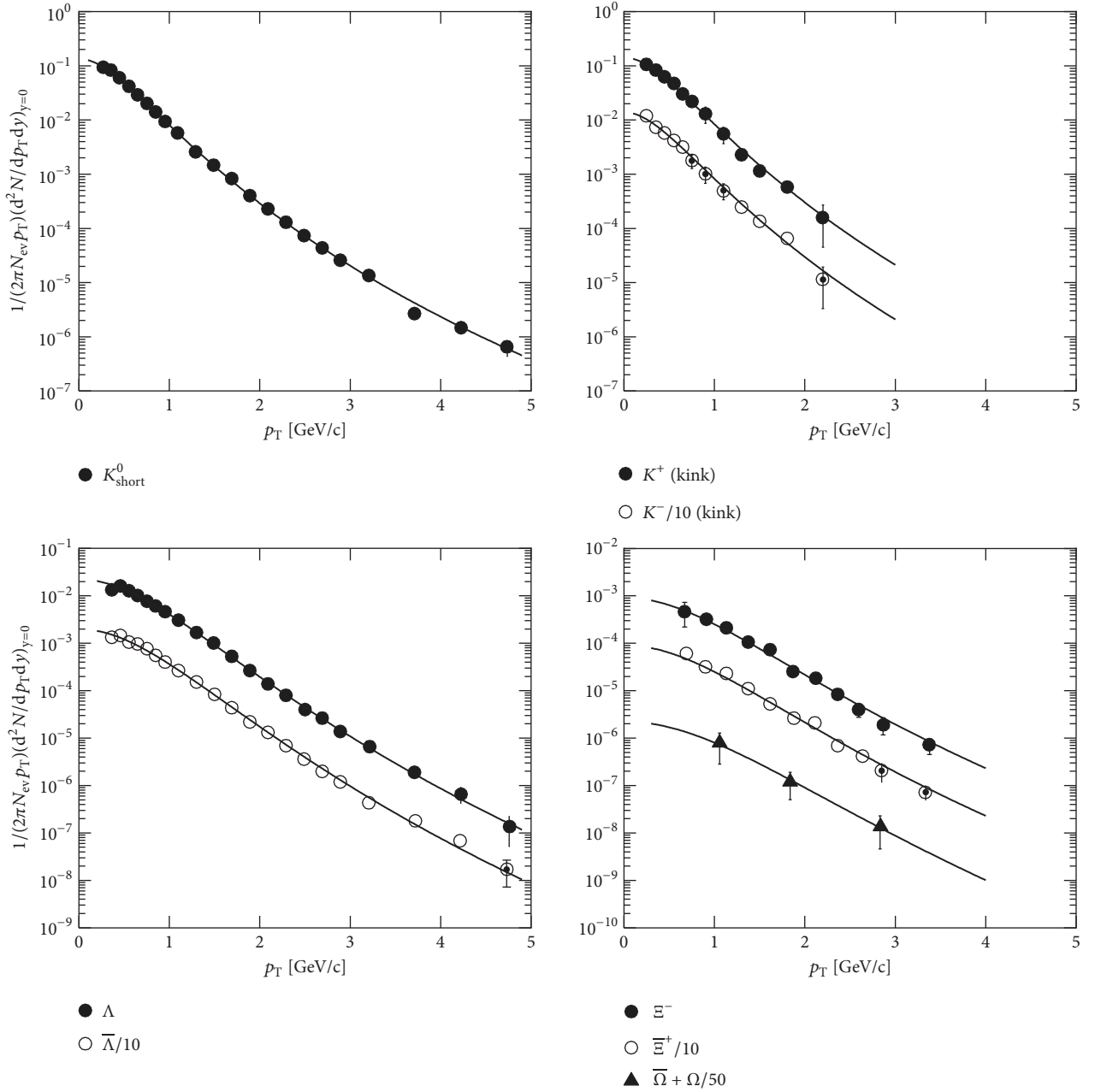
FIGURE 1: The transverse momentum distributions of strange particles ($|y| < 0.5$) produced in $p + p$ collisions at $\sqrt{s} = 200$ GeV. The solid dots, circles, and solid triangles represent the experimental data of the STAR Collaboration [44]. The solid curves are the results calculated from Equation (19).

TABLE 1: The values of q, Q_0, and χ^2/NDF obtained from the analyses of STAR data [44] in $p + p$ collisions at $\sqrt{s} = 200$ GeV.

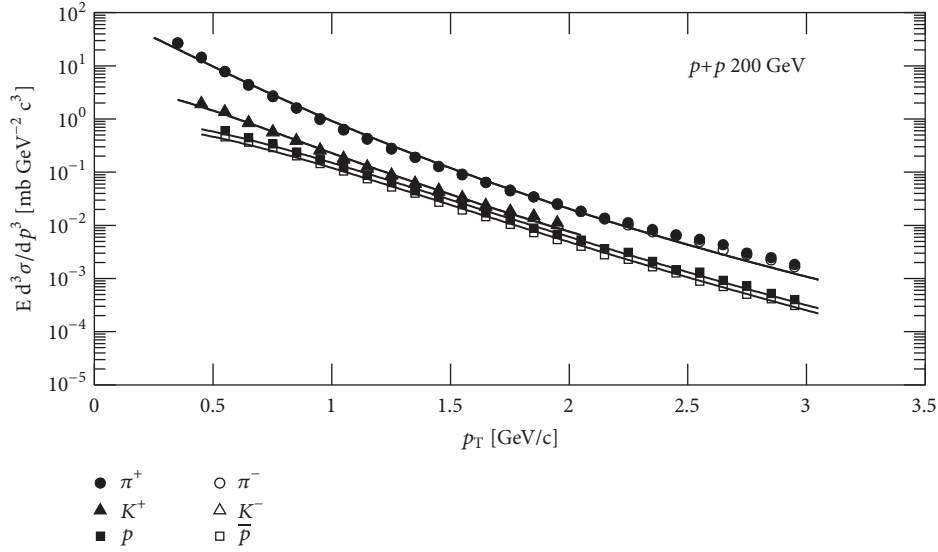| Parameters	K_S^0	K^+/K^-	$\Lambda/\overline{\Lambda}$	$\Xi^-/\overline{\Xi}^+$	$\Omega^- + \overline{\Omega}^+$
q	1.083±0.002	1.083±0.005	1.062±0.001	1.075±0.003	1.068±0.007
		1.083±0.006	1.062±0.001	1.075±0.003	
Q_0	0.084±0.005	0.087±0.012	0.379±0.026	0.026±0.006	0.016±0.010
		0.086±0.012	0.337±0.023	0.026±0.005	
χ^2/NDF	0.68	0.32/0.39	0.47/0.90	0.47/0.64	0.02

FIGURE 2: The transverse momentum distributions of π^+, π^-, K^+, K^-, p, and $\overline{p}$ produced in $p + p$ collisions at $\sqrt{s}$ = 200 GeV at midrapidity. The solid dots, solid triangles, solid squares, circles, triangles, and squares represent the experimental data of the PHENIX Collaboration [45]. The solid curves are the results calculated from Equation (19).

FIGURE 3: The transverse momentum distributions of p and $\overline{p}$ produced in $p + p$ collisions at $\sqrt{s}$ = 200 GeV in the whole measured p_T range. The solid squares and squares represent the experimental data of the PHENIX Collaboration [45]. The solid curves are the results calculated from Equation (19).
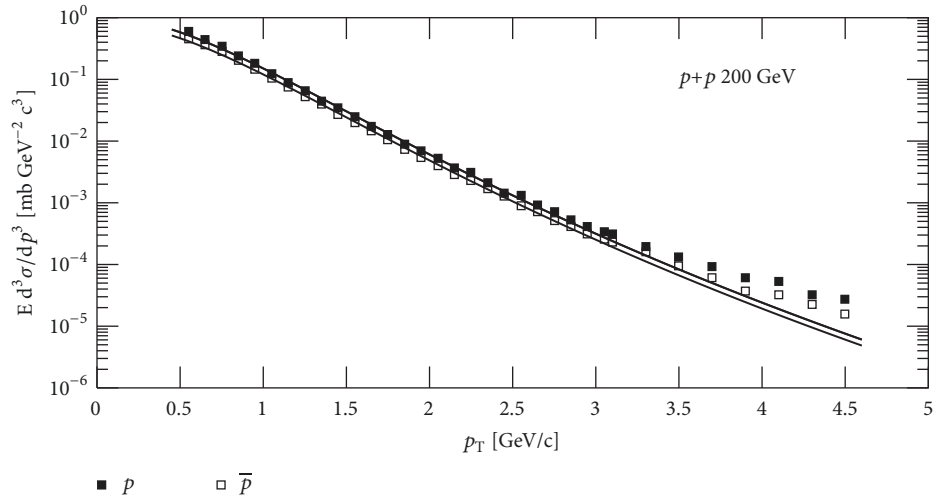
collisions, this proves the reasonableness of hypothesis given at the beginning of this paper that sQGP might appear in $p+p$ collisions.

Figure 2 presents the transverse momentum spectra of π^+, π^-, K^+, K^-, p, and $\overline{p}$ produced in $p + p$ collisions at $\sqrt{s}$ = 200 GeV. The solid dots, solid triangles, solid squares, circles, triangles, and squares represent the experimental data of the PHENIX Collaboration [45]. The solid curves are the results calculated from Equation (19). The values of free parameters q, Q_0, and χ^2/NDF are summarized in Table 2. The theoretical model can give a good description of the experimental data for π^+, π^-, K^+, K^- in the whole measured transverse momentum range, and for p and $\overline{p}$ in the range of

$p_T \leq 3.0$ GeV/c. In the range of $p_T > 3.0$ GeV/c, the deviation appears as shown in Figure 3, which shows the transverse momentum distributions of p and $\overline{p}$ in the whole measured p_T range.

Figure 4 shows the transverse momentum spectra of π^+, π^-, K^+, K^-, p, and $\overline{p}$ produced in $p + p$ collisions at $\sqrt{s}$ = 0.9, 2.76, and 7 TeV. The solid dots, solid triangles, solid squares, circles, triangles, and squares represent the experimental data of the CMS Collaboration [46]. The solid curves are the results calculated from Equation (19). The values of free parameters q, Q_0, and χ^2/NDF are summarized in Table 3.

In calculations, the sound speed in hadronic state takes the value of $c_h = 0.35$ [47, 48]. The critical temperature takes
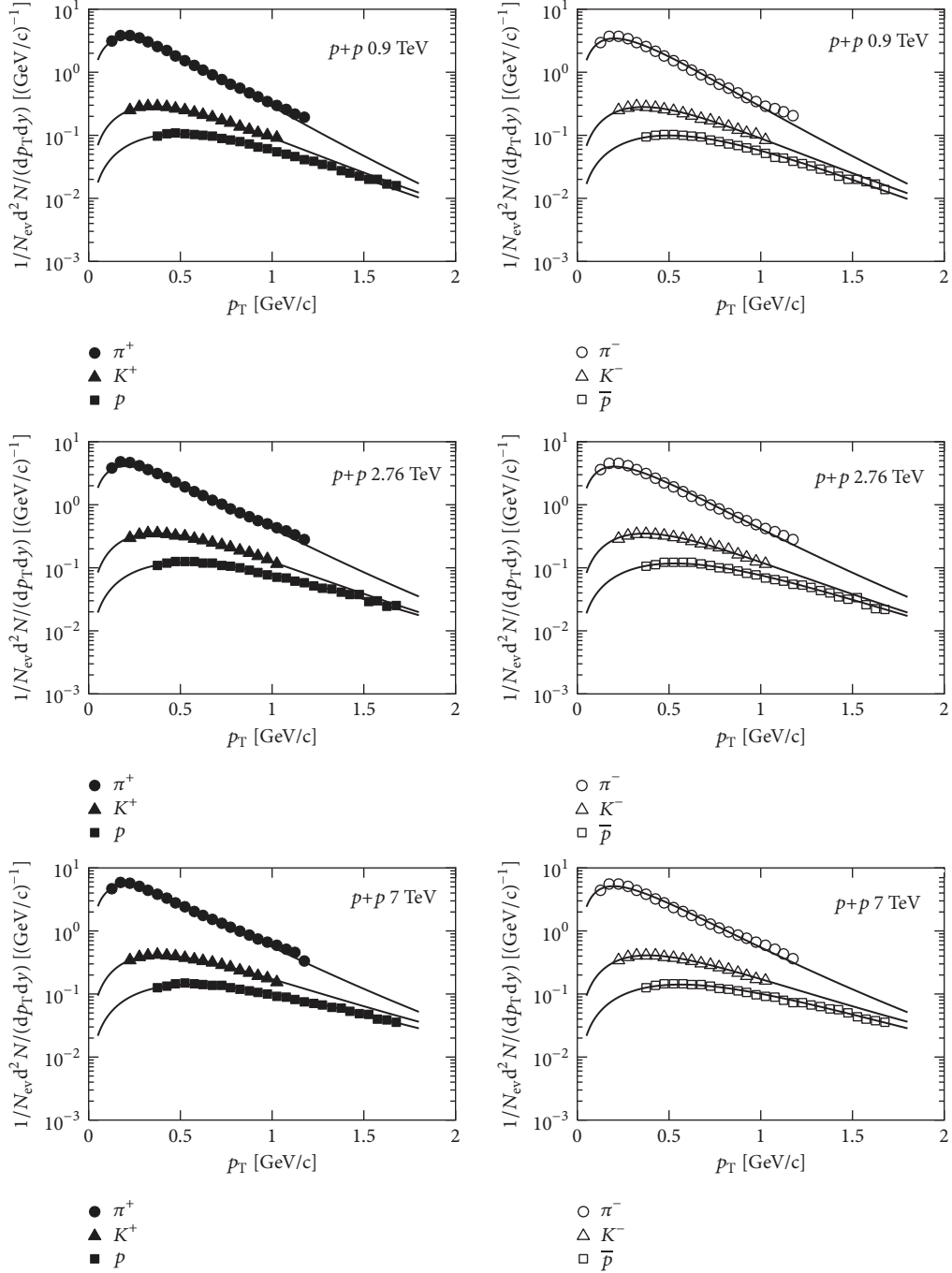
FIGURE 4: The transverse momentum distributions of the identified charged particles ($|y| < 1$) produced in $p + p$ collisions at $\sqrt{s} = 0.9$, 2.76, and 7 TeV (from top to bottom). The solid dots, solid triangles, solid squares, circles, triangles, and squares represent the experimental data of the CMS Collaboration [46]. The solid curves are the results calculated from Equation (19).

TABLE 2: The values of q, Q_0, and χ^2/NDF obtained from the analyses of PHENIX data [45] in $p + p$ collisions at $\sqrt{s} = 200$ GeV.

Parameters	π^+/π^-	K^+/K^-	$p/\overline{p}$
q	1.075±0.003	1.080±0.003	1.060±0.002
	1.075±0.003	1.080±0.003	1.060±0.001
Q_0	10.439±0.015	3.699±0.005	13.099±1.551
	10.342±0.015	3.602±0.006	10.479±1.221
χ^2/NDF	5.25/3.28	1.57/1.01	0.47/0.17

TABLE 3: The values of q, Q_0, and χ^2/NDF obtained from the analyses of CMS data [46] in $p + p$ collisions at LHC energies.

$\sqrt{s}$	Parameters	π^+/π^-	K^+/K^-	$p/\overline{p}$
	q	1.064±0.002	1.090±0.002	1.071±0.001
		1.064±0.003	1.090±0.002	1.071±0.001
0.9 TeV	Q_0	0.161±0.004	0.045±0.001	0.152±0.005
		0.159±0.004	0.044±0.002	0.145±0.003
	χ^2/NDF	8.50/10.85	0.37/0.47	1.10/1.84
	q	1.078±0.002	1.100±0.002	1.088±0.001
		1.078±0.002	1.100±0.002	1.088±0.001
2.76 TeV	Q_0	0.051±0.001	0.015±0.0004	0.037±0.001
		0.050±0.001	0.014±0.0004	0.036±0.001
	χ^2/NDF	8.90/8.25	0.30/0.62	1.75/1.35
	q	1.084±0.002	1.120±0.003	1.105±0.001
		1.084±0.003	1.120±0.002	1.105±0.001
7 TeV	Q_0	0.004±0.00004	0.001±0.00002	0.002±0.00004
		0.004±0.00008	0.001±0.00002	0.002±0.00002
	χ^2/NDF	7.28/7.69	0.23/0.35	1.13/1.43

the value of T_c = 0.16 GeV [49]. For $\sqrt{s}$ = 200 GeV, the initial temperature takes the value of T_0 = 0.35 GeV [50], the kinetic freeze-out temperature takes the values of T_f = 0.12 GeV for strange particles and pions, and, for protons, T_f =0.13 GeV from the investigation of [51], which also shows that the baryochemical potential takes the value of μ_B =0.01 GeV. For $\sqrt{s}$ = 0.9, 2.76, and 7 TeV, referring to [50], the initial temperatures are estimated to be T_0 = 0.4, 0.6, and 1.5 GeV, respectively. The kinetic freeze-out temperature takes the values of T_f =0.12 GeV for pions and kaons, and, for protons, T_f =0.13 GeV. The baryochemical potential takes the value of μ_B = 0 [51].

The parameters Q_0 and T_0 have the same effects. They all affect the amplitudes of the theoretical curves. They are different from parameter q which affects the slopes of the theoretical curves. From the above analysis we can see that the value of the parameter q increases with the increase of the CMS beam energy. However, the values of q do not seem completely consistent with the CMS and the RHIC beam energies.

4. Conclusions

By assuming the existence of longitudinal collective motion and long-range interactions in sQGP produced in $p + p$ collisions, the relativistic hydrodynamics including phase transition together with the nonextensive statistics is used to discuss the transverse momentum distributions of the particles produced in $p + p$ collisions at $\sqrt{s}$ = 0.2, 0.9, 2.76, and 7 TeV.

The theoretical model used in this paper contains rich information about the transport coefficients of fluid, such as the sound speed c_0 in sQGP, the sound speed c_h in hadronic state, the initial temperature T_0, the critical temperature T_c, the kinetic freeze-out temperature T_f, and the baryochemical potential μ_B. Except for T_0, the other five parameters take the values either from the widely accepted theoretical results or from experimental measurements. As for T_0, there are no

acknowledged values so far. In this paper, T_0 takes the values from other studies. The investigations of the present paper show the conclusions as follows.

(a) The theoretical model can give a good description of the currently available experimental data collected in $p + p$ collisions at RHIC and LHC energies with the only exception of p and $\overline{p}$ measured in the range of p_T > 3.0 GeV/c at $\sqrt{s}$ = 200 GeV, which might be caused by the hard scattering process [52]. To improve the fitting conditions, the results of perturbative QCD should be taken into account.

(b) The fitted values of q are close to 1. This means that the deviation between nonextensive statistics and conventional statistics is small, while it is this small difference that plays an essential role in fitting the experimental data.

Data Availability

The experimental data used to support the findings of this study have been deposited in https://doi.org/ 10.1103/PhysRevC.75.064901; https://doi.org/10.1103/Phys-RevC.83.064903; and https://doi.org/10.1140/epjc/s10052-012-2164-1.

Conflicts of Interest

The authors declare that there are no conflicts of interest regarding the publication of this paper.

Acknowledgments

References

[1] I. Arsene, I. G. Bearden, and D. Beavis, "Quark-gluon plasma and color glass condensate at RHIC? The perspective from the

BRAHMS experiment," *Nuclear Physics A*, vol. 757, no. 1-2, pp. 1–27, 2005.

[2] B. B. Back, M. D. Baker, and M. Ballintijn, "The PHOBOS perspective on discoveries at RHIC," *Nuclear Physics A*, vol. 757, no. 1-2, pp. 28–101, 2005.

[3] J. Adams, M. M. Aggarwal, and Z. Ahammed, "Experimental and theoretical challenges in the search for the quark–gluon plasma: The STAR Collaboration's critical assessment of the evidence from RHIC collisions," *Nuclear Physics A*, vol. 757, no. 1-2, pp. 102–183, 2005.

[4] K. Adcox, S. S. Adler, S. Afanasiev et al., "RHIC: Experimental evaluation by the PHENIX Collaboration," *Nuclear Physics A*, vol. 757, no. 1-2, pp. 184–283, 2005.

[5] T. Alexopoulos et al., "Mass-identified particle production in proton-antiproton collisions at $\sqrt{s}$ = 300, 540, 1000, and 1800 GeV," *Physical Review D*, vol. 48, Article ID 984, 1993.

[6] P. Lévai and B. Müller, "Transverse baryon flow as possible evidence for a quark-gluon-plasma phase," *Physical Review Letters*, vol. 67, no. 12, pp. 1519–1522, 1991.

[7] G. N. Fowler, E. M. Friedlander, R. M. Weiner, and G. Wilk, "Possible manifestation of quark-gluon plasma in multiplicity distributions from high-energy reactions," *Physical Review Letters*, vol. 57, no. 17, pp. 2119–2122, 1986.

[8] E. M. Friedlander and R. M. Weiner, "Evidence from very large transverse momenta of a change with temperature of velocity of sound in hadronic matter," *Physical Review Letters*, vol. 43, pp. 15–18, 1979.

[9] M. G. Albrow, S. Almehed, P. S. L. Booth et al., "Studies of proton-proton collisions at the CERN ISR with an identified charged hadron of high transverse momentum at 90°: (II) On the distribution of charged particles in the central region," *Nuclear Physics B*, vol. 145, no. 2-3, pp. 305–348, 1978.

[10] A. Bialas, R. A. Janik, and R. Peschanski, "Unified description of Bjorken and Landau 1+1 hydrodynamics," *Physical Review C nuclear physics*, vol. 76, no. 5, Article ID 054901, 2007.

[11] C. Y. Wong, "Landau hydrodynamics reexamined," *Physical Review C: Nuclear Physics*, vol. 78, no. 5, Article ID 054902, 2008.

[12] G. Beuf, R. Peschanski, and E. N. Saridakis, "Entropy flow of a perfect fluid in (1+1) hydrodynamics," *Physical Review C: Nuclear Physics*, vol. 78, no. 6, Article ID 064909, 2008.

[13] Z. J. Jiang, Y. Huang, and J. Wang, "A combined model for pseudorapidity distributions in p-p collisions at center-of-mass energies from 23.6 to 7000 GeV," *Chinese Physics C: Nuclear Physics*, vol. 40, no. 7, Article ID 074104, 2016.

[14] Z. W. Wang, Z. J. Jiang, and Y. S. Zhang, "The investigations of pseudorapidity distributions of final state multiplicities in Au+Au collisions at high energies," *University of Shanghai for Science and Technology*, vol. 31, p. 322, 2009.

[15] N. Suzuki, "One-dimensional hydrodynamical model including phase transition," *Physical Review C*, vol. 81, no. 4, Article ID 044911, 2010.

[16] E. K. G. Sarkisyan and A. S. Sakharov, "Relating multihadron production in hadronic and nuclear collisions," *The European Physical Journal C*, vol. 70, no. 3, pp. 533–541, 2010.

[17] A. Bialas and R. Peschanski, "Asymmetric (1+1)-dimensional hydrodynamics in high-energy collisions," *Physical Review C: Nuclear Physics*, vol. 83, no. 5, Article ID 054905, 2011.

[18] Z.-J. Jiang, J.-Q. Hui, and H.-P. Deng, "Unified hydrodynamics and pseudorapidity distributions of charged particles produced in heavy ion collisions at low energies at RHIC," *Chinese Physics Letters*, vol. 34, no. 5, Article ID 052501, 2017.

[19] Z. J. Jiang, Q. G. Li, and H. L. Zhang, "Revised Landau hydrodynamic model and the pseudorapidity distributions of charged particles produced in nucleus-nucleus collisions at maximum energy at the BNL Relativistic Heavy Ion Collider," *Physical Review C: Nuclear Physics*, vol. 87, no. 4, Article ID 044902, 2013.

[20] C. Gale, S. Jeon, and B. Schenke, "Hydrodynamic modeling of heavy-ion collisions," *International Journal of Modern Physics A*, vol. 28, no. 11, Article ID 1340011, 2013.

[21] U. Heinz and R. Snellings, "Collective flow and viscosity in relativistic heavy-ion collisions," *Annual Review of Nuclear and Particle Science*, vol. 63, no. 1, pp. 123–151, 2013.

[22] A. N. Mishra, R. Sahoo, E. K. G. Sarkisyan, and A. S. Sakharov, "Effective-energy budget in multiparticle production in nuclear collisions," *The European Physical Journal C*, vol. 74, Article ID 3147, 2014.

[23] Z. J. Jiang, Y. Zhang, H. L. Zhang, and H. P. Deng, "A description of the pseudorapidity distributions in heavy ion collisions at RHIC and LHC energies," *Nuclear Physics A*, vol. 941, pp. 188–200, 2015.

[24] H. Niemi, K. J. Eskola, and R. Paatelainen, "Event-by-event fluctuations in a perturbative QCD + saturation + hydrodynamics model: Determining QCD matter shear viscosity in ultrarelativistic heavy-ion collisions," *Physical Review C*, vol. 93, Article ID 024907, 2016.

[25] J. Noronha-Hostler, M. Luzum, and J.-Y. Ollitrault, "Hydrodynamic predictions for 5.02 TeV Pb-Pb collisions," *Physical Review C Nuclear Physics*, vol. 93, no. 3, Article ID 034912, 2016.

[26] J. S. Moreland and R. A. Soltz, "Hydrodynamic simulations of relativistic heavy-ion collisions with different lattice quantum chromodynamics calculations of the equation of state," *Physical Review C*, vol. 93, Article ID 044913, 2016.

[27] E. K. G. Sarkisyan, A. N. Mishra, R. Sahoo, and A. S. Sakharov, "Multihadron production dynamics exploring the energy balance in hadronic and nuclear collisions," *Physical Review D: Particles, Fields, Gravitation and Cosmology*, vol. 93, Article ID 054046, 2016.

[28] E. K. G. Sarkisyan, A. N. Mishra, R. Sahoo, and A. S. Sakharov, "Centrality dependence of midrapidity density from GeV to TeV heavy-ion collisions in the effective-energy universality picture of hadroproduction," *Physical Review D*, vol. 94, Article ID 011501, 2016.

[29] K. Jiang, Y. Zhu, W. Liu et al., "Onset of radial flow in $p + p$ collisions," *Physical Review C: Nuclear Physics*, vol. 91, no. 2, Article ID 024910, 2015.

[30] W. Alberico, A. Lavagno, and P. Quarati, "Non-extensive statistics, fluctuations and correlations in high-energy nuclear collisions," *The European Physical Journal C*, vol. 12, no. 3, pp. 499–506, 2000.

[31] M. Biyajima, T. Mizoguchi, N. Nakajima, N. Suzuki, and G. Wilk, "Modified Hagedorn formula including temperature fluctuation: Estimation of temperatures at RHIC experiments," *The European Physical Journal C*, vol. 48, no. 2, pp. 597–603, 2006.

[32] C. Tsallis, "Possible generalization of Boltzmann-Gibbs statistics," *Journal of Statistical Physics*, vol. 52, no. 1-2, pp. 479–487, 1988.

[33] D. F. Torres, H. Vucetich, and A. Plastino, "Early universe test of nonextensive statistics," *Physical Review Letters*, vol. 79, no. 9, pp. 1588–1590, 1997.

[34] D. B. Ion and M. L. Ion, "Entropic lower bound for the quantum scattering of spinless particles," *Physical Review Letters*, vol. 81, no. 26, pp. 5714–5717, 1998.

[35] A. K. Rajagopal, R. S. Mendes, and E. K. Lenzi, "Quantum statistical mechanics for nonextensive systems: Prediction for possible experimental tests," *Physical Review Letters*, vol. 80, no. 18, pp. 3907–3910, 1998.

[36] G. Kaniadakis, A. Lavagno, M. Lissia, and P. Quarati, "Anomalous diffusion modifies solar neutrino fluxes," *Physica A: Statistical Mechanics and its Applications*, vol. 261, no. 3-4, pp. 359–373, 1998.

[37] A. R. Plastino and A. Plastino, "Information theory, approximate time dependent solutions of Boltzmann's equation and Tsallis' entropy," *Physics Letters A*, vol. 193, no. 3, pp. 251–258, 1994.

[38] U. Tirnakli, F. Bykkilic, and D. Demirhan, "Some bounds upon the nonextensivity parameter using the approximate generalized distribution functions," *Physics Letters A*, vol. 245, no. 1-2, pp. 62–66, 1998.

[39] S. Grigoryan, "Using the Tsallis distribution for hadron spectra in pp collisions: pions and quarkonia at $\sqrt{s} = 5 - 13000$ Gev," *Physical Review D: Particles, Fields, Gravitation and Cosmology*, vol. 95, Article ID 056021, 2017.

[40] D. Thakur, S. Tripathy, P. Garg, R. Sahoo, and J. Cleymans, "Indication of a differential freeze-out in proton-proton and heavy-ion collisions at RHIC and LHC energies," *Advances in High Energy Physics*, vol. 2016, Article ID 4149352, 13 pages, 2016.

[41] J.-Q. Hui, Z.-J. Jiang, and D.-F. Xu, "A description of the transverse momentum distributions of charged particles produced in heavy ion collisions at RHIC and LHC energies," *Advances in High Energy Physics*, vol. 2018, Article ID 7682325, 9 pages, 2018.

[42] J. Cleymans and D. Worku, "The Tsallis distribution in proton–proton collisions at $\sqrt{s} = 0.9$ TeV at the LHC," *Journal of Physics G: Nuclear and Particle Physics*, vol. 39, no. 2, Article ID 025006, 2012.

[43] F. Cooper and G. Frye, "Landau's hydrodynamic model of particle production and electron-positron annihilation into hadrons," *Physical Review D*, vol. 11, Article ID 192, 1975.

[44] B. I. Abelev, J. Adams, and M. M. Aggarwal, "Strange particle production in $p + p$ collisions at $\sqrt{s} = 200$ GeV," *Physical Review C: Nuclear Physics*, vol. 75, Article ID 64901, 2007.

[45] A. Adare, S. Afanasiev, and C. Aidala, "Identified charged hadron production in $p + p$ collisions at $\sqrt{s} = 200$ and 62.4 GeV," *Physical Review C: Nuclear Physics*, vol. 83, Article ID 064903, 2011.

[46] S. Chatrchyan, V. Khachatryan, and A. M. Sirunyan, "Study of the inclusive production of charged pions, kaons, and protons in pp collisions at $\sqrt{s} = 0.9$, 2.76, and 7 TeV," *The European Physical Journal C*, vol. 72, Article ID 2164, 2012.

[47] A. Adare, S. Afanasiev, and C. Aidala, "Scaling Properties of Azimuthal Anisotropy in Au + Au and Cu + Cu Collisions at $\sqrt{s_{NN}} = 200$ GeV," *Physical Review Letters*, vol. 98, Article ID 162301, 2007.

[48] F.-H. Liu, T. Tian, J.-X. Sun, and B.-C. Li, "What can we learn from (Pseudo) rapidity distribution in high energy collisions?" *Advances in High Energy Physics*, vol. 2014, Article ID 863863, 10 pages, 2014.

[49] D. Teaney, J. Lauret, and E. V. Shuryak, "Flow at the SPS and RHIC as a quark-gluon plasma signature," *Physical Review Letters*, vol. 86, no. 21, pp. 4783–4786, 2001.

[50] M. Strickland, "Thermal $\Upsilon(1s)$ and χ_{b1} suppression at $\sqrt{(s_{NN})} = 2.76$ TeV Pb-Pb Collisions at the LHC," *Physical Review Letters*, vol. 107, Article ID 132301, 2011.

[51] B. I. Abelev, M. M. Aggarwal, and Z. Ahammed, "Systematic measurements of identified particle spectra in pp, d+Au, and Au+Au collisions at the STAR detector," *Physical Review C: Nuclear Physics*, vol. 79, no. 3, Article ID 034909, p. 58, 2009.

[52] H. L. Lao, F. H. Liu, and R. A. Lacey, "Extracting kinetic freeze-out temperature and radial flow velocity from an improved Tsallis distribution," *The European Physical Journal A*, vol. 53, p. 44, 2017.